



UNIVERSITY OF
BIRMINGHAM

**Synthesis and Characterization of
Porous Zinc Carboxyethylphosphonates:
a New Class of Ion-exchangeable Metal-organic
Framework Compounds**

by

Chao Zhao

Supervisors: Dr. Paul A. Anderson
Dr. Ian J. Shannon

A thesis submitted to The University of Birmingham for
the degree of Doctor of Philosophy

The School of Chemistry
College of Engineering and Physical Sciences
The University of Birmingham
October 2012

UNIVERSITY OF
BIRMINGHAM

University of Birmingham Research Archive

e-theses repository

This unpublished thesis/dissertation is copyright of the author and/or third parties. The intellectual property rights of the author or third parties in respect of this work are as defined by The Copyright Designs and Patents Act 1988 or as modified by any successor legislation.

Any use made of information contained in this thesis/dissertation must be in accordance with that legislation and must be properly acknowledged. Further distribution or reproduction in any format is prohibited without the permission of the copyright holder.

Abstract

Metal-organic framework (MOF) materials, assembled by the connection of metal cations or clusters through different organic groups, have been the subject of great interest recently. Unfortunately to date, although several hundred different metal-organic frameworks have been discovered and the properties as well as possible applications have been widely investigated, the number of MOFs known to undergo ion exchange remains a tiny subset of the total¹⁻⁴. In a significant proportion of those the exchange involves coordinatively saturated metal ions, whose effect on the desired properties is usually rather limited. In this thesis we present a synthetic route to the formation of a series of new zinc carboxyethylphosphonate materials, exemplified by $(\text{NH}_4)_2[\text{Zn}_2(\text{O}_3\text{PCH}_2\text{CH}_2\text{COO})_2] \cdot 5\text{H}_2\text{O}$ (henceforth denoted BIRM-1, standing for the first MOF synthesized in the University of Birmingham). It is a novel highly crystalline ion exchangeable phosphonate based metal organic framework with a three dimensional porous structure. Compared to most other metal organic frameworks, BIRM-1 has the advantage of containing exchangeable ammonium cations within the channels. The ability to undergo ion-exchange is of interest in its own right, but also enables fine-tuning of the properties with a view to produce functional porous MOF material. The investigations performed into the ion-exchange properties of BIRM-1

with Li^+ , Na^+ , K^+ , Mg^{2+} , Mn^{2+} and Co^{2+} by a variety of techniques were described in this thesis. The structural frameworks of K^+ , Mg^{2+} and Co^{2+} exchanged products were investigated with both powder X-ray diffraction data by Rietveld refinement and the single crystal X-ray diffraction structure analysis. In addition, the dehydration and rehydration as well as the structure flexibility for BIRM-1 and the exchanged products were explored and the hydrogen storage attempts with K^+ exchanged product were also investigated.

Acknowledgement

In the first place, I would like to express my deepest sense of gratitude to Dr. Paul A. Anderson and Dr. Ian J. Shannon for giving me the chance to collaborate in their research groups, and also for their patient supervisions and support during my PhD research as well as giving me their invaluable comments and corrections to get this thesis to its final shape. Also as an international student, I would like to record my thankfulness to them for their help in my five years life in Birmingham. Above all and the most needed, they provided me unflinching encouragement and support in various ways. Thank you both very much.

Many thanks to all the past and present members of Paul and Ian's groups. Thanks to Dr. Philip Chater, Dr. Alvaro Garcia, Dr. Matt Turnbull, Dr. Laura Perkins, Dr. Ian Evans, Dr. Marco López Martínez, Dr. Alex Kersting, Dr. David Hewett, Dr. Suparb Tamuang (aka Ying), Tom Carey, Selina Omonmhenle and Trang Nguyen for science discussions and the pleasure of working together. It is a pleasure to express my gratitude wholeheartedly to the rest of my colleagues on 5th floor Chemistry for sharing experiences and knowledge during the time of study and creating such a great friendship at the office, at the football pitch and many places in between.

I am thankful to Dr. Louise Male for her kind assistance on the single crystal X-ray diffraction analysis. And my sincere thanks to Dr. Jackie Deans for always willing to give help and advice on the instruments. I would also like to thank Dr. Steve Tedds and Dr. Dan Reed for their assistance on collecting IGA data and their valuable advice on hydrogen adsorption results. I have also benefited from advice and guidance from Paul Stanley and Theresa Morris for their technical assistance in SEM/EDX.

I convey special acknowledgement to Dr. Tzu-Yu Chen (aka Evin) for her enjoyable company in the office and especially for her great delicacies, and for Dr. Benjamin de Laume and Dr. Yasmin Begum who are always willing to lend a helping hand. And also a big thank you to Dr. Chengbo Mou who accompanied me through the tough viva preparing time and always reminded me to be passionate about my research. Many thanks to my brother, a great listener, Mr. Yaoze Liu for your support, encouragement and the precious friendship. I would also like to take this opportunity to deliver my thanks to the School of Chemistry and the Henry Lester Trust for providing financial support for my PhD research.

Dedication

This thesis is dedicated to my father (Mr. Zhongdi Zhao) and my mother (Mrs. Fei Zheng) for their guidance and sacrifice throughout my life, and also for giving me the foundations and values that I've had to be the person I am today. Without their support this would not have been possible.

This thesis is also dedicated to one special person.

To my wife Zhonghua Du. Never did I think I could be embarking on the journey of my life with such an understanding, gentle and amazing person to travel with. This is for you.

List of Abbreviations and Symbols

Abbreviation	Description
MOFs	Metal Organic Frameworks
BIRM-1	(NH ₄) ₂ [Zn ₂ (O ₃ PCH ₂ CH ₂ COO) ₂] · 5H ₂ O, the first MOF synthesized in the University of Birmingham
Li ⁺ -BIRM-1	Lithium ion exchanged BIRM-1
Na ⁺ -BIRM-1	Sodium ion exchanged BIRM-1
K ⁺ -BIRM-1	Potassium ion exchanged BIRM-1
Mg ²⁺ -BIRM-1	Magnesium ion exchanged BIRM-1
Mn ²⁺ -BIRM-1	Manganese ion exchanged BIRM-1
Co ²⁺ -BIRM-1	Cobalt ion exchanged BIRM-1
SBU	Secondary building units
BET surface area	Brunauer-Emmett-Teller surface area
PSD	Position sensitive detector
XRD	X-ray diffractometer
DTA	Differential thermal analysis
TGA	Thermogravimetric analysis
MS	Mass spectrometry
SEM	Scanning electron microscopy
EDX	Energy-dispersive X-ray spectroscopy
IGA	Intelligent gravimetric analyser
ICDD	International center for diffraction data
bdc	1,4-benzenedicarboxylate
tmbdc	tetramethylterephthalate
bte	4,4',4''-[benzene-1,3,5-triyl-tris(ethyne-2,1-diyl)]tribenzoate
btb	4,4',4''-benzene-1,3,5-triyltribenzoate
bbc	4,4',4''-[benzene-1,3,5-triyl-tris(benzene-4,1-diyl)]tribenzoate
dabco	4-diazabicyclo[2.2.2]octane
4,4'-bipy	4,4'-bipyridine
dma	dimethylamine
dmf	<i>N,N</i> -dimethylformamide
teta	triethylene tetramine
H ₃ bt	1,3,5-benzene-tristetrazol-5-yl
ed	ethylenediamine
deta	diethylenetriamine
aps	3-aminopropyltriethoxysilane
H ₃ pb	4-phosphonobenzoic acid
bpdc	biphenyl-4,4'-dicarboxylate

Content

1. INTRODUCTION.....	1
1.1 HISTORICAL DEVELOPMENT OF METAL–ORGANIC FRAMEWORKS	1
1.2 SYNTHESIS OF MOFs	4
1.3 CARBOXYLATE-BASED MOFs	8
1.4 PHOSPHONATE-BASED MOFs	16
1.5 APPLICATIONS FOR POROUS MOFs.....	28
1.5.1 Gas Storage and Separation in MOFs.....	28
1.5.2 Catalysis in MOFs.....	32
1.5.3 Other Applications	35
1.6 AIMS OF THESIS	35
 2. EXPERIMENTAL	 37
2.1 SOLID STATE SYNTHESIS.....	37
2.1.1 Hydrothermal Synthesis.....	37
2.1.2 Cation Exchange.....	37
2.2 CRYSTALLOGRAPHY AND DIFFRACTION	38
2.2.1 Fundamental Crystallography ¹¹⁵	38
2.2.2 Lattice Planes and Miller Indices	40
2.2.3 Diffraction and Interference.....	41
2.2.4 Powder X-ray Diffraction ^{114, 117}	44
2.3 STRUCTURE DETERMINATION FROM POWDER X-RAY DIFFRACTION ¹¹⁷⁻¹¹⁹	49
2.3.1 Unit Cell Parameter Determination	49
2.3.2 Initial Structural Model Determination	50
2.3.3 Rietveld Refinement.....	51

2.4	PHASE IDENTIFICATION BY POWDER X-RAY DIFFRACTION	55
2.4.1	Quantitative Phase Analysis ¹¹⁴	55
2.5	SCANNING ELECTRON MICROSCOPY.....	56
2.6	ENERGY-DISPERSIVE X-RAY SPECTROSCOPY	57
2.7	FOURIER TRANSFORM INFRARED SPECTROSCOPY	58
2.8	FLAME PHOTOMETRY.....	60
2.9	THERMOGRAVIMETRIC ANALYSIS.....	61
2.10	MASS SPECTROMETRY	62
2.11	HYDROGEN UPTAKE MEASUREMENT.....	63

3. SYNTHESIS AND CHARACTERIZATION OF A NEW ZINC PHOSPHONATE

FRAMEWORK MATERIAL BIRM-1	65
3.1 INTRODUCTION	65
3.2 EXPERIMENTAL	66
3.2.1 Synthesis of $\text{Zn}(\text{O}_3\text{PCH}_2\text{CH}_2\text{COOH})\cdot\text{H}_2\text{O}$	66
3.2.2 Synthesis of BIRM-1	67
3.2.3 Synthesis of $(\text{NH}_4)[\text{Zn}(\text{O}_3\text{PCH}_2\text{CH}_2\text{COO})]$	68
3.3 SYNTHESIS OPTIMIZATION	68
3.3.1 Synthesis of $\text{Zn}(\text{O}_3\text{PCH}_2\text{CH}_2\text{COOH})\cdot\text{H}_2\text{O}$	68
3.3.2 Synthesis of $(\text{NH}_4)_2[\text{Zn}_2(\text{O}_3\text{PCH}_2\text{CH}_2\text{COO})_2]\cdot 5\text{H}_2\text{O}$	70
3.3.3 Characterization of BIRM-1	71
3.4 OPTIMIZATIONS OF THE SYNTHESIS OF BIRM-1	80
3.5 SYNTHESIS OF $(\text{NH}_4)[\text{Zn}(\text{O}_3\text{PCH}_2\text{CH}_2\text{COO})]$	83
3.6 DISCUSSION	85
3.7 CONCLUSION	87

4. ION EXCHANGE STUDIES WITH ALKALI METAL CATIONS: LITHIUM (I), SODIUM (I) AND POTASSIUM (I)

4.1	INTRODUCTION.....	88
4.2	EXPERIMENTAL	89

4.2.1	Ion Exchange Optimization with Li^+ , Na^+ and K^+	89
4.3	POTASSIUM-EXCHANGED BIRM-1 (K^+ -BIRM-1).....	90
4.3.1	Laboratory Powder XRD	91
4.3.2	SEM and EDX.....	92
4.3.3	Thermal Stability	94
4.3.4	Fourier Transform Infrared Spectroscopy	97
4.4	LITHIUM-EXCHANGED BIRM-1 (Li^+ -BIRM-1).....	99
4.4.1	Laboratory Powder XRD	99
4.4.2	Flame Photometry.....	101
4.4.3	Thermal Stability	102
4.4.4	Fourier Transform Infrared Spectroscopy	104
4.5	SODIUM-EXCHANGED BIRM-1 (Na^+ -BIRM-1)	106
4.5.1	Laboratory Powder XRD	106
4.5.2	Flame Photometry.....	108
4.5.3	Thermal Stability	109
4.5.4	Fourier Transform Infrared Spectroscopy	111
4.6	CRYSTAL STRUCTURE DETERMINATION	112
4.6.1	K^+ -BIRM-1 Structure Determination from Powder Diffraction Data..	113
4.6.2	Single Crystal XRD Structure of K^+ -BIRM-1	131
4.6.3	Structure Comparison	135
4.6.4	Na^+ -BIRM-1 Structure Determination	138
4.7	CONCLUSION	139

5.	ION EXCHANGE OF BIRM-1 WITH DIVALENT CATIONS: COBALT(II),	
	MANGANESE(II) AND MAGNESIUM(II)	140
5.1	INTRODUCTION.....	140
5.2	EXPERIMENTAL	140
5.2.1	Ion Exchange with Cobalt(II), Magnesium and Manganese(II) Ions...	140
5.3	COBALT(II)-EXCHANGED BIRM-1 (Co^{2+} -BIRM-1)	141
5.3.1	Laboratory Powder XRD	141
5.3.2	SEM and EDX.....	143
5.3.3	Thermal Stability	144

5.3.4	Fourier Transform Infrared Spectroscopy	146
5.4	MANGANESE (II)-EXCHANGED BIRM-1 (Mn^{2+} -BIRM-1).....	148
5.4.1	Laboratory Powder XRD	148
5.4.2	SEM and EDX.....	149
5.4.3	Thermal Stability	150
5.4.4	Fourier Transform Infrared Spectroscopy	153
5.5	MAGNESIUM-EXCHANGED BIRM-1 (Mg^{2+} -BIRM-1).....	154
5.5.1	Laboratory Powder XRD	154
5.5.2	SEM and EDX.....	155
5.5.3	Thermal Stability	157
5.5.4	Fourier Transform Infrared Spectroscopy	159
5.6	STRUCTURE DETERMINATION OF Co^{2+} -BIRM-1	161
5.6.1	Structure Determination by Single Crystal X-ray Diffraction	161
5.6.2	Structure Determination by Powder X-ray Diffraction.....	162
5.6.3	Discussion	173
5.7	STRUCTURE DETERMINATION OF Mg^{2+} -BIRM-1.....	175
5.8	STRUCTURE DETERMINATION OF Mn^{2+} -BIRM-1	180
5.9	CONCLUSION	180

6. HYDROGEN UPTAKE ATTEMPTS AND DE/REHYDRATION

INVESTIGATIONS.....	181
6.1 INTRODUCTION.....	181
6.2 EXPERIMENTAL	182
6.2.1 Hydrogen Uptake Measurement	182
6.2.2 Dehydration and Rehydration Attempts	183
6.2.3 Organic Solvent Treatment of K^{+} -BIRM-1	184
6.3 HYDROGEN UPTAKE ATTEMPTS WITH K^{+} -BIRM-1	185
6.4 DEHYDRATION AND REHYDRATION ATTEMPTS WITH K^{+} -BIRM-1.....	188
6.5 DEHYDRATION AND REHYDRATION ATTEMPTS WITH BIRM-1 AND OTHER ION-EXCHANGED FORMS.....	192
6.6 EVACUATION ATTEMPTS WITH ORGANIC SOLVENT TREATED K^{+} -BIRM-1	198
6.7 CONCLUSION	204

7. CONCLUSION AND FUTURE WORK	206
REFERENCE	212
APPENDIX 1 CRYSTALLOGRAPHIC DATA OF BIRM-1	220
APPENDIX 2 INDEX DETAILS	224
2.1 K ⁺ -BIRM-1.....	224
2.2 Li ⁺ -BIRM-1.....	225
2.3 Na ⁺ -BIRM-1.....	226
2.4 Co ²⁺ -BIRM-1.....	227
2.5 Mn ²⁺ -BIRM-1.....	228
2.6 Mg ²⁺ -BIRM-1	229
APPENDIX 3 FLAME PHOTOMETRY.....	230
3.1 Li ⁺ -BIRM-1.....	230
3.1.1 Li ⁺ -BIRM-1 Sample Solution Preparation.....	230
3.1.2 Lithium ion Content Calculation	230
3.2 Na ⁺ -BIRM-1.....	231
3.2.1 Na ⁺ -BIRM-1 Sample Solution Preparation.....	231
3.2.2 Sodium ion Content Calculation.....	231
APPENDIX 4 CRYSTALLOGRAPHIC DATA OF K⁺-BIRM-1	232
APPENDIX 5 CRYSTALLOGRAPHIC DATA OF THE PREVIOUSLY PARTIALLY SOLVED CO²⁺-BIRM-1	238
APPENDIX 6 CRYSTALLOGRAPHIC DATA OF MG²⁺-BIRM-1	242
APPENDIX 7 IR SPECTRA.....	248
7.1 DEHYDRATED AND REHYDRATED BIRM-1	248
7.2 IR SPECTRA FOR ORGANIC TREATED K ⁺ -BIRM-1	251

Chapter 1

Introduction

1.1 Historical Development of Metal–Organic Frameworks

As a relatively new family of porous materials, metal–organic frameworks (MOFs) have attracted attention from a wide range of industrial and academic researchers in recent years, and have developed into one of the most prolific fields in chemistry and materials science^{5, 6}. These compounds are highly crystalline inorganic–organic hybrid materials constructed of single metal ions or polynuclear metal clusters linked by multidentate organic ligands principally through coordinate bonds^{7, 8}. The dynamic behind the very rapid development in this area is potentially superior characteristics and properties, with the possibility of designing new three-dimensional (3D) frameworks and functionality^{9, 10}.

The synthesis of MOFs can be recognized to have developed from the fields of coordination and solid state chemistry¹¹, in which a long history has been dedicated to the investigation of coordination polymers that formed with metal ions linked with various organic ligands^{12, 13}. The first review of this area was published in 1964, but the interest in porous coordination networks was raised much later, starting around 1990. In 1989 and 1990, the foundations for future MOFs was set by Hoskins *et al.*¹⁴.

¹⁵ for the synthesis of a series of 3D rod-linked frameworks with large cavities and windows (exemplified by $\{\text{Cu}^{\text{I}}[\text{C}(\text{C}_6\text{H}_4\text{CN})_4]\}_n^{n+}$, Figure 1.1), which demonstrated a wide range of general synthetic approaches to a variety of new, unusual and useful materials. This forecast has been subsequently validated by many scientists around the world, through the synthesis of a large range of stable crystalline solid porous materials¹⁶ for a wide number of potential applications^{9, 10, 17-19}.

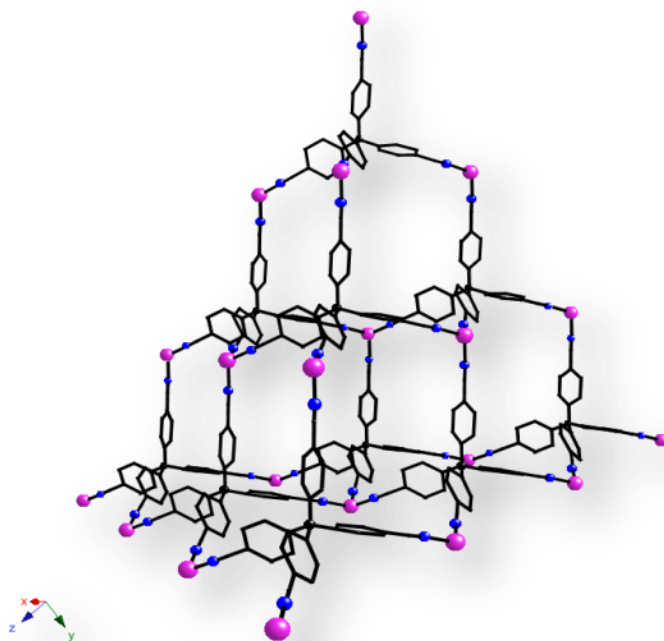


Fig. 1.1 Framework structure of $\{\text{Cu}^{\text{I}}[\text{C}(\text{C}_6\text{H}_4\text{CN})_4]\}_n^{n+}$, demonstrating the rod-linked (C-C₆H₄-CN-Cu) diamond-like network; hydrogen atoms and internal solvent have been omitted for clarity; colour scheme: Cu – purple, N – blue, C – black.

From 1995, the field of coordination polymers expanded greatly. In 1995, the group of O. M. Yaghi demonstrated the synthesis of a layered Co microporous MOF, which showed reversible sorption properties with aromatic molecules²⁰. Two years later, Kitagawa *et al.* reported three MOFs with 3D porous structure, and were able to demonstrate room temperature gas adsorption properties with O₂, N₂ and CH₄²¹. In 1999, the synthesis of a very interesting 3D material MOF-5 with pore topology was

reported by Li *et al.*²² This work introduced the concept of isorecticular synthesis and led to further developments in the design of new crystalline solid state materials^{23, 24}. As the syntheses and structures of a large number of isorecticular metal organic frameworks (IRMOFs, IR standing for isorecticular, indicating the structures have the same topology²³) were published by Yaghi's group in 2002²⁵ (Figure 1.2), the concept of isorecticular chemistry became widespread and the name of MOF was made prevalent²⁶.

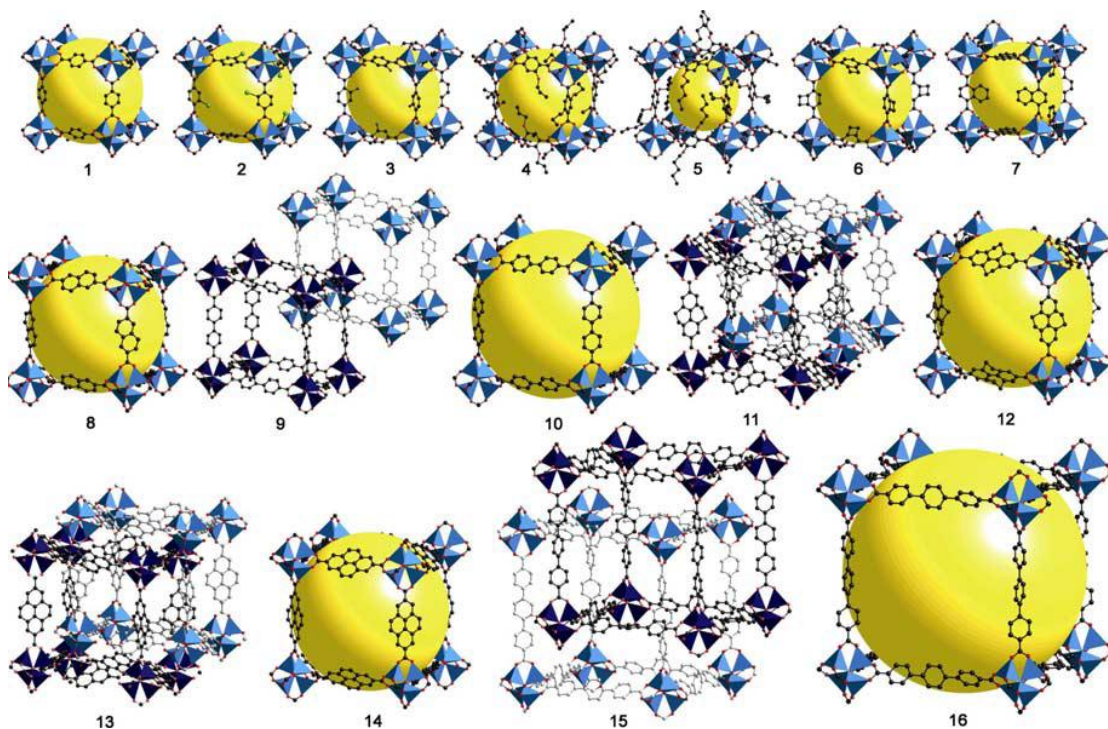


Fig. 1.2 Framework structures of IRMOF family synthesized with different dicarboxylic acid ligands, differing in functionality (IRMOF-1 to IRMOF-7), in length (IRMOF-8 to IRMOF-16) and catenated phases (IRMOF-9, -11, -13 and -15); hydrogen atoms and internal solvent molecules have been omitted for clarity; colour scheme: ZnO_4 – blue tetrahedra, Br – green, N – blue, O – red and C – black; the yellow spheres illustrate the void space inside the framework (reproduced from reference 5⁵).

Based on this concept, a large number of exciting compounds are being created and investigated currently. Starting from 2002, the group of Férey reported an

extensive series of porous MOFs termed MIL-n (MIL standing for Materials of Institute Lavoisier), some of which exhibit very interesting large-magnitude reversible swelling properties (MIL-53²⁷ and MIL-88²⁸, -89²⁹). Since the structural model for a mixed ligand compound [Cu₂(dicarboxylate)₂(diamine)] was first published by Seki *et al.*³⁰, numerous studies have been dedicated to the synthesis of this type of mixed-component metal–organic framework by varying these organic components directly during synthesis or via post-synthetic modifications to further enhance the functionalities^{31–33}. Nowadays, the MOF family has been extended to imidazolate-based compounds (known as zeolitic imidazole frameworks, ZIFs). They are a special class of MOFs, in which the metal ions are linked by substituted imidazolate³⁴ with a wide range of different functional groups to form zeolite-type materials, which normally have excellent chemical, and thermal stabilities and show the potential for selective gas adsorption^{33, 35, 36}.

The historical development of this new class of porous solids demonstrates only the tip of the iceberg of exhilarating MOFs, with different structural topologies and possible applications, over the last two decades. The field of MOF chemistry has matured, and researchers from different areas beyond chemistry are involved in the construction of possible combinations of new functional ligands with different metal clusters, which facilitates the navigation within this field for current and future research.

1.2 Synthesis of MOFs

Naturally, as in any mature research area, a systematic investigation of the material is always needed and a set of principles should be established for the creation of porous

solid state materials. For MOFs, crystal growth techniques such as slow diffusion, layering solution, hydrothermal and solvothermal are usually used to obtain such crystalline porous materials²³. As exemplified by the work of Hoskins and Robson^{14, 15}, early MOF synthesis was largely achieved by low temperature methods such as precipitation reactions, assisted by recrystallization or slow evaporation of the solvent¹¹. However, as the field has shifted towards the design of larger and more functional pore materials, with bigger molecules and more complicated reagents used to construct the framework, hydro/solvothermal synthesis with comparatively high temperatures (100 °C – 250 °C) have become a more convenient method³⁷. Reactions based on this method are generally carried out in a polytetrafluoroethylene (Teflon™) liner sealed by a stainless steel autoclave under elevated temperature (above 100 °C) and elevated or autogeneous pressure (above 1 bar) conditions. Under the resultant pressure–temperature conditions, the solubility of the reagents is amplified and the chemical behaviour of the solution is modified to favour formation of desired phases³⁸.

Even with the convenience of the hydrothermal synthesis techniques, an understanding of how to obtain desired porous frameworks and more importantly tune the chemical environment of the internal space for certain applications remains a longstanding challenge. Before Yaghi *et al.* first raised the concept of Isorecticular Chemistry²³, most of the MOFs obtained were synthesized rather than designed. In the reticular synthesis, a design of an open network can be assembled by holding the rigid secondary building units (SBUs) with the organic linkers²³. In most cases, reaction conditions could result in SBUs with specific geometry leading the formation of a predetermined structure. Thus 3D framework MOFs can be constructed by following

a target network “blueprint” and identification of the required building blocks and linkers, as well as the conditions^{8, 16} (See Figure 1.3 for example).

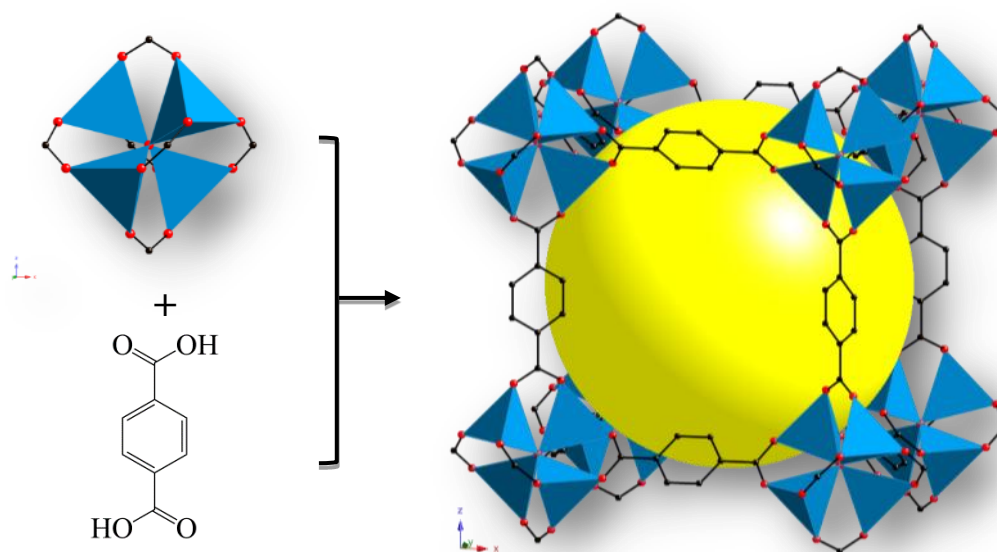


Fig. 1.3 Framework structure of SBU (upper left) of IRMOF family, $\text{Zn}_4\text{O}(\text{COO})_6$, comprising four ZnO_4 tetrahedra and six carboxylate groups, connected with organic ligand 1,4-benzenedicarboxylate (bdc) to form MOF-5; hydrogen atoms and internal solvent molecules have been omitted for clarity; colour scheme: ZnO_4 – blue tetrahedra, O – red and C – black; yellow sphere illustrates the void space inside the framework.

An important step forward for the synthesis of MOFs is to use the same SBUs but using extended or functional linkers to create larger porous MOFs or functional porous frameworks. The best example to demonstrate this is the IRMOF family²⁵. These MOFs shared the same SBU geometry with MOF-5, but are linked with different ditopic ligands.

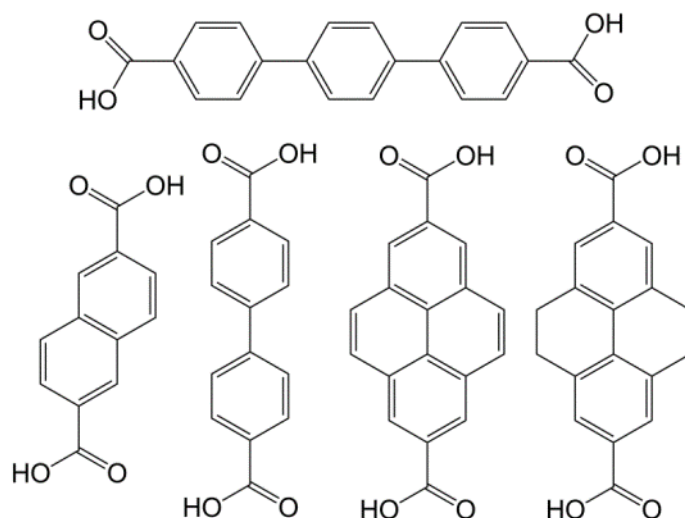


Fig. 1.4 A series of carboxylic ligands with different lengths used for the constructions of IRMOFs.

Compared with the ligand bdc used in MOF-5, pore enlargement was found to be easily achievable if progressively larger linkers (Figure 1.4) were used for the construction of MOFs. Furthermore, if the following ligands (Figure 1.5) were used to link the SBUs and reticulate the frameworks, the nature of the MOFs will be different as the functional group decorates the pore structures.

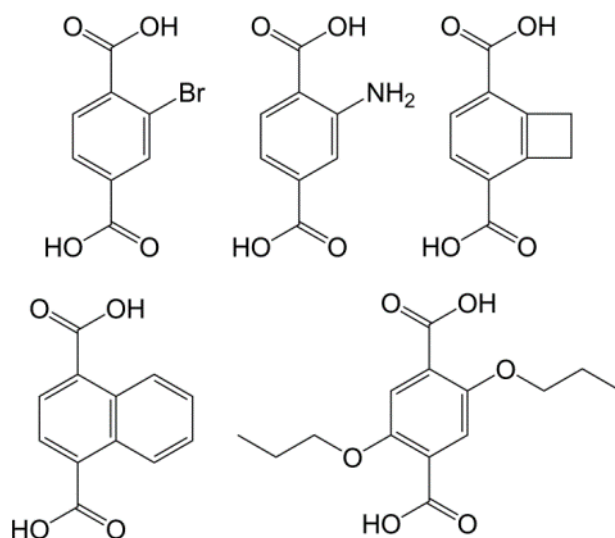


Fig. 1.5 A series of carboxylic ligands with different functionality used for the construction of IRMOFs.

1.3 Carboxylate-based MOFs

Besides the previously outlined IRMOF family, by combining possible ligands, co-ligands and metals, there is a large number of other compounds that have been explored in recent years³⁹. Most of them are carboxylate-based MOFs and have been proved to have wide-ranging properties.

One of the most important features of MOFs is their high accessible surface areas, which are important in many possible applications. Three years after Yaghi and colleagues reported the IRMOF series, a group in Versailles designed an extensive series of carboxylate MOFs following the same concept of reticular chemistry, named MIL-*n* (MIL standing for Materials of Institute Lavoisier). One of the most interesting products, $\text{Cr}_3\text{F}(\text{H}_2\text{O})_2\text{O}[(\text{O}_2\text{C}-\text{C}_6\text{H}_4-\text{CO}_2)] n\text{H}_2\text{O}$ (MIL-101) exhibited an ultra-high porosity which had never been reached before⁴⁰. The SBU for this structure is actually constructed from a “super-tetrahedron” (Figure 1.6b). It is formed from a linkage of bdc ligands and four inorganic trimers which are composed of three CrO_6 octahedra (Figure 1.6a). These super-tetrahedra are linked to each other through the four vertices, constructing the framework which contains two types of cages (Figure 1.6d), and finally resulting in a structure with a topology similar to the zeotype, Mobil Thirty-Nine (MTN) (Figure 1.6c). This porous material exhibits a giant accessible pore volume and has a surface area for N_2 of $5900 \text{ m}^2 \text{ g}^{-1}$ (77 K), which was the highest porosity of any material synthesized at that time⁴⁰.

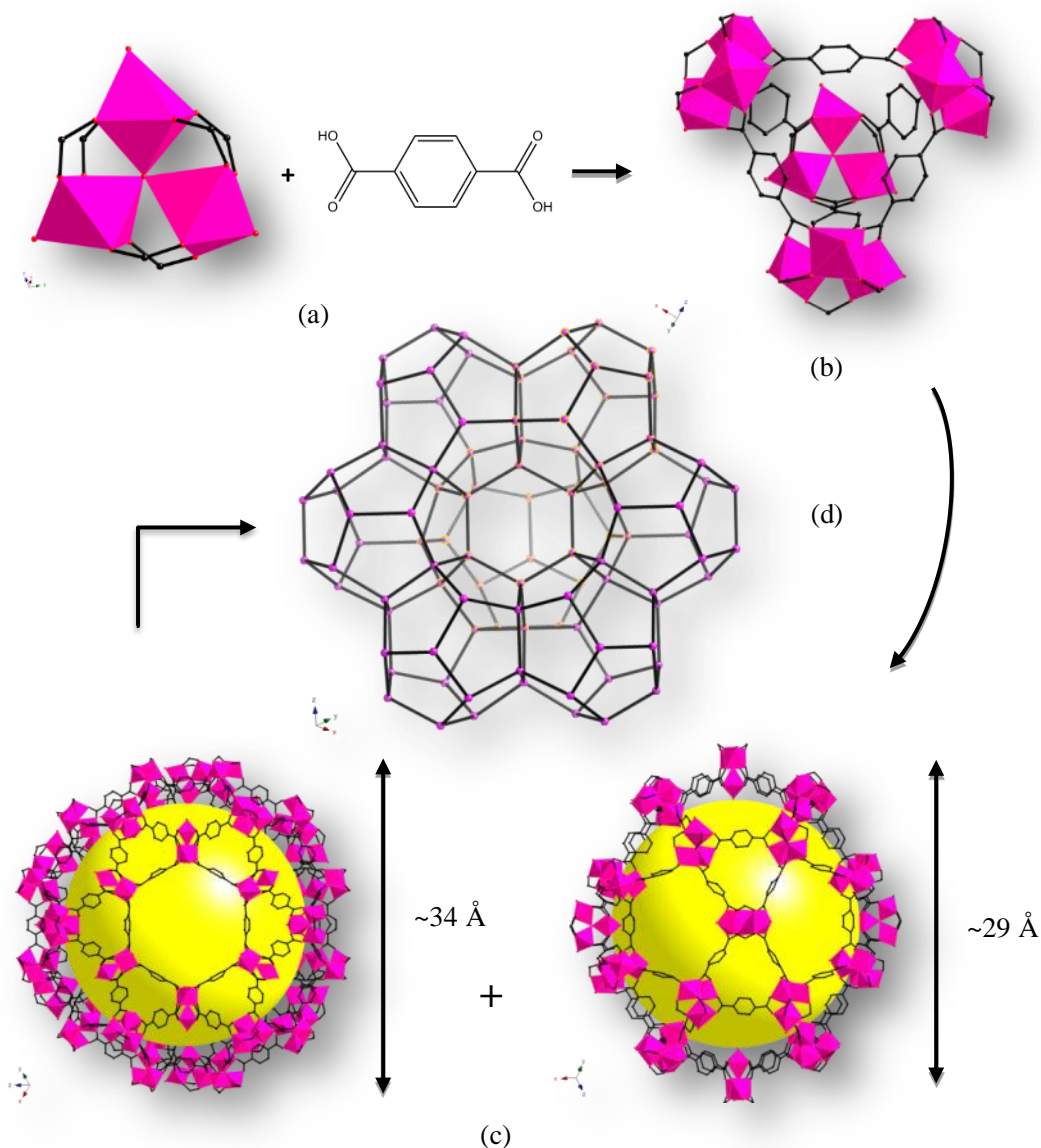


Fig. 1.6 Framework structures of (a) trimeric building block chelated by three carboxylic function groups and the ligand bdc, (b) the super-tetrahedron, (c) two types of cages, showing the hexagonal and pentagonal windows, with internal diameters of ~ 29 Å and ~ 34 Å, (d) example of MTN zeotype structure, with two types of cages highlighted by small spheres coating with yellow colour; hydrogen atoms and internal solvent molecules have been omitted for clarity; colour scheme: CrO₆ – pink octahedra, O – red and C – black, small pink spheres in (d) represent the super-tetrahedral units; the yellow sphere illustrates the void space inside the cage.

However, this surface area record was soon broken. In early 2004, Chae *et al.* published a new MOF named MOF-117⁴¹. This material used the typical SBU

$[\text{Zn}_4\text{O}(\text{COO})_6]$ as in other IRMOFs, but a triipsoic carboxylic acid, 4,4',4''-benzene-1,3,5-triyltribenzoate (btb) (Figure 1.7a) was employed to extend the framework, which resulted a very big 3D porous MOF. Based on this exciting result, in 2010, a novel isorecticular MOF with ultra-high porosity was synthesized, named MOF-200⁴² (Figure 1.7b). For this material, the even larger ligand 4,4',4''-[benzene-1,3,5-triyl-tris(benzene-4,1-diyl)]tribenzoate (bbc) was used to link the $\text{Zn}_4\text{O}(\text{COO})_6$ SBU, which immensely extended the framework and resulted in a surface area of about $10400 \text{ m}^2 \text{ g}^{-1}$ of material⁴² which is the highest porosity MOF ever synthesized with a single ligand.

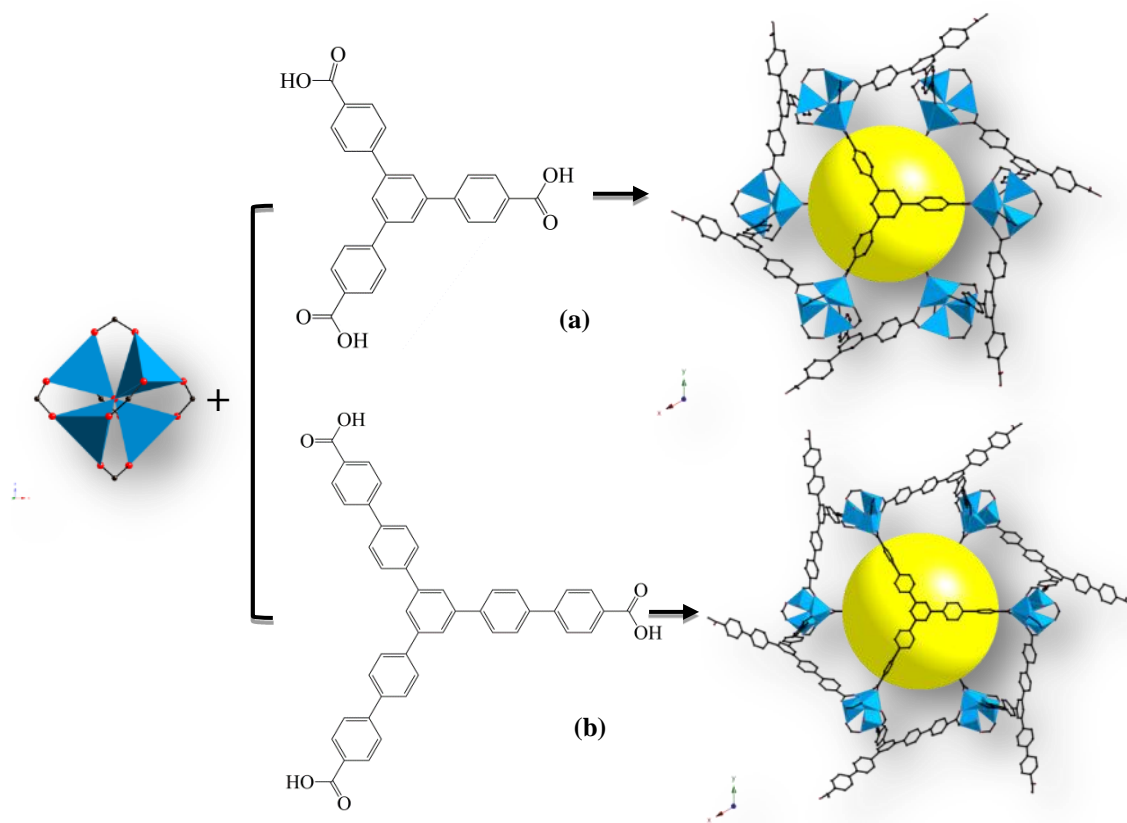


Fig. 1.7 Framework structures of MOF-117 and MOF-200; $\text{Zn}_4\text{O}(\text{COO})_6$ SBU (left) connect with organic linkers (upper middle btb, lower middle bbc) to form MOFs; hydrogen atoms and internal solvent molecules have been omitted for clarity; colour scheme: ZnO_4 – blue tetrahedra, O – red and C – black; yellow spheres illustrate the void space inside the framework.

The structures of conventional crystalline MOFs are usually considered “simple” as such materials can be constructed from a small number of secondary building units, and modified and extended with carboxylic acid linkers⁴³. Linkers are diverse, hence plenty of such materials are explored, resulting in the ability to tailor the properties of compounds via bigger molecular size or different functionalities. In order to further increase diversity, people start to consider the synthesis of MOFs with mixed ligands. However, endeavoring to rise the number of linkers in the synthesis usually leads to either mixed phases or amorphous materials³².

Yaghi and co-workers reported a mixed ligand MOF with exceptional porosity, named MOF-210⁴². In the synthesis of this material, two organic ligands, 4,4',4''-[benzene-1,3,5-triyl-tris(ethyne-2,1-diyl)]tribenzoate (bte) and biphenyl-4,4'-dicarboxylate (bpdc), were coordinated with octahedral $\text{Zn}_4\text{O}(\text{COO})_6$ SBUs (Figure 1.8), to yield a 3D porous framework containing two types of pore. The Langmuir surface area for this mixed ligand MOF is about $10400 \text{ m}^2 \text{ g}^{-1}$, similar to that of MOF-200, but the Brunauer-Emmett-Teller (BET) surface area ($6240 \text{ m}^2 \text{ g}^{-1}$), is the highest ever reported for crystalline materials⁴².

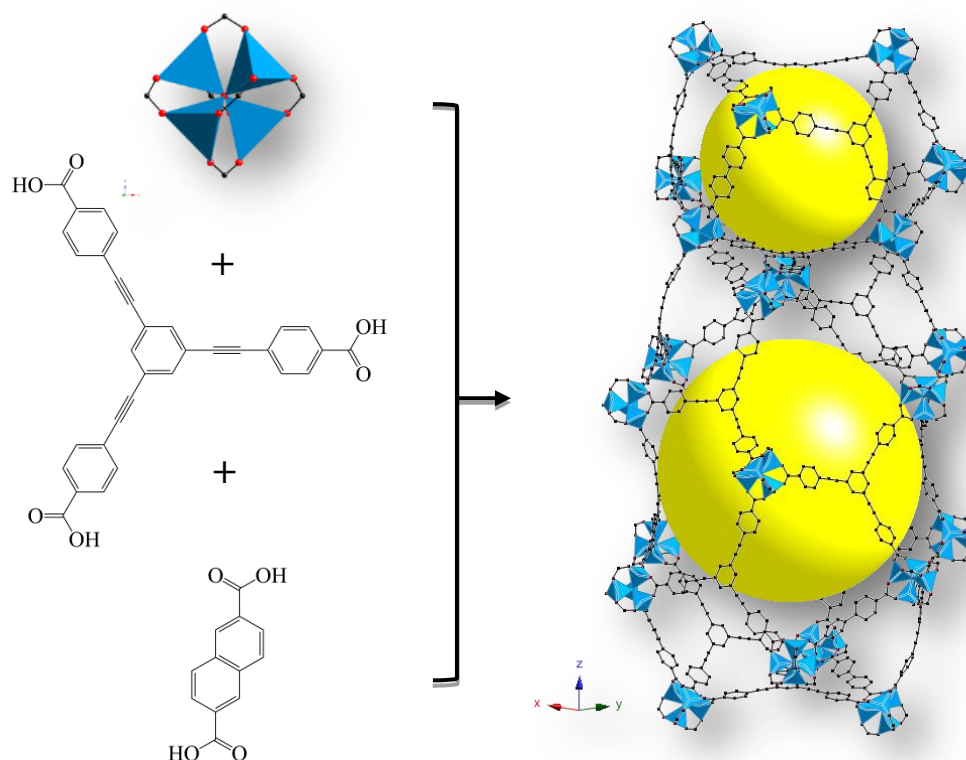


Fig. 1.8 Framework structure views of MOF-210, $\text{Zn}_4\text{O}(\text{COO})_6$ SBU (left) connects with organic linkers (middle left bte, lower left bpdc) to form MOF; hydrogen atoms and internal solvent molecules have been omitted for clarity; colour scheme: ZnO_4 – blue tetrahedra, O – red and C – black; yellow spheres illustrate the void space inside the framework.

Other than making mixed ligand MOFs to break the record of porosity, lots of new porous materials are created with mixed ligands to enhance the functionalities of resultant materials compared with the parent material with a single type of linker³². Such materials have been systematically studied by Deng *et al.*⁴³ Based on the structure of MOF-5, eighteen isorecticular MOF-5 type structures with different functionalities on the linking groups were synthesized (Figure 1.9), with one material that could contain up to eight distinct functional groups in one single phase. With more than one type of ligand, by carefully tailoring the reaction conditions, pure phases still can be achieved with ordered structures, but the dissemination of the functional groups is difficult to control.

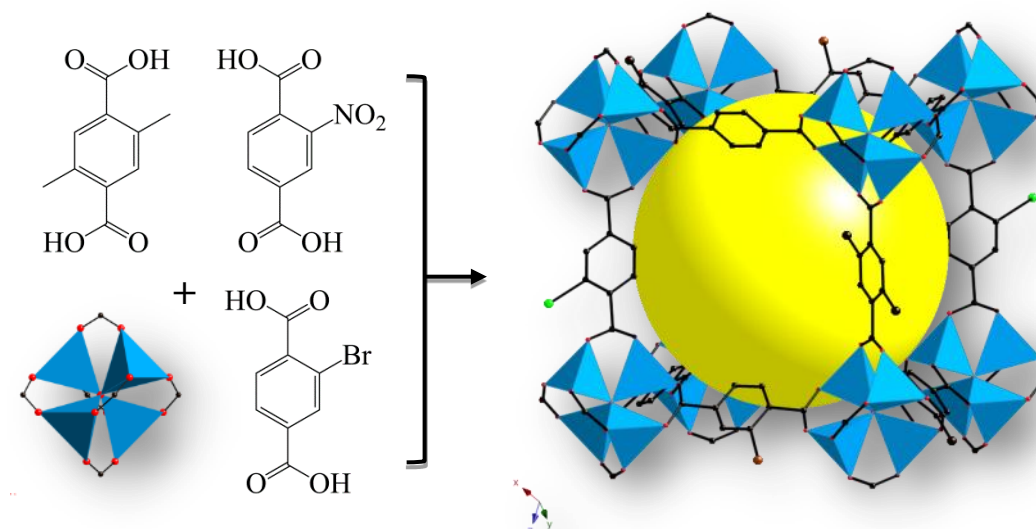


Fig. 1.9 Framework structure example of MTV-MOF-5 (Multivariate MOF-5) series material, MTV-MOF-5-CEF (right), constructed with $\text{Zn}_4\text{O}(\text{COO})_6$, $(\text{CH}_3)_2\text{-bdc}$, $\text{NO}_2\text{-bdc}$ and Br-bdc (left); hydrogen atoms and internal solvent molecules have been omitted for clarity; colour scheme: ZnO_4 – blue tetrahedra, Br – brown, N – green, O – red and C – black; yellow sphere illustrates the void space inside the framework.

Mixed ligand materials with several functional groups within the structure exhibit extraordinary functionalities. Examples in this series of materials are the so called MTV-MOF-AHI [multivariate MOF-5 combined with three linkers: A: bdc, H: $(\text{OC}_3\text{H}_5)_2\text{-bdc}$, I: $(\text{OC}_7\text{H}_7)_2\text{-bdc}$], and MTV-MOF-5-EHI [multivariate MOF-5 combined with three linkers: E: $\text{NO}_2\text{-bdc}$, H: $(\text{OC}_3\text{H}_5)_2\text{-bdc}$ and I: $(\text{OC}_7\text{H}_7)_2\text{-bdc}$]. The selectivity $[V_{(\text{CO}_2)}/V_{(\text{CO})}]$ for carbon dioxide over carbon monoxide of MTV-MOF-4EHI is much better than the MOF-5 or MTV-MOF-5-EI, and the H_2 storage capacities of MTV-MOF-5-AHI is superior than that of MTV-MOF-5-AH, -AI and MOF-5.

Besides the MTV-MOF examples, Chun *et al.* reported that $\text{Zn}_2(\text{bdc})(\text{tmbdc})(\text{dabco})$ (tmbdc: tetramethylterephthalate, dabco:

4-diazabicyclo[2.2.2]octane) showed enhanced H₂ uptake capacity (2.1 wt%) over the Zn₂(bdc)₂(dabco) (1.9 wt%) and Zn₂(tmbdc)₂(dabco) (1.8 wt%)⁴⁴, and the mixed ligands MOFs [Zn(1,3-bdc-NO₂)_{0.13}(1,3-bdc-OMe)_{0.87}(4,4'-bipy)] (4,4'-bipy:4,4'-bipyridine) synthesized by Fukushima *et al.*⁴⁵ exhibited much greater CO₂ adsorption than [Zn(1,3-bdc-NO₂)(4,4'-bipy)] and better CO₂ selectivity over CH₄ than [Zn(1,3-bdc-OMe)(4,4'-bipy)]. The possible presence of distinct sequences of functional linkers along the MOFs structures demonstrates that the integration of various functionalities within MOFs might be useful for the enhancement of a particular functionality or achieving novel properties.

Besides the porosity and functionalities of MOFs, another interesting feature arising with certain MOFs relates to their flexible structures. Depending on the nature of the framework, the input (or the removal) of the guest will result either in an extension or a contraction of the unit cell volume. Such a phenomenon can be well illustrated by MIL-53 type MOFs [M₃(OH)(bdc)(H₂bdc), M = Cr²⁷, Al⁴⁶ and Ga⁴⁷], and MIL-88 type MOFs^{28, 48} [M₃O(H₂O)₂X(L)₃ (guest), where M = Fe, Cr; X = F, Cl; L = fumarate (88A), bdc (88B), 2,6-naphthalenedicarboxylate (88C), 4,4'-biphenyldicarboxylate (88D)] and MIL-89²⁹ [Fe₃O(CH₃OH)₃Cl(O₂C-C₄H₄-CO₂)₃ (guest), where guest = methanol or water].

The as-synthesized MIL-53Cr (Figure 1.10a) is a 3D structure with one-dimensional (1D) large channels (projected into the paper) filled with excess bdc molecules. When the internal solvent was removed under high temperature, this resulted an expanded porous solid with the diameter enlarged from 12.18 Å to 13.04 Å (Figure 1.10b).

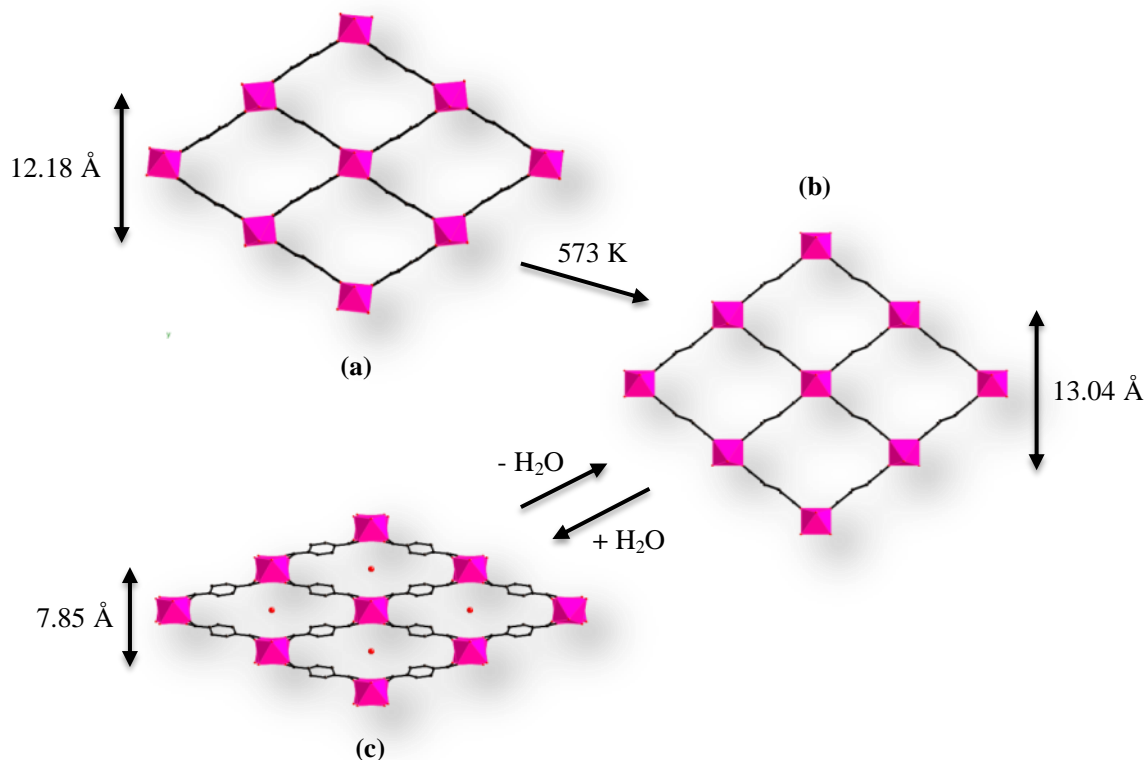


Fig. 1.10 Structures of MIL-53Cr, illustrating the framework extension from (a) as-synthesized MIL-53 to (b) framework opened upon high temperature, and (c) after reversible rehydration; Hydrogen atoms and bdc molecules inside the channels of (a) have been omitted for clarity; colour scheme: CrO₆ – pink octahedra, O – red and C – black.

On rehydration of this anhydrous form, a structure transition was observed. The pore was condensed when the water molecules were present (Figure 1.10c) and reopened when the guest was removed, which is fully reversible and allows a very large ‘breathing’ effect from 13.04 Å to 7.85 Å²⁷. The water hydrogen bonding inside the channel is believed to be responsible for this large effect^{37, 46}. The Al and Ga version of MIL-53 MOFs show very similar breathing effects as well⁴⁷, but in the Ga version of the dehydrated form, the pore performed in both open and closed forms depends on the temperature. The dehydrated form is stable until the temperature reaches 653 K. Above 493 K, an expanded porous structure can be formed, which is similar to the dehydrated MIL-53Cr. At temperatures between 333 K and 493 K, this

dehydrated form barely exhibited any porosity. Below 333 K, water was coordinated, resulting in a rehydrated structure. This unusually large framework expansion is even more obvious in the MIL-88 and MIL-89 type MOFs. For the MIL-88D the extended pore diameter of the dehydrated phase was up to 200% bigger than the shrunken form (from 10.1 Å to 20.4 Å)²⁸.

Examples demonstrated here illustrate the current investigations for carboxylate-based MOFs, showing the remarkably high surface area and tunable properties of the pore sizes and functionalities as well as the dynamic properties. However due to the inexhaustible possible combinations of inorganic and organic moieties, an abundance of other types of MOFs have also been developed. Such materials as zeolitic imidazolate frameworks, sulfonate metal organic frameworks and metal phosphonate frameworks increase the diversity of porous materials and increase the potential for further applications.

1.4 Phosphonate-based MOFs

Phosphonate-based MOFs (characterized by a chemically stable carbon to phosphorus bond) are considerably rarer in recently published literature than carboxylate-based counterparts, but owing to the ability of forming stronger bonds than carboxylates with metal atoms, still there are a considerable number of investigations dedicated to this area^{39, 49}. Phosphonates have three oxygen atoms capable of bonding to metals. This results in many possible modes of coordination and different topologies. In early studies, the majority of metal phosphonate compounds were formed of densely packed layered structures, which do not have porosity. Attempts have been carried out to modify the chemical environment within the interlayer either directly or by post

synthetic methods to include functionalities such as catalysis⁵⁰, hosts for intercalation compounds⁵¹, and protonic conductors⁵², or even introduce pillaring moieties to create more interlayer space^{53,54}. However, when the first 3D metal phosphonate framework β -Cu(O₃PCH₃) was created by Le Bideau and co-workers in 1994⁵⁵ (Figure 1.11), the research field for phosphonate-based MOFs became more attractive^{49,56}.

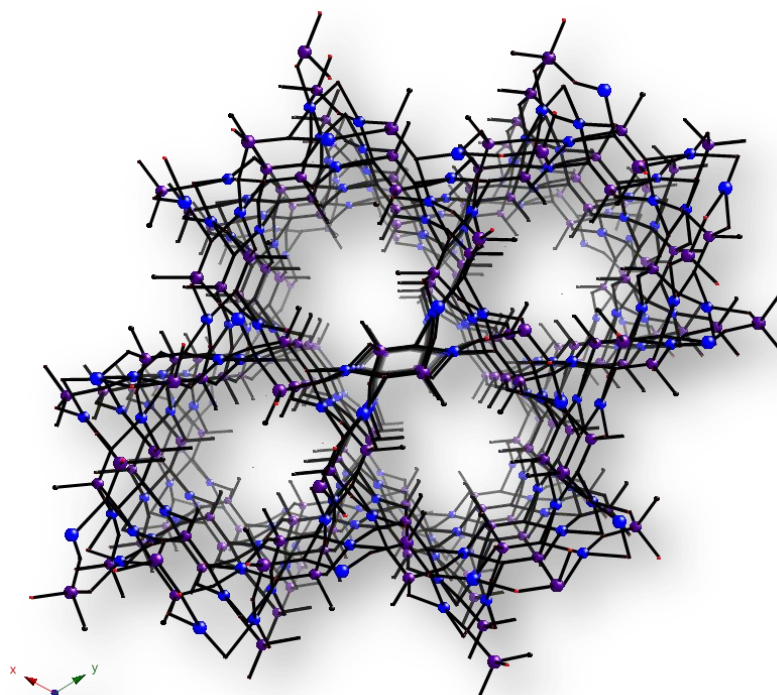


Fig. 1.11 Framework structure of β -Cu(O₃PCH₃), illustrating the 1D channels running along the framework; hydrogen atoms and internal solvent have been omitted for clarity; colour scheme: Cu – blue, P – purple, C – black, O – red.

The reviews of Maeda⁵⁶ and Gagnon³⁹ covered most of the progress dating from 1994 to 2011 for phosphonate-based MOFs. Among these products, most were synthesized with three main ligand types: alkylphosphonic acids, piperazinyolphosphonic acid and carboxylphosphonic acids (Figure 1.12) to extend the structure with different topologies and properties.

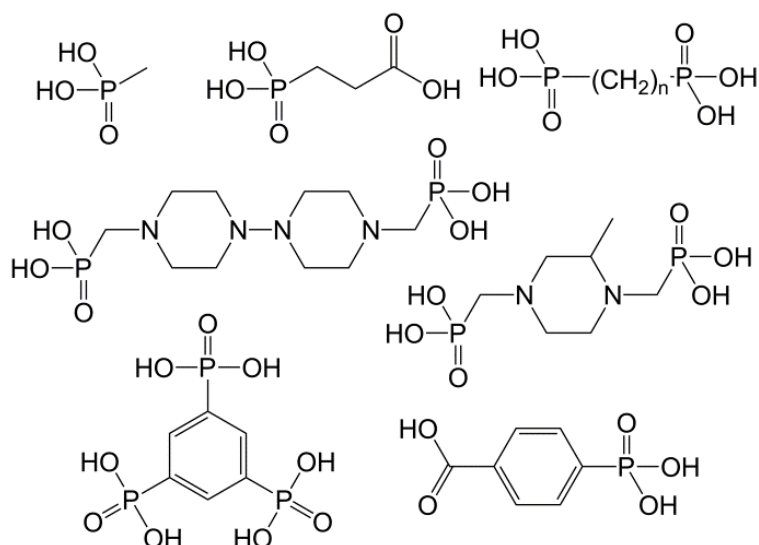


Fig. 1.12 Phosphonic acids used for the construction of phosphonate-based MOFs.

As outlined above, $\beta\text{-Cu}(\text{O}_3\text{PCH}_3)$ is the first porous phosphonate framework synthesized with methylphosphonic acid. After this, aside from only a few papers published by Maede and co-workers for the synthesis of other comparable porous phosphonates $\alpha\text{-AlMePO}^{57, 58}$ and $\beta\text{-AlMePO}^{57, 59}$ by the coordination of methylphosphonic acid with alumina, other discoveries in this field have proved unfavorable. In 1997, Lohse *et al.*⁶⁰ successfully used methylenediphosphonic acid as a ligand to synthesize a 3D porous phosphonate material. In this material $\text{Co}_2(\text{O}_3\text{PCH}_2\text{PO}_3) \cdot \text{H}_2\text{O}$ (Figure 1.13), divalent cobalt cations are found in both tetrahedral and octahedral geometries. The structure can be visualized as sheets of CoO_6 trimers cross linked by CoO_4 tetrahedra, and then extensively decorated with $\text{P}-\text{CH}_2-\text{P}$ units. The cross-linking of the layers by CoO_4 tetrahedra constructs the methylene-lined pores.

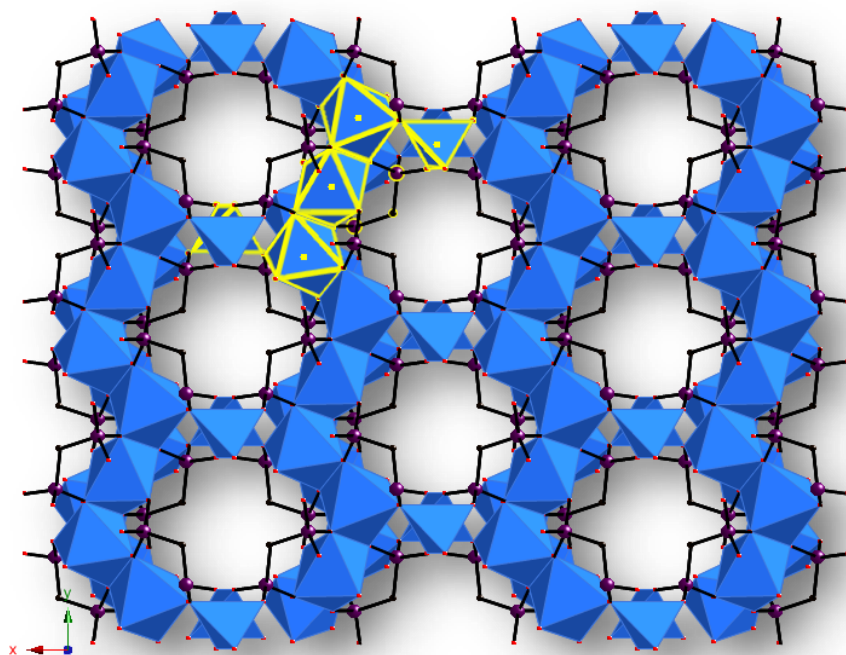


Fig. 1.13 Framework structure of $\text{Co}_2(\text{O}_3\text{PCH}_2\text{PO}_3) \cdot \text{H}_2\text{O}$, illustrating the construction of the structure; hydrogen atoms and internal solvent have been omitted for clarity; colour scheme: CoO_6 – blue octahedra, CoO_4 – blue tetrahedra, P – purple, O – red and C – black.

Spurred by the synthesis of this structure, following investigations were then focused on increasing the chain length of the alkybisphosphonic acid $[\text{H}_2\text{PO}_3(\text{CH}_2)_n\text{PO}_3\text{H}_2]$ to extend further the pore size of the target metal phosphonate framework in an isorecticular manner. However, compounds with the chain length $n = 2$ -5 usually form pillared layered structures (Figure 1.14), rather than a 3D porous framework⁶¹⁻⁶³, in which the metal cations were coordinated with oxygen atoms provided from CPO_3 units and linked with each other to form inorganic layers connected by the organic linkers. The stacking between the layers varies due to the conformation of the numbered organic chains and the coordination states of the metal used. Only a few reported success with n greater than 6^{39, 64}. Most are condensed layer structures, but as an exception, the pillared layered structure can be formed ($n = 10$)⁶⁵ (Figure 1.14e).

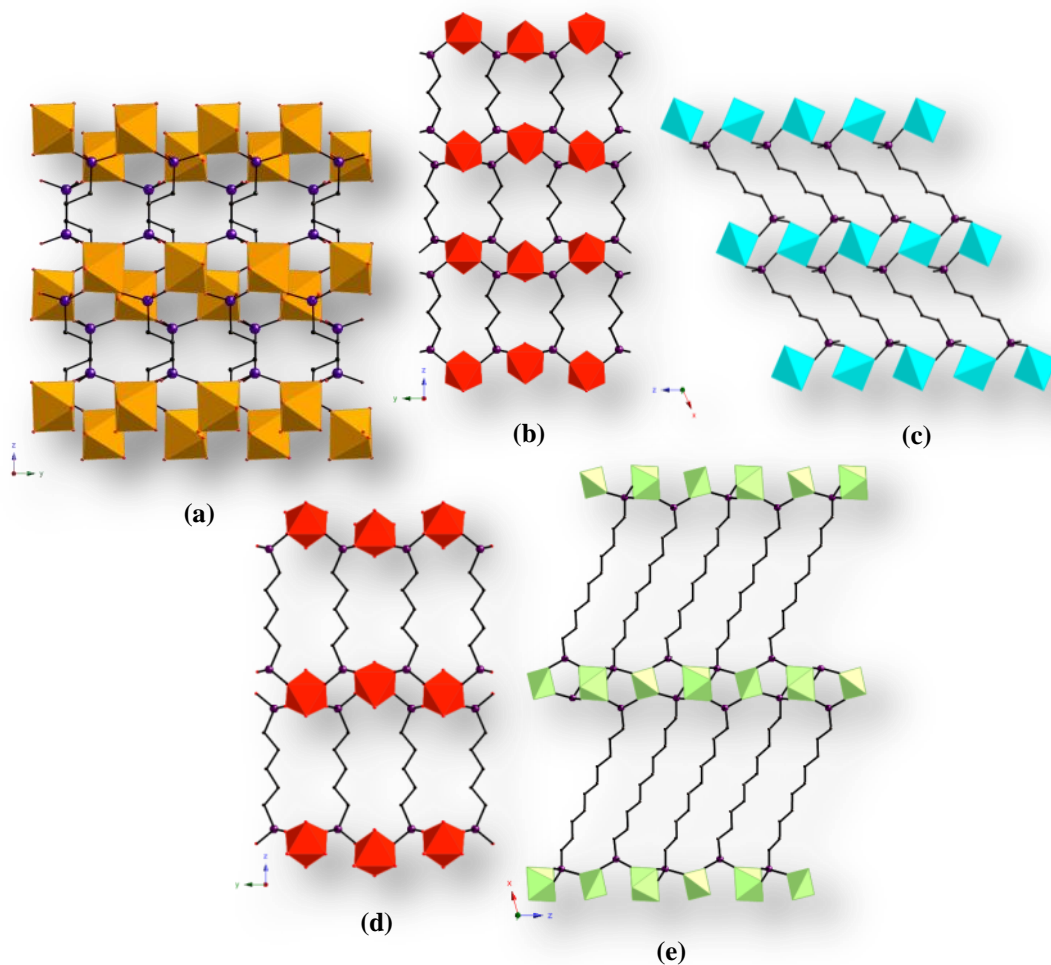


Fig. 1.14 Framework structures of alkylldiphosphonates with different chain lengths: (a) $\text{Fe}(\text{HO}_3\text{P}(\text{CH}_2)_2\text{PO}_3) (\text{H}_2\text{O})^{61}$, built with FeO_6 octahedra and CPO_3 tetrahedra, linked with $(\text{CH}_2)_2$; (b) $\text{V}_2\text{O}_2(\text{H}_2\text{O})[\text{O}_3\text{P}(\text{CH}_2)_3\text{PO}_3] 2\text{H}_2\text{O}^{64}$, built with VO_6 octahedra and CPO_3 tetrahedra, linked with $(\text{CH}_2)_3$; (c) $\text{Zn}[\text{HO}_3\text{P}(\text{CH}_2)_4\text{PO}_3\text{H}] 2\text{H}_2\text{O}^{63}$, built with ZnO_4 tetrahedra and CPO_3 tetrahedra, linked with $(\text{CH}_2)_4$; (d) $\text{V}_2\text{O}_2(\text{H}_2\text{O})[\text{O}_3\text{P}(\text{CH}_2)_5\text{PO}_3] 3\text{H}_2\text{O}^{64}$, built with VO_6 octahedra and CPO_3 tetrahedra, linked with $(\text{CH}_2)_5$; (e) $\text{Ga}[\text{HO}_3\text{P}(\text{CH}_2)_{10}\text{PO}_3]^{65}$, built with GaO_6 octahedra and CPO_3 octahedra, linked with $(\text{CH}_2)_{10}$; hydrogen atoms and internal solvent molecules have been omitted for clarity; colour scheme: FeO_6 – brown octahedra, VO_6 – dark orange octahedra, ZnO_4 – turquoise tetrahedra, GaO_6 – light green octahedra, P – purple, O – red and C – black.

The alkylphosphonates provided good examples of isoreticularly synthesized larger 3D pillared layered structures, which is a short distance from the 3D open frameworks, but unquestionably, the latter still present quite a challenge. Hence, some

groups were starting to explore the possibility of synthesizing open metal phosphonate frameworks with other ligands. Piperazinyolphosphonic acid is one such ligand, which alongside some of its derivatives have proved very interesting as they contain two phosphonic acids, both capable of three states of protonation as well as the amino nitrogen atom giving rise to greater versatility in the formation of more cross-linked structures.

Porous phosphonate frameworks using piperazone-derived ligands were first reported in Zubieta's group in 1996⁶⁶. *N,N'*-piperazinebis(methylenephosphonic acid) was combined with Mn and Co to form dense 3D frameworks containing 1D channels. Following this discovery, lots of metal piperazine-based open phosphonate structures were published³⁹. The most notable examples are the STA-12⁶⁷ series (St Andrews microporous material number 12) and STA-16⁶⁸.

STA-12 is a crystalline microporous metal *N,N'*-piperazinebis(methylene-phosphonate) with a hexagonal array of 1D channels, 9 Å (Figure 1.15a) in diameter. The structure is based on inorganic chains of octahedrally coordinated metal cations, MO_5N ($\text{M} = \text{Ni}^{2+}$, Mn^{2+} , Fe^{2+} and Co^{2+}). Each MO_5N octahedron consists of a metal cation and in coordination with four oxygen atoms from two different phosphonate tetrahedra and one water oxygen atom, plus a nitrogen atom from the piperazine ring of the phosphonic acid. It was the first 3-dimensional large pore metal phosphonate to be synthesized⁶⁹. For STA-16, this structure is isorecticular to STA-12 but with a larger phosphonic acid *N,N'*-4,4'-bipiperidinebis(methylenephosphonic acid) to further extend the wall size. This resulted a very similar framework to that of STA-12, but with much greater pore

size diameter (18.5 Å) (Figure 1.15b). These two compounds are interesting not only because of the very large pore size, but also both porous structures could be maintained upon dehydration. More importantly the pores of both materials contained phosphonate oxygen atoms, and the water bonded to the metal centre can be removed, leaving unsaturated metal sites, which can therefore undergo further interaction with gas or solvent molecules^{39, 70}.

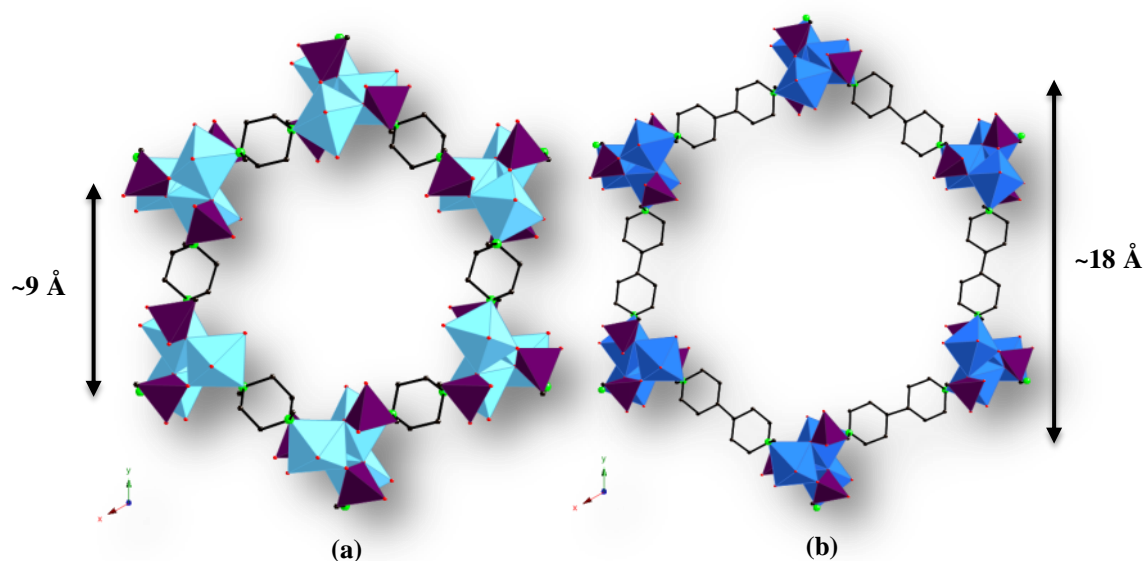


Fig. 1.15 Framework structures of (a) STA-12(Ni) and (b) STA-16 (Co), illustrating the isorecticular structures; hydrogen atoms and internal solvent molecules have been omitted for clarity; colour scheme: NiO₅N – cyan octahedra, CoO₅N – blue octahedra, CPO₃ – purple tetrahedra, N – green, O – red and C – black.

Owing to the large coordination shell and wide variety of coordination environments of lanthanides⁶⁹, as well as their interesting magnetic and luminescent properties³⁹, investigations were carried out using lanthanide metals to construct piperazinylphosphonates. From Wright's group^{69, 71, 72}, a series of 3D porous frameworks have been obtained by coordination of piperazinylbisphosphonates with Yd³⁺, Y³⁺, Dy³⁺, Gd³⁺, Nd³⁺, Ce³⁺ and La³⁺, exhibiting permanent porosity and considerable structural variation upon dehydration. These results also revealed

relationships between cation size and the structural types. 1D lanthanide phosphonate chains are the main feature of those structures. With smaller lanthanide cations (smaller than Eu^{3+}), octahedrally coordinated Ln^{3+} ions are usually observed (Figure 1.16a), whereas the larger cations such as Nd^{3+} form different types of structure with eight-fold coordination (Figure 1.16b)^{69, 72}. Further increasing the cation size to Ce^{3+} and La^{3+} to react with 2-methyl and 2,5-dimethyl derivatives of *N,N'*-piperazinebis(methylenephosphonic acid), resulted in more new structures, with lanthanides adopting seven or eight fold coordination⁷¹.

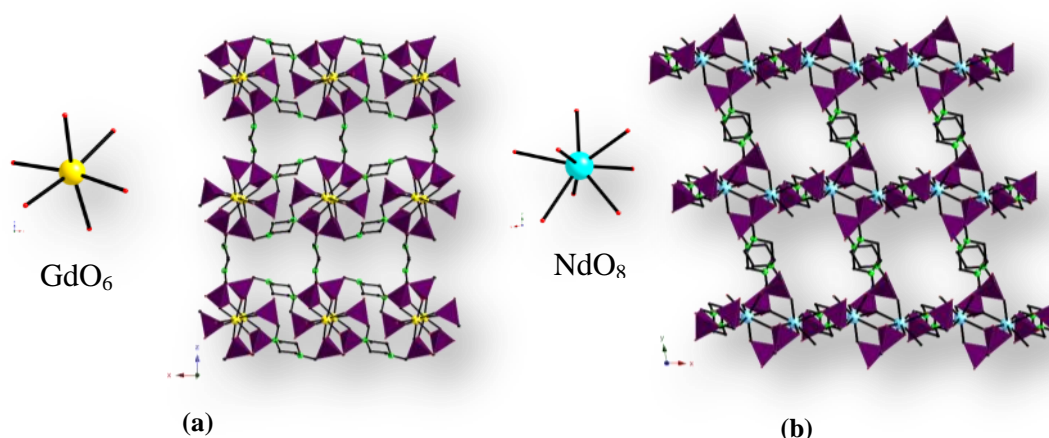


Fig. 1.16 Framework structures of (a) $\text{Gd}_2(\text{O}_3\text{PCH}_2\text{N}(\text{C}_2\text{H}_4)_2\text{NCH}_2\text{PO}_3\text{H}_2)_3 \cdot 3\text{H}_2\text{O}$ and (b) $\text{Nd}_2(\text{O}_3\text{PCH}_2\text{N}(\text{C}_2\text{H}_4)_2\text{NCH}_2\text{PO}_3\text{H}_2)_3 \cdot 9\text{H}_2\text{O}$, illustrating the 3D porous structure and the coordination environments of Gd^{3+} and Nd^{3+} ; hydrogen atoms and internal solvent molecules have been omitted for clarity; color scheme: Gd – yellow, Nd – cyan CPO_3 – purple tetrahedra, N – green, O – red and C – black.

Open framework metal phosphonate materials can also be obtained by coordination with carboxylphosphonic acid. With the development of different synthetic methods, more and more different structures have been published in the literature^{39, 56}. Hix *et al.* reported a number of metal phosphonate frameworks⁷³⁻⁷⁵, of which one published structure $\text{Zn}_3(\text{O}_3\text{PCH}_2\text{CO}_2)_2$ has a framework with large channels ($10 \times 6.8 \text{ \AA}$) (Figure 1.17a). With the same ligand, Cu ^{76, 77}, Mn ^{78, 79} and Pd ⁸⁰

structures have been reported later by other groups, however, most of these exhibited dense framework and do not contain large pores (Figure 1.17b–d). In order to assemble more extended frameworks, attempts with larger ligands were therefore carried out.

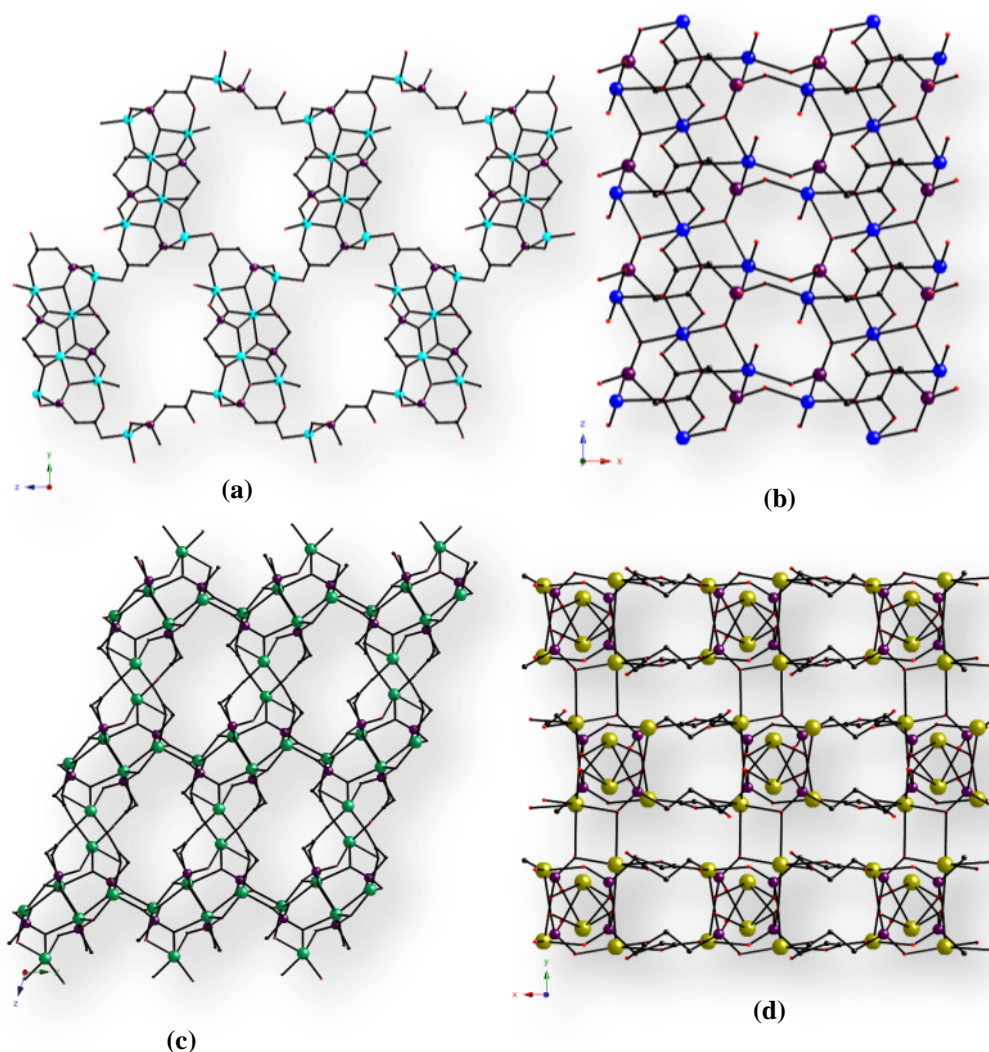


Fig. 1.17 Framework structures of (a) $\text{Zn}_3(\text{O}_3\text{PCH}_2\text{CO}_2)_2 \cdot 3\text{H}_2\text{O}$ ⁷³, (b) $\text{Cu}_{1.5}(\text{O}_3\text{PCH}_2\text{CO}_2) \cdot \text{H}_2\text{O}$ ⁷⁶, (c) $\text{Mn}_3(\text{O}_3\text{PCH}_2\text{CO}_2)_2$ ⁷⁸, (d) $\text{Pb}_3(\text{O}_3\text{PCH}_2\text{CO}_2)_2$ ⁸⁰, illustrating the channels present; hydrogen atoms and internal solvent have been omitted for clarity; colour scheme: Zn – cyan, Cu – blue, Mn – green, Pb – gold, P – purple, O – red and C – black.

One interesting investigation in this area was carried out by Chen *et al.*⁸¹ Using 4-phosphonobenzoic acid (H_3pbc), six zinc carboxylphosphonates with open

frameworks were obtained under mixed solvothermal conditions with the presence of organic amines as structure templates agent. Three of the products have 3D zeolite-type structures.

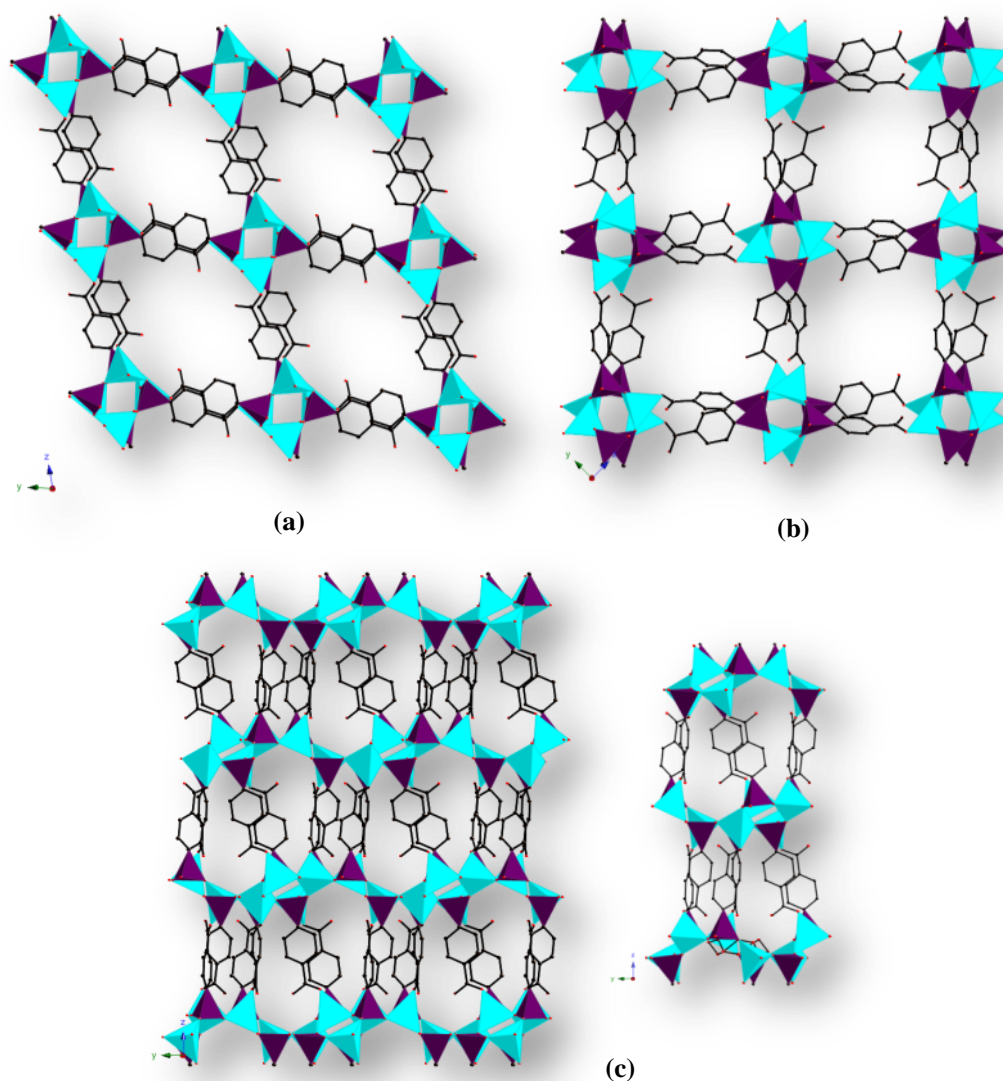


Fig. 1.18 Framework structures of (a) $\text{Zn}_2(\text{pbc})_2 \cdot 2\text{Hdma} \cdot \text{dmf} \cdot \text{H}_2\text{O}$, (b) $\text{Zn}_2(\text{pbc})_2 \cdot \text{H}_2\text{teta} \cdot \text{H}_2\text{O}$, (c) $\text{Zn}(\text{pbc}) \cdot \text{H}_3\text{O}$, showing the zeolite-type topologies; hydrogen atoms and internal solvent have been omitted for clarity; colour scheme: ZnO_4 – cyan tetrahedra, CPO_3 – purple tetrahedra, O – red and C – black.

As shown in the Figure 1.18a and b, the double-crankshaft inorganic chains of $\text{Zn}_2(\text{pbc})_2 \cdot 2\text{Hdma} \cdot \text{DMF} \cdot \text{H}_2\text{O}$ and $\text{Zn}_2(\text{pbc})_2 \cdot \text{H}_2\text{teta} \cdot \text{H}_2\text{O}$ (dma = dimethylamine; dmf = *N,N*-dimethylformamide; tetra = triethylene tetramine) were constructed by the

corner sharing of ZnO_4 and CPO_3 tetrahedra connected by the organic moieties into gismondine-like zeolite topologies⁸¹. The structure of $\text{Zn}(\text{pbc}) \cdot \text{H}_2\text{O}$ (Figure 1.18c) featured cages which are normally found in zeolites. The work itself expanded the synthetic methods for achieving 3D porous structures and revealed that structure-directing agents were effective in constructing a variety of zinc-carboxylphosphonate structures.

Following Chen's work, Li and co-workers used the same ligand to construct a pillared layered compound $\text{Zn}(\text{H}_2\text{O})_6[\text{Zn}_8(\text{pbc})_6(4,4'\text{-bipy})]$ by hydrothermal synthesis in the presence of an additional organic ligand 4,4'-bipyridine (Figure 1.19a)⁸². The inorganic layer was formed of ZnO_4 , ZnO_3N and CPO_3 tetrahedra, which contained 12-membered rings (Figure 1.19b), cross-linked by both 4-phosphonobenzoic acid and 4,4'-bipyridine through the coordination of the carboxylate oxygen and pyridyl nitrogen with zinc atoms. The charge of the anionic framework was balanced by hexaaqua zinc atoms located inside the cages generated by the inorganic window and the organic pillars. However, by using dabco as a second ligand, a neutral and isostructural framework $(\text{Hdabco})_2[\text{Zn}_8(\text{pbc})_6] \cdot 6\text{H}_2\text{O}$ can be obtained with only water contained inside the channels (Figure 1.19c). This work is very interesting, as the cavity structures contained 12-membered windows, and demonstrated an approach to control the pore size distribution by employing a second organic ligand to template the structure.

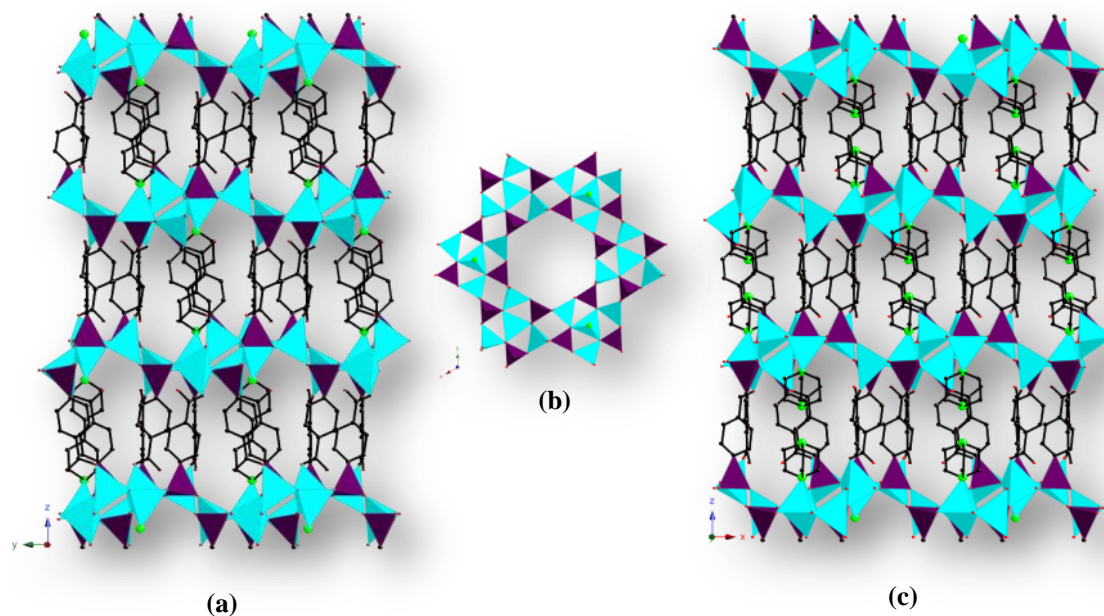


Fig. 1.19 Framework structures of (a) $\text{Zn}(\text{H}_2\text{O})_6[\text{Zn}_8(\text{pbc})_6(4,4'\text{-bipy})]$, (b) 12-membered inorganic layer, (c) $(\text{Hdabco})_2[\text{Zn}_8(\text{pbc})_6] 6\text{H}_2\text{O}$, illustrating the 3D open frameworks and the cavities constructed by the 12-membered windows and ligands; hydrogen atoms and internal solvent have been omitted for clarity; colour scheme: ZnO_4 – cyan tetrahedra, CPO_3 – purple tetrahedra, N – green, O – red and C – black.

From the range of structures discussed, as a relatively new classification of porous material phosphonate-based MOFs have exhibited a diversity and complexity different from other materials, and represent attractive candidates for further applications and investigation. One big difference of the phosphonate-based MOFs is their very low solubility, especially for trivalent and tetravalent metal phosphonates, which makes it difficult to prepare large enough single crystals, making the determination of the crystal structure a challenge^{39, 49}. As more advances are made with powder XRD structure modelling and refinement, it is expected that further interesting porous phosphonate structures will be discovered and analyzed, and consequently novel properties will be identified.

1.5 Applications for Porous MOFs

Within the past 20 years, the field of MOF chemistry has passed from curiosities to strategic materials. Other than focusing on deeply understanding the synthesis procedures, more and more studies are taking a closer look at their specific properties. The ability to fine-tune frameworks to adjust the chemical environment inside the structure, and especially the high porosity of MOFs, render them useful for volume specific applications such as catalysis, gas storage, gas purification, gas separations, and drug delivery^{7, 9, 10, 19, 83}.

1.5.1 Gas Storage and Separation in MOFs

Amongst various porous materials, MOFs owing to their low density, high accessible porosity, ability to tune the pore geometries and tailor the surface properties, have received growing attention from chemists and materials scientists for gas separation and storage materials, especially for hydrogen^{7, 10, 83, 84}. In order to deal with the foreseeable depletion of fossil energy resources, hydrogen has been considered as a potential energy carrier for a long time. Unfortunately it is a low density gas under ambient conditions, which means the energy density is much too low for practical use. It is therefore desirable to develop a commercially viable and safe, on-board solid hydrogen storage system to facilitate the use of hydrogen as a clean energy source instead of fossil fuels.

Since the first report of hydrogen adsorption on a porous MOF by Rosi *et al.* in 2003⁸⁵, there have been around 200 different MOFs that have been studied⁷. Hydrogen storage in MOFs is based on physisorption¹⁰. With just two electrons, the

hydrogen molecule forms very weak Van der Waals bonds (mainly dispersive and electrostatic interactions) with the surface of the MOFs⁸⁶, which results in a low interaction energy (between 4 and 10 kJ/mol H₂)⁸⁷. Thus it is not surprising that as surface area is increased, the contact between hydrogen and the adsorbent will be enhanced leading to a higher uptake. One of the most remarkable results is provided by Furukawa *et al.*⁴². An ultra-high porosity material MOF-210 was created in their group in 2010, which has the highest BET surface area (6240 m²/g) among porous solids. Hydrogen storage investigations revealed a total gravimetric uptake of 15 wt% (11.0 wt% for MOF-117^{88, 89} at 70 bar and 77 K) at 80 bar and 77 K⁹⁰ (Figure 1.20). Although fast loading and unloading is achieved in MOFs, significant hydrogen uptake has only been achieved at extreme temperature conditions⁸⁷. When the temperature is raised to ambient temperature, the hydrogen uptake will drop significantly in general¹⁰. For MOF-210, the total hydrogen uptake is lowered to 2.7 wt% at 80 bar and 293 K⁹⁰. To date, none of these MOFs can take up sufficient hydrogen to fulfil the U.S. Department of Energy 2015 hydrogen storage target [7.5 wt% and 70% kg H₂/kg system at near ambient temperature (−40 °C to 85 °C) and pressure (less than 100 atm)]⁹¹. Therefore efforts are currently being devoted to the investigation of various strategies to enhance hydrogen uptake in MOFs under ambient conditions.

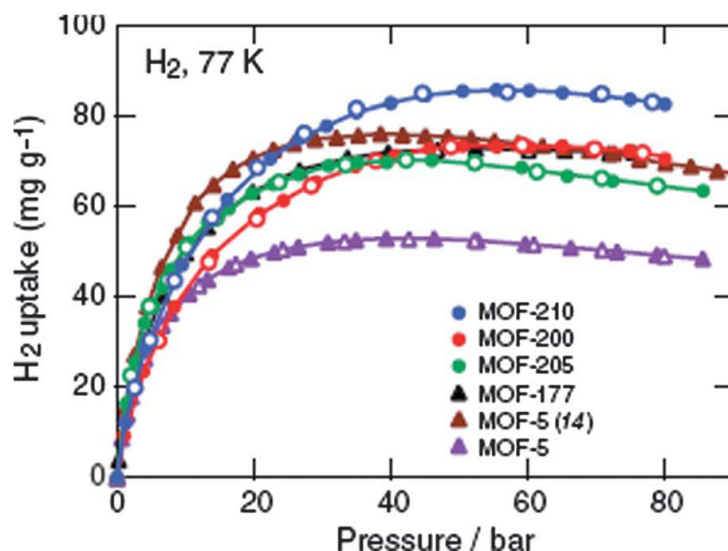


Fig. 1.20 High pressure H₂ isotherms at 77 K of selected high porosity MOFs (reproduced from reference 42⁴²).

In order to achieve high hydrogen uptake under ambient conditions, hydrogen should be absorbed with an optimal interaction energy of about 20 kJ/mol^{92, 93} in host materials, avoiding the orbital interaction that leads to strong metal hydrogen bonds and utilizing a simple charge-induced dipole interaction. This could technically give the materials the ability to absorb hydrogen under milder, even ambient conditions⁹². Two main strategies have been pursued recently for enhancing hydrogen storage within MOFs. One is to optimize the accessible surface area within a framework. It is widely recognized that a high surface area correlates almost linearly with the overall hydrogen uptake in a homogeneous, physisorption system⁹⁴⁻⁹⁶. By tailoring the framework with long and narrow pores, hydrogen can be absorbed inside such materials with higher binding energies by overlapping the interaction potential from the surrounding walls^{97, 98}. Theoretical⁹⁹ and experimental¹⁰⁰ results suggested that the optimal pore size is around 6 Å.

The second approach is to create more attractive surface sites within the MOFs

by using the strong metal hydrogen interactions between unsaturated metal centres and hydrogen to enhance the uptake. This route is thought to be a promising way to increase the hydrogen uptake capability at higher temperature and lower pressure^{101, 102}, because the interaction energy between hydrogen and the unsaturated metal centre is much higher than weak Van der Waals bonds. Dincă *et al.*¹⁰³ reported a microporous MOF with exposed Mn^{2+} coordination sites, which exhibited a good hydrogen uptake capacity (6.9 wt% at 90 bar and 77 K). This high uptake is attributed to the interaction of hydrogen molecules with the unsaturated Mn^{2+} sites and was supported by the high maximum isosteric heat of adsorption (10.1 kJ/mol). Lee *et al.*¹⁰⁴ prepared isostructural MOFs with and without unsaturated metal sites. The hydrogen uptake results showed the materials with open metal sites had higher hydrogen uptake at 77 K (2.07 wt% vs. 2.87 wt% at 1 bar and 3.70 wt% vs. 5.22 wt% at 50 bar).

For certain MOFs with saturated metal centres, by post synthetic modifications such ion exchange and doping, unsaturated metal centres can also be introduced, which is one of the most important advantages for using MOFs as an absorbent over other porous solids¹⁰. Several investigations have been dedicated to this area¹⁰⁵. Mavrandonakis and co-workers computationally explored the effects of introducing Li on various MOFs. They showed that the introduction of a single Li^+ ion per organic ligand in IRMOF-14, resulted in a hydrogen storage capacity 7.5 times larger than the original IRMOF-14⁸⁷. Hupp and co-workers introduced alkali metals ($\text{M} = \text{Li}^+, \text{Na}^+$ and K^+) into the structure of porous MOFs, and revealed that the hydrogen uptake was increased after introducing these metal cations, despite the greater contribution to the molecular weight of the framework². The highest uptake was the K^+ -exchanged case (1.54 wt%), which was 65% higher than the original material (0.93 wt%).

Hydrogen storage is one of the most important applications for MOFs currently in connection with pollution and energy problems³⁷. This requires not only sufficient capacity as well as acceptable uptake and release kinetics, but also favourable thermodynamics at ambient temperature and pressure⁸³. To date, MOFs have shown moderate uptake capacity for hydrogen, but lack the interaction energy to retain hydrogen inside the structure under milder conditions. Thus synthesis of MOFs with high porosity and high binding energy for hydrogen will be a great challenge for future research. Other than absorbing hydrogen, MOFs are very promising candidates for other gas storage applications, as well as for selective gas adsorption, resulting from gas separation by size exclusion and adsorbate–surface interactions¹⁰.

1.5.2 Catalysis in MOFs

As porous materials, MOFs have been proven to be very useful in the area of catalysis. Advantages of such materials over others are that these materials have highly ordered uniform crystalline pore structure, which benefits the shape and size selectivity in many catalytic processes¹⁰. Furthermore, the very open architecture of the framework, the homogeneous nature of the internal void space and the giant surface area offer the opportunity to distribute a high density of catalytic active centres inside the structure⁹, resulting in a very effective catalytic system.

For MOF-based catalysts, the catalytic reaction mainly occurs inside the MOF structures. MOFs therefore work as carriers of the active mass. The introduction of such active sites can be achieved from various approaches such as direct synthesis or post synthetic modification. Long *et al.*¹⁰⁶ undertook investigations of the catalytic activity a sodalite type (SOD) compound $\text{Mn}_3[(\text{Mn}_4\text{Cl})_3(\text{btt})_8(\text{CH}_3\text{OH})_{10}]_2$ ($\text{H}_3\text{btt} =$

1,3,5-benzene-tristetrazol-5-yl). The compound is a thermally stable microporous material presenting a cubic network of 10 Å pores (Figure 1.21), in which the unsaturated Mn ions are exposed on the channel surface, suggesting the metal centres will interact with guest molecules and should serve as potent Lewis acids for an active heterogeneous catalyst.

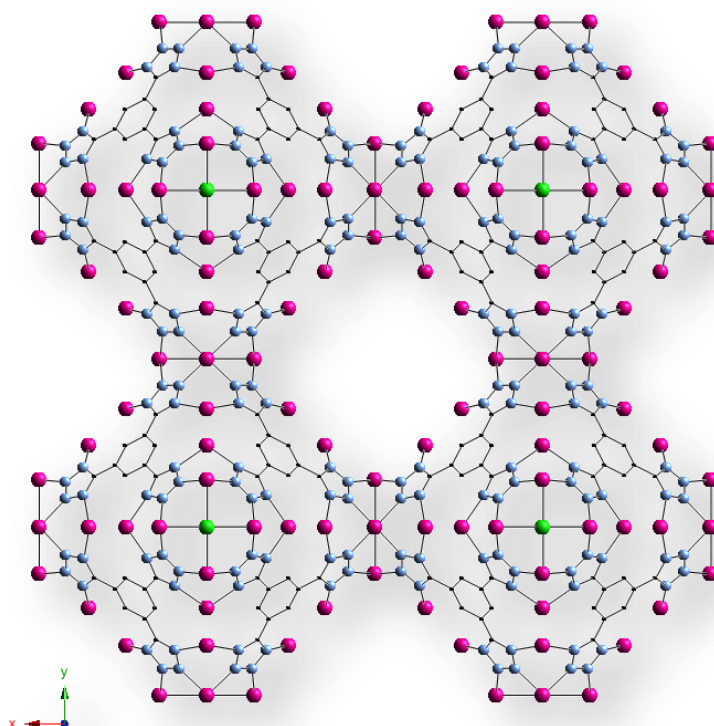


Fig. 1.21 Framework structure of $\text{Mn}_3[(\text{Mn}_4\text{Cl})_3(\text{btt})_8(\text{CH}_3\text{OH})_{10}]_2$, showing the Mn sites exposed within the 10 Å wide channels; hydrogen atoms and internal solvent have been omitted for clarity; colour scheme: Mn – pink, N – sky blue, Cl – green, O – red and C – black.

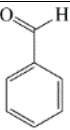
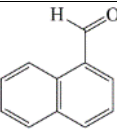
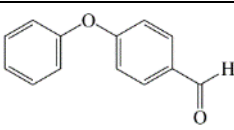
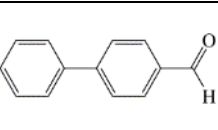
This compound was found to catalyze the cyanosilylation of aromatic aldehydes and ketones (Scheme 1.1). Benzaldehyde and 1-naphthaldehyde proved to have good conversion, but in contrast the conversion yields for other substrates produced negligible results, implicating a relationship between the size of reactants

and the pore diameter (Table 1.1)¹⁰⁶.

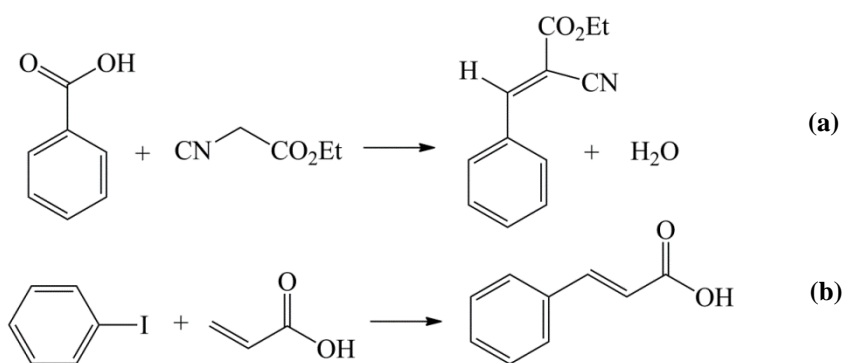


Scheme 1.1 Cyanosilylation of carbonylfunctionalized organic substrates

Table 1.1 Conversion results for the cyanosilylation of carbonyl substrates (reproduced from reference 106)

Carbonyl Substrates				
Time (h)	9	9	9	9
Yield (%)	98	90	19	18

Férey and co-workers demonstrated a post synthetic route to surface grafting of porous materials allowing the introduction of functional organic sites into the structure¹⁰⁷. They found for the material MIL-101 that coordinatively unsaturated Cr(III) sites could be generated by dehydration, which could then be chelated by electron-rich functional groups, resulting in a thermally stable amine species grafted to the internal surface¹⁰⁷. By introducing ethylenediamine (ed) and diethylenetriamine (deta) to the structure, this amine grafted MIL-101 exhibited remarkably high activities in the Knoevenagel condensation of benzaldehyde and ethyl cyanoacetate (Scheme 1.2a)¹⁰⁷. Furthermore, palladium-loaded 3-aminopropyltrialkoxysilane (aps) grafted MIL-101 (Pd/aps-MIL-101) and Pd/ed-MIL-101 also exhibit high activities for the Heck coupling reaction (Scheme 1.2b), which is an effective route to couple alkenes with organic moieties.



Scheme 1.2 (a) Knoevenagel condensation reaction between benzaldehyde and ethyl cyanoacetate, (b) Heck coupling reaction between acrylic acid and iodobenzene.

1.5.3 Other Applications

Due to their very large pore volume and ultra-high surface area, as well as the adjustability of the framework functional groups, MOFs also have the potential for use in drug delivery, by designing in specific binding interactions between the host and substrate^{46, 83, 108}, and applications related to magnetic properties^{109, 110} and luminescent sensors for ions¹¹¹ and guest molecules¹¹² have also been developed. Most of these specific properties were achieved in MOFs through use of the post synthetic method to modify the functionality. Hence further effort should be applied to various post synthetic modifications to design optimal MOFs with much enhanced properties to cater to a wide range of needs.

1.6 Aims of Thesis

In the work carried out in this thesis, the aim was to investigate the synthesis and the properties of new MOF materials with an ion exchange capacity as well as to explore their potential applications. As a result of this work, a synthetic route has been developed to a series of new zinc phosphonate materials, exemplified by $(\text{NH}_4)_2$

$[\text{Zn}_2(\text{O}_3\text{PCH}_2\text{CH}_2\text{COO})_2] \cdot 5\text{H}_2\text{O}$ (henceforth denoted BIRM-1, University of Birmingham porous material number 1). Ion exchange properties with certain monovalent and divalent metal cations are explored on BIRM-1 with a view to develop MOFs with an ion exchange capacity, whose properties would be tunable using well established techniques of ion exchange, and to explore potential applications.

Chapter 2

Experimental

2.1 Solid State Synthesis

2.1.1 Hydrothermal Synthesis

Hydrothermal synthesis is a technique to crystallize crystals from comparatively high temperature at high vapour pressures³⁸. It is the main method employed to prepare a series of carboxyethylphosphonates in this project. All chemicals were weighed out using an analytical balance (up to ± 0.1 mg accuracy) in the desired mole ratios, then mixed with water and stirred at room temperature. After stirring, the resulting solution was placed into a Telfon™ liner and sealed in a stainless steel autoclave in a preheated oven under autogeneous pressure conditions. In this unique pressure–temperature interaction system, by carefully adjusting other reaction conditions such as pH value, reaction time and temperature, the solubility of the reagents involved is amplified and the chemical behaviour of the solution is modified to be able to achieve the desired phases.

2.1.2 Cation Exchange

Ion exchange experiments were carried out in this project to produce the enhanced

functional materials by post synthetic modification. Ion exchange occurs when cations present inside the porous structure are exchanged for other cations externally from the immersed liquid phase¹¹³. For this project, the cation existing inside the structure is NH_4^+ , and the target ions for exchange are from lithium, sodium, potassium, magnesium, manganese and cobalt salts solutions respectively.

2.2 Crystallography and Diffraction

Crystallography and diffraction are widely used for studying solid state materials¹¹⁴. Crystallography is the science describing the way in which the component atoms in a (crystalline) solid are arranged, and diffraction techniques provide very powerful tools to understand this arrangement.

2.2.1 Fundamental Crystallography¹¹⁵

A crystal structure is constructed of a unique arrangement of atoms exhibiting long range order and symmetry in three dimensions. The lattice is a mathematical concept, describing an infinite pattern of points, each of which must have the equivalent surroundings in the same orientation. Hence the ideal crystal structure can be described as being made up from a lattice by introducing atoms or bulky groups of atoms at each lattice point, each of which will then have the same surroundings identical to other points. The smallest repeating unit in a lattice that completely represents the atomic arrangement and reveals the whole symmetry of the crystal structure is entitled unit cell. Hence for an ideal crystal framework, the whole structure can be assembled from the repetition of the unit cell following the translational symmetry. The three lengths of the edges (a , b and c) and the angles

between them (α , β and γ) of the unit cell are known as lattice parameters.

Variations of the unit cell lengths and angles give rise to seven types of subunits, associated with seven crystal systems. These seven lattice systems can be further categorized by combination with four distinct lattice centring: primitive centring (P), body centring (I), face centring (F) and base centring (C), to result in fourteen Bravais lattices (Figure 2.1). Besides these basic atom positions present in the unit cells of these fourteen Bravais lattices, the positions of which can be described by the fractional coordinates in each axis with the inherent symmetry (Table 2.1), further symmetry elements are also compulsorily required to describe the atomic arrangement of other additional atoms contained in the Bravais lattice. Hence these fourteen lattice systems can be further categorized depending on the various symmetry elements present: both the point symmetry elements (mirror planes, rotary inversion axes, rotation axes and centres of symmetry) which have 32 different possible combinations (crystallographic point groups) to describe the symmetry of the three dimensional motif, and the translational symmetry elements (glide planes and screw axes) to describe all the possible patterns which are raised by merging motifs of different symmetries with their applicable lattices¹¹⁶. Combining all the possible symmetry arrangements in different crystal systems and the lattice types results in 230 space groups. These space groups completely describe the symmetry of the crystal structure and can be adopted to assist in the definition of the atomic arrangements in the crystal structures.

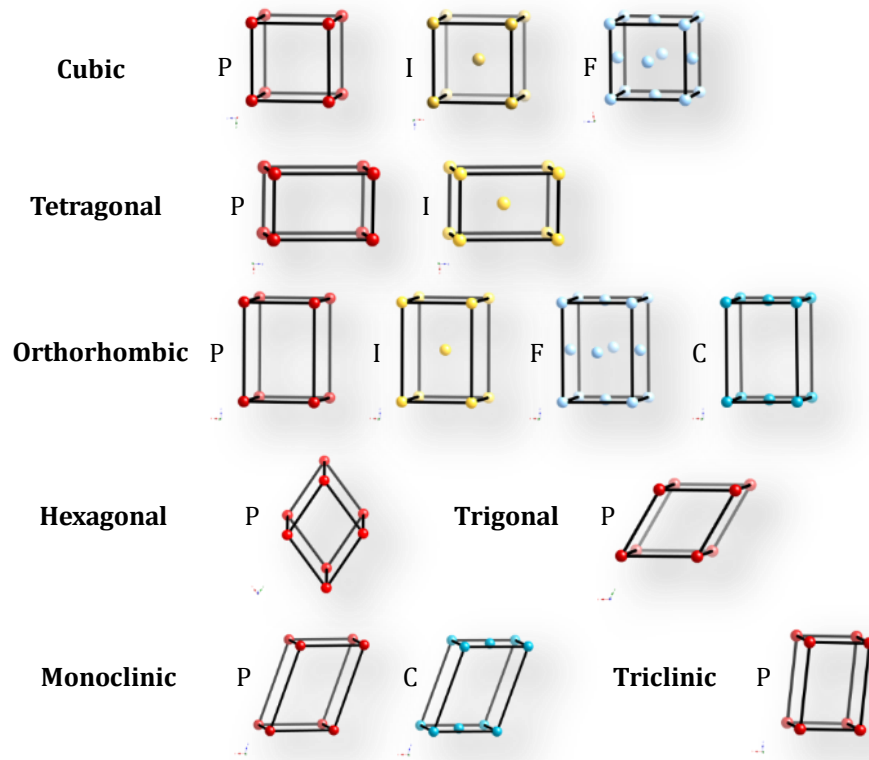


Fig. 2.1 the fourteen Bravais lattices.

Table 2.1 The seven crystal systems and essential symmetry features.

Crystal System	Unit Cell Dimensions	Essential Symmetry
Cubic	$a = b = c; \alpha = \beta = \gamma = 90^\circ$	Four threefold axes
Tetragonal	$a = b \neq c; \alpha = \beta = \gamma = 90^\circ$	One fourfold axis
Orthorhombic	$a \neq b \neq c; \alpha = \beta = \gamma = 90^\circ$	Three twofold axes
Hexagonal	$a = b \neq c; \alpha = \beta = 90^\circ; \gamma = 120^\circ$	One six fold axis
Trigonal	$a = b = c; \alpha = \beta = \gamma \neq 90^\circ$	One threefold axis
Monoclinic	$a \neq b \neq c; \alpha = \gamma = 90^\circ; \beta \neq 90^\circ$	One twofold axis
Triclinic	$a \neq b \neq c; \alpha \neq \beta \neq \gamma \neq 90^\circ$	N/A

2.2.2 Lattice Planes and Miller Indices

The faces of the unit cells or internal planes that intersect the structure can be described in terms of three integers (hkl), known as Miller Indices (Figure 2.2). Each index denotes the value of the reciprocal of a fraction of the unit cell vectors, a , b and c , respectively. Miller Indices represent not just one single plane, but a series of

parallel lattice planes. Hence any equivalent lattice plane will have the same (hkl) values denoted as $\{hkl\}$. The perpendicular distance between such two planes is known as the d -spacing (d_{hkl}). For the tetragonal and orthorhombic systems, the d_{hkl} can be derived from Equations 2.1 and 2.2.

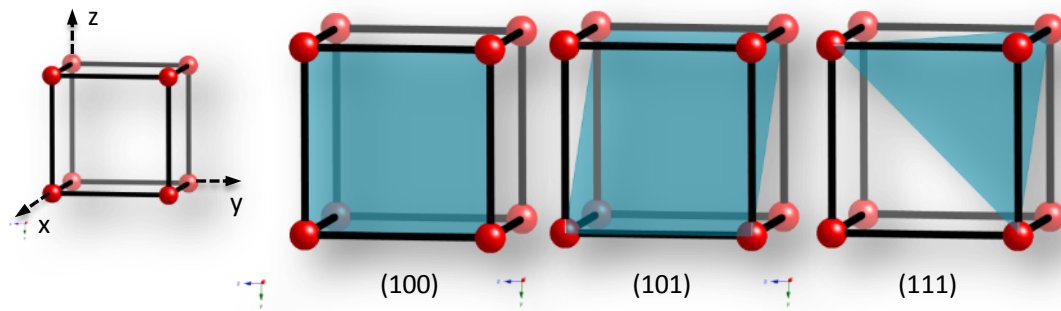


Fig. 2.2 Lattice planes described by Miller indices.

$$\text{Tetragonal:} \quad \frac{1}{d_{hkl}^2} = \frac{h^2 + k^2}{a^2} + \frac{l^2}{c^2} \quad (\text{Equation 2.1})$$

$$\text{Orthorhombic:} \quad \frac{1}{d_{hkl}^2} = \frac{h^2}{a^2} + \frac{k^2}{b^2} + \frac{l^2}{c^2} \quad (\text{Equation 2.2})$$

2.2.3 Diffraction and Interference

In order to appreciate how diffraction assists the understanding of the structural properties of solid states, a basic understanding of diffraction is necessary. In classical physics, the diffraction phenomenon refers to the apparent bending of waves that occurs when they encounter small obstacles or spread out through narrow chinks. This phenomenon happens with all types of waves, including sound waves, water waves and electromagnetic waves such as X-rays. When diffraction occurs, if waves with the same frequency are travelling in the same medium and direction, they will superimpose to form a wave with greater or lower amplitude. The total displacement

is equal to the vector sum of the displacements of the individual waves. In the case of two waves, the observed intensity at any point from the resultant wave can be determined by the phase difference between the two waves. If this shift is equal to zero, it will lead to completely constructive interference for the final formed wave, while if this is equal to half of the wavelength, it will result in completely destructive interference (Figure 2.3).

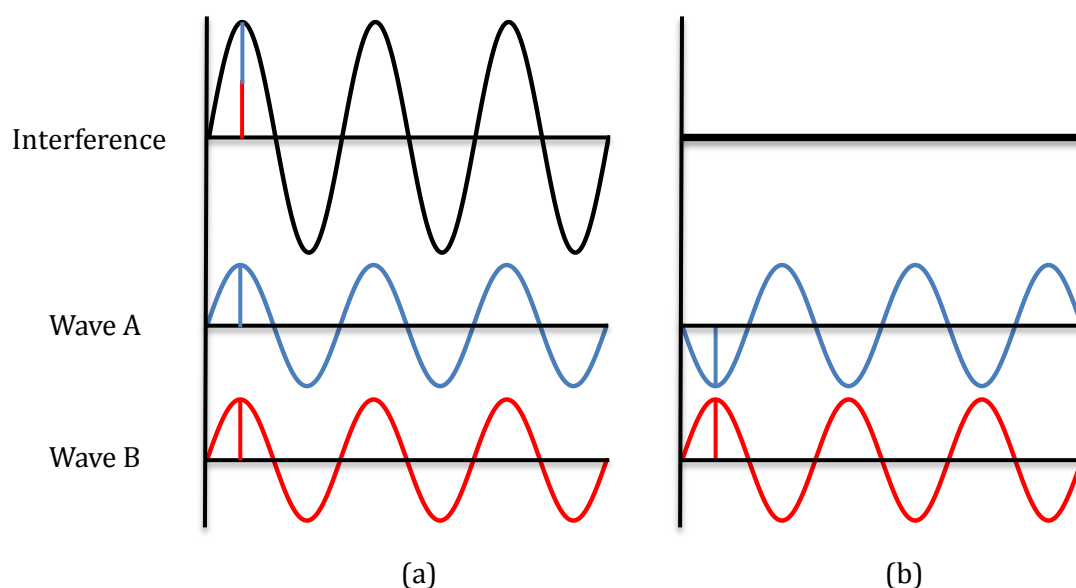


Fig. 2.3 Superposition of two waves gives rise to interference, (a) zero shift and (b) half wavelength shift.

2.2.3.1 The Bragg Law

This interference effect is generally most noticeable for waves whose wavelength is roughly similar to the dimensions of the diffracting obstacles. If the obstructing object provides multiple, closely spaced openings, a complex diffraction pattern of various intensities can be formed. Crystalline solids are such materials, the plane spacings of which are similar to the wavelength of X-rays, and hence can provide perfect three-dimensional diffraction gratings. X-ray diffraction is grounded on constructive

interference of monochromatic X-rays. When the diffraction occurs, waves are scattered from the electron cloud of atoms at different positions. These differences in path lengths result in phase differences between the waves. If the travel path difference of the waves is equal to integer multiples of the wavelength, then they could interfere constructively. Thus various superpositions are generated and result in observed intensity. Hence employing X-rays for the structural investigation of crystalline materials becomes one of the most fundamental and useful techniques.

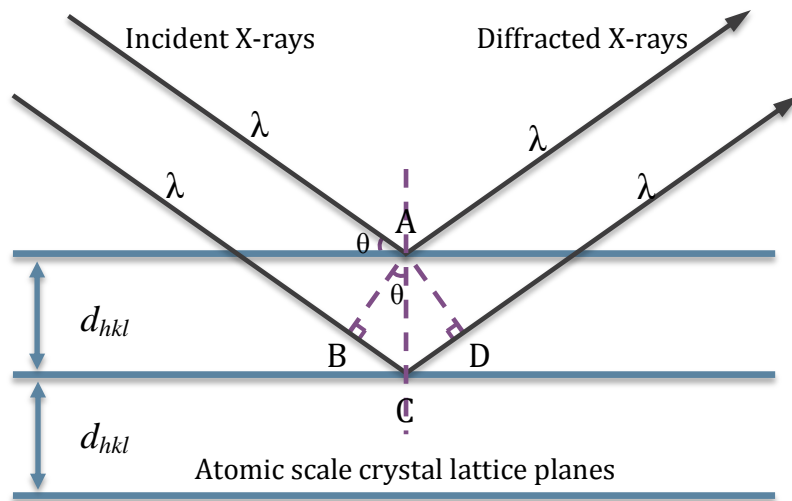


Fig. 2.4 Schematic for the path difference derivation for Bragg's law.

The general relationship between the wavelength of the incident X-rays and the path lengths in the crystal lattice planes of atoms is illustrated in Figure 2.4. Applying simple trigonometry to the geometrical arrangement leads to the Bragg equation (Equation 2.2):

$$BC + CD = (d_{hkl} \sin \theta) + (d_{hkl} \sin \theta) = 2d_{hkl} \sin \theta \quad (\text{Equation 2.2})$$

where:

d_{hkl} is the interplanar distance between the planes with the same Miller indices, and θ is the incident angle of the radiation.

Superposition generated in constructive interference only happens if the path difference is equal to a multiple of the wavelength ($n\lambda$), thus this equation can be further simplified to (Equation 2.3):

$$n\lambda = 2d_{hkl} \sin \theta \quad (\text{Equation 2.3})$$

2.2.4 Powder X-ray Diffraction^{114, 117}

X-ray diffraction (XRD) is frequently the primary monitoring method for routine phase identification of a crystalline material. Most of the samples prepared in this project were polycrystalline powders that consist of large amount of tiny crystals too small to be examined by single crystal methods. Hence powder X-ray diffraction was a very convenient technique to investigate such materials. In a powder sample, a large amount of the randomly orientated crystals are packed together. When irradiated by X-rays, diffractions will arise from the tiny sample crystals at all possible angles defined by Bragg's Law and provide a great wealth of information on the micro-structural properties of the material and in many cases can be used to reconstruct the 3D framework.

A typical X-ray diffraction pattern (Figure 2.5) can be plotted in the form of the measured intensity diffracted by a polycrystalline sample corresponding to the Bragg angle as the independent variable (2θ). As apparent from Figure 2.5, several discrete diffraction peaks are isolated over a continuous background. Such noise is mainly generated through experimental and instrumental factors such as amorphous phases, detector noise and incoherent scattering. Although information may be extracted from the background, in the major powder applications, attempts are

generally made to minimize the background during the experiment and it is often disregarded in routine pattern analysis.

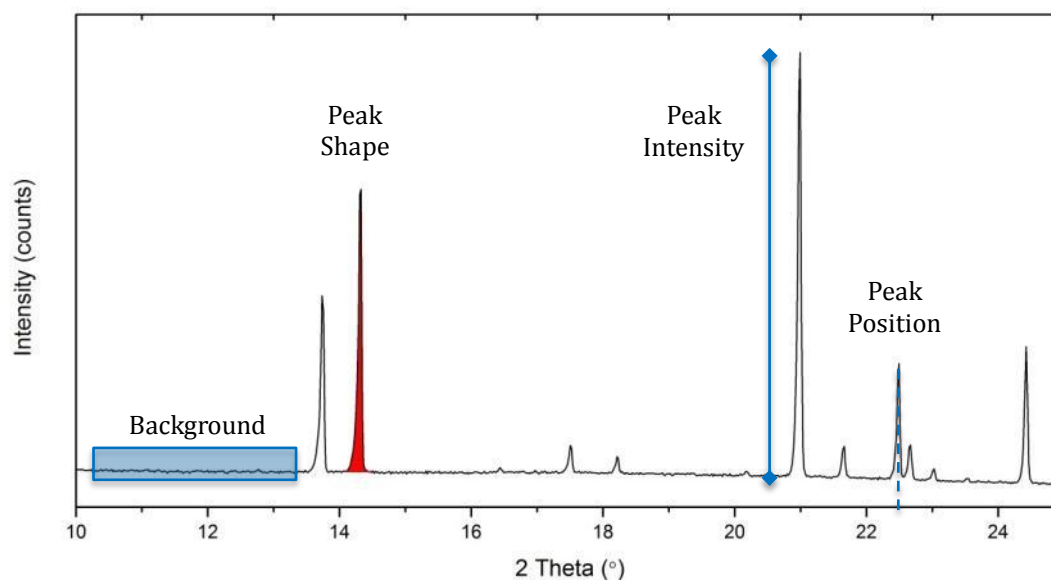


Fig. 2.5 Typical X-ray diffraction pattern.

The diffraction peaks are the most investigated aspect in an X-ray diffraction pattern. There are many important features for a Bragg reflected peak, including peak position, peak profile and peak intensity. Peak position is a fundamental factor generated from the scattering within lattices. Based on the Bragg equation (Equation 2.3), diffraction peaks appear at specific angles determined by the wavelength of the incident radiation and the unit cell dimensions. These positions can also be inaccurate because of some instrumental parameters such as zero point errors.

Peak shape profile is a factor to describe the broadening of the diffraction peaks. It is important because this parameter contains information of the crystallite size which is of interest in materials characterization. This relationship can be approximately described by the Scherrer equation (Equation 2.4):

$$\beta = \frac{K\lambda}{\tau \cos \theta} \quad (\text{Equation 2.4})$$

where:

- β is the Bragg peak broadening, in radians,
- K is the shape factor (typically around 0.89),
- λ is the X-ray wavelength,
- θ is the Bragg angle of the peak position, and
- τ is the average crystallite diameter.

It is important to realize that other parameters made contributions to the broadening of a diffraction peak as well. The most important of these are usually inhomogeneous strain in the crystals and certain instrumental effects.

A powder diffraction pattern is composed of many Bragg peaks with various peak intensities. Numbers of factors have either central or secondary roles in the determination of the peak intensities. Such factors as the scattering power of the X-ray source, efficiency of the detector and data collection time, will affect the absolute intensity of the X-ray diffraction pattern. The relative intensities of different Bragg peaks in one phase are mainly dependent on the type and position of the atoms located inside the unit cell. Certain crystal shapes, especially the case of needle-shaped and plate-shaped crystallites will cause a disproportionate amount of intensity generated from certain lattice planes and alter the relative intensities. The relative overall intensity of a mixed phase largely depends on the relative concentration of each phase.

2.2.4.1 Laboratory X-ray Diffractometer

All the X-ray powder diffraction patterns in this project were collected on a laboratory

X-ray diffractometer. The X-rays are generated by bombarding a copper anode target with a beam of high energy electrons in a vacuum tube. These electrons are emitted from an electrically heated tungsten cathode and accelerated toward the copper target by applying a 40 kV voltage. When these high energy electrons irradiate the copper target, the inner shell electrons of copper atoms will be dislodged creating vacancies in lower orbitals. These vacancies are then filled by other electrons from outer shells inducing a cascade of electronic transitions which results in the emission of radiation in the form of X-rays. These emitted spectra mostly consist of the radiation profiles K_α and K_β , respectively, for filling with electrons from L and M shells into the K shell. In the case of the copper target (Figure 2.6), the K_α radiation is a doublet at the wavelengths of $K_{\alpha1} = 1.5406 \text{ \AA}$ and $K_{\alpha2} = 1.5433 \text{ \AA}$. These lines are created due to the total angular momentum quantum numbers for the 2p electrons of $1/2$ and $3/2$. Thus two possible spin states exist, which results in a small difference in the energy transitions and X-ray wavelengths.

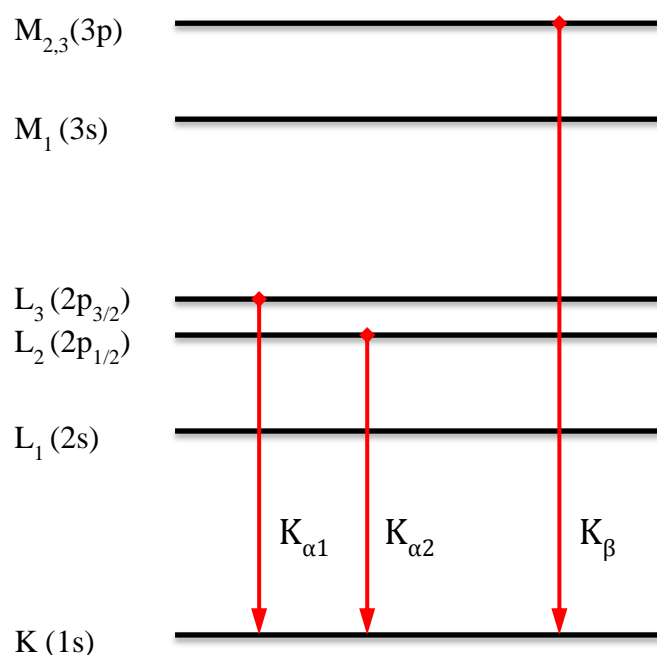


Fig. 2.6 Energy level diagram for neutral Cu atom.

The K_{α} wavelength is more intense than K_{β} . As a single and intense beam of radiation is required for X-ray diffraction, a monochromator is necessary to filter $K_{\alpha 2}$ and K_{β} to yield a monochromatic radiation of $K_{\alpha 1}$. X-ray diffraction from the examined sample can be detected and a position sensitive detector (PSD) is applied to count the intensity over a 2θ range. The intensity is directly proportional to the amount of X-ray beam hitting the detector.

As a Laboratory powder X-ray diffraction patterns for phase identification and comparison in this project were all collected on a Bruker D8 Advance X-ray diffractometer with transmission (Debye-Scherrer) geometry (Figure 2.7). Cu $K_{\alpha 1}$ radiation ($\lambda = 1.54056 \text{ \AA}$) was employed as the X-ray source to scan powder samples from 5° to 70° (2θ) with the given step size 0.0197° for 30 minutes. Prior to characterization samples were dried in air for 3 days and ground, and then sealed in-between two layers of ScotchTM magic tape. Samples were rotated perpendicular to the X-ray beam during the examination.

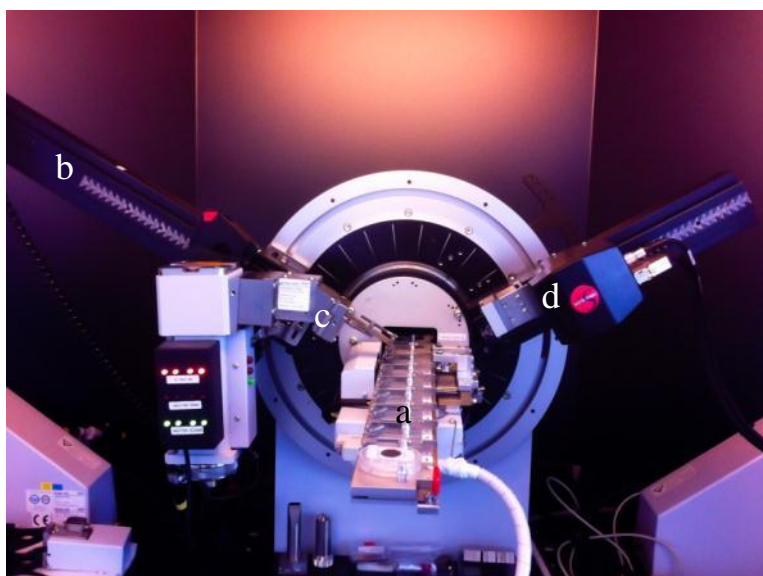


Fig. 2.7 D8 X-ray diffractometer setup used in this project; (a) sample holder, (b) X-ray source, (c) monochromator and (d) detector.

2.3 Structure Determination from Powder X-ray Diffraction¹¹⁷⁻¹¹⁹

The phenomenon of X-ray diffraction by a crystalline material fundamentally relies on the scattering of X-rays from the periodically repeating array of atoms. Hence the important features of a powder pattern such as peak positions and intensities will give information on the atomic arrangements in a crystal structure. The common process for the determination of an unknown structure from a powder X-ray diffraction pattern is shown in a flowchart (Figure 2.8). For the data collection, a high resolution and accurate X-ray diffraction pattern is required to provide sufficient information of the peak positions, intensities and peak shape profiles with minimized background. In this project, the patterns used for structure determination were all collected for 5 hours on a Bruker D8 Advance X-ray diffractometer with transmission geometry with a 2θ range from 5° to 90° .

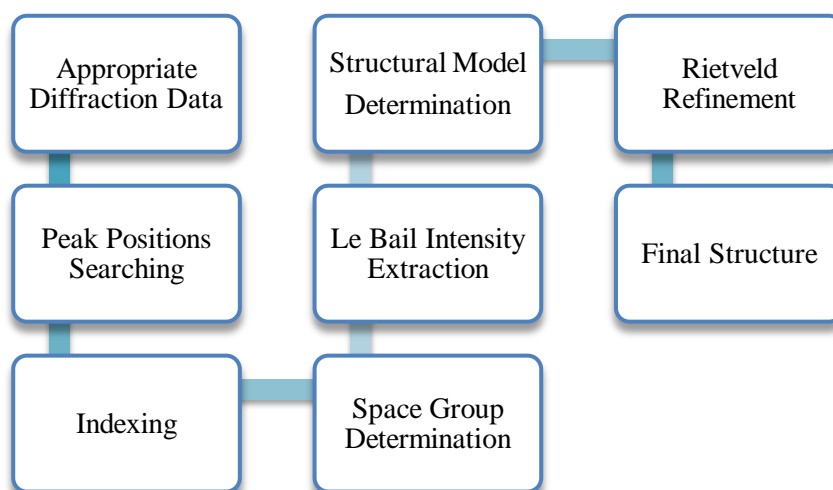


Fig. 2.8 Diagram of common structure determination procedure¹¹⁷.

2.3.1 Unit Cell Parameter Determination

After collecting good quality diffraction data, the following step is to determine the

position of each diffraction peak. As the location of the peaks only relies on the crystal system and the size of the unit cell under the radiation of a constant wavelength light source, hence the peak positions can be used to determine the possible crystal system and the unit cell parameters by inputting them into an indexing program. Crysfire¹²⁰ was employed in this project for indexing. It integrates a set of different indexing programs in its suite, and the programs of Taup¹²¹, Dicvol¹²² and Treor¹²³ are those most frequently used in this project, which are well suited for searching the high symmetry crystal systems from cubic down to orthorhombic¹²⁰. By using these programs to analyze the pattern, the result is usually generated as a combination of different possible solutions. Hence Chekcell¹²⁴ was employed for the unit cell parameters and space group assignments by comparing the fit of the peak positions calculated from the indexed cell with the observed ones. The most probable solution was further examined by Le Bail¹²⁵ (whole pattern structure less) fitting in GSAS^{126, 127} to refine the cell parameters and obtain good experimental parameters such as background and profile parameters before fitting the structure.

2.3.2 Initial Structural Model Determination

Once the unit cell has been determined and the associated space group has been selected, there follows a critical step to determine an accurate initial structural model for the further analysis. The structural model can be adopted from a previously solved single crystal structure of a related material. If a comparable single crystal structure model is available for a structure determination, sufficient structure information can be easily obtained in the following structure determination. If a similar structural model cannot be easily found, then an alternative method could be used. These structure solution methods can be divided into two broad categories: those based on

real-space methods and those based on reciprocal-space methods. For the first ones, the structure model is attempted to be geometrically constructed based on the chemical information, possible connectivity, typical bond lengths and bond angles as well as analogies with closely related compounds, then test against the experimental diffraction data to examine various ways of structural packing and differences in conformations of model until a general model is found with physical, chemical and crystallographic sense. The second group of methods uses an experimental array of the diffraction data, which is the absolute value of structure amplitudes to provide initial clues about the construction of the crystal structure, exploit these relationships and attempt to determine the phases directly. Two very widely used reciprocal space methods are Patterson method and direct method. As these real-space methods and reciprocal-space methods takes advantage of prior chemical knowledge, sometimes a very accurate structure model could be built. However, powered by the modern computing technique, large amount of chemically reasonable structural models can be generated occasionally for certain cases, hence finding the best one could be very time consuming and uncomfortable^{114, 128}. In this project, the structural model used for K⁺-BIRM-1 to determine the exchanged structure was directly adopted from the single crystal structure of BIRM-1. For Co²⁺-BIRM-1, a previously unfinished single crystal structure of Co²⁺-BIRM-1 was employed as a starting structural model for the following structure determination.

2.3.3 Rietveld Refinement

Rietveld refinement was frequently employed for detailed structural analysis. This method was named after a Dutch crystallographer Hugo M. Rietveld. A fundamental keystone of the method is that a very accurate diffraction pattern can be calculated

with sufficient necessary information. By information we mean a very precise structural model built from the unit cell parameters, atomic fractional coordinates, atomic occupancies, thermal oscillations as well as certain experimental parameters such as diffractometer constants, pattern background shape and peak profiles. These parameters can then be very carefully refined in a logical sequence with a nonlinear least-squares method to achieve agreement between all the data points from the observed and the calculated diffraction patterns. The aim of a Rietveld refinement is to determine a very accurate structure model for the actual phase present in the diffraction pattern by minimizing the difference between the observed and calculated pattern (Equation 2.5¹²⁹).

$$S_y = \sum_i w_i (y_i - y_{ci})^2 \quad (\text{Equation 2.5})$$

where:

- S_y is the residual need to be minimized,
- w_i is weighting factor which is equal to $1/y_i$,
- y_i is the observed intensity at the i th step, and
- y_{ci} is the calculated intensity at the i th step.

The calculated intensity of a Bragg peak I_{hkl} can then be illustrated in the form of Equation 2.6¹¹⁴:

$$I_{hkl} = K m_{hkl} L P A T_{hkl} E_{hkl} |F_{hkl}|^2 \quad (\text{Equation 2.6})$$

where:

- K is the scale factor, it is a proportionality constant to normalize experimentally observed integrated intensities with absolute calculated intensities,
- m_{hkl} is the multiplicity of the Bragg reflection,
- L is the Lorentz multiplier,
- P is the polarization correction factor,
- A is the absorption multiplier,

T_{hkl} is the preferred orientation factor,

E_{hkl} is the extinction multiplier, and

F_{hkl} is the structure factor, which describes how atomic arrangement including the atom type, coordinates and distribution influences the intensity of the scattered beam.

As the structure factor contains the information the atomic positions, it is a very important factor. The F_{hkl} can be given by Equation 2.7¹¹⁴:

$$F_{hkl} = \sum_j f_j g_j t_j \exp[2\pi i(hx_j + ky_j + lz_j)] \quad (\text{Equation 2.7})$$

where:

f_j is the atomic scattering factor of the j th atom,

g_j is the occupancy of the j th atomic site, $g_j = 1$ for a fully occupied site,

t_j is the temperature factor, which describes thermal motions of the j th atom,

$i = \sqrt{-1}$, and

x_j , y_j , and z_j are the fractional coordinates of the j th atom.

The quality of the refinement can mostly be described with a number of statistical measures, such as the profile reliability factor (R_p) and weighted profile factor (R_{wp}) expressed as percentages (Equation 2.5 and 2.6). The minimum achievable value with the refinement experimental parameters in Rietveld analysis is also of interest and can be written as R_{exp} (Equation 2.7)¹²⁹.

$$R_p = \frac{\sum |I_i(obs) - I_i(cal)|}{\sum I_i(obs)} \times 100\% \quad (\text{Equation 2.5})$$

$$R_{wp} = \left\{ \frac{\sum w_i [I_i(obs) - I_i(cal)]^2}{\sum w_i [I_i(obs)]^2} \right\}^{\frac{1}{2}} \times 100\% \quad (\text{Equation 2.6})$$

$$R_{exp} = \left\{ \frac{n - p - c}{\sum w_i [I_i(obs)]^2} \right\}^{\frac{1}{2}} \times 100\% \quad (\text{Equation 2.7})$$

where:

$I_i(obs)$ and $I_i(cal)$ are the observed and calculated diffraction intensities at point i ,

w_i is the weighting factor assigned to the point i ,
 n is the number of the points measured from the diffraction pattern,
 p is the number of the refinement parameters, and
 c is the number of the constraints used in the refinement.

Combining the R_{wp} and R_{exp} factors together will get the factor for the goodness of the fit (χ^2 , Equation 2.8). When the model is poor, the χ^2 starts out large and decreases as the model alters to achieve better agreement with the data during the refinement process.

$$\chi^2 = \left(\frac{R_{wp}}{R_{exp}} \right)^2 \quad (\text{Equation 2.8})$$

2.3.3.1 Difference Fourier Map

In certain cases, the structural model does not perfectly include all the electron density measured by the diffraction experiment, such as solvent molecules inside many porous materials, and in this project, it would be the exchanged metal cations introduced to the parent materials by post synthetic modification. The missing electron density distribution can be further analyzed by using difference Fourier mapping.

$$\rho_{xyz} = \frac{1}{V} \sum_{hkl} (F_{obs} - F_{cal}) \cos[2\pi(hx + ky + lz) - \alpha_{hkl}] \quad (\text{Equation 2.9})$$

where:

ρ is the electron density distribution,
 V is the volume of the unit cell,
 F is the structure factor,
 x, y and z are the position parameters, and
 α_{hkl} is the phase angle of the reflection (hkl).

The resulting electron density ρ can be determined with Equation 2.9 and will correspond to atoms missing in the calculated model structure. Chemically sensible positions with higher scattering intensity produced from the difference Fourier map may therefore be added as missing atom positions in the structural model for further refinement, minimizing the difference between observed and calculated patterns.

In this project, all the Rietveld refinements were carried out with the GSAS¹²⁶,¹²⁷ suite of programs. The crystal structure of BIRM-1 was refined against powder XRD data using the single crystal structure as starting model, to confirm the phase purity. For the structures of the potassium and cobalt ion-exchanged products, they were refined using the single crystal structure of BIRM-1 and Co²⁺-BIRM-1 respectively as starting models to obtain structural information and to evaluate the locations of the exchanged metal ions with the assistance of difference Fourier maps.

2.4 Phase Identification by Powder X-ray Diffraction

Other than the structural analysis based on Rietveld refinement, powder X-ray diffraction patterns were also used to identify phases by searching the standard patterns (peak positions) provided from the international center for diffraction data (ICDD) structure databases¹³⁰ for comparison with the measured XRD data via the Bruker DIFFRAC^{plus} EVA program. All the phases of the TGA solid residues after heating were identified by this method.

2.4.1 Quantitative Phase Analysis¹¹⁴

Quantitative phase analysis was carried out to determine the concentrations of various

phases present in the solid residual TGA product after the identification of each phase had been established. All quantitative analysis requires accurate determination of the diffraction pattern for both the peak positions and intensities, and the phase fractions are then estimated through Rietveld analysis relying on the relationship (Equation 2.10):

$$W_i = \frac{S_i(ZMV)_i}{\sum_{j=1}^n S_j(ZMV)_j} \quad (\text{Equation 2.10})$$

where:

W is the relative weight fraction of phase *i* in a mixture of n phases,

S is the Rietveld analysis scale factor,

Z is the number of the formula units in the unit cell,

M is the molecular mass of the formula unit, and

V is the unit cell volume.

Quantitative phase analysis by the Rietveld method is one of the fastest and most convenient tools in quantifying phase fractions. Any factor which could affect the peak intensities of each phase, such as preferred orientation, fluorescence or extinction can cause errors in the phase content determination. Hence the results provided from this method are highly dependent on the experimental parameters, and are usually considered as a semi-quantitative determination of the weight fraction of constituents.

2.5 Scanning Electron Microscopy

Scanning electron microscopy (SEM) is a widely used surface analytical technique for investigating the morphology. It is an electron microscope that images a sample by scanning it with a finely focused electron beam. The incident electron beam is

generated from a thermal emission source such as tungsten filament, the energy of which is usually higher than 10 keV depending on the evaluation objectives. Then the electrons are focused by a series of condenser lenses and scanned on to the sample surface by the direction of scanning coils.

When the electron beam is positioned onto the surface and interacts with the materials, many signals are generated from the sample, such as secondary electrons and X-rays. The secondary electrons are generated from collisions between the incident electrons and surface atoms where substantial energy loss occurs or by the ejection of loosely bound electrons. Such electrons typically have a very low energy (<50 eV), and therefore can only escape from a very thin surface layer of the sample, as a result, providing information on the surface appearance. When these released electrons are detected from every position in the scanned area by an electron detector and converted into electrical signals, an SEM image will be rendered with a large depth of field, and high resolution and magnification.

2.6 Energy-dispersive X-ray Spectroscopy

Energy-dispersive X-ray spectroscopy (EDX) is an analytical technique used for the elemental analysis which usually accompanies SEM. It depends on the analysis of X-ray excitation from the sample. When an incident electron beam generated from SEM drives deeper into the sample, these high energy electrons irradiate the sample atoms causing the removal of core electrons. Other electrons in higher energy levels can then relax to fill the hole, releasing X-ray radiation which is detected by the spectrometer (Figure 2.9). The energy emitted is related to the energy gap between two energy levels of the atoms in the sample. As every element has a different

electronic configuration, this technique can be used for elemental analysis.

Morphology and stoichiometry in this project were studied with a Jeol JSM 6060 scanning electron microscope equipped with energy dispersive X-ray analysis to confirm the presence of exchanged metal ions and roughly estimate the degree of ion exchange. Each sample was applied to an adhesive carbon film on the sample holder and coated with carbon before examination.

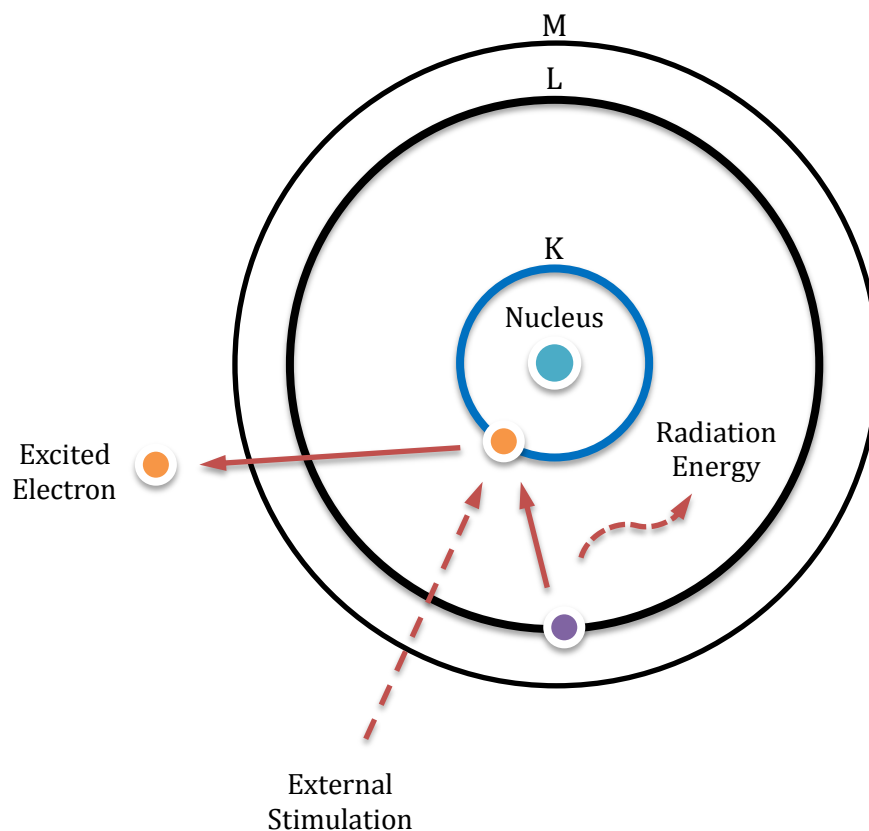


Fig. 2.9 Interactions between the electron beam and sample atom.

2.7 Fourier Transform Infrared Spectroscopy

Infrared spectroscopy is a widely used analytical technique to determine the presence of a wide variety of functional groups in a molecule. Infrared refers to a part of the

electromagnetic spectrum between the visible and microwave regions. When a material is irradiated with infrared radiation, atoms and molecules can absorb electromagnetic radiation, but only at certain energies (wavelengths). This energy is related to the molecular bonds that vibrate at various frequencies which correspond to the ground state and several excited states. If the energy of the incident photon is exactly equal to that of the energy gap between vibrational states, the photon can be absorbed to excite molecules from the ground vibrational state into a higher vibrational state. The infrared spectrum is thus generated from the transitions between vibrational energy states. The energy corresponding to these transitions between a vibrational ground state and the first excited state is generally 1–10 kcal/mol (E) which corresponds to the mid-infrared portion (wavenumber = 400 cm^{-1} to 4000 cm^{-1}) of the electromagnetic spectrum (Equation 2.11) and these are the most frequently observed transitions.

$$E = \frac{hc}{\lambda} \quad (\text{Equation 2.11})$$

where:

h is Planck's constant, and

c is the speed of the light.

In order for the photon to transfer its energy to excite the molecules to a higher vibrational state, this vibration must result in an alteration in the dipole moment of the molecule (Figure 2.10). In a Fourier Transform Infrared (FTIR) spectrometer, all optical frequencies of the infrared source are observed simultaneously over a period of scan time. Then the detector measures the intensity of transmitted radiation as a function of its wavelength, analyzed by a computer using Fourier transforms to obtain a constituent infrared spectrum.

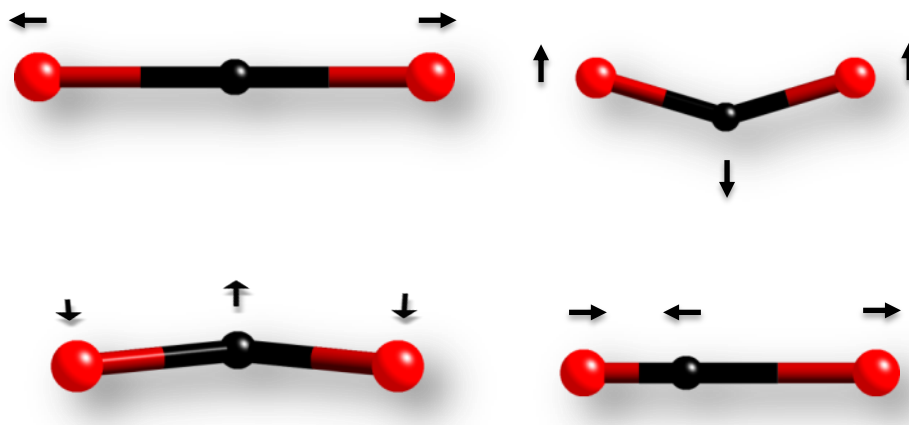


Fig. 2.10 Four fundamental vibrations for CO₂; the symmetric stretch of CO₂ (upper left) is inactive in the IR spectrum owing to no alteration in the dipole moment.

FTIR measurements carried out in this project were recorded on a Perkin Elmer Spectrum 100 FTIR spectrometer with universal ATR sampling accessory from the wavenumber 500 cm⁻¹ to 4000 cm⁻¹. This allows an in-depth characterization of the rehydration and dehydration of products.

2.8 Flame Photometry

Flame photometry is an atomic emission method to detect trace amounts of metal salts. Sample solution is transferred into a flame through an aspirator. The solvent is evaporated by this hot flame and the metal was atomized consequently, and then valence electrons are excited to higher energy levels by absorbing energy from the flame. As excited electrons return to the ground state, radiation is emitted as a characteristic atomic line spectrum. Optical filters are then used to select the emission wavelength of the examined metal. Comparing the emission intensities of unknown concentration solutions to those of standard solutions, the metal ion concentration in the target solution can be quantitative analyzed. The intensity of the emitted light can

be described by the Scheibe-Lomakin equation (Equation 2.12):

$$I = k \cdot c^n \quad \text{(Equation 2.12)}$$

where:

- c is the concentration of the metal ion,
- k is the constant of proportionality, and
- $n = 1$, at the linear part of the calibration curve.

The emitted intensity of the investigated metal ion is directly relative to the concentration of the sample. However, due to the nature of this technique, errors may be easily introduced during the preparation of the standard solutions and in the use of the calibration curve. Thus it is not a very precise method to measure the concentration of metal ions. In this project, flame photometry was performed on a Model 400 Flame Photometer developed by Corning to investigate the concentration of lithium and sodium ions in the exchanged products. Low concentration lithium standard solutions of 1, 2, 5, 8, 10ppm and sodium standard solutions of 1, 1.5, 2, 2.5 and 3 ppm were directly prepared by diluting aliquots of the standard solutions ordered from Acros Organics (1mg/ml) with deionised water to maintain the linearity of the standard curve.

2.9 Thermogravimetric Analysis

Thermogravimetric analysis (TGA) is a kind of material characterization procedure performed on samples to precisely determine mass change in relation to a temperature programme in a controlled atmosphere such as N₂, O₂, H₂, Ar, air or vacuum. This allows monitoring of the decomposition kinetics and thermal stability of materials. Differential thermal analysis (DTA) is usually coupled with TGA in common thermal

analysis. When the sample experiences a structural phase transformation, it will either absorb (endothermic) or release (exothermic) heat. This thermal difference between the reactive sample and the inert reference crucible is then recorded as a function of time or temperature. Simultaneous TGA with DTA will measure both heat and weight changes in one examination and provide useful information about endothermic and exothermic events with either no associated weight loss such as melting, phase changes or degradation of the structure involving a weight loss.

2.10 Mass Spectrometry

Thermogravimetric analysis can be used with mass spectrometry (MS) to determine the gas generated during the heating process and further assign specific gaseous species. A mass spectrometry experiment basically consists of four main processes: ionization, acceleration, separation and detection. Charged ions can be deflected when moving in magnetic fields, thus atoms/gaseous molecules are first turned into ions. The method used in this project is electron ionization (EI). An electron beam is employed to knock electrons from the sample particles to create charged cations. Then these cations are accelerated to a finely focused beam with the same kinetic energy and directed into an electromagnetic field generated by a quadrupole mass analyzer. The motion of cations will depend on the electromagnetic fields, thus only ions with a particular mass to charge ratio (m/z) will have a stable trajectory through a specific field and further pass to the detector. Other ions with different m/z values will have unstable routes and collide with the quadrupole walls and therefore will not be detected. When a flow of such cations hits the surface of the detector, the electrons are picked up and thus a current is generated, further amplified and recorded. The cations after contacting the detector are neutralized and then removed from the system by a

vacuum pump. By varying the magnetic field, ions with different m/z values can be detected and constitute a mass spectrum.

Thermogravimetric analysis and differential thermal analysis in this project were carried out from 30 °C to 900 °C under an oxygen atmosphere at a heating rate of 5 °C/min using a Netzsch STA 449 F1Jupiter thermogravimetric analyzer with mass spectrometric detection (Netzsch QMS 403C A ölos).

2.11 Hydrogen Uptake Measurement

The investigation of hydrogen adsorption properties was performed on an intelligent gravimetric analyzer (IGA). This method integrates a precise computer control with the measurement of weight change, after a step change in the system pressure and temperature. Hence the weight change isotherm will rely on the pressure step size and the temperature and subsequently gives insight into the dynamics of the absorption/desorption process.

Hydrogen adsorption capacities in this project were determined on a Hiden constant pressure thermogravimetric analyzer, which is known as an IGA-001. Samples examined on the IGA were all inertly loaded to minimize the exposure to atmosphere. Around 200 mg of sample was loaded into a glass sample bulb and degassed. After that the sample was cooled to 77 K. Pressure–composition isotherms were then determined from 0 to 20 bar. The purity of the hydrogen source was 99.995%, and a liquid nitrogen trap was used on the hydrogen gas inlet stream. The sample, microbalance as well as counterweights all share the same experimental environment which helps to correct and reduce the effects of buoyancy on the

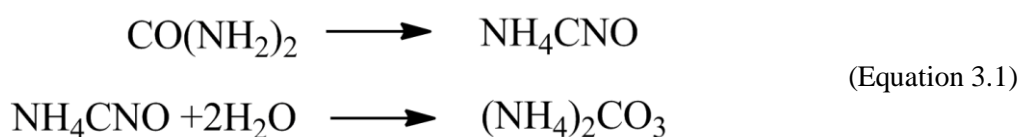
observed sample mass. After examinations were completed, the sample was inertly unloaded by flushing for 1 hour with Argon, allowing further investigation by XRD.

Chapter 3

Synthesis and Characterization of a New Zinc Phosphonate Framework Material BIRM-1

3.1 Introduction

When this research was started, a synthesis route had been developed for the formation of metal phosphonates which uses urea to control the pH, as during heating the urea decomposes in aqueous solution to form ammonium carbonate (Equation 3.1). The rate of the urea hydrolysis is controlled by the temperature, which in turn controls the pH of the solution and the crystallization process.



Base on this strategy, a few novel zinc phosphonates with different pore sizes and framework topologies had already been successfully isolated. However the one with the largest three dimensional pore structure (BIRM-1) was synthesized serendipitously (Figure 3.1). This product contains ammonium cations within the pores, which may give the material the ability to undergo ion exchange and enable the fine-tuning of its functionality. Hence initially investigation was into the development

of synthesis conditions under which BIRM-1 could be reliably prepared as a single phase. In this chapter, the strategies for the synthesis of BIRM-1 were explored, and the characterizations of its structure and properties were investigated.

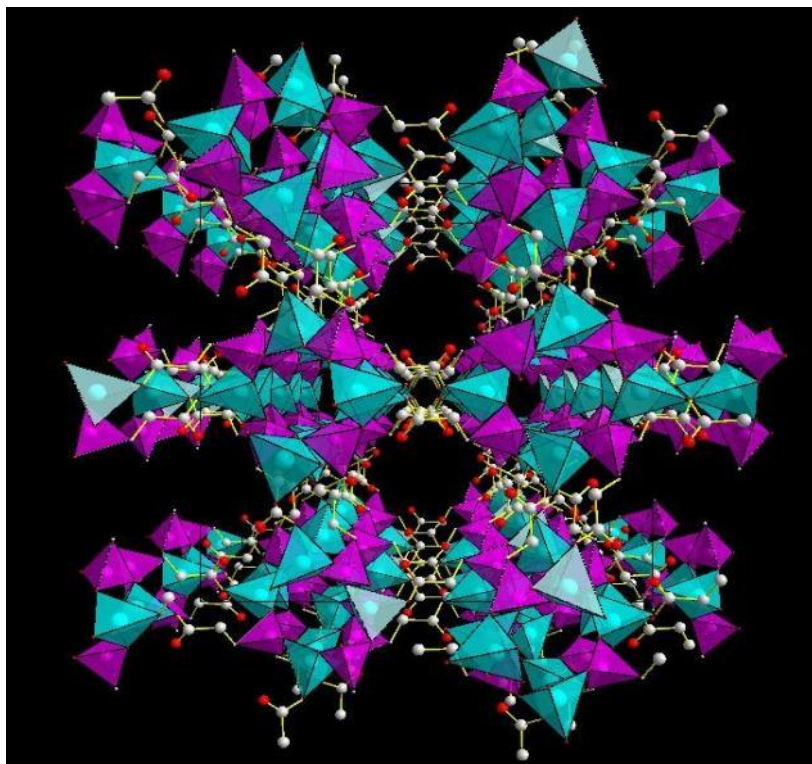


Fig. 3.1 Polyhedral view along the z-axis of the zinc phosphonate with the largest three dimensional porous structure obtained from previous research; hydrogen atoms and internal solvent molecules have been omitted for clarity; colour scheme: ZnO_4 – turquoise tetrahedra, CPO_3 – purple tetrahedra, O – red and C – light grey.

3.2 Experimental

Unless otherwise specified, all the chemicals used were of reagent quality obtained directly from Sigma Aldrich and used without further purification.

3.2.1 Synthesis of $\text{Zn}(\text{O}_3\text{PCH}_2\text{CH}_2\text{COOH})\cdot\text{H}_2\text{O}$

$\text{Zn}(\text{O}_3\text{PCH}_2\text{CH}_2\text{COOH})\cdot\text{H}_2\text{O}$ is the first product discovered during the investigation for the synthesis of BIRM-1. It can be synthesized under hydrothermal conditions.

1.68 g zinc nitrate hexahydrate was dissolved in 11.25 ml of deionized H₂O. To this solution, 1.13 g 2-carboxyethylphosphonate acid, 1.54 g tetraethylammonium bromide and 1.76 g urea were added to give a clear solution after stirring for 30 minutes. Then the resulting mixture was placed in a Parr Teflon-lined stainless steel autoclave, which has a capacity of 23 ml. The reaction mixture was heated under autogeneous pressure at 85 °C for a period of 24 hours, after which it was removed and allowed to cool in the air. The layered product was then washed with water recovered by filtration.

3.2.2 Synthesis of BIRM-1

BIRM-1 was initially prepared hydrothermally in a Teflon-lined stainless steel autoclave with a fill capacity of 23 ml. 1.68 g zinc nitrate hexahydrate was dissolved in 11.25 ml deionized H₂O. The solution was stirred till the zinc nitrate was fully dissolved, after which 1.13 g 2-carboxyethylphosphonate acid and 1.76 g urea were added. Then 1.54 g tetraethylammonium bromide was added to the solution (Table 3.1, Method I). After 30 minutes stirring, the resulting mixture was transferred to a Teflon-lined autoclave. Then the autoclave was placed in a 110 °C oven for 24 hours. The product was recovered by filtration, washed with distilled water, and allowed to dry in the air to yield a white crystalline product. After further research during this project, the molar ratios of the starting chemicals for synthesis of BIRM-1 were optimized (Table 3.1 Method II and Method III) in order to yield crystals with better morphology, but the reaction conditions and the methods remained the same.

Table 3.1 Chemicals used to synthesize BIRM-1.

	Molar Ratio		
	Method I	Method II	Method III
Zinc Nitrate	1	1	1
CEPA [†]	1.3	1.75	1.75
TEAB [‡]	1.3	1.3	1.3
Urea	5.2	5.2	9
H ₂ O	112	112	112

[†] 2-carboxyethylphosphonic acid, [‡] tetraethylammonium bromide

3.2.3 Synthesis of (NH₄)[Zn(O₃PCH₂CH₂COO)]

The preparation of (NH₄)[Zn(O₃PCH₂CH₂COO)] was very similar to the synthesis of BIRM-1 (Table 3.1 Method I and Method III), if the reaction was extended from 24 hours to 5 days or longer, white bulk crystals were formed on the bottom of the autoclave. The product was then recovered by filtration and washed with distilled water.

3.3 Synthesis Optimization

3.3.1 Synthesis of Zn(O₃PCH₂CH₂COOH)·H₂O

Previously attempts for the synthesis of BIRM-1 were carried out by heating a mixture of zinc nitrate, 2-carboxyethylphosphonic acid, tetrabutylammonium bromide and urea in an oil bath at 85 °C. With this method it was found very difficult to maintain the reaction temperature accurately and proved difficult to synthesize a pure phase; correspondingly the reproducibility was not satisfactory. Therefore the experimental method was amended to use a Teflon-lined autoclave, which was heated in an oven. With the same chemical mixture, an unexpected layered product was isolated after heating at 85 °C for 24 hours (Figure 3.2). This product was identified as

a previously known layered zinc carboxyethylphosphonate hydrate with the molecular formula $\text{Zn}(\text{O}_3\text{PCH}_2\text{CH}_2\text{COOH}) \cdot \text{H}_2\text{O}$ (Table 3.2), whose structure had been previously solved by single crystal XRD (Figure 3.3).

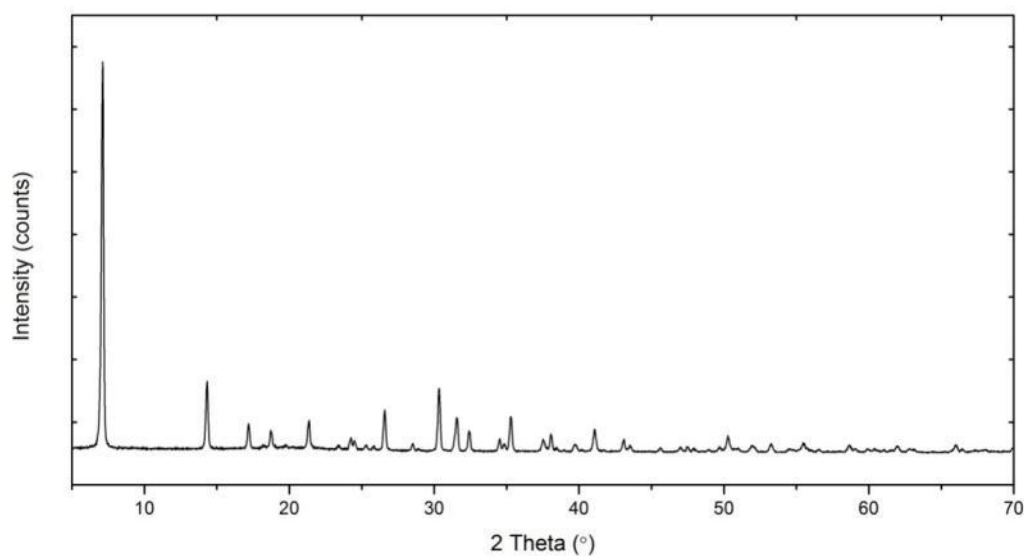


Fig. 3.2 Powder XRD pattern of the layered zinc phosphonate $\text{Zn}(\text{O}_3\text{PCH}_2\text{CH}_2\text{COOH}) \cdot \text{H}_2\text{O}$.

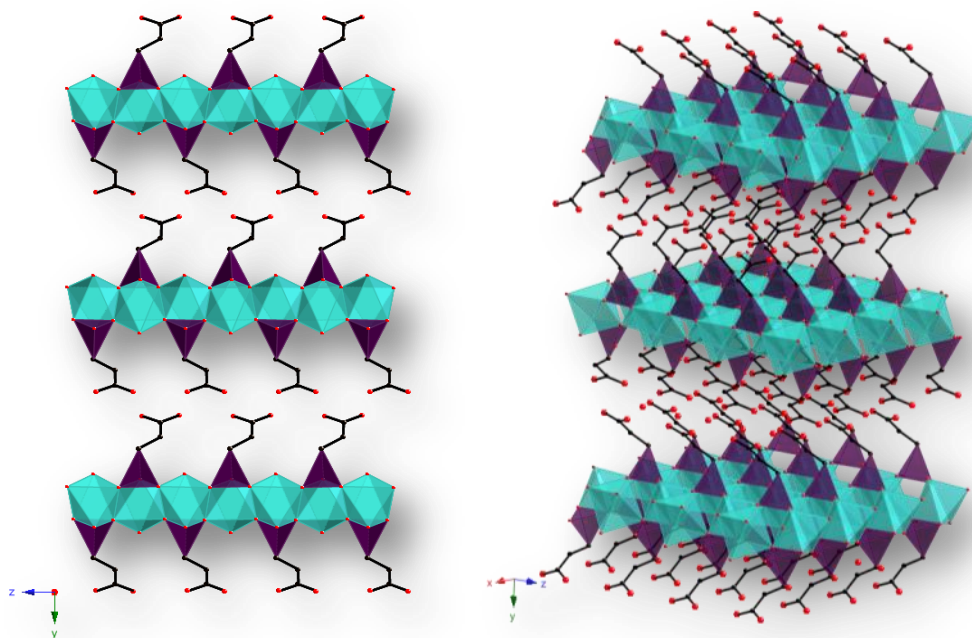


Fig. 3.3 Polyhedral view of the structure of $\text{Zn}(\text{O}_3\text{PCH}_2\text{CH}_2\text{COOH}) \cdot \text{H}_2\text{O}$ showing a layered framework; hydrogen atoms and internal water molecules have been omitted for clarity; colour scheme: ZnO_4 – turquoise tetrahedra, CPO_3 – purple tetrahedra, O – red and C – black.

Table 3.2 Crystallographic data for $\text{Zn}(\text{O}_3\text{PCH}_2\text{CH}_2\text{COOH}) \cdot \text{H}_2\text{O}$.

Crystal System	Orthorhombic
Space Group	$P b n 2_1$
a (Å)	4.8021(6)
b (Å)	24.6753(27)
c (Å)	5.6528(6)
Volume (Å ³)	669.82(13)

3.3.2 Synthesis of $(\text{NH}_4)_2[\text{Zn}_2(\text{O}_3\text{PCH}_2\text{CH}_2\text{COO})_2] \cdot 5\text{H}_2\text{O}$

From the single crystal data of $\text{Zn}(\text{O}_3\text{PCH}_2\text{CH}_2\text{COOH}) \cdot \text{H}_2\text{O}$, the carboxylic acid groups appear to be hydrogen-bonded across the layers and there are no ammonium ions observed between the layers. This may have been because the short reaction time and the low reaction temperature did not give urea sufficient energy to hydrolyze properly. Thus if a phase with the ammonium ions inside that structure is to be synthesized, higher temperature or longer reaction time may be required. Hence in the following attempts, the reaction time was increased, coinciding with raising the reaction temperature, with the hope of obtaining the product BIRM-1 in a reasonable time. After a lot of attempts at temperatures between 85 °C and 170 °C (10 °C per step), 110 °C was found to be the optimum temperature. So following the recipe mentioned in the Table 3.1 (method I), a suitable and reproducible method for the synthesis of the three dimensional BIRM-1, by using a mixture of urea and tetraethylammonium bromide as the reaction medium for a reaction between zinc nitrate and 2-carboxyethylphosphonic acid, was obtained (Figure 3.4 and 3.5).

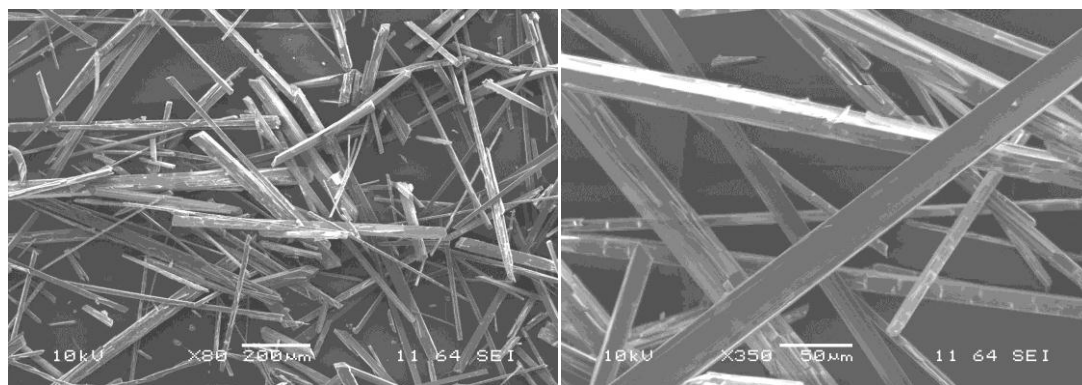


Fig. 3.4 SEM images for BIRM-1 crystals.

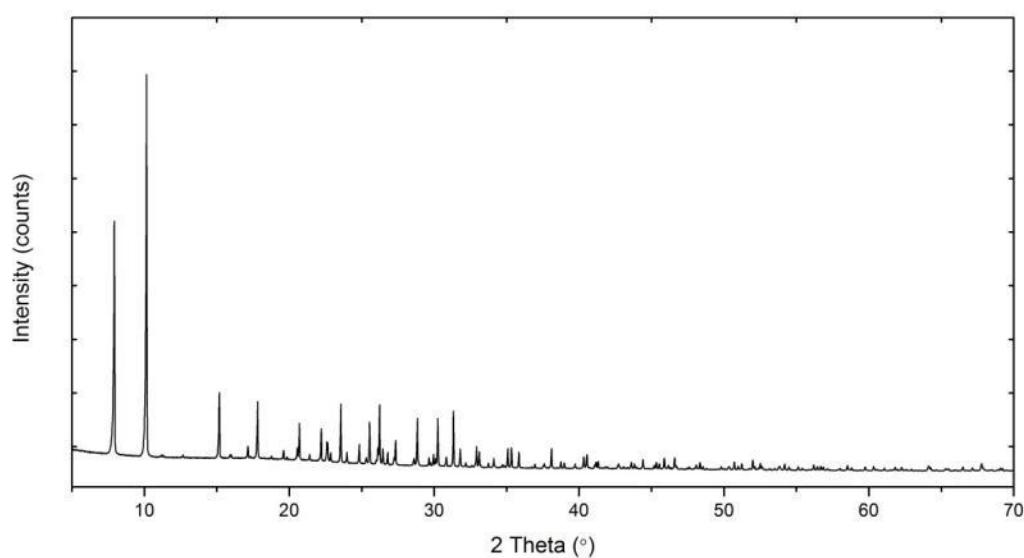


Fig. 3.5 Powder XRD pattern of BIRM-1.

3.3.3 Characterization of BIRM-1

Single crystal X-ray diffraction analysis (Table 3.4 and Appendix 1 for structure details, selected bond lengths and angles) revealed the material to be BIRM-1 with a three dimensional coordination network and one ammonium cation per Zn atom, located in two different sites in the channels with half a cation per site labeled N(10x) and N(20x) (Figure 3.6 and 3.7). Each half cation is then further disordered, N(10x) over two positions and N(20x) over three positions. Each phosphorus atom is tetrahedrally bonded to three oxygen atoms and one carbon atom. The Zn atom is also

tetrahedrally coordinated by four oxygen atoms, one of which is from a carboxylate group of the $(\text{O}_3\text{PC}_2\text{H}_4\text{CO}_2)^{3-}$ ligand and the other three from three different CPO_3 groups. The structure also contains 2.5 molecules of water per Zn atom which are highly disordered over several sites. The occupancies of these water oxygen atoms were generally small and fixed to certain value during the refinement. Due to the disorder it was not possible to refine the ammonium cation or water molecules anisotropically or locate the hydrogen atom positions belonging to these species, however according to their site positions, interactions with framework atoms via H-bonding were suggested¹³¹ (Table 3.3 and Figure 3.6). The whole structure is constructed by the connection of inorganic double chains through the organic ligand $(\text{O}_3\text{PC}_2\text{H}_4\text{CO}_2)^{3-}$ (Figure 3.8). These double chains are built from ZnO_4 and CPO_3 tetrahedral units.

Table 3.3 Selected interatomic distances for ammonium nitrogen atoms and water oxygen atoms.

Bond	Distance (Å)
N101–O5	2.9
N102–O5	2.9
N201–O2	2.8
N202–O4	2.8
N203–O2	2.9
O301–O1	2.8
O302–O1	2.8
O303–O1	2.8
O304–H3A	2.8
O305–O1	2.8
O306–O1	2.8
O401–O5	2.9
O402–O5	2.9
O403–O5	2.7
O501–O5	2.8
O502–O5	2.8
O601–O3	2.9
O602–O3	2.9

Note: atom distances were directly measured by Crystal Maker

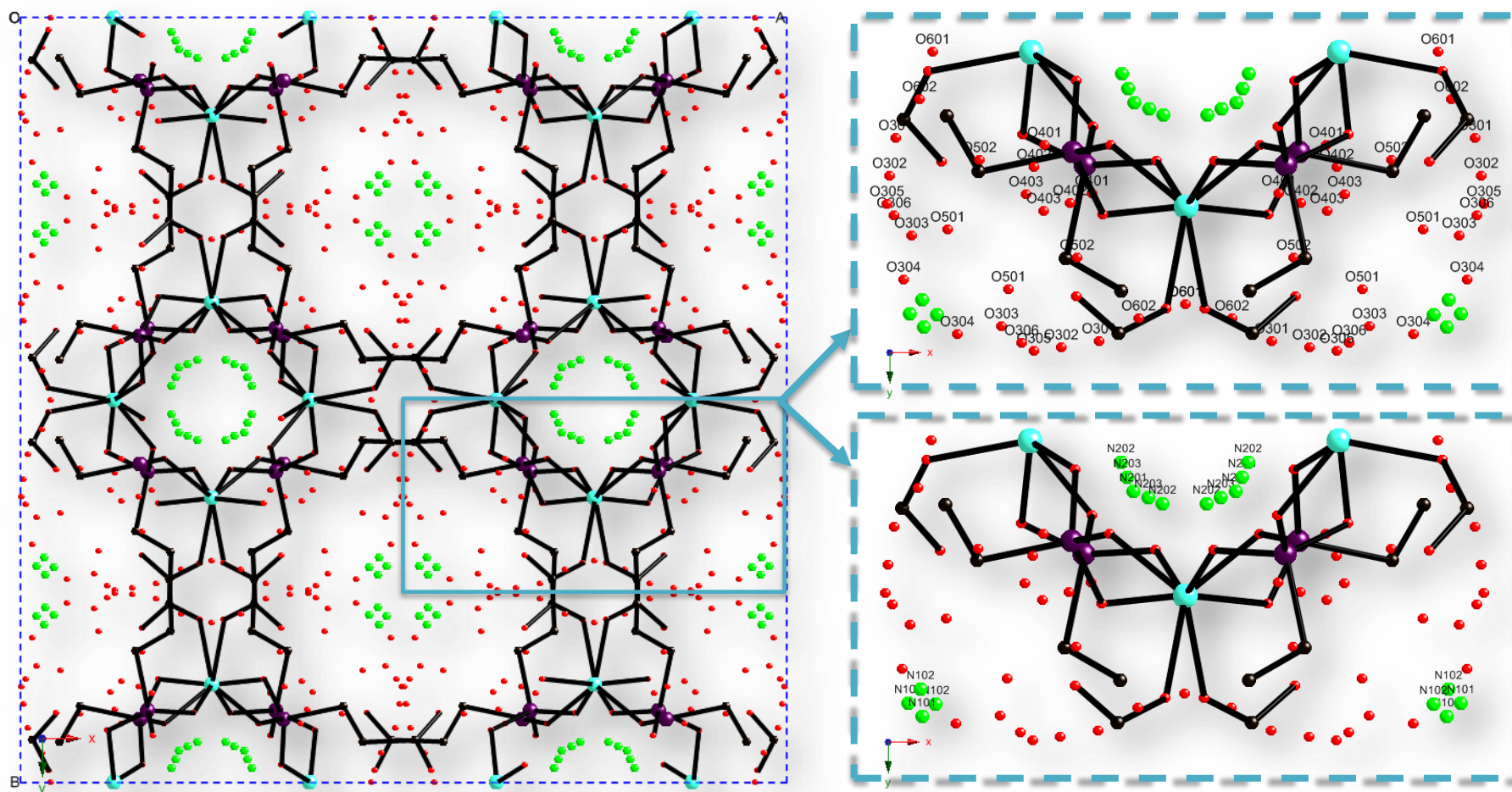


Fig. 3.6 Single crystal structure of BIRM-1 viewed along the z -axis, illustrating the atomic positions of ammonium nitrogen atoms and water oxygen atoms (right). Blue dashed lines indicate one unit cell (left); hydrogen atoms have been omitted for clarity; colour scheme: Zn – turquoise, P – purple, N – green, O – red and C – black.

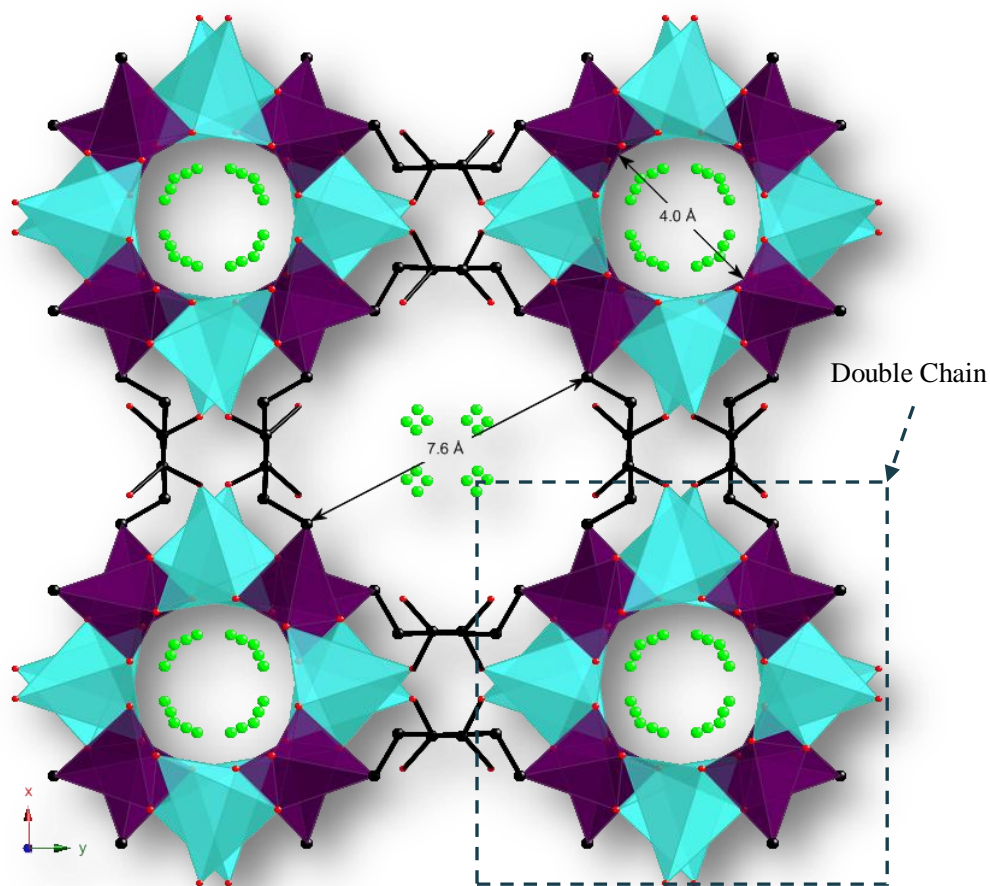


Fig. 3.7 Polyhedral view of the structure of $(\text{NH}_4)_2[\text{Zn}_2(\text{O}_3\text{PCH}_2\text{CH}_2\text{COO})_2] \cdot 5\text{H}_2\text{O}$ showing a three dimensional channel network with pores of ca 7.6 Å diameter projected into the page and smaller sinusoidal channels with diameter of 4.0 Å; channels are filled with NH_4^+ and H_2O molecules; hydrogen atoms and internal water molecules have been omitted for clarity; colour scheme: ZnO_4 – turquoise tetrahedra, CPO_3 – purple tetrahedra, O – red, N – green and C – black.

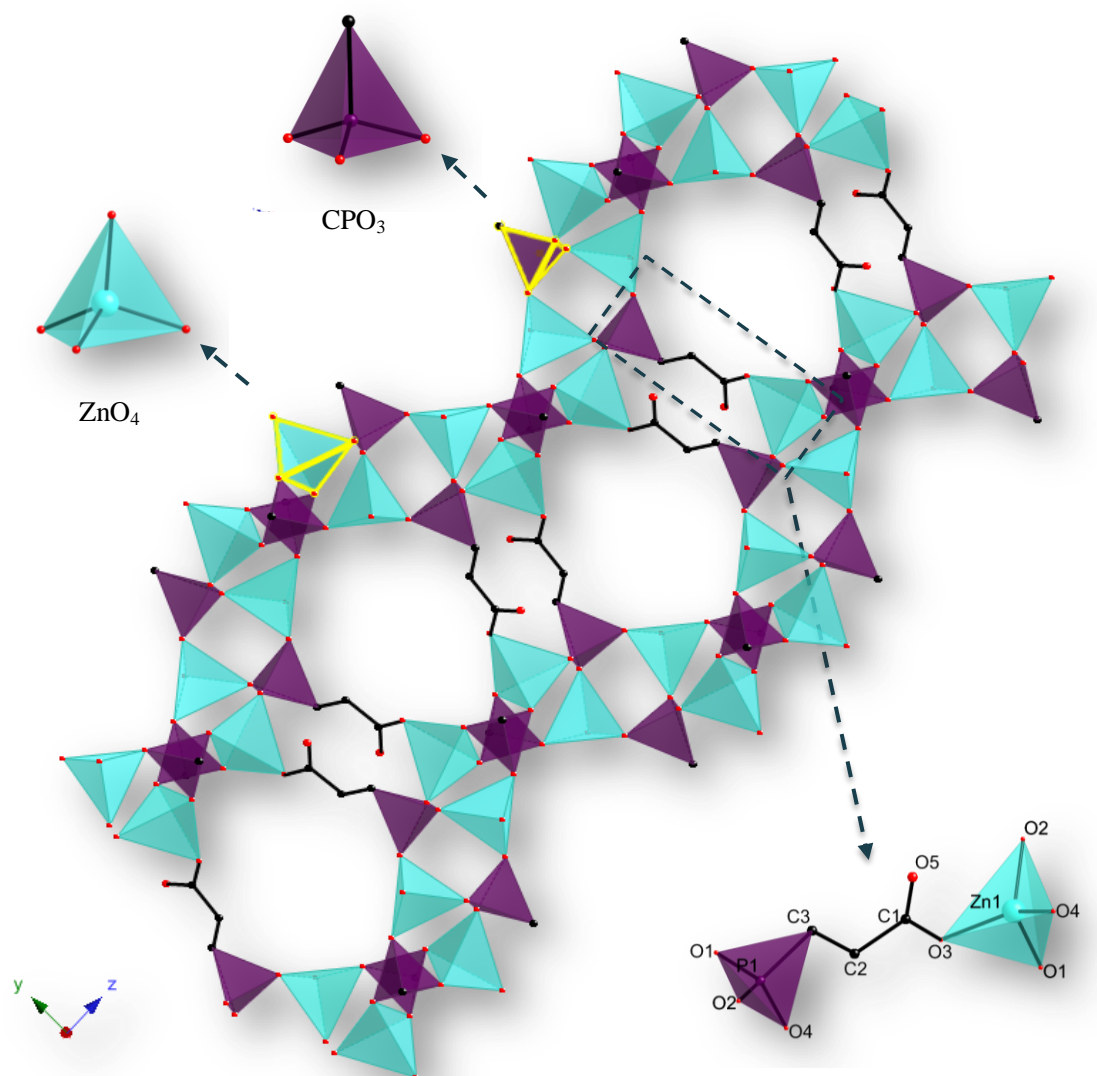


Fig. 3.8 Representation of the connection of two inorganic chains showing the arrangement between ZnO_4 tetrahedra and CPO_3 tetrahedra; hydrogen atoms and internal water molecules have been omitted for clarity; colour scheme: ZnO_4 – turquoise tetrahedra, CPO_3 – purple tetrahedra, O – red and C – black.

Table 3.4 Crystallographic data for BIRM-1.

Empirical formula	(NH ₄) ₂ [Zn ₂ (O ₃ PCH ₂ CH ₂ COO) ₂] 5H ₂ O
Formula weight	558.96
Temperature	120(2) K
Wavelength	0.71073 Å
Crystal system	Tetragonal
Space group	<i>I</i> 4 ₁ / <i>acd</i>
Unit cell dimensions	<i>a</i> = 22.3019(2) Å <i>c</i> = 17.7384(1) Å
Volume	8822.6(11) Å ³
Z	16
Density (calculated)	1.683 mg/m ³
Absorption coefficient	2.385 mm ⁻¹
F(000)	4576
Crystal size	0.30 × 0.06 × 0.05 mm ³
Theta range for data collection	2.93 to 27.51 °
Index ranges	-28 ≤ <i>h</i> ≤ 22, -28 ≤ <i>k</i> ≤ 16, -22 ≤ <i>l</i> ≤ 23
Reflections collected	20693
Independent reflections	2541 [R(int) = 0.0828]
Completeness to theta = 27.51 °	99.7%
Absorption correction	Semi-empirical from equivalents
Max. and min. transmission	0.8900 and 0.5347
Refinement method	Full-matrix least-squares on F ²
Data / restraints / parameters	2541 / 0 / 159
Goodness of fit on F2	1.099
Final R indices [I>2sigma(I)]	R1 = 0.0718, wR2 = 0.1649
R indices (all data)	R1 = 0.1110, wR2 = 0.1889
Largest diff. peak and hole	0.780 and -0.587 e/Å ³

Rietveld refinement of the crystal structure against lab powder X-ray diffraction data confirmed the structure and verified the as-made sample contained only one crystalline phase (Figure 3.9).

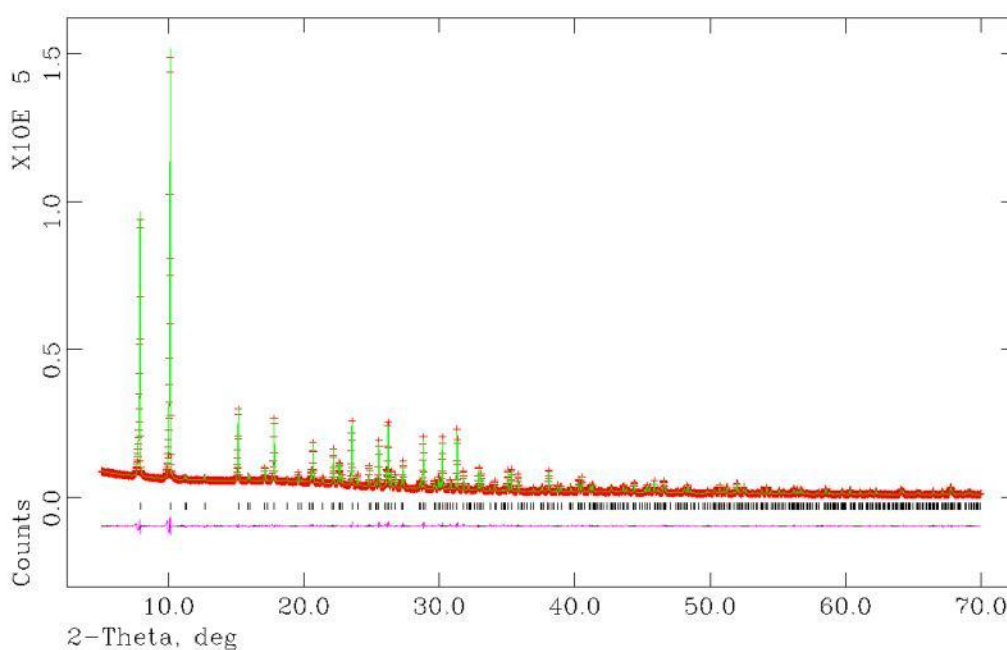


Fig. 3.9 Final observed (crosses), calculated (solid line), difference (below) and reflection positions (middle), for the final Rietveld refinement against powder XRD data for BIRM-1, $\chi^2 = 4.56$, $R_{wp} = 3.42\%$, $R_p = 2.41\%$.

The thermal properties of BIRM-1 were then examined by TGA with mass spectrometry. Before the temperature reached 100°C , a small amount of physisorbed water was left in the system (Figure 3.10), which began to desorb as soon as heating was initiated. In the range 100°C to 150°C , a total weight loss of about 13.5% was observed. As elimination of the entire coordinated water will result in a 16.1% of weight loss, this weight change can be attributed to the partial removal of the coordinated water, accompanied by the release of a small amount of NH_3 (Figure 3.11). Above this temperature, the product showed a nearly continuous mass loss without a clear step. At about 450°C , a small exothermic peak was observed, which may be assigned to the condensation of the hydroxyl groups in phosphonate ligands. The broad exothermic peaks at around 500°C and 520°C in the DTA curve mark the decomposition of the coordination networks and the organic ligand groups with the

loss of NH_3 , H_2O and CO_2 (Figure 3.10). Eventually the residue reacted further with O_2 and released more CO_2 , which generated the second exothermic peak at 740°C . This transformation was complete at about 810°C , resulting in a grey solid after a total weight loss of 45.1%, which was in good agreement with the calculated value of 45.5%.

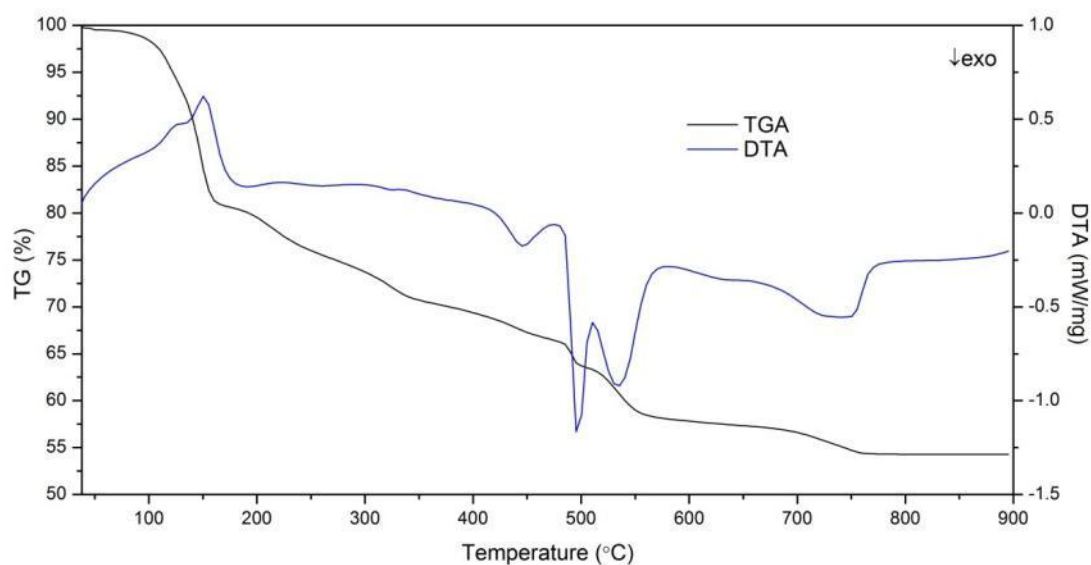


Fig. 3.10 TGA (black trace) and DTA (blue trace) of BIRM-1.

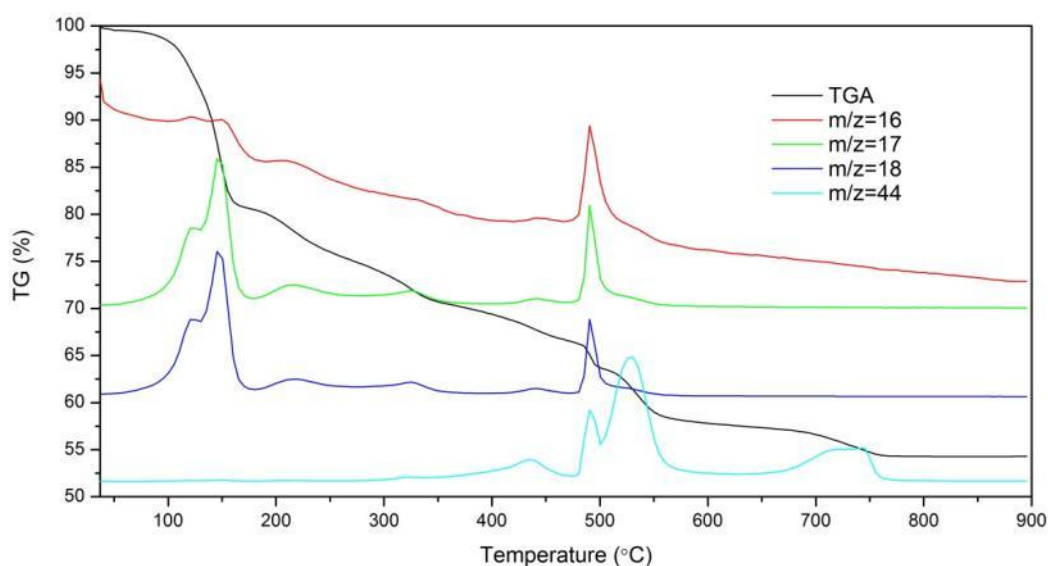


Fig. 3.11 TGA (black trace) of BIRM-1, and mass analysis of $m/z = 16$ (red trace), $m/z = 17$ (green trace), $m/z = 18$ (blue trace) and $m/z = 44$ (cyan trace).

The infrared spectra of similar metal phosphonates have been investigated (Table 3.5) and partially assigned by Hix et al.^{73, 132, 133} and Drumel et al.⁷⁷ The FTIR spectrum for BIRM-1 was recorded to obtain some additional crystallochemical information (Figure 3.12), using these literature assignments. A very broad and overlapped peak was found at around 3400 cm⁻¹ and 3200 cm⁻¹ due to stretching vibrations of O–H from the coordinated water molecules. Peak arose from about 3050 cm⁻¹ was attributed to the N–H stretches from ammonium ion. The symmetric and asymmetric stretching vibrations of carboxyl group are evident as strong bands at 1594 cm⁻¹ and 1401 cm⁻¹ respectively. This frequency is lower than one may expect to observe for such a group due to the carboxylate group is coordinated to zinc atom. P–C stretching mode was seen at 1420 cm⁻¹. The stretching band of the C–O group was observed as a sharp peak at around 1305 cm⁻¹, and the P–O stretching modes were seen as a series of sharp bands in the region 1150–950 cm⁻¹.

Table 3.5 Observed FTIR shifts and assignments for BIRM-1.

Infrared shift (cm ⁻¹)	Assignment
3400, 3200	O–H (H ₂ O)
3050	N–H (NH ₄ ⁺)
1594	COO ⁻ (sym)
1305	C–O
1401	COO ⁻ (asym)
1420	P–C
1150–950	P–O

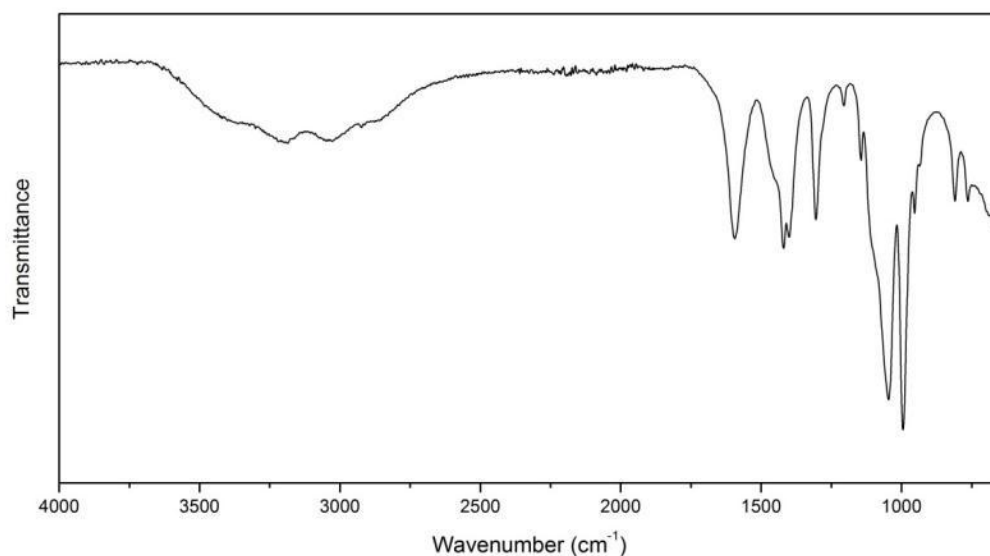


Fig. 3.12 FTIR spectrum for BIRM-1.

3.4 Optimizations of the Synthesis of BIRM-1

As the research continued, larger crystals were needed for further applications, but the crystals yield from the current recipe for this material were usually tiny, and most of them were not even suitable for a single crystal XRD examination. Thus the modifications of the synthesis were carried out based on this consideration in order to improve the morphology and crystal size of the product. At the beginning, lower temperature and longer reaction time was considered to permit the reagents to grow bigger crystals in relatively milder conditions. Although a lot of effort was being spent on different time and temperature combinations, it usually turned out that the product contained some other zinc phosphonate phase and crystal morphology was not actually improved. Thus a different approach was taken using the same amount of TEAB and urea, and the reaction conditions as described in the Table 3.1 (Method I), but varying the metal to ligand (zinc nitrate to CEPA) ratio from 1:0.5 to 1:2.0. The ligand plays a dual role, initially promoting the formation of a cross-linked structure

and subsequently affecting the pH during the reaction. Reactions with a molar ratio close to 1: 1.75 (Table 3.1, method II) were found to yield very long and shiny white crystals. This reaction was much more reproducible in giving a pure phase most of the time, but a tiny amount of other mixed zinc phosphonate phase(s) are found in the powder XRD patterns occasionally. Sometimes an unexpected phase (Figure 3.13) can be obtained as well.

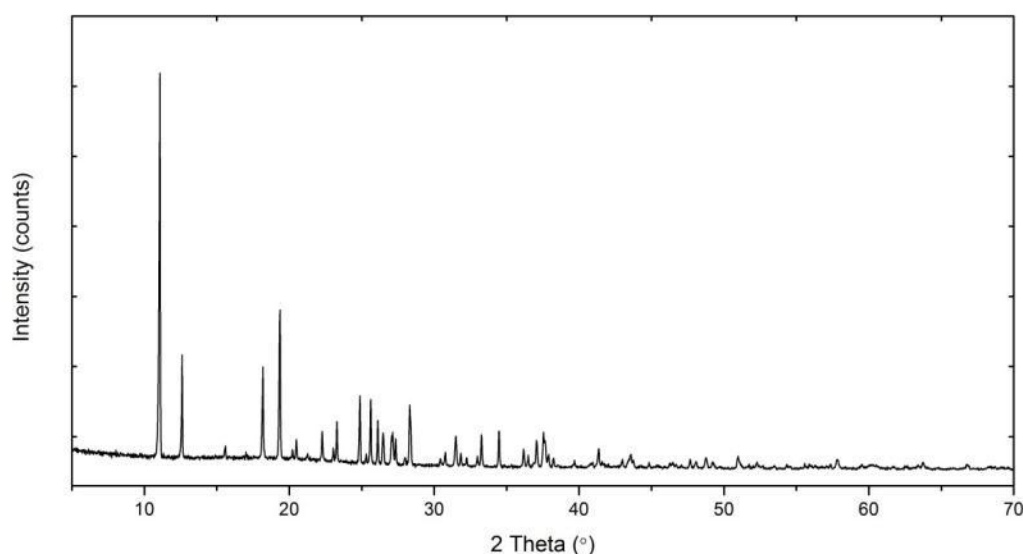


Fig. 3.13 Powder XRD pattern of $(\text{NH}_4)[\text{Zn}(\text{O}_3\text{PCH}_2\text{CH}_2\text{COO})]$.

The structure of this most frequently occurring product had previously been solved by our group with the molecular formula $(\text{NH}_4)[\text{Zn}(\text{O}_3\text{PCH}_2\text{CH}_2\text{COO})]$ (Table 3.6 and Figure 3.14). It turned out this phase is derived from the structure of BIRM-1 with collapsed pores running through the structure, which were filled with ammonium ions. Thus this is not perfect for the synthesis of large BIRM-1 crystals. It probably just stands around the critical point for the synthesis of both BIRM-1 and this phase. Any tiny influence during the reaction such as the homogeneity of the starting mixture or the tightness of the seal in the autoclaves etc. could change the reaction balance to yield the other phase.

Table 3.6 Crystallographic data for (NH₄)[Zn(O₃PCH₂CH₂COO)].

Crystal System	Monoclinic
Space Group	$P 2_1/c$
a (Å)	5.1807(2)
b (Å)	14.0010(7)
c (Å)	9.6965(4)
β (°)	91.13(3)
Volume (Å ³)	703.2(7)

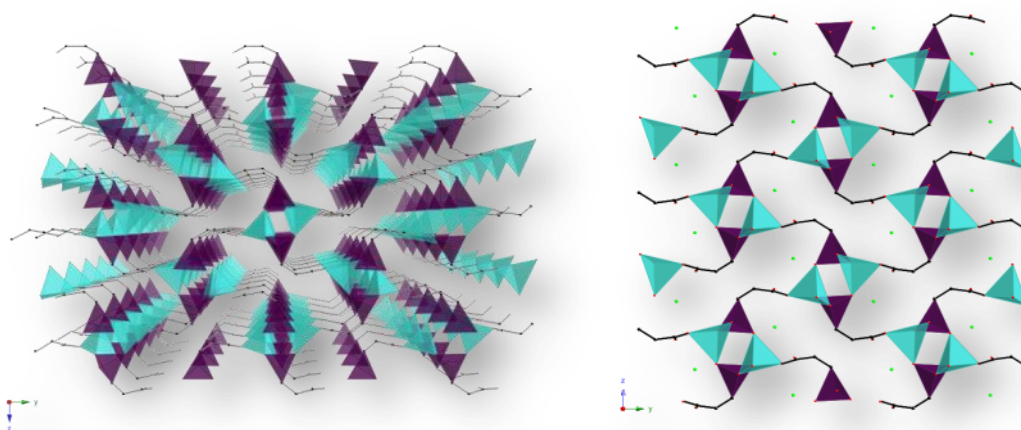


Fig. 3.14 Polyhedral view of the structure of (NH₄)[Zn(O₃PCH₂CH₂COO)] showing a three dimensional network, channels are filled with NH₄⁺ molecules; hydrogen atoms have been omitted for clarity; colour scheme: ZnO₄ – turquoise tetrahedra, CPO₃ – purple tetrahedra, O – red, N – green and C – black.

Based on the above investigation, the reaction conditions were thought to take a step forward to produce BIRM-1 with a larger crystal size. In the following attempts, we opted to study the easier of the variable first to optimize the synthesis method which was aware of the pH consequence the crystallization during the reaction. Hence, the molar ratio between zinc and CEAB was set the same at 1:1.75 and the zinc to urea ratio was modified from 1:1 to 1:15 to see if the hydrolysis of different amount of urea could control the pH and affect the morphology of the structure to achieve the BIRM-1 product. It was found that with a zinc to urea ratio of 1:9 (Table 3.1 method III), large shiny needle-shaped white crystals were produced after heating at 110 °C for

24 hours. The powder XRD patterns were indistinguishable from that of previously synthesized BIRM-1 and gave a good indication of the phase purity, but the morphology and reproducibility were much improved.

3.5 Synthesis of $(\text{NH}_4)[\text{Zn}(\text{O}_3\text{PCH}_2\text{CH}_2\text{COO})]$

If the crystallization inside the autoclave was allowed to progress further to approximately 5 days or longer, another dense isomer phase of the previously mentioned product $(\text{NH}_4)[\text{Zn}(\text{O}_3\text{PCH}_2\text{CH}_2\text{COO})]$ could be obtained (Figure 3.15). The structure of this novel zinc phosphonate was solved from single crystal XRD by Dr. Louise Male. It has a three dimensional framework with ammonium ions located inside the channels; the crystallographic data (Table 3.7) and polyhedral view (Figure 3.16) of the structure are listed below.

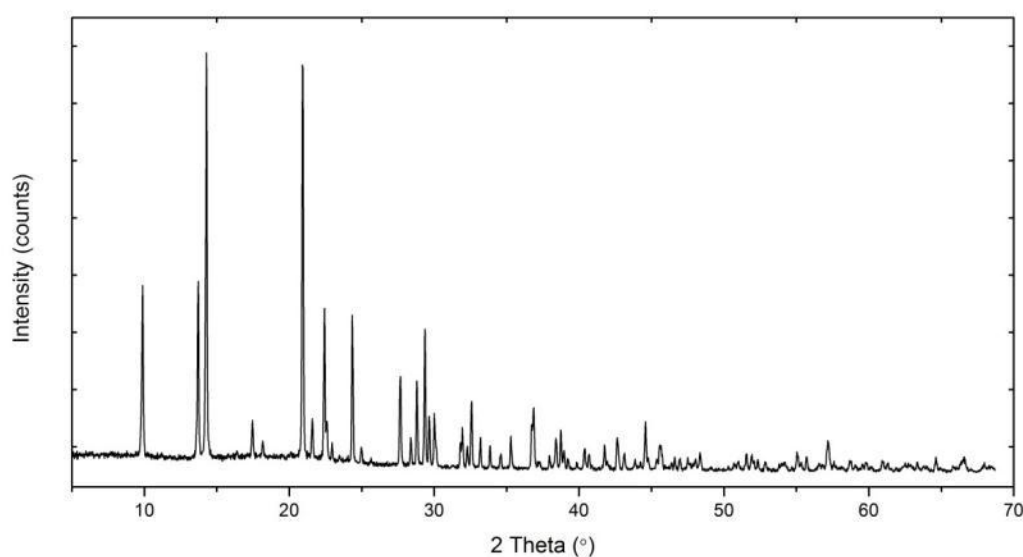


Fig. 3.15 Powder XRD pattern of $(\text{NH}_4)[\text{Zn}(\text{O}_3\text{PCH}_2\text{CH}_2\text{COO})]$.

Table 3.7 Crystallographic data for $(\text{NH}_4)[\text{Zn}(\text{O}_3\text{PCH}_2\text{CH}_2\text{COO})]$.

Crystal System	Monoclinic
Space Group	$P 2_1/c$
a (Å)	8.9458(1)
b (Å)	8.5427(1)
c (Å)	9.7352(1)
β (°)	96.3234(5)
Volume (Å ³)	739.451(14)

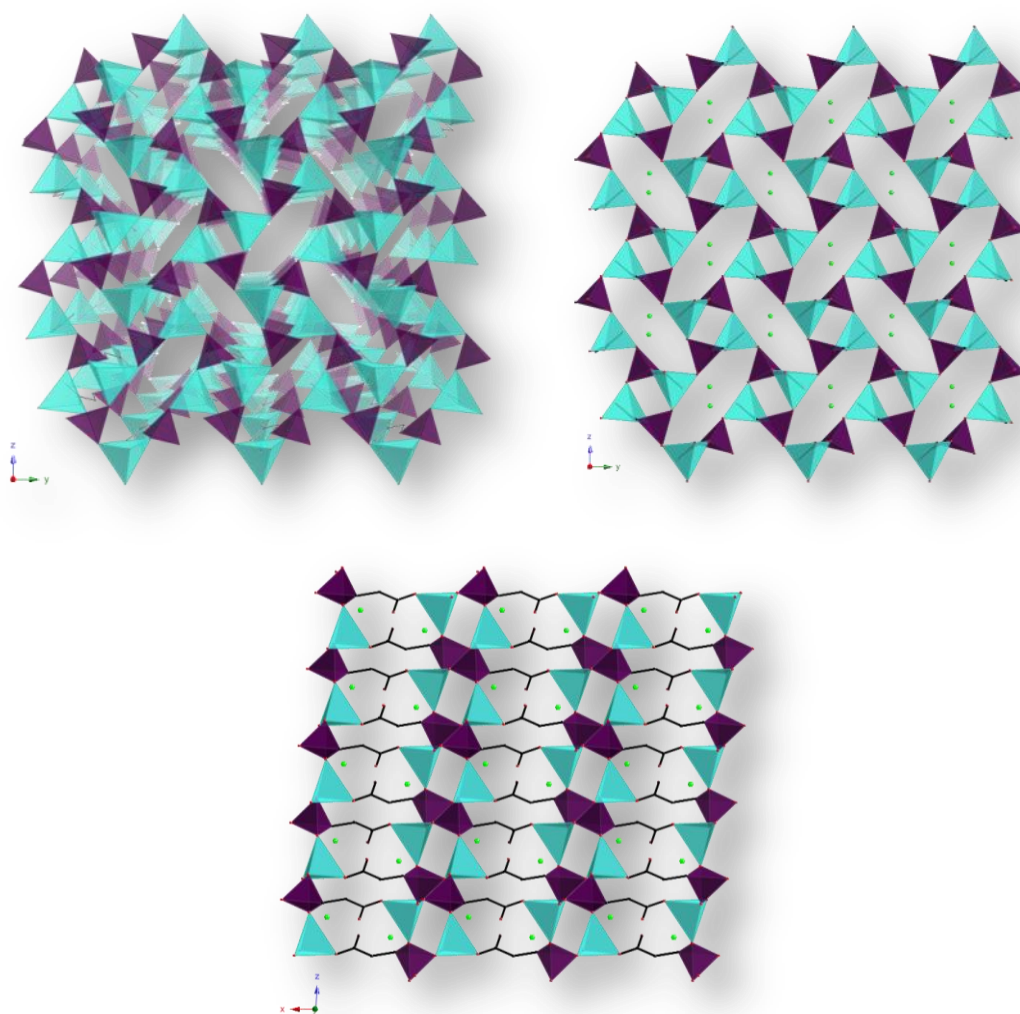


Fig. 3.16 Polyhedral view of the structure of $(\text{NH}_4)[\text{Zn}(\text{O}_3\text{PCH}_2\text{CH}_2\text{COO})]$ showing a three dimensional network, channels are filled with NH_4^+ molecules; hydrogen atoms have been omitted for clarity; colour scheme: ZnO_4 – turquoise tetrahedra, CPO_3 – purple tetrahedra, O – red, N – green and C – black.

3.6 Discussion

Under hydrothermal conditions, four zinc carboxyethylphosphonates with different pore sizes and topologies have been formed from the same reagents but varying the reaction temperature and the amount of one or some reagent(s) during this research. At 85 °C, a layered phase was synthesized, which indicated that the energy is not enough to yield a porous structure with ammonium ions inside. When the temperature was raised to 110 °C, the novel MOF material BIRM-1 with a large three dimensional pore structure was synthesized, however, the crystal size was not good enough for some further analyses such as single crystal XRD, SEM and EDX examinations. By adding more organic ligands to introduce more chance to form a cross-linked structure, BIRM-1 with bigger crystals could be achieved, but the recipe was still not reliable enough. A different phase with a collapsed porous structure appeared sporadically. Then by adjusting the amount of urea, hence affecting the pH accordingly, BIRM-1 with larger crystals were finally synthesized after 24 hours. If the reaction was extended to five days or longer, a very stable and dense phase was the product.

Clearly there is a relatively complicated phase diagram, which describes the necessary condition ranges for the synthesis of a particular phase depending on many possible factors such as reaction temperature, reaction time, pressure inside the autoclave, pH concentration according the reaction time or the starting mixture, the cleanliness and smoothness of the Teflon-lined internal layer and the seal-tightness of the autoclave. This behaviour is akin to zeolite synthesis and illustrates that in the formation of zinc phosphonate, different phases are metastable converting over time or other condition(s) to form a more stable and dense phase. The surviving or predominant phase would be the one which is best suited under current conditions.

The expected sequence in this whole synthesis process, prior to beginning the experiments, was that the layered porous materials would be made first, then the large pore structure with ammonium cations located inside would be synthesized after this, and this would collapse later to produce the smaller pore phase and finally break down to give the most dense phase (Figure 3.17). Probably some other phases or intermediate products also need to be added into this sequence to demonstrate the process in its entirety, but only these four phases were successfully isolated in this research.

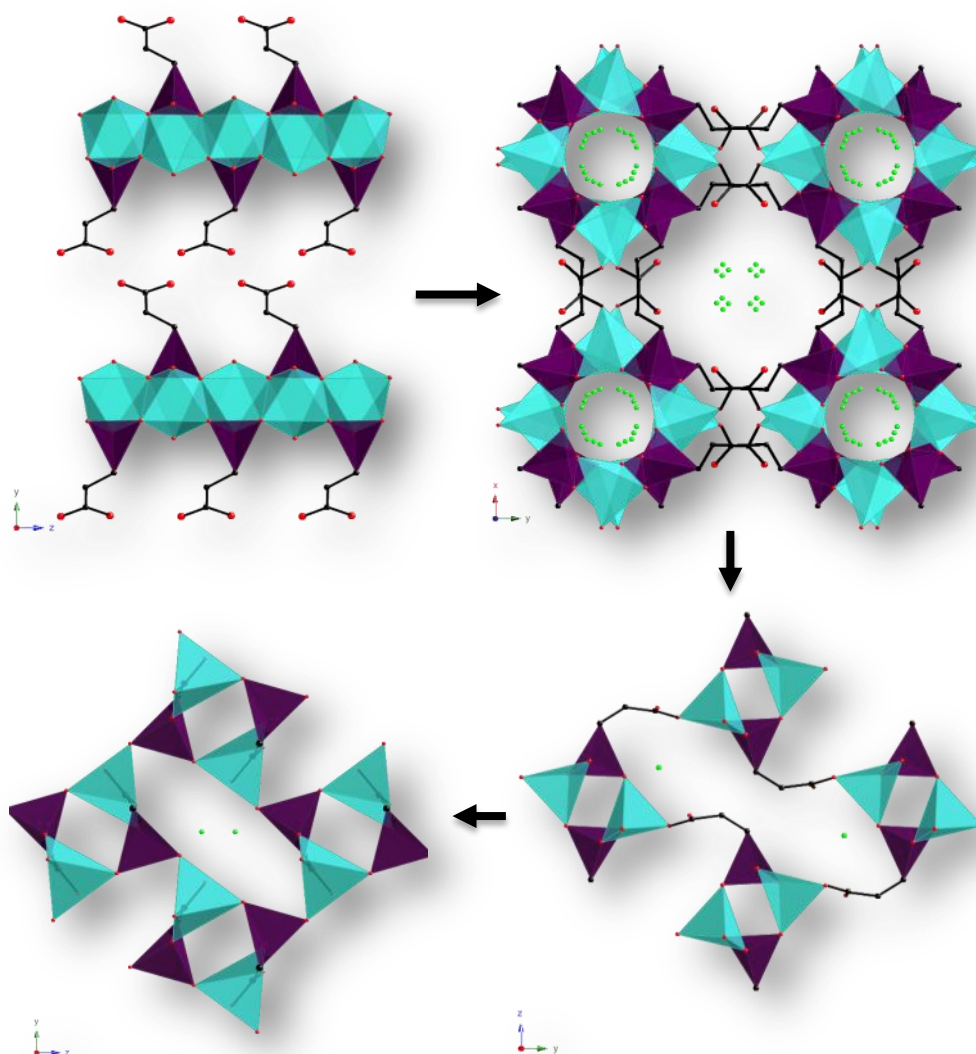


Fig. 3.17 Expected reaction sequence for the zinc carboxyethylphosphonate synthesis;

hydrogen atoms have been omitted for clarity; colour scheme: ZnO_4 – turquoise tetrahedra, CPO_3 – purple tetrahedra, O – red, N – green and C – black.

3.7 Conclusion

By using a mixture of urea (pH controller) and tetraethylammonium bromide (mineralizer) as the reaction medium for a reaction between zinc nitrate and 2-carboxyethylphosphonic acid under hydrothermal conditions, four zinc carboxyethylphosphonates have been synthesized. These phases can all be prepared from the same synthesis mixture by minor adjustments to the temperature or reaction time. Among these four, only BIRM-1 has a large three dimensional porous structure providing potential access to a high internal surface area. In common with many other MOFs and/or metal phosphonates, this material is prepared under hydrothermal conditions, but unlike most others, it has the advantage of containing ammonium cations within the pores, derived from the hydrolysed urea, which are present to balance the charge of the deprotonated carboxylic acid groups, and have the potential to undergo ion exchange. The ability to undergo ion exchange is of interest in its own right, but also enables fine tuning of the properties of the material. In zeolites the hydrogen sorption properties have been successfully improved by varying the exchangeable cations^{84, 134, 135}. So in the following chapters, ion exchange experiments on BIRM-1 with different metal cations will be reported with a view to produce a functional porous MOF material.

Chapter 4

Ion Exchange Studies with Alkali Metal Cations: Lithium (I), Sodium (I) and Potassium (I)

4.1 Introduction

Many applications of existing porous framework materials such as zeolites and metal organic frameworks, including important ones relating to the environment and energy, either depend upon, or are considerably enhanced by, the ability to undergo post-synthetic modification by ion exchange. This crucial property both facilitates the removal and trapping¹³⁶ of harmful (toxic, radioactive) ions, and the fine-tuning of properties such as catalysis¹³⁷, gas adsorption, separation and storage (water, hydrogen, carbon dioxide)^{13, 18, 138-140}, and ionic conductivity^{141, 142}. Unfortunately to date, although several hundred different metal-organic frameworks have been discovered and the properties as well as possible applications have been widely studied¹⁹, the number of MOFs known to undergo ion exchange remains a tiny subset of the total^{1-3, 84}. However for BIRM-1, the structure framework itself is negatively charged and this charge is balanced by the weakly bound ammonium cations inside the channels of BIRM-1. If an ionic solution is brought into contact with BIRM-1, it is possible that the cations from the solution will be diffused into the structure and

interchange with equivalent quantity of ammonium cations. Therefore the electrical neutrality of BIRM-1 structure should be maintained throughout this exchange. In this chapter, ion exchange properties with potassium, lithium and sodium cations were investigated in detail with a view to producing functional porous MOF materials. The powder XRD patterns of the potassium and lithium cation exchanged products were similar to that of BIRM-1 suggesting the structure remained intact and reasonably similar to the parent material, which should help with structural characterization.

4.2 Experimental

4.2.1 Ion Exchange Optimization with Li⁺, Na⁺ and K⁺

Ion exchange experiments on BIRM-1 were attempted by two different approaches in this project. In initial experiments, 1×10^{-3} moles of BIRM-1 powder were mixed with 50 ml of 0.2 M lithium, sodium or potassium acetate solution. After stirring for 30 minutes, the resulting suspension was placed in a round bottom flask and slowly stirred for 24 hours at ambient temperature. The product was then separated by filtration and washed sequentially with deionized water several times to remove excess salt, and dried in air. Subsequently, ion exchange experiments on unground BIRM-1 crystals were carried out by almost the same procedure. After the suspension was stirred for 30 minutes, 0.1 M HCl solution was added dropwise into the solvent to adjust the pH to about 5.5. Then the reaction was sealed by a ground glass stopper and very slowly stirred for 24 hours at ambient temperature and the solvents were washed with deionized water and filtered off to give the exchanged product. When ion exchange experiments were carried out with the bigger crystals obtained from the optimized synthesis method (Table 3.1 Method III in Chapter 3), bigger size

exchanged crystals could be achieved.

Initial ion exchange attempts in this project were unsuccessful. Products were always crushed to small pieces and the structure changed to amorphous after the experiment. Eventually after many attempts at improving and optimizing the ion exchange conditions, the pH value of the mixture was found to play a key role in the ion exchange process. With this knowledge, the following ion exchange attempts were continued with a pH adjustment. Before performing the ion exchange experiment, the pH value of the ion exchange mixture was adjusted to the same value as the final solution in the BIRM-1 synthesis reaction which was approximately 5.5. This resulted in a huge improvement in the ion exchange results. As the project developed, large crystals were desired to facilitate further characterization. The larger BIRM-1 crystals obtained from the optimized synthesis route, which could yield BIRM-1 crystals with bigger and better morphology, were then directly used to carry out ion exchange experiments with different metal ions. Most of the bigger exchanged crystals produced at this stage were used for the SEM/EDX examinations as well as single crystal XRD. Single crystal XRD data were obtained using a Bruker APEXII CCD diffractometer at the window of a Bruker FR591 rotating anode with Mo-K α ($\lambda_{\text{Mo-K}\alpha}$ = 0.71073 Å) radiation at 120 K, and the structures were analyzed by Dr. Louise Male[†].

4.3 Potassium-Exchanged BIRM-1 (K⁺-BIRM-1)

Since the potassium ion has a similar hydrated radius (2.12 Å) to that of ammonium (2.13 Å)¹⁴³, both of which are smaller than both the pore diameters (7.6 Å and 4.0

[†] Dr. Louise Male: X-ray Diffraction Facility Officer of School of Chemistry, University of Birmingham, UK.

Å), the first ion exchange experiments in this project were carried out with potassium ions.

4.3.1 Laboratory Powder XRD

After 24 hours ion exchange, the powder XRD pattern of the exchanged product (Figure 4.1) was similar to the as-synthesized material, but the relative intensities of certain peaks had changed significantly.

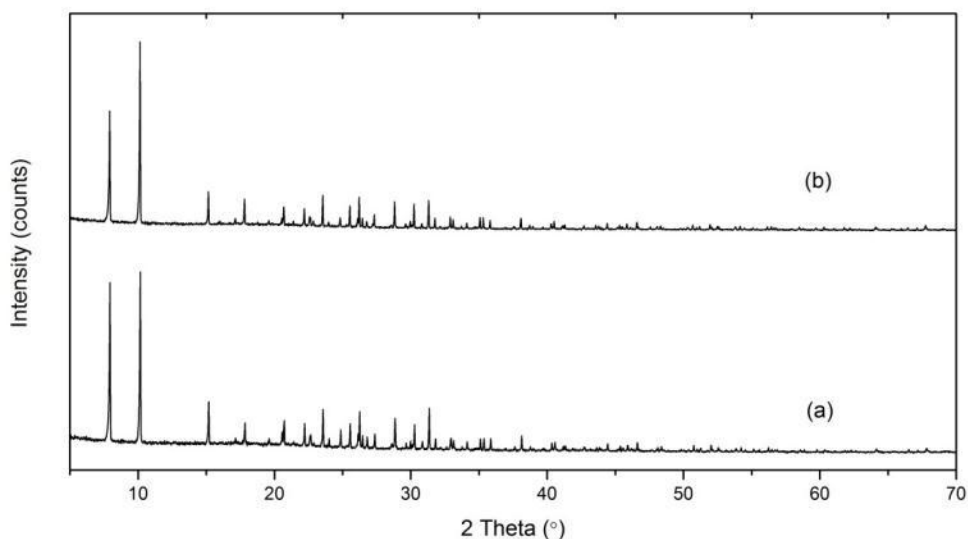


Fig. 4.1 (a) Powder XRD patterns of K⁺-BIRM-1 and (b) BIRM-1.

Powder XRD patterns were initially indexed with the computer program Crysfire¹²⁰. The most probable assignment determined by Chekcell¹²⁴ was for a tetragonal unit cell with $a = 22.201(3)$ Å, $c = 17.8576(1)$ Å, $I4_1/acd$ (see Appendix 2.1 for full index details). Then this unit cell was refined by Le Bail fitting¹²⁵ in GSAS^{126, 127} to give a final cell of $a = 22.1937(2)$ Å, $c = 17.8525(1)$ Å. This tetragonal cell was slightly different from the unit cell of BIRM-1 (Table 4.1). The modification of the relative intensities of some of the peaks in the pattern is a possible pointer to

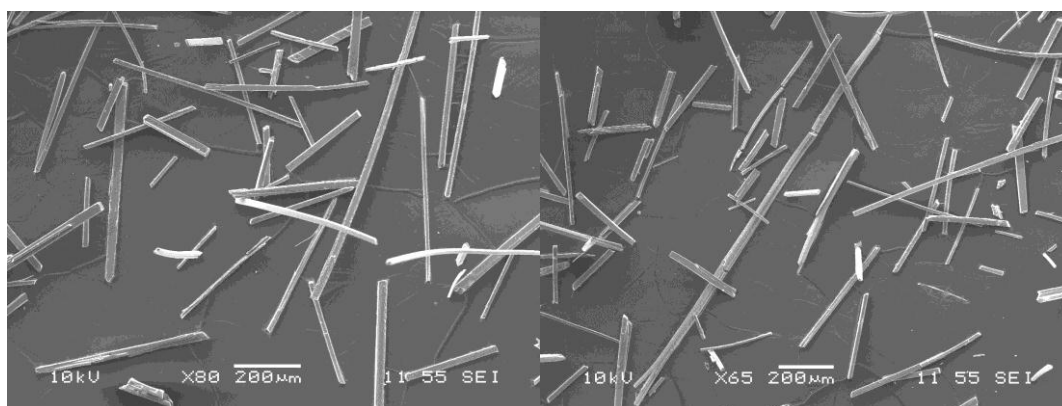
successful ion exchange as this behaviour is often observed in ion exchange of porous inorganic materials such as zeolites^{144,145, 146}.

Table 4.1 Lattice parameters of BIRM-1 and K⁺-BIRM-1.

	BIRM-1	K ⁺ -BIRM-1
Crystal System	Tetragonal	Tetragonal
Space Group	<i>I4₁/acd</i>	<i>I4₁/acd</i>
<i>a</i> /Å	22.302(2)	22.1937(2)
<i>c</i> /Å	17.738(1)	17.8525(1)
Volume/Å ³	8822.6(1)	8793.5(1)

4.3.2 SEM and EDX

The potassium-exchanged products were slightly crushed into smaller pieces after 24 hours ion exchange (Figure 4.2). Morphology and the presence of the potassium ion in K⁺-BIRM-1 were studied with SEM and EDX. As the profiling depth of EDX is about 1 µm in comparison to the unit cell dimensions of the exchanged product of around 20 Å × 20 Å × 18 Å, if the exchanged metal cations are present in the result, this will be convincing evidence to show that metal cations have been exchanged into the structure.



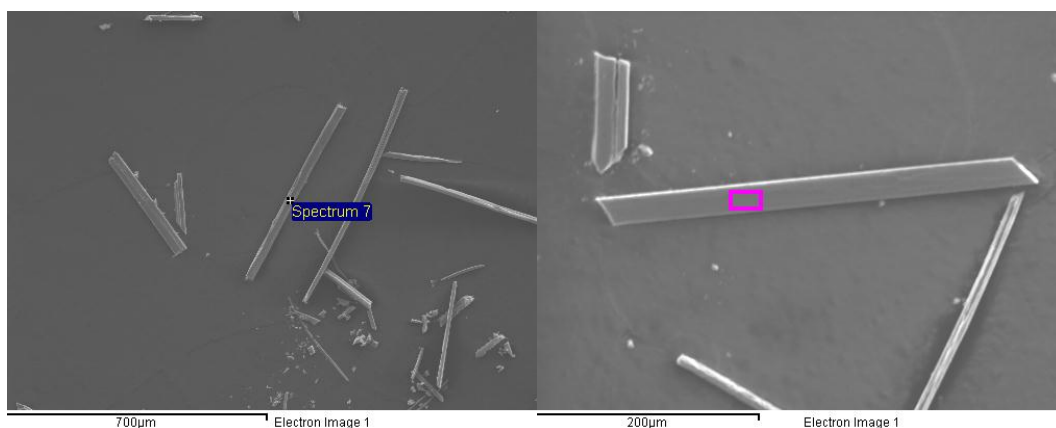


Fig. 4.2 Selected SEM images for K^+ -BIRM-1; spots and areas marked indicate the positions of EDX examinations.

From spot and area analysis (Table 4.2) on the smooth surface of different exchanged crystals, the results revealed that ion exchange was successfully achieved. The average molar ratios of Zn: P: K observed were 1.05: 1: 0.79. The molar ratio of Zn to P is very close to the theoretical value 1: 1, and the average molar ratio of K to Zn/P is about 0.8: 1. The degree of ion exchange is therefore estimated to be roughly 80%.

Table 4.2 Energy dispersive X-ray spectroscopy results for K^+ -BIRM-1 crystals.

	Zn	P	K
Spectrum (Atomic %)	16.65	16.29	13.52
	17.94	17.62	14.16
	18.01	16.97	14.67
	16.86	16.36	14.59
	16.72	17.62	13.74
	20.40	17.88	15.11
	15.79	16.30	13.07
	17.07	16.69	13.72
	15.37	16.27	13.24
	18.22	17.35	14.50
	18.36	16.97	13.69
	17.00	16.71	13.58
	21.03	18.78	14.96
	16.94	17.09	12.32

	21.75	17.92	15.04
	13.99	14.21	8.64
	17.67	15.02	10.60
	18.08	15.19	11.13
	17.88	14.66	11.40
	16.55	15.84	10.58
	17.90	15.05	10.46
	16.45	17.12	13.21
	18.45	16.36	13.18
	16.19	16.68	13.25
	18.48	16.47	13.55
	17.48	17.16	13.87
	16.40	16.47	13.65
	16.19	17.36	14.15
Std. Deviation	1.60	1.42	1.58
Mean	17.49	16.59	13.13
Molar Ratio	1.05	1	0.79

4.3.3 Thermal Stability

Thermal stability of K⁺-BIRM-1 was examined by TGA (Figure 4.3). Clearly the TGA and DTA curves were different from those of BIRM-1 (Figure 3.10, Chapter 3). After losing coordinated water and ammonia at around 130 °C, there followed a plateau till around 350 °C in the TGA trace, which was not seen in the BIRM-1 TGA trace. This structure preservation capability was probably obtained after exchanging potassium ions as they could interact with the framework and hold the structure stable to higher temperature. In principle, this could allow the structure to be dehydrated by heating around this temperature to form a stable dehydrated phase, which would be necessary to facilitate gas storage by creating more space in the porous structure by the removal of internal solvent as well as providing access to the additional open binding sites. The potassium-exchanged product exhibited a weight loss of 38.5% up to 900 °C.

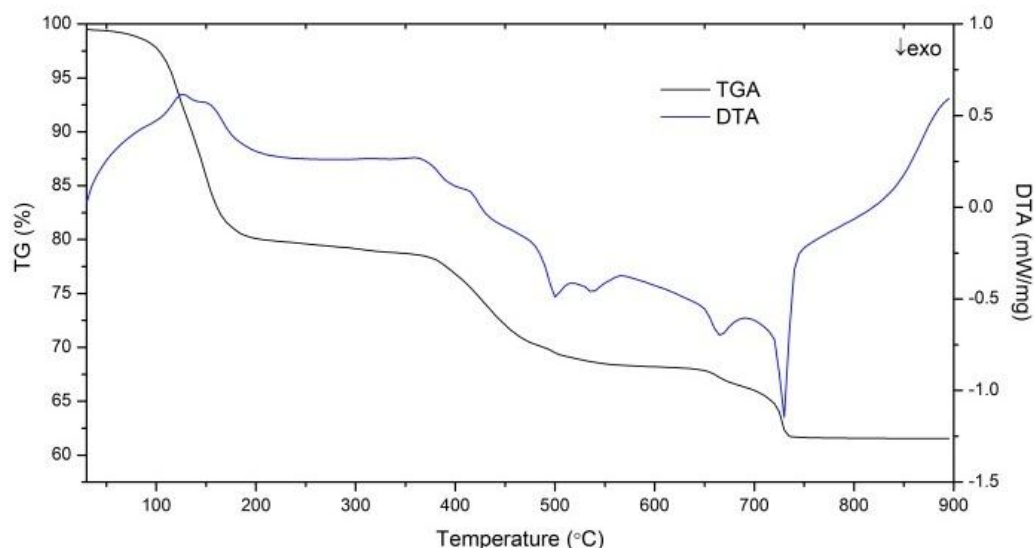


Fig. 4.3 TGA (black trace) and DTA (blue trace) of K^+ -BIRM-1.

An endothermic peak appeared on the DTA curves at 130°C , which on the basis of the mass spectrum curves (Figure 4.4) was assigned to the dehydration of the materials and the release of residual ammonia. Exothermic peaks observed in the TG/DTA curves at 510°C , 540°C , are associated with breakdown of the structure and release of NH_3 , CO_2 , and H_2O . This is consistent with that seen for BIRM-1 but differs in that relatively little gas was released at this temperature. After that there was almost no weight loss until the temperature reached 650°C . Two other exothermic peaks on the DTA curve were observed, which are attributed to the release of CO_2 with a small amount of H_2O and NH_3 .

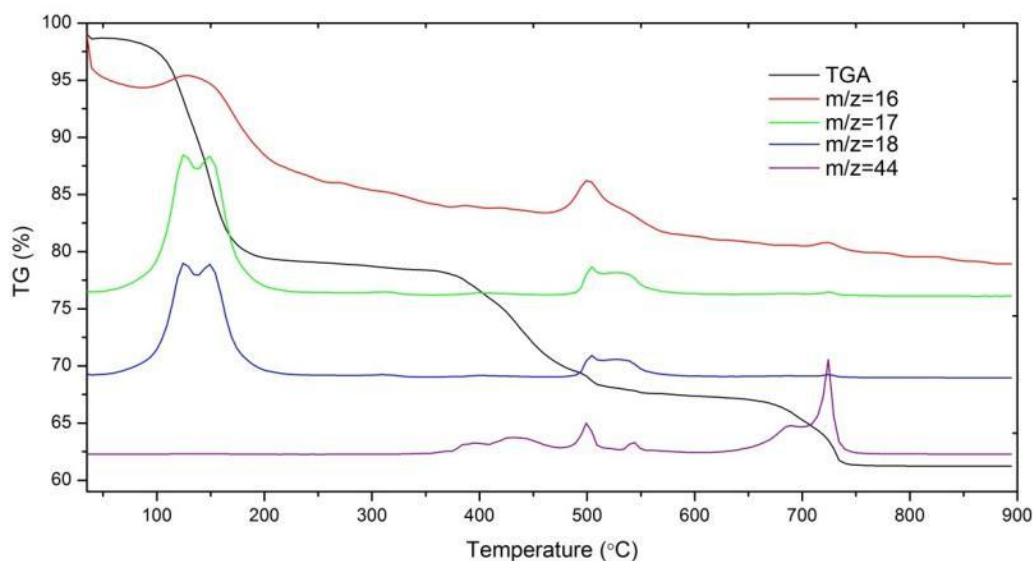


Fig. 4.4 TGA (black trace) of K^+ -BIRM-1, and mass analysis of $m/z = 16$ (red trace), $m/z = 17$ (green trace), $m/z = 18$ (blue trace) and $m/z = 44$ (purple trace).

The product left in the TGA crucible was identified as a mixture of $KZn_4(PO_4)_3$ and $KZnPO_4$ (Figure 4.5). Quantitative phase analysis was carried out through Rietveld refinement of the structures in GSAS^{126, 127} (Table 4.3) and suggested that molar ratio of Zn: P: K was 1:0.85:0.55, a significantly lower potassium content than the results obtained from the EDX examinations. This discrepancy could be explained by the formation of an amorphous or poorly crystalline potassium compound during the heating process that does not contribute to diffraction peaks, and so is not determined by the Rietveld quantification formula. The bump observed at lower two-theta angles in the power XRD pattern of the TGA products is consistent with this interpretation.

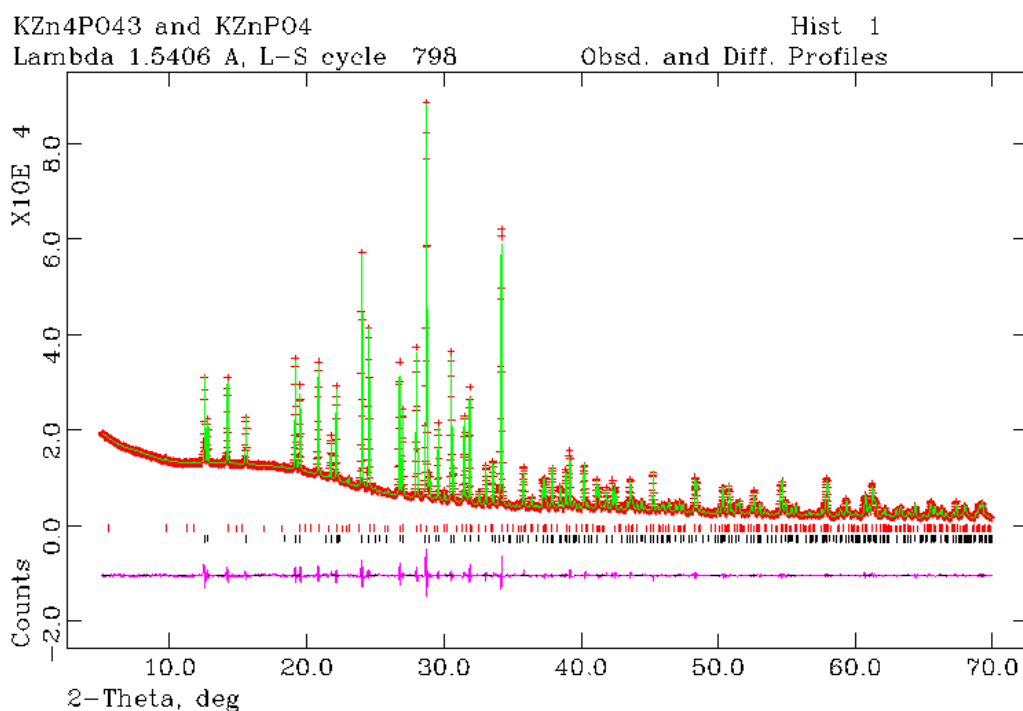


Fig. 4.5 Final observed (crosses), calculated (solid line), difference (below) and reflection positions [red top lines indicate peaks from KZnPO_4 and black lower lines indicate peaks from $\text{KZn}_4(\text{PO}_4)_3$] for the final Rietveld refinements against powder XRD data for potassium-exchanged BIRM-1 TGA products, $\chi^2 = 8.072$, $R_{\text{wp}} = 3.29\%$, $R_p = 2.17\%$.

Table 4.3 Quantitative phase analysis results.

Phase	Weight percentage (%)
$\text{KZn}_4(\text{PO}_4)_3$	51.81(6)
KZnPO_4	48.19(6)

4.3.4 Fourier Transform Infrared Spectroscopy

One of the characteristic bands in the IR spectrum for BIRM-1 was the doublet at 3200 cm^{-1} and 3050 cm^{-1} due to stretching vibrations of O–H from the coordinated water molecular and N–H stretches from ammonium (Figure 4.6a). However, the broad band occurring at around 3050 cm^{-1} almost disappeared after ion exchange, which could be related to the decrease of N–H vibrations engendered by the removal of the exchangeable ammonium cations by ion exchange (Figure 4.6b). For the rest of

the IR data, the two spectra shown are qualitatively similar. The band representations are shown in Table 4.4. The IR data once again indicate that the structure was maintained after ion exchange and potassium cations were introduced into the porous structure by exchanging with ammonium cations.

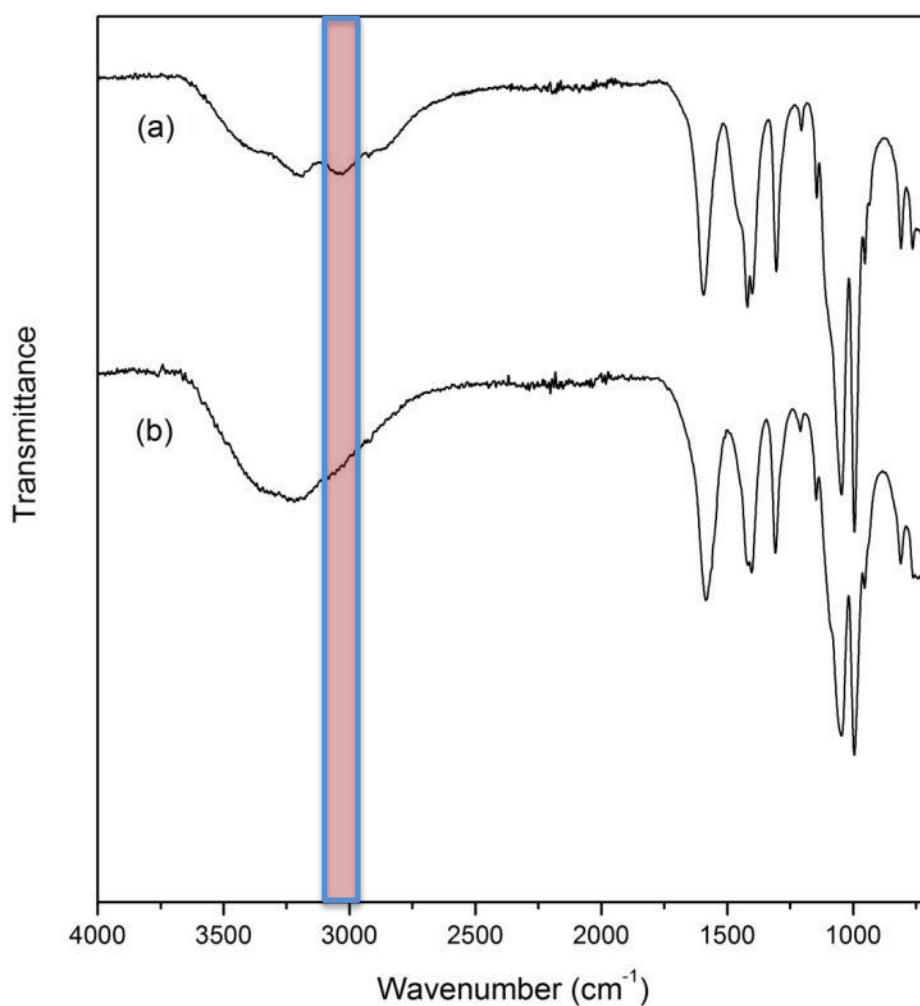


Fig. 4.6 FTIR spectra for (a) BIRM-1 and (b) K⁺-BIRM-1; the pink area illustrates the peak disappearing after the ion exchange

Table 4.4 Observed FTIR shifts and assignment for K⁺-BIRM-1.

Peak (cm ⁻¹)	Assignment
3200	O–H (H ₂ O)
1585	COO ⁻ (sym)
1309	C–O
1403	COO ⁻ (asym)
1418	P–C
1150–950	P–O

4.4 Lithium-Exchanged BIRM-1(Li⁺-BIRM-1)

Following the success of the potassium ion exchange, attempts were made at lithium ion exchange, as this metal ion could provide good metal binding sites for gas adsorption^{3, 87, 147}. Again the hydrated radius (1.72 Å)¹⁴³ is smaller than the pore diameter (7.6 Å).

4.4.1 Laboratory Powder XRD

After ion exchange, the powder XRD pattern (Figure 4.7) and SEM images (Figure 4.8) showed that the structure and morphology remained intact during the treatment. The XRD pattern of the lithium-exchanged product showed clear changes compared to the original pattern. The relative intensities were noticeably modified after ion exchange as was observed in the XRD pattern of the potassium-exchanged product. Again, some new peaks were present after ion exchange and some peaks had disappeared or appeared slightly split. The similarity observed in the unit cell parameters and, in particular, the modifications of the relative intensities of the some peaks in the XRD pattern were possible pointers to successful ion exchange.

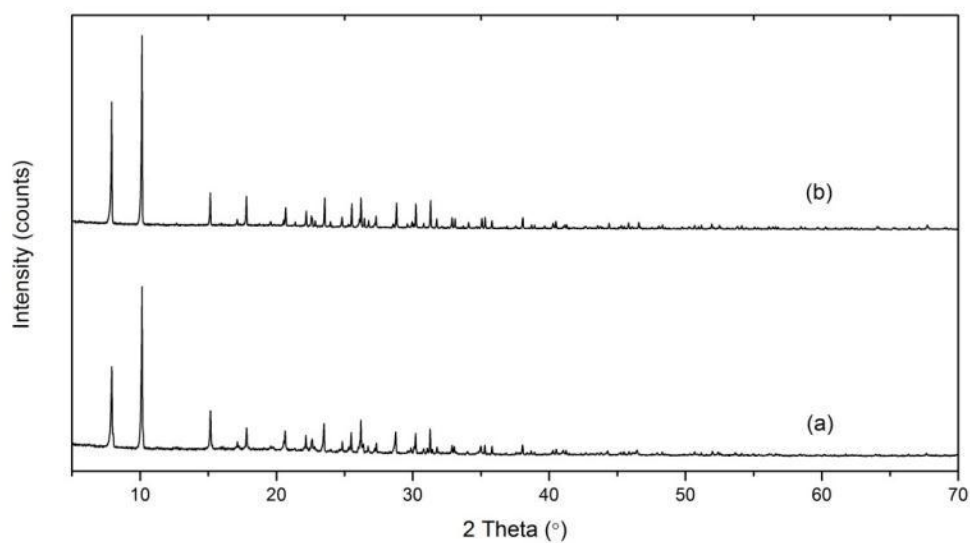


Fig. 4.7 (a) Powder XRD patterns of Li^+ -BIRM-1 and (b) BIRM-1, illustrating the modification of the relative peak intensities.

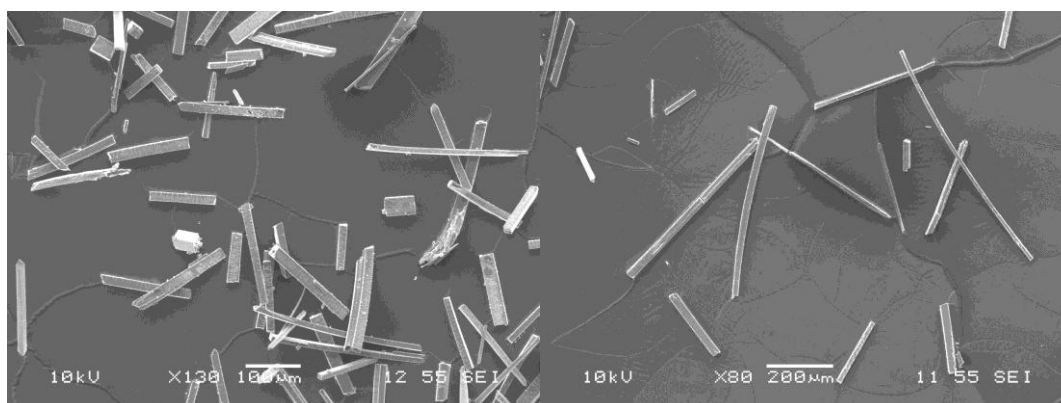


Fig. 4.8 SEM images for Li^+ -BIRM-1.

Diffraction data were initially indexed with Crysfire¹²⁰. Then Chekcell¹²⁴ was employed to determine the best solution with $a = b = 22.228(7) \text{ \AA}$, $c = 17.9179(4) \text{ \AA}$, $I4_1/acd$. A Le Bail refinement¹²⁵ was carried out in GSAS^{126, 127} using the same space group to give a final unit cell as $a = b = 22.2099(4) \text{ \AA}$, $c = 17.9155(3) \text{ \AA}$. The lattice parameters of this product again were very similar to those of BIRM-1 (Table 4.5), suggesting that the framework was preserved during the ion exchange process.(see Appendix 2.2 for full index details)

Table 4.5 Lattice parameters of BIRM-1 and Li⁺-BIRM-1.

	BIRM-1	Li ⁺ -BIRM-1
Crystal System	Tetragonal	Tetragonal
Space Group	<i>I4₁/acd</i>	<i>I4₁/acd</i>
<i>a</i> /Å	22.302(2)	22.2099(4)
<i>c</i> /Å	17.738(1)	17.9155(3)
Volume/Å ³	8822.6(1)	8837.3(4)

4.4.2 Flame Photometry

As there are only two electrons contained in the lithium ion, this extremely low electron density makes using EDX to determine the content of lithium in the exchanged product unreliable. Thus flame photometry was employed to estimate the degree of ion exchange (Table 4.6). This confirmed that the phase had effectively undergone lithium ion exchange. The exchange rate was calculated according to the standard curve (Figure 4.9); the average lithium exchange rate was about 55%. (See Appendix 3.1 for calculation details)

Table 4.6 Flame photometry data.

	Concentration	1 st Reading	2 nd Reading	3 rd Reading	Average
Standard Li ⁺ solution	1 ppm	10	10	10	10
	2 ppm	20.5	21.5	21.5	21.17
	5 ppm	51	51.5	51.5	51.33
	8 ppm	81	81.5	80.5	81
	10 ppm	100	100	100	100
Li ⁺ exchanged product	Sample 1	70	70	71	70.33
	Sample 2	71.5	71	72	71.5
	Sample 3	70	70.5	70	70.17

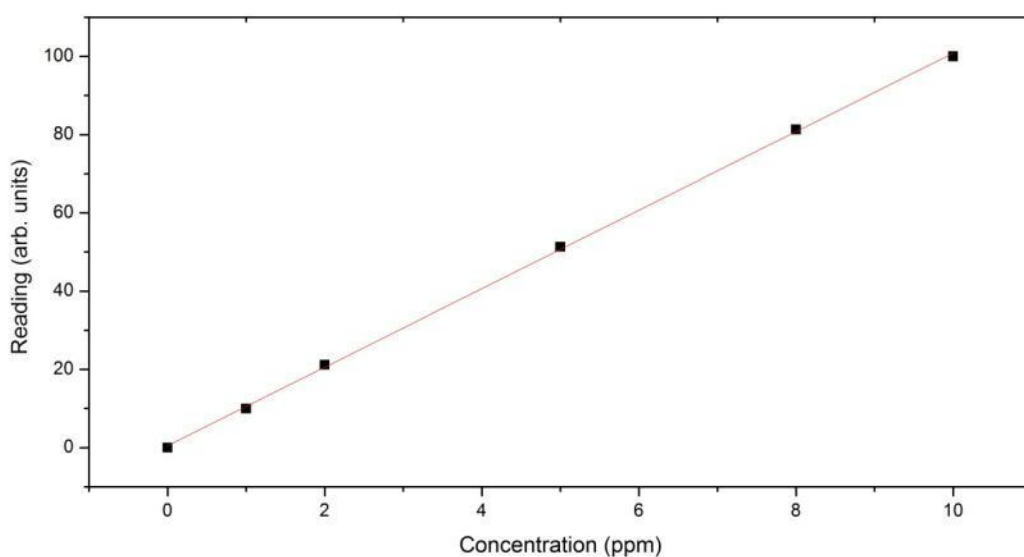


Fig. 4.9 Standard curve for Li^+ -BIRM-1 flame photometry examination; $y = 10.0373x + 0.4767$, $R^2 = 0.9996$.

4.4.3 Thermal Stability

As apparent from the weight loss curve (Figure 4.10), the lithium-exchanged product revealed a weight loss of 42.8% up to 900 °C. Looking at the DTA trace, the endothermic peak at 120 °C is attributable to loss of water and ammonia from residual NH_4^+ ions (Figure 4.11). Above this temperature the material kept on losing weight gradually and did not show very clear weight loss steps. At about 500 °C, an exothermic peak was observed which indicates collapse of the structure. Release of NH_3 , H_2O and CO_2 were detected by mass spectrometry. This exothermic peak in the DTA curve was quite broad as a result of the CO_2 release step. Eventually the residue reacted further with O_2 and released more CO_2 , which generated the second exothermic peak at 630 °C. The final phase change took place at a slightly higher temperature accompanied by an exothermic peak found after 800 °C. There was no weight loss or gas emission detected in this step. After heating, the material left in the

crucible was found melted on the internal surface of the crucible (Figure 4.12). It was impossible to remove without damaging the crucible, therefore it could not be examined by XRD to identify the composition. This unusual TGA behaviour could be taken as evidence of a successful ion exchange, as it was not observed in either the BIRM-1 or K^+ -BIRM-1 TGA result.

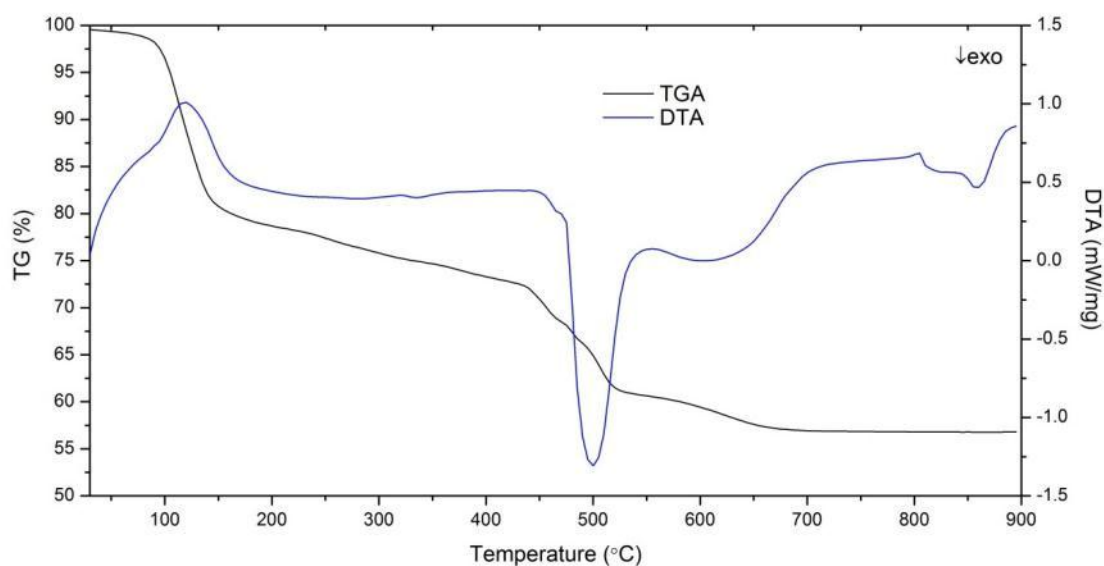


Fig. 4.10 TGA (black trace) and DTA (blue trace) of Li^+ -BIRM-1.

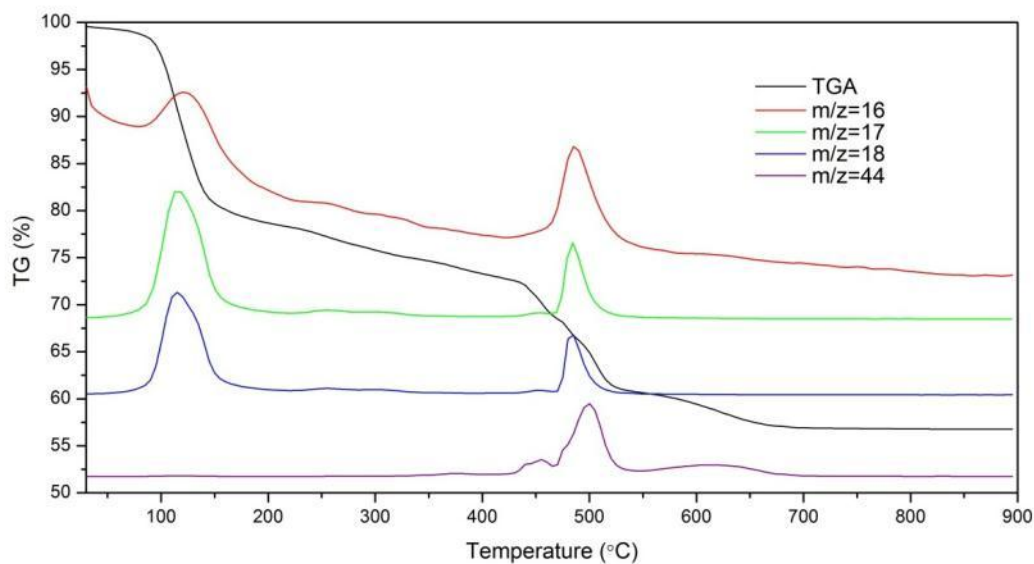


Fig. 4.11 TGA (black trace) of Li^+ -BIRM-1, and mass analysis of $m/z = 16$ (red trace), $m/z = 17$ (green trace), $m/z = 18$ (blue trace) and $m/z = 44$ (purple trace).



Fig. 4.12 Image of TGA crucibles after heating the Li^+ -BIRM-1 to $900\text{ }^{\circ}\text{C}$, illustrating the solid residue thin layer melted on the internal layer of the crucibles.

4.4.4 Fourier Transform Infrared Spectroscopy

FTIR spectra for both BIRM-1 and Li^+ -BIRM-1 were recorded to obtain some additional crystallochemical information for both materials. The IR spectrum of BIRM-1 (Figure 4.13a) exhibited a very broad and overlapped peak at around 3200 cm^{-1} and 3050 cm^{-1} due to stretching vibrations of O–H from the coordinated water molecules and N–H stretches from ammonium. A similar spectrum was observed from the lithium-exchanged product (Figure 4.13b and Table 4.7), the broad band occurring at around 3050 cm^{-1} almost disappeared after ion exchange, which is attributed to the decrease of N–H vibrations generated by the removal of the exchangeable ammonium cations. The IR data reinforce the evidence from above that the structure was maintained after ion exchange and lithium cations were introduced into the porous structure by exchanging with ammonium cations.

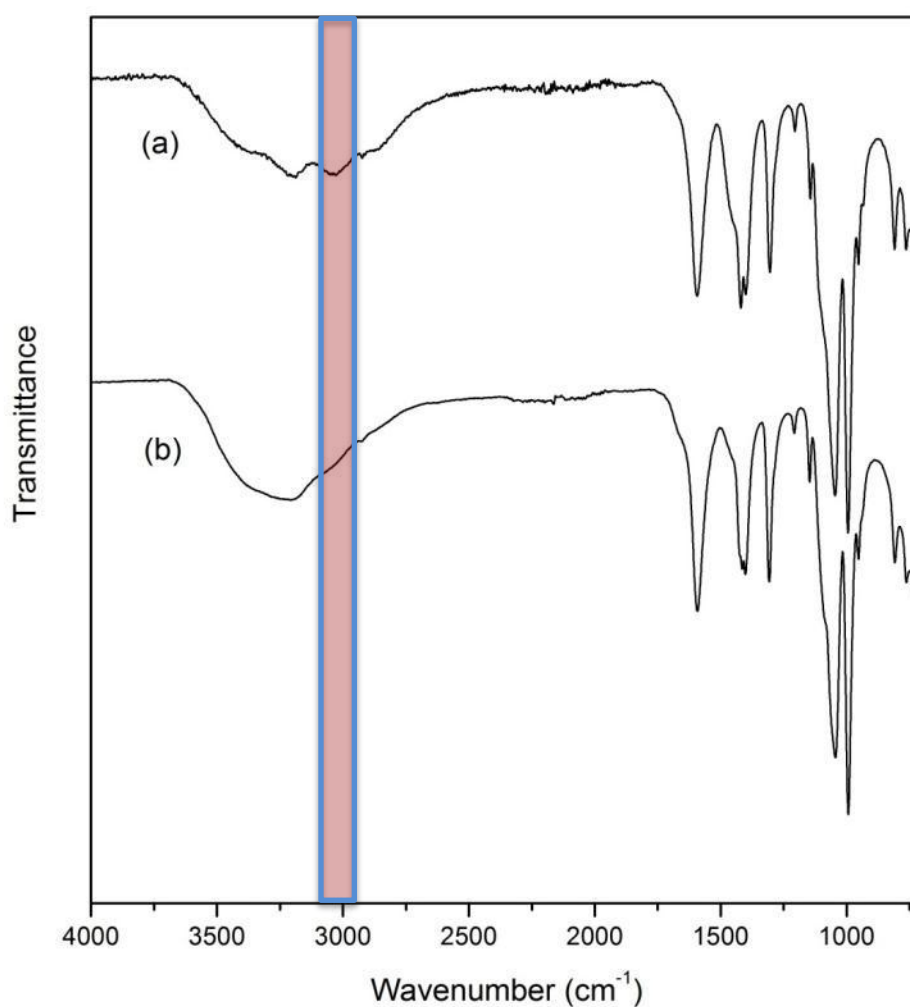


Fig. 4.13 FTIR spectra for (a) BIRM-1 and (b) Li⁺-BIRM-1; the pink area illustrates the peak disappearing after the ion exchange.

Table 4.7 Observed FTIR peaks and assignments for Li⁺-BIRM-1.

Peak (cm ⁻¹)	Assignment
3200	O-H (H ₂ O)
1693	COO ⁻ (sym)
1308	C-O
1402	COO ⁻ (asym)
1415	P-C
1150-950	P-O

4.5 Sodium-Exchanged BIRM-1 (Na⁺-BIRM-1)

As another alkali metal between lithium and potassium, the hydrated radius of sodium ion is 2.18 Å¹⁴³ and thus smaller than pore diameter. Sodium exchange was selected as the last set of experiments to be carried out.

4.5.1 Laboratory Powder XRD

Powder XRD patterns (Figure 4.14) of the sodium ion-exchanged products showed clear changes compared to the BIRM-1 and K⁺/Li⁺-BIRM-1 XRD patterns. However, although the morphology of these exchanged crystals was maintained, some of them were crashed into small pieces after ion exchange (Figure 4.15). From the XRD pattern, there were peaks broadly in the same place and also extra peaks appeared which could indicate that the exchanged product contained both the original unchanged BIRM-1 material as well as some of a newly formed sodium phase which has slightly different lattice parameters. Alternatively, an exchanged sample may have been formed, in which a small structure change occurred resulting in a lowering of symmetry that led to the splitting of peaks in the XRD patterns.

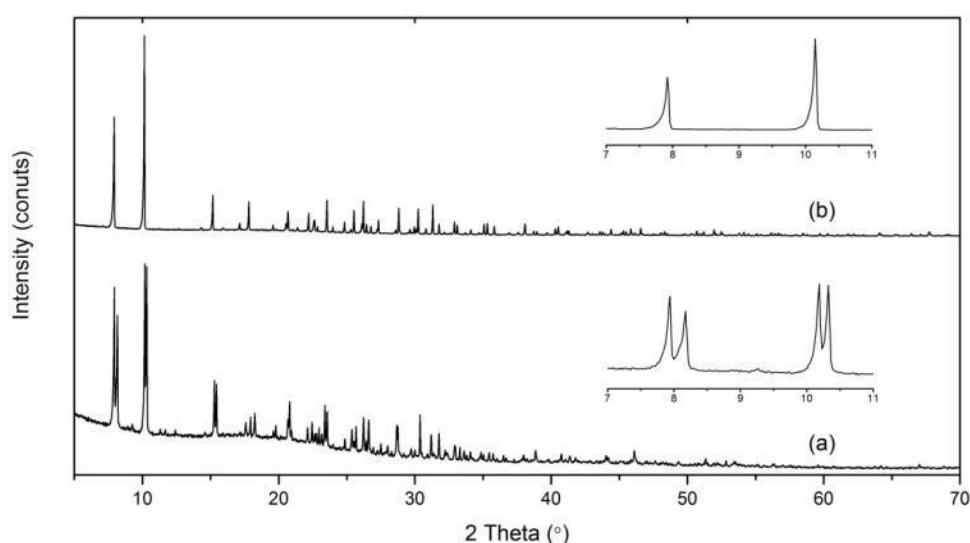


Fig. 4.14 (a) Powder XRD patterns of Na⁺-BIRM-1 and (b) BIRM-1 illustrating the

appearance of peak splits and additional peaks after ion exchange.

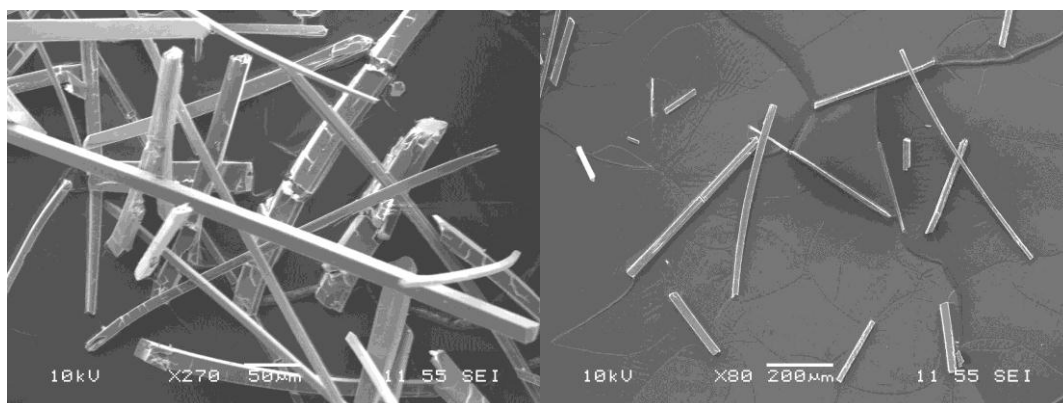


Fig. 4.15 SEM images for Na⁺-BIRM-1.

All the peaks from the exchanged pattern were indexed (Table 4.8) using Crysfire¹²⁰ and Chekcell¹²⁴, and refined by Le Bail fitting¹²⁵ in the programme GSAS^{126, 127}. The crystal system was revealed to be changed from tetragonal to orthorhombic but the lattice parameters remained very similar. This crystallographic data indicated that structure was not significantly modified to a totally different phase, and with the lowering of the symmetry together, it bears out the conjecture mentioned above and explains the peak splitting (see Appendix 2.3 for index details).

Table 4.8 Lattice parameters of BIRM-1 and Na⁺-BIRM-1.

	BIRM-1	Na ⁺ -BIRM-1
Crystal System	Tetragonal	Orthorhombic
Space Group	<i>I4₁/acd</i>	<i>Pnma</i>
<i>a</i> /Å	22.302(2)	22.2150(5)
<i>b</i> /Å	22.302(2)	21.5250(5)
<i>c</i> /Å	17.738(1)	18.0773(3)
Volume/Å ³	8822.6(1)	8844.2(4)

4.5.2 Flame Photometry

Determination of the sodium ion concentration in the exchanged product was attempted by EDX initially. However, with the interference from the zinc $L\beta_1$ emission line (1.0 keV), which was very close to the $K\alpha_{1.2}$ (1.0 keV) and $K\beta_1$ (1.1 keV) emission line, it is really difficult to find a strong evidence to prove the existence of sodium from a high zinc content compound by EDX. Again flame photometry was used to evaluate the ion exchange proportion (Table 4.9). The ion exchange degree was then determined with the support of the standard curve (Figure 4.16) generated from the standard sodium ion solutions. The average sodium exchange rate was approximately 78%. (See Appendix 3.2 for calculation details)

Table 4.9 Flame photometry data.

	Concentration	1 st Reading	2 nd Reading	3 rd Reading	Average
Standard Na ⁺ solution	1 ppm	38	38	37.5	37.83
	1.5 ppm	54.5	54	54.5	54.33
	2 ppm	70	70	70.5	70.17
	2.5 ppm	86	85.5	86	85.83
	3 ppm	100	100	100	100
Na ⁺ -exchanged product	Sample 1	48	47.5	48	47.83
	Sample 2	48.5	48	48	48.17
	Sample 3	47	47.5	47.5	47.33

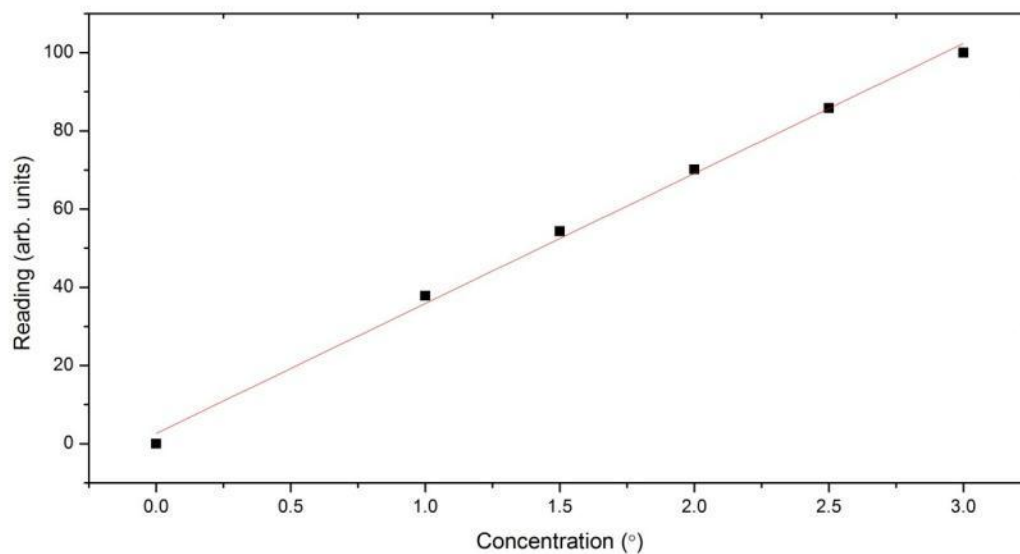


Fig. 4.16 Standard curve for Na^+ -BIRM-1 flame photometry examination; $y = 33.2526x + 2.6057$, $R^2 = 0.996$.

4.5.3 Thermal Stability

For the sodium-exchanged product, the TGA and DTA traces (Figure 4.17) were slightly different from those of the BIRM-1. According to the mass spectrum curves in Figure 4.18, an endothermic peak on the DTA curves at 120 °C is attributable to loss of physisorbed water and accompanied by the release of some ammonia. Two exothermic peaks were observed in the DTA/TGA curves at 510 °C and 650 °C. The first exothermic peak is associated with breakdown of the structure and release of a large amount of CO_2 . After that the second exothermic peak is attributed to the further release of CO_2 generated from the residue left in the TGA chamber.

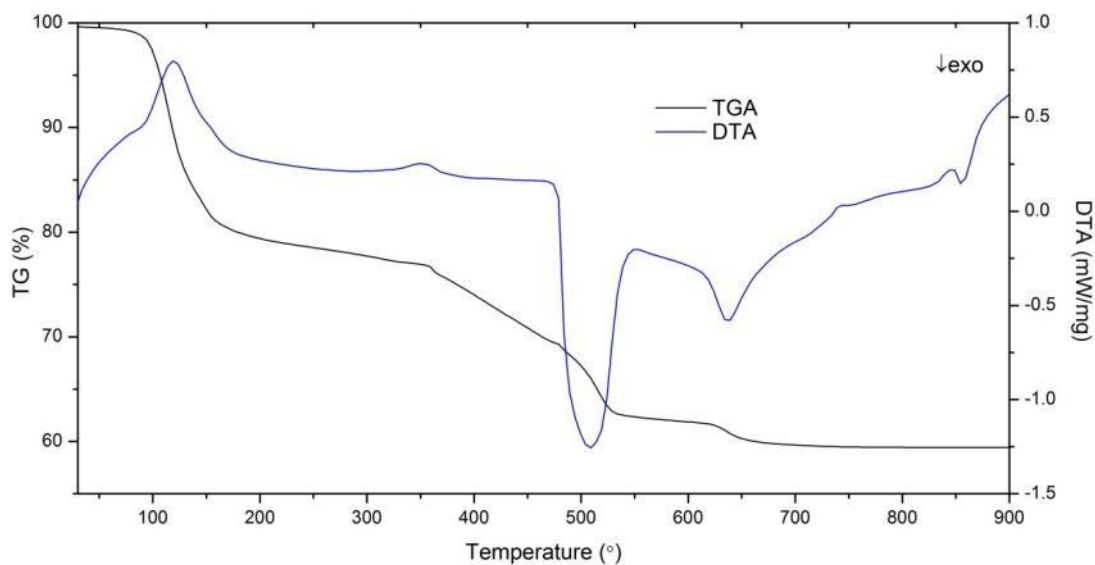


Fig. 4.17 TGA (black trace) and DTA (blue trace) of Na^+ -BIRM-1.

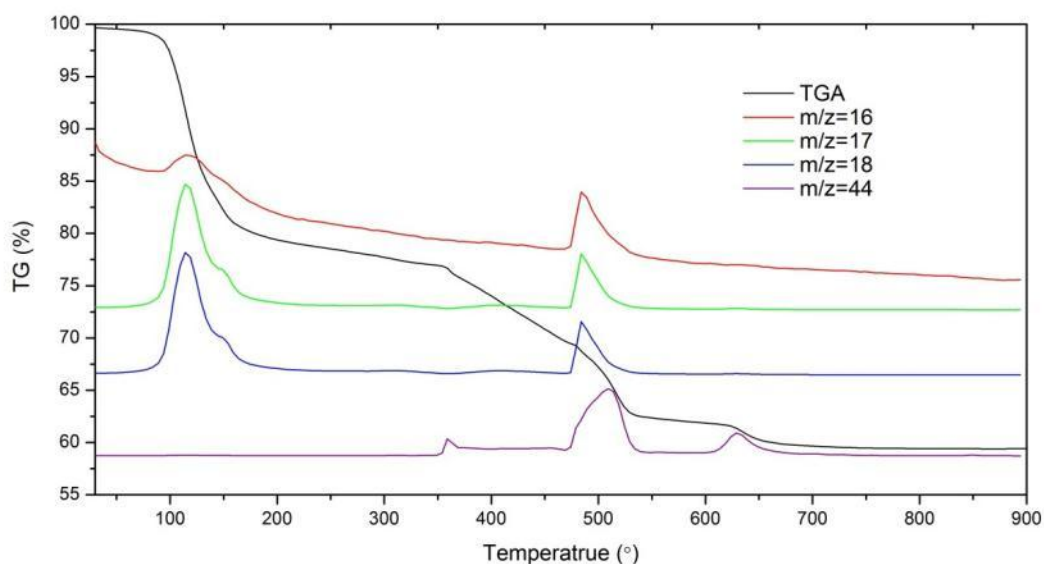


Fig. 4.18 TGA (black trace) of Na^+ -BIRM-1, and mass analysis of $m/z = 16$ (red trace), $m/z = 17$ (green trace), $m/z = 18$ (blue trace) and $m/z = 44$ (purple trace).

Similarly to what occurred with the Li^+ -BIRM-1 TGA solid residue, after heating the sodium-exchanged product was melted on the internal surface of the crucible. Thus it could not be characterized by XRD. Since this phenomenon was not observed from BIRM-1, this could provide some evidence for a successful ion

exchange.

4.5.4 Fourier Transform Infrared Spectroscopy

FTIR spectra (Figure 4.19) were collected to obtain crystallochemical information. The IR spectrum for Na⁺-BIRM-1 is similar to the other two exchanged products and the mother material BIRM-1 (Table 4.10). Like K⁺-BIRM-1 and Li⁺-BIRM-1, the broad absorption band at about 3050 cm⁻¹ was greatly reduced after the sodium ion exchange which is assigned to the removal of the N–H vibration by exchanging ammonium cations out from the structure. These IR data strengthen the analysis discussed above that the framework was still maintained after the ion exchange as well as sodium ions introduced into the structure.

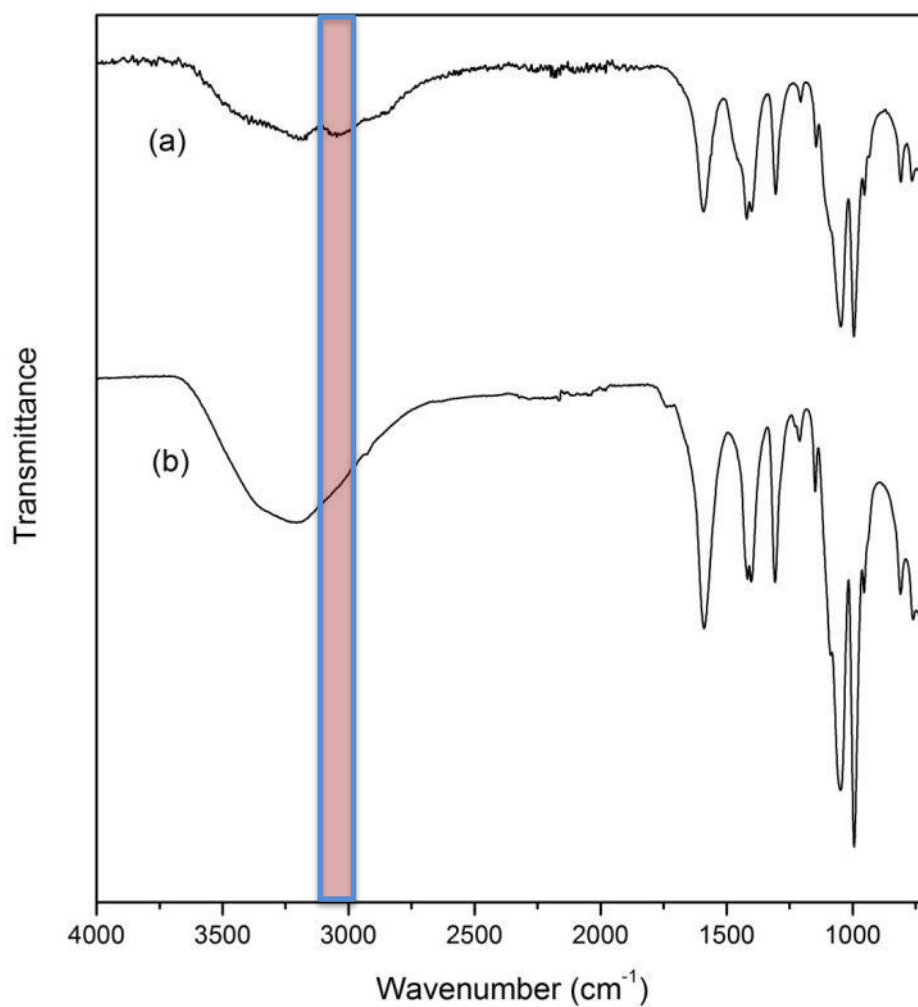


Fig. 4.19 FTIR spectra for (a) BIRM-1 and (b) Na⁺-BIRM-1; the pink area illustrates the peak disappearing after the ion exchange.

Table 4.10 Observed FTIR peaks and assignments for Na⁺-BIRM-1.

Peak (cm ⁻¹)	Assignment
3200	O–H (H ₂ O)
1589	COO ⁻ (sym)
1308	C–O
1402	COO ⁻ (asym)
1417	P–C
1150–950	P–O

4.6 Crystal Structure Determination

After confirming metal ions were successfully exchanged into the structure of

BIRM-1 from the above analyses, the following work was initiated to use Rietveld refinement to analyze the exchanged structure and try to locate the exchanged ion positions. Of these three exchanged products, the XRD patterns as well as the cell parameters of the Li^+ -BIRM-1 and K^+ -BIRM-1 were much the same as those of the parent material BIRM-1 indicating the structure may be similar after ion exchange. Due to the very weak scattering power of Li for X-rays, this structure refinement attempt was begun with the potassium-exchanged product. The starting unit cell was obtained directly from the Le Bail fit¹²⁵ described above (Table 4.1). The model for this refinement was constructed from the as-prepared BIRM-1 structure. Then this model and the cell were used as a starting point for Rietveld refinement against the laboratory X-ray data using the computer program GSAS^{126, 127}.

4.6.1 K^+ -BIRM-1 Structure Determination from Powder Diffraction Data

To begin this refinement, the structure model was slightly modified to minimize the effect from other molecules within the channels when utilizing Fourier difference maps. All the molecules inside the channels which are water and ammonium ions were removed, and the H atoms from the organic ligand were removed as well as these atoms have almost no scattering power for X-rays (Figure 4.20).

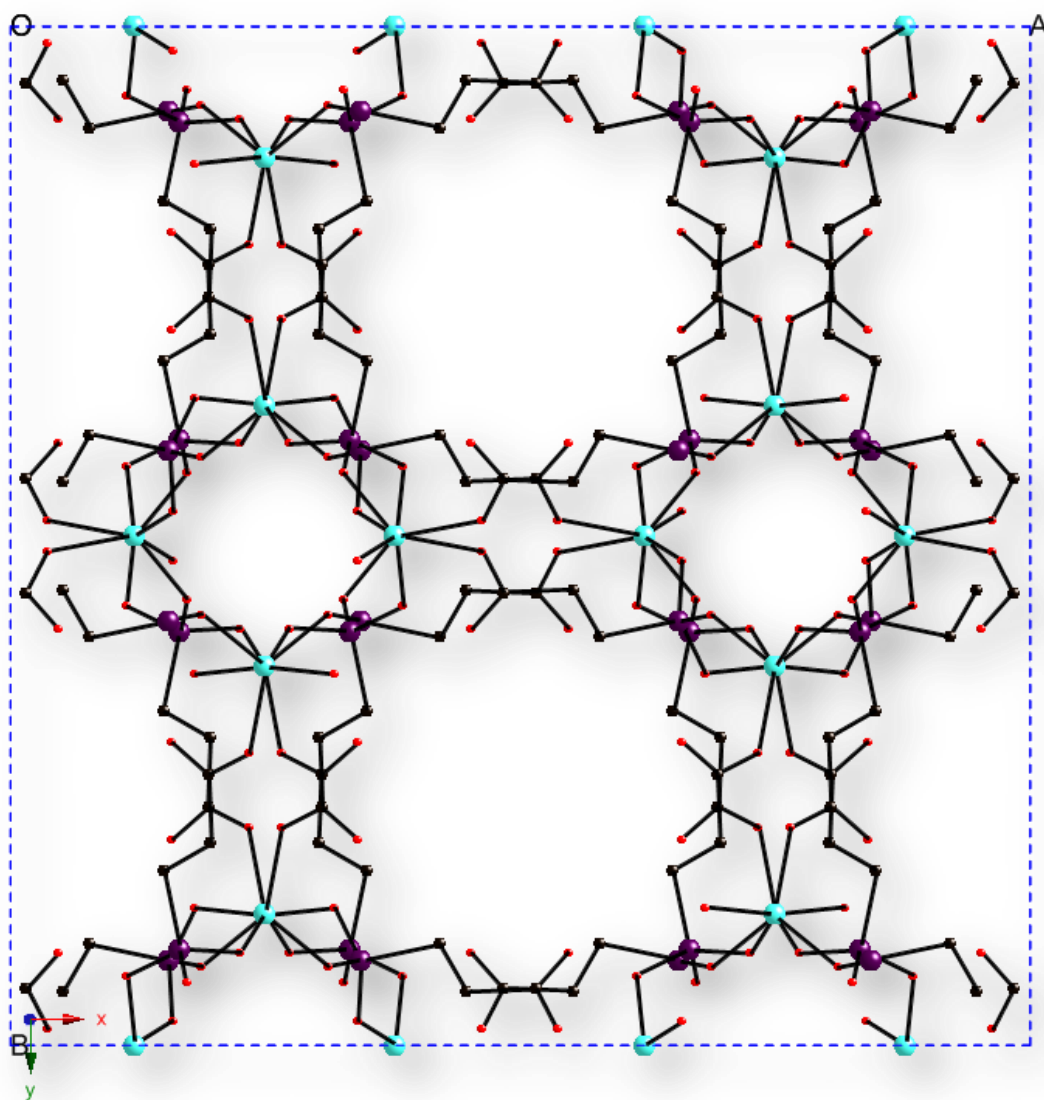
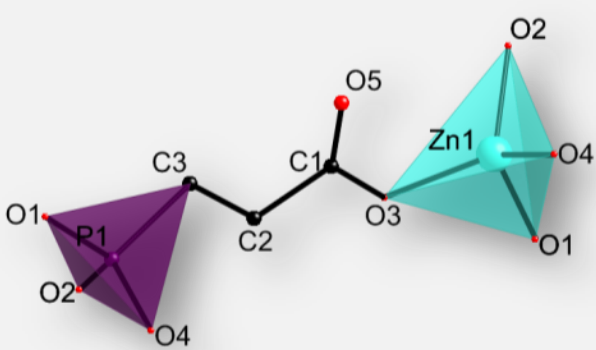


Fig. 4.20 Structural model for K^+ -BIRM-1 viewed along the c -axis; hydrogen atoms have been omitted for clarity; colour scheme: Zn – turquoise, P – purple, K – blue, O – red and C – black.

The background was fitted by a shifted Chebyshev polynomial with 20 parameters. The peak profiles of reflections were modeled with the pseudo-Voigt peak profile function (CW profile function 3 in GSAS^{126, 127}). When starting to refine the empty framework, it was noticed that if there was no limitation applied to bond length, a great level of distortion would occur to the structure after the refinement. The lightweight atoms such as carbon and oxygen from the organic ligand were removed

dramatically from the positions where they used to be. Therefore soft restraints were imposed on selected framework atomic bonding parameters which set the variation of organic ligand and tetrahedral distances (Table 4.11). The weighting factor of the restraint was started at 1000, and then gradually reduced to 20 to allow the structure to relax slightly.

Table 4.11 Refinement parameters of bond length soft restraints.

	Bond	Distance (Å)
	C1–C2	1.5
	C1–O3	1.3
	C1–O5	1.2
	C2–C3	1.5
	P1–C3	1.8
	P1–O1	1.5
	P1–O2	1.5
	P1–O4	1.5
	Zn1–O1	2.0
	Zn1–O2	2.0
	Zn1–O3	2.0
	Zn1–O4	2.0

The structure obtained from the restrained refinement was satisfactory ($R_{wp} = 11\%$) and it turned out the bond angle soft restraint was not necessary. Difference Fourier maps were employed to locate additional electron density in the structure. Based on the above refinement of the framework, more than 70 positions can be found due to the potassium atoms, water oxygen atoms and ammonium nitrogen atoms absent from the channels.

Unfortunately, it is hard to distinguish which position should be designated a potassium atom site or which one should be an oxygen or nitrogen atom site, but some

assistance can be gained from the knowledge that in principle the heavier potassium atom would have greater scattering of X-rays compared to oxygen atoms and nitrogen atoms, which should make it possible to distinguish potassium atom sites from oxygen and nitrogen sites. However, investigation of the structure of the parent material BIRM-1 indicates that nitrogen positions as well as free water molecules (oxygen atoms) are highly disordered inside the channels. This means for each position found in the difference Fourier map, it could be a fully occupied site, or have partial or mixed occupation. Thus each single site generated from difference Fourier maps could be a site for any of these three atoms in accordance with their site occupancy. Comparison of the typical coordination bond lengths of potassium, oxygen and nitrogen with the surrounding framework atoms could help determine some non-potassium atom sites. However, taking the similarity of scattering power for oxygen and nitrogen atoms in X-ray diffraction, as well as the complexity of the structure into consideration, it makes identifying the positions of oxygen and nitrogen atoms from X-ray difference Fourier maps extremely difficult. Thus it is very challenging to find a satisfactory solution to this thorny problem.

An alternative possibility considered was that potassium atoms may preferentially substitute at nitrogen positions and the rest of nitrogen atoms are still in their original sites. Applying these as initial atomic positions for both potassium and nitrogen atoms, only water oxygen atoms need to be located by difference Fourier maps, therefore obviating some of the difficulties in determining the extra framework atoms.

Hence as starting structure model was then constructed by removing water molecules from the structure and positioning five potassium atom sites to the same

locations as the five nitrogen atom sites in the parent material (Figure 4.21). Occupancy constraints were initially applied to each potassium/nitrogen atom shared site to allow nitrogen atoms to be replaced by potassium atoms with concurrent appropriate reduction, and the preliminary occupancy for potassium atoms in each site was 0.8 and for nitrogen atoms was 0.2, in accordance with EDX results. Newly added atoms of identical element type were constrained to have the same isotropic thermal displacement parameter, $U_{\text{iso}} = 0.025$.

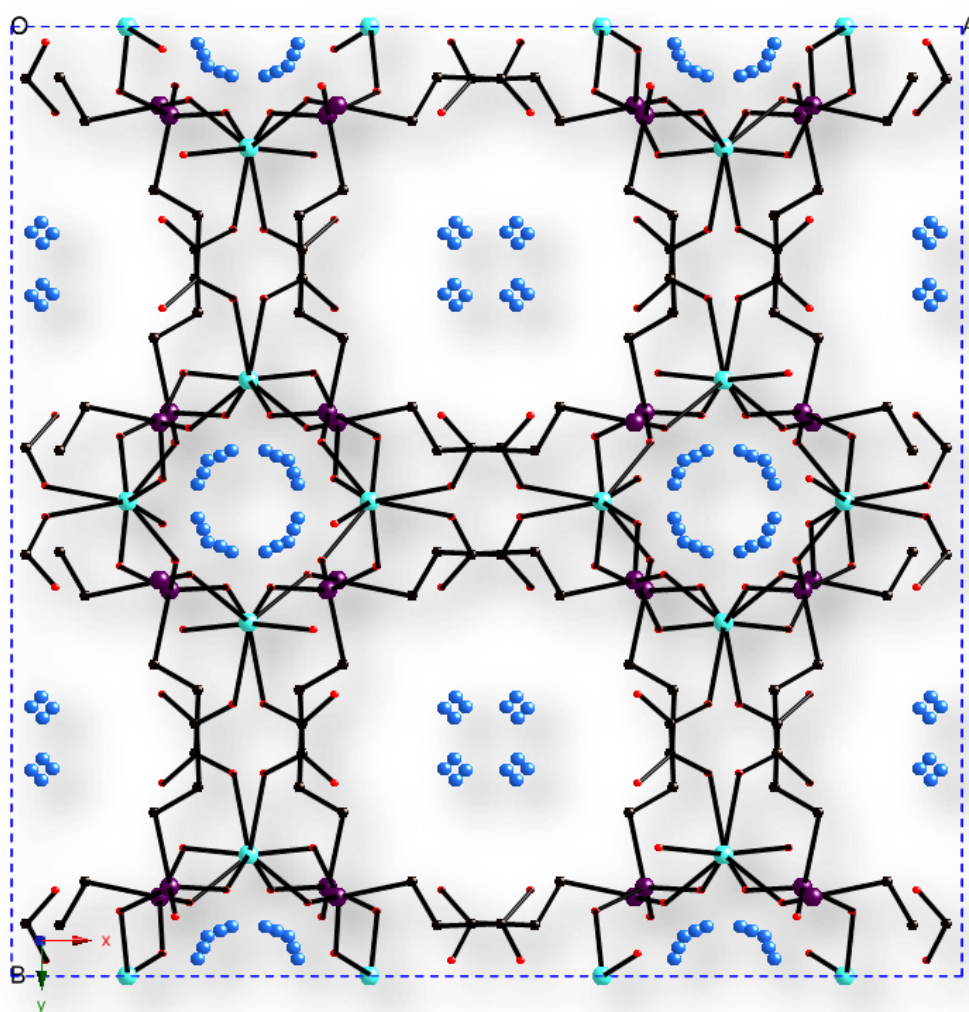


Fig. 4.21 Starting positions for the newly added potassium atoms viewed along the *c*-axis; hydrogen atoms have been omitted for clarity; colour scheme: Zn – turquoise, P – purple, K – blue, O – red and C – black.

By exploiting the structure soft restraint, the Rietveld refinement of the new structure resulted in a good fit ($R_{wp} = 8.00\%$). Then further refinement of the fractional occupancies was carried out which resulted in a total occupancy of potassium consistently higher than 1, and the occupancies of nitrogen atoms were changed to negative values correspondingly. This unreasonable result may derive from the absence of the water molecules inside the structure. Without these water molecules, the occupancy of the potassium atoms had to be elevated to compensate (at least in part) for their electron density. Due to the existence of the occupancy constraint between these two types of atoms, the occupancies of the nitrogen atoms were changed to minus consequently. It was concluded that modeling the structure with this occupancy constraint was underestimating the total scattering by oxygen atoms, and as such was resulting in a physically meaningless refinement.

Thus the total occupancies of potassium atoms and nitrogen atoms were constrained in a different way in the following Rietveld refinement. The starting model remained the same as the previous attempt, and constraints were used to fix the total occupancies of potassium atoms at 0.8 and nitrogen atoms at 0.2 in accordance with EDX results. Then by carefully refining the occupancies of potassium atoms and nitrogen atoms, a stable Rietveld refinement was obtained with $R_{wp} = 5.64\%$. Inspection of the refinement showed that the occupancies of the potassium atoms had reasonable values. However, even if a hard constraint was applied to fix the total occupancy of the nitrogen atoms, the occupancies of atoms N3 and N5 became negative on refinement resulting in the sum of other nitrogen atom occupancies being bigger than 0.2 (Table 4.12). These two nitrogen sites were eliminated from further refinements. Investigation of the structure suggested that the positions of sites N1 and

N4 were closely related to the water oxygen sites from the structure of BIRM-1, and selecting oxygen atoms could account for this increased scattering as the occupancy of water oxygen need be kept as 0.2 or lower. Thus two oxygen positions were proposed and assigned with the same occupancy as they were nitrogen. The nitrogen site N2, was located at appropriate positions in the large channel, but the occupancy refined to a value of 0.4444, which was higher than the theoretical value 0.2 (0.2 per Zn/P atom), so it was fixed at 0.2 in the subsequent refinements.

Table 4.12 Decisions made for nitrogen atoms.

Positions	Occupancy	Decision
N1	0.3886	Oxygen
N2	0.4444	Remain Nitrogen
N3	-0.2432	Delete
N4	0.5641	Oxygen
N5	-1.0745	Delete

Ten additional extra-framework water oxygen sites were then identified in powder X-ray diffraction difference Fourier maps. Two of the site positions, one with a very short distance to zinc ($d_{\text{Zn-O}} = 0.39 \text{ \AA}$) and one to potassium ($d_{\text{K-O}} = 0.29 \text{ \AA}$), were not added into the refinement. The other eight newly added water oxygen atoms helped the refinement to reach final goodness of fit values: $\chi^2 = 2.809$, $R_{\text{wp}} = 4.39\%$ and $R_{\text{p}} = 3.10\%$. By reviewing the atoms positions of this refined structure, it was then noticed that one potassium atom inside the large channel was located at a very similar site to that of a water oxygen atom from BIRM-1 with a very low occupancy of 0.0528, and another low occupancy (0.0864) potassium site on a special position inside the smaller channel was very close to that of a nitrogen atom from BIRM-1 as well. In this case, it seemed sensible to change these two potassium sites to be a water oxygen site and an ammonium nitrogen site, respectively, with higher occupancy.

Refinement of this new model proceeded smoothly with the structure soft restraint released in the final refinement. Bond lengths and bond angles converged to reasonable values and improved the Rietveld refinement fit with $\chi^2 = 2.574$, $R_{wp} = 4.21\%$ and $R_p = 3.01\%$ (Figure 4.22 and 4.23). A summary of the atomic parameters (Table 4.13) and selected bond lengths (Table 4.14), bond angles (Table 4.15) are shown below.

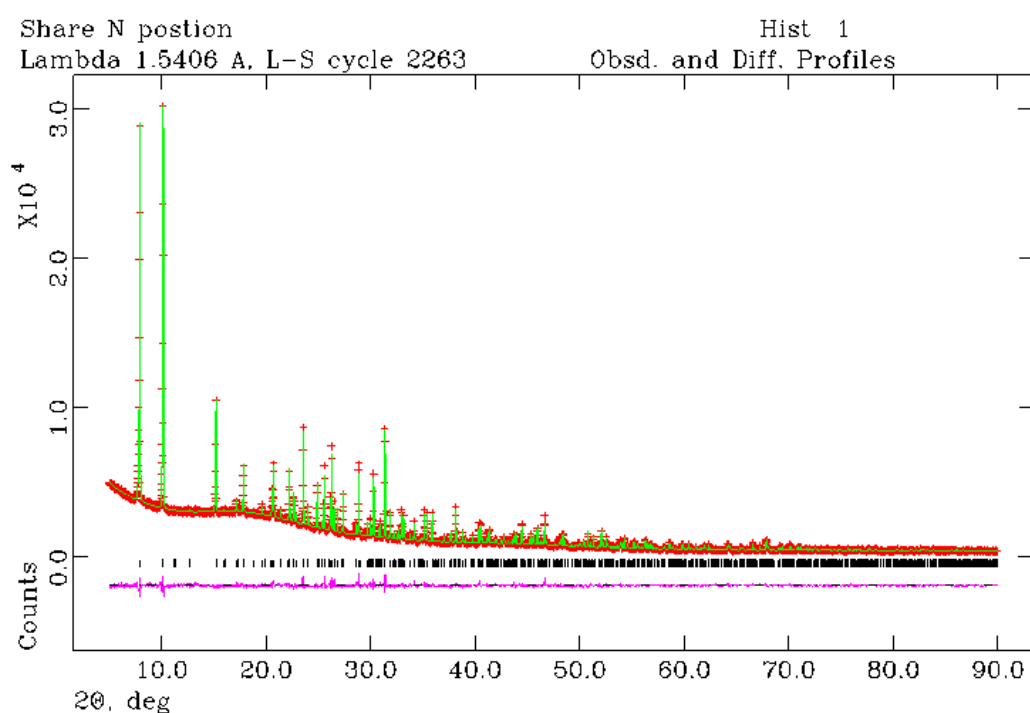


Fig. 4.22 Final observed (crosses), calculated (solid line), difference (below) and reflection positions (middle) for the final Rietveld refinement of K⁺-BIRM-1; $\chi^2 = 2.574$, $R_{wp} = 4.21\%$ and $R_p = 3.01\%$.

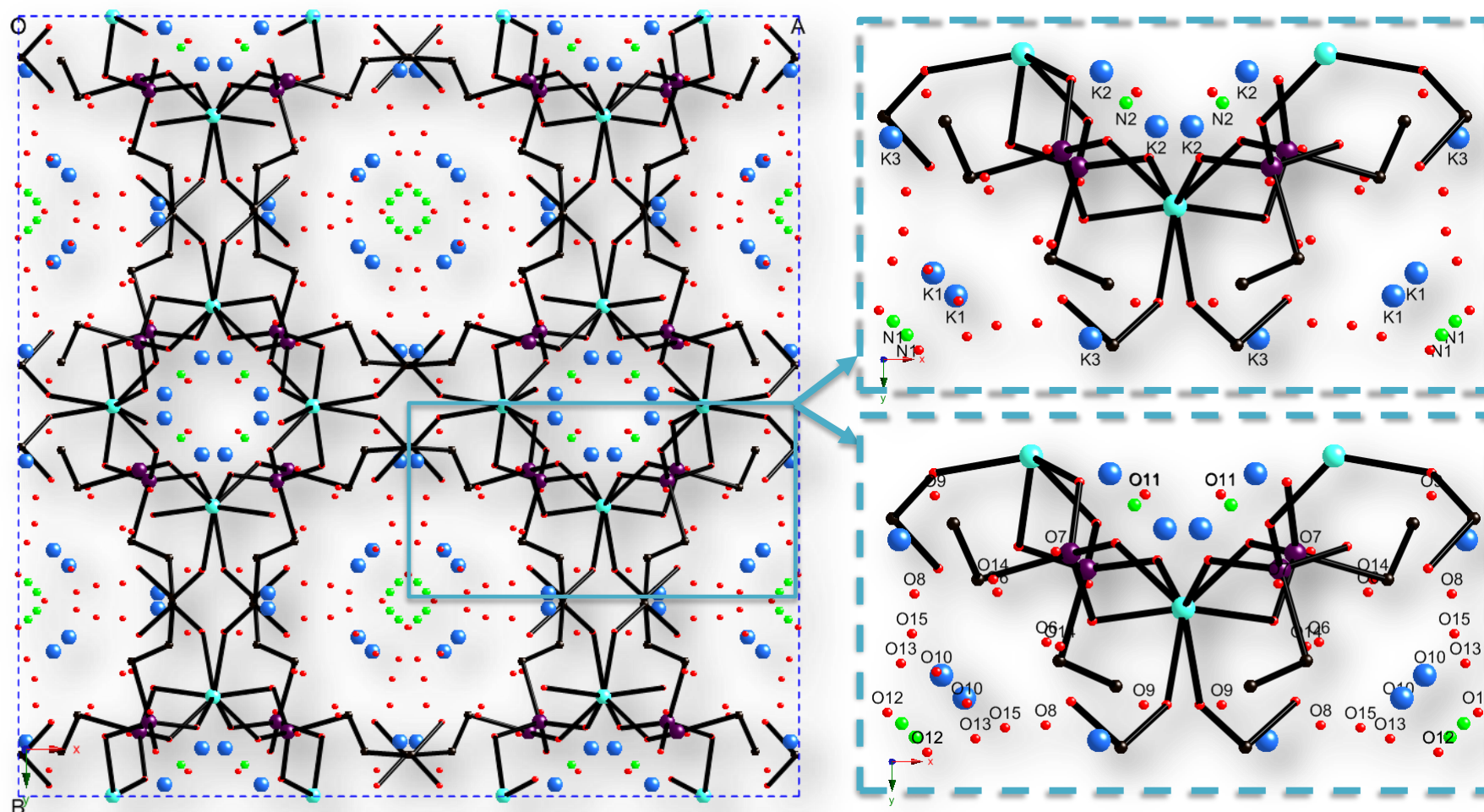


Fig. 4.23 Refined structure of K⁺-BIRM-1 viewed along the z-axis, illustrating the atomic positions of exchanged potassium atoms, ammonium nitrogen atoms (upper right) and water oxygen atoms (lower right); hydrogen atoms have been omitted for clarity; blue dashed lines indicate one unit cell (left); colour scheme: Zn – turquoise, P – purple, K – blue, N – green, O – red and C – black.

Table 4.13 Refined atomic positions of K⁺-BIRM-1; hydrogen atoms placed geometrically after refinement was complete.

Atom	Mult.	<i>x</i>	<i>y</i>	<i>z</i>	Occupancy	<i>U</i> _{iso}
C1	32	0.302(1)	0.246(1)	0.162(2)	1	0.031 (9)
C2	32	0.307(1)	0.306(1)	0.183(1)	1	0.016 (8)
H21	32	0.3104	0.3295	0.1356	1	-
H22	32	0.2679	0.3157	0.2083	1	-
C3	32	0.354(1)	0.327(1)	0.232(1)	1	0.040 (9)
H31	32	0.3946	0.3248	0.2071	1	-
H32	32	0.3556	0.3032	0.2798	1	-
O1	32	0.3890(7)	0.4234(7)	0.2902(8)	1	0.022 (5)
O2	32	0.3233(7)	0.4431(6)	0.1726(9)	1	0.018 (5)
O3	32	0.2639(7)	0.2104(7)	0.1236(9)	1	0.029 (5)
O4	32	0.2718(7)	0.4123(6)	0.2834(7)	1	0.017 (5)
O5	32	0.3449(7)	0.2075(8)	0.1995(9)	1	0.042 (6)
P1	32	0.3320(4)	0.4047(3)	0.2494(5)	1	0.025 (2)
Zn1	32	0.2496(2)	0.1283(2)	0.1135(2)	1	0.023 (1)
N1	32	0.512(8)	0.226(9)	0.411(8)	0.103(5)	0.025
N2	16	0.291(7)	0.959(7)	0.125	0.19(1)	0.025
K1	32	0.454(1)	0.185(2)	0.199(2)	0.236(4)	0.06(1)
K2	32	0.265(1)	0.938(1)	0.055(1)	0.239(3)	0.05(1)
K3	32	0.3207(9)	0.7600(7)	0.027(1)	0.330(5)	0.024(7)
O6	32	0.407(2)	0.115(2)	0.304(2)	0.45(2)	0.025
O7	32	0.3304(9)	0.8924(8)	-0.203 (1)	0.73(1)	0.025
O8	32	0.366(2)	-0.227(2)	0.037(3)	0.34(2)	0.025
O9	32	0.433(2)	0.209(2)	0.333(3)	0.30(1)	0.025
O10	32	0.217(2)	-0.210(2)	-0.020(3)	0.36(1)	0.025
O11	32	0.282(2)	-0.032(2)	0.087(2)	0.42(1)	0.025
O12	32	-0.272(3)	-0.216(2)	0.042(2)	0.30(1)	0.025
O13	32	0.075(4)	-0.239(3)	0.045(4)	0.25(2)	0.025
O14	32	0.411(2)	-0.104(2)	0.088(2)	0.37(1)	0.025
O15	32	0.098(1)	0.229(1)	0.077(2)	0.52(2)	0.025

Table 4.14 Selected bond distances for K⁺-BIRM-1 framework.

Bond	Distance (Å)	Bond	Distance (Å)
C1–C2	1.382(28)	P1–O2	1.626(15)
C1–O3	1.347(25)	P1–O4	1.479(14)
C1–O5	1.440(27)	Zn1–O1	2.152(14)
C2–C3	1.454(28)	Zn1–O2	1.876(15)
P1–C3	1.822(22)	Zn1–O3	1.858(14)
P1–O1	1.518(15)	Zn1–O4	2.104(13)

Table 4.15 Selected bond angles for K⁺-BIRM-1.

Bond Angle	Angle (°)	Bond Angle	Angle (°)
O1–P1–C3	96.5(10)	O1–Zn1–O4	113.7(6)
O2–P1–C3	112.8(11)	P1–C3–C2	102.2(17)
O2–P1–O1	111.1(9)	C3–C2–C1	121.9(24)
O4–P1–C3	115.1(10)	O5–C1–O3	107.8(23)
O4–P1–O1	121.7(10)	C2–C1–O5	113.2(24)
O4–P1–O2	100.3(9)	C2–C1–O3	138.0(28)
O3–Zn1–O2	123.8(8)	Zn1–O1–P1	114.5(9)
O1–Zn1–O2	113.3(6)	Zn1–O2–P1	124.6(10)
O4–Zn1–O2	100.1(6)	Zn1–O3–C1	137.0(18)
O3–Zn1–O1	94.8(7)	Zn1–O4–P1	121.0(10)
O3–Zn1–O4	111.9(7)		

Table 4.16 Selected interatomic distances for potassium atoms (within 0–3 Å).

Bond	Distance (Å)
K1–O5	2.48(4)
K2–O2	2.877(33)
K2–O4	2.917(33)
K2–O4	2.959(34)
K3–O1	2.699(22)
K3–O3	2.780(25)

In this refined structure, the framework structure is very close to that of BIRM-1, suggesting a reasonable structure determination. The entire structure is constructed by the connection of ZnO₄/CPO₃ inorganic chains through the organic ligand. Each phosphorus atoms is tetrahedrally bonded to three oxygen atoms and one carbon atom and the zinc atom is tetrahedrally coordinated by four oxygen atoms with reasonable bond lengths. The interatomic distance (Table 4.16) between the potassium site positions and the nearby framework atoms were in the range of the coordination distances of K⁺ in the compilation of extra-framework sites in zeolite¹⁴⁸ (which is about 2.5 Å – 3.5 Å, mainly around 2.9 Å). Due to the unreliability of the free water oxygen sites positions, the coordination environments of the exchanged potassium cations were not further discussed. Potassium ions and ammonium nitrogen ions were

distributed into both the channels. For smaller channel, this was considered acceptable, but for the large channels, it was not entirely clear that this made chemical sense. The ammonium ions in the large channel in BIRM-1 are quite far away from the framework and will have more opportunity to exchange with potassium ions as they are more accessible. Hence the ammonium ions are judged likely to be fully exchanged from there. In addition, the potassium ion is thought more likely to find a relatively stable position coordinated to the framework atoms and not near the centre of the large channel. In view of this, a further structure refinement attempt was carried out. The nitrogen site inside the large channel (N1) was removed and replaced by an oxygen site in this refinement. For the potassium ions, the K3 site had the highest occupancy and also had reasonable distances to coordinate with framework oxygens O1 and O3 (Figure 4.24a and Table 4.16). However, the other potassium site inside the large channel K1, was relatively remote from the framework with only one possible coordination distance to O5 of the framework (Figure 4.24b and Table 4.16). Therefore the K1 site was also tested as an oxygen site in this attempt.

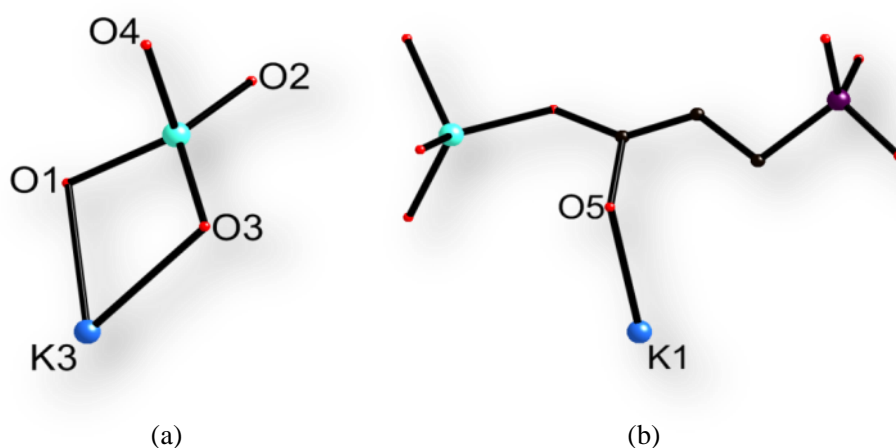


Fig 4.24 Possible coordination of potassium ions (a) K3 and (b) K1 with framework oxygen atoms; colour scheme: Zn – turquoise, P – purple, K – blue, O – red and C – black.

The final refinement of this modified model reached a fit with $\chi^2 = 2.590$, R_{wp}

= 4.22% and $R_p = 3.00\%$ (Figure 4.25 and 4.26). Atomic parameters, selected bond lengths and angles and distances between potassium atoms and the nearby framework atoms were shown below (Table 4.17-4.20). Comparing with the previous refinement result, this one was neither improved nor significantly worse. Besides the absence of the potassium ion and the ammonium nitrogen ion inside the large channel, the structures are essentially the same. It is perhaps not surprising that this attempt yielded a very similar result, as the refinement can not readily distinguish between an oxygen atom site and a nitrogen atom site, or a low occupancy potassium site and a high occupancy oxygen site.

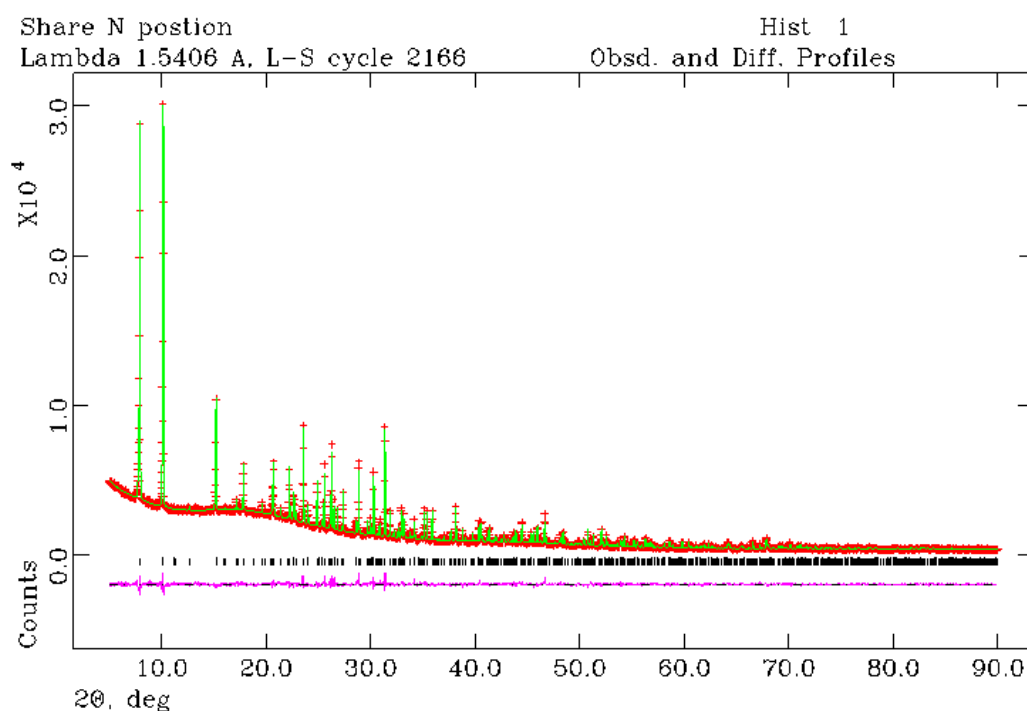


Fig. 4.25 Final observed (crosses), calculated (solid line), difference (below) and reflection positions (middle) for the Rietveld refinement of K^+ -BIRM-1 with modified structure model; $\chi^2 = 2.590$, $R_{wp} = 4.22\%$ and $R_p = 3.00\%$.

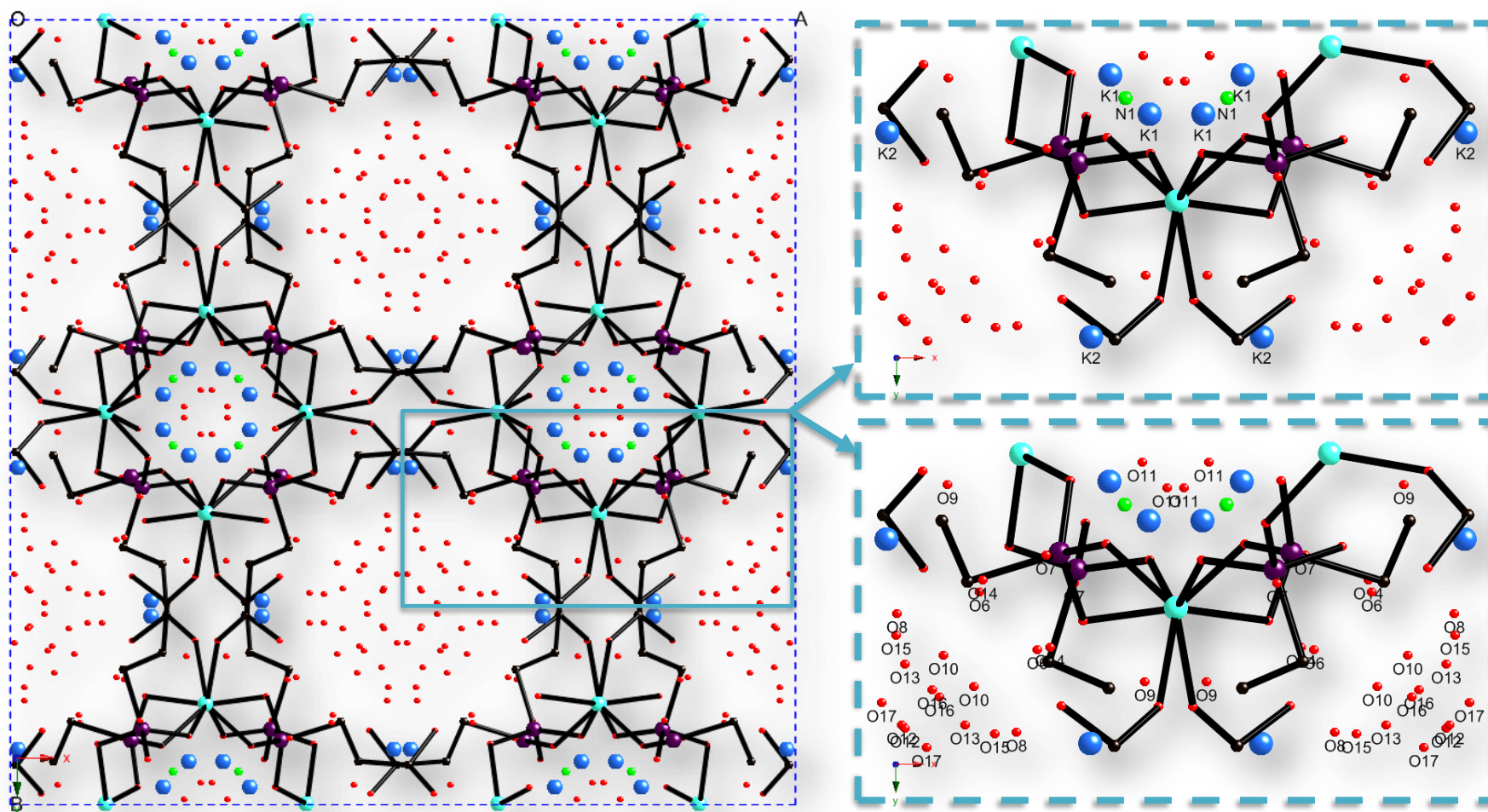


Fig. 4.26 Refined structure of K^+ -BIRM-1 with the modified structure model, viewed along the z-axis, illustrating the atomic positions of potassium atoms, nitrogen atoms (upper right) and water oxygen atoms (lower right); hydrogen atoms have been omitted for clarity; blue dashed lines indicate one unit cell (left); colour scheme: Zn – turquoise, P – purple, K – blue, N – green, O – red and C – black.

Table 4.17 Refined atomic positions of K⁺-BIRM-1 with the modified structure model; hydrogen atoms placed geometrically after refinement was complete.

Atom	Mult.	<i>x</i>	<i>y</i>	<i>z</i>	Occupancy	<i>U</i> _{iso}
C1	32	0.301(1)	0.242(1)	0.160(2)	1	0.027(9)
C2	32	0.306(1)	0.306(1)	0.180(1)	1	0.017(8)
H21	32	0.3094	0.3293	0.1325	1	-
H22	32	0.2668	0.3172	0.2055	1	-
C3	32	0.356(1)	0.328(1)	0.231(1)	1	0.027(8)
H31	32	0.3954	0.3267	0.2052	1	-
H32	32	0.3576	0.3034	0.2781	1	-
O1	32	0.388(7)	0.4232(7)	0.2920(8)	1	0.023(5)
O2	32	0.3245(7)	0.4427(7)	0.1736(9)	1	0.013(5)
O3	32	0.2640(7)	0.2094(7)	0.123(1)	1	0.023(5)
O4	32	0.2717(7)	0.4123(7)	0.2836(7)	1	0.017(5)
O5	32	0.3444(7)	0.2090(8)	0.1991(9)	1	0.042(6)
P1	32	0.3320(4)	0.4042(3)	0.2499(5)	1	0.025(2)
Zn1	32	0.2496(2)	0.1279(2)	0.1138(2)	1	0.0224(8)
N2	16	0.292(3)	0.958(3)	0.125	0.4	0.025
K1	32	0.2724(9)	0.9450(7)	0.0615(8)	0.358(5)	0.063(7)
K2	32	0.3206(7)	0.7603(5)	0.0279(8)	0.448(5)	0.031(5)
O6	32	0.412(2)	0.114(2)	0.305(2)	0.47(2)	0.025
O7	32	0.3338(9)	0.8928(9)	-0.003(1)	0.69(1)	0.025
O10	32	0.417(3)	0.193(3)	0.340(3)	0.24(1)	0.025
O8	32	0.382(4)	-0.231(4)	0.038(4)	0.19(2)	0.025
O9	32	0.225(2)	-0.189(2)	-0.012(4)	0.26(1)	0.025
O11	32	0.278(3)	-0.007(4)	0.087(5)	0.20(1)	0.025
O12	32	-0.025(3)	-0.227(3)	0.042(3)	0.27(1)	0.025
O13	32	0.076(2)	-0.225(3)	0.053(3)	0.35(2)	0.025
O14	32	0.410(2)	-0.104(2)	0.083(3)	0.34(1)	0.025
O15	32	0.100(1)	0.232(1)	0.075(2)	0.58(2)	0.025
O16	32	0.451(2)	0.196(2)	0.204(3)	0.43(2)	0.025
O17	32	0.493(2)	0.206(2)	0.420(3)	0.29(2)	0.025

Table 4.18 Selected bond distances for K⁺-BIRM-1 with the modified structure model.

Bond	Distance (Å)	Bond	Distance (Å)
C1–C2	1.478(29)	P1–O2	1.616(15)
C1–O3	1.272(25)	P1–O4	1.478(14)
C1–O5	1.407(26)	Zn1–O1	2.137(14)
C2–C3	1.510(28)	Zn1–O2	1.869(15)
P1–C3	1.806(22)	Zn1–O3	1.843(15)
P1–O1	1.516(16)	Zn1–O4	2.092(13)

Table 4.19 Selected bond angles for K⁺-BIRM-1 with the modified structure model.

Bond Angle	Angle (°)	Bond Angle	Angle (°)
O1–P1–C3	96.6(10)	O1–Zn1–O4	113.1(6)
O2–P1–C3	111.7(11)	P1–C3–C2	101.3(17)
O2–P1–O1	110.8(9)	C3–C2–C1	120.7(22)
O4–P1–C3	116.8(11)	O5–C1–O3	113.9(24)
O4–P1–O1	120.7(10)	C2–C1–O5	109.0(23)
O4–P1–O2	100.8(10)	C2–C1–O3	136.5(28)
O3–Zn1–O2	122.3(8)	Zn1–O1–P1	115.4(9)
O1–Zn1–O2	113.4(6)	Zn1–O2–P1	126.8(10)
O4–Zn1–O2	101.4(6)	Zn1–O3–C1	135.5(19)
O3–Zn1–O1	94.8(7)	Zn1–O4–P1	120.6(10)
O3–Zn1–O4	112.5(7)		

Table 4.20 Selected interatomic distances for potassium atoms (within 0–3 Å).

Bond	Distance (Å)
K1–O4	2.807(26)
K1–O2	2.938(27)
K1–O2	2.989(25)
K2–O1	2.725(19)
K2–O3	2.769(21)

Comparing these two refined structure models, the essential difference is the extra potassium ion and nitrogen sites in the large channel. It is actually the refinement method that led to these being there. Reviewing the entire refinement procedure, when the structure was emptied and potassium ions were put into the same positions as the ammonium nitrogen ions, the whole structure was lacking water oxygen atoms, and when the potassium ions and the ammonium nitrogen atoms started to refine, they were moved to certain places in the large channel to cover the scattering which is supposed actually to be generated from the water oxygen atoms. As refinements with and without these two sites are of virtually indistinguishable quality, our data does not provide clear evidence for their presence in K⁺-BIRM-1.

4.6.1.1 Discussion

As outlined above, two tentative structures for the K^+ -BIRM-1 product were refined using the Rietveld method (Table 4.21). The main strategy used here was to first refine the structure framework, then rely on ammonium nitrogen positions from BIRM-1 to find out the most important channel atoms, and use difference Fourier maps to locate the other atom sites inside the channels, which is often the tricky part in porous framework solids.

Table 4.21 Experimental parameters and crystallographic data for K^+ -BIRM-1.

X-ray facility	Bruker D8, in transition geometry	
Wavelength (Å)	1.54056	
Temperature	Ambient temperature	
Profile range (°, 2 θ)	5 – 90	
Step size(2 θ)	0.0197	
	Attempt I	Attempt II
Chemical formula	$C_3K_{0.8}N_{0.2}O_{9.04}PZn$	$C_3K_{0.8}N_{0.2}O_{9.31}PZn$
Chemical formula weight	311.32	315.64
Space group	$I4_1/acd$	$I4_1/acd$
a (Å)	22.1942 (2)	22.1943 (2)
c (Å)	17.8532 (2)	17.8532 (2)
V (Å ³)	8794.2 (2)	8794.2 (2)
Background parameters	20	20
Profile parameters	7	7
R_{wp}	4.21%	4.22%
R_p	3.01%	3.00%
χ^2	2.574	2.590

Our attempts to refine the structure of K^+ -BIRM-1 were not entirely satisfactory due to the quality of the data. It is likely that the site positions for the low occupancy extra-framework atoms are not very reliable, and some potassium ion sites could be occupied by water oxygen or nitrogen atoms with higher occupancies and the reverse is also possible. This does not affect the structure of the framework. Because both the refined structures resulted in chemically sensible frameworks, and also as the

agreement between the experiment and calculated profiles is quite good, we believe that one of these two models are reasonably close to the actual structure.

For Rietveld refinement of powder data, endeavours towards a successful structure determination should begin with two simple steps. The first is correct indexing with accurate unit cell parameters, and preferably a correct space group determination. The other is to extract a sufficient number of reliable reflection intensities from the powder patterns^{149, 150}. So for compounds containing elements having weak scattering, higher energy X-rays are desirable to avoid the obscuring from low resolution patterns caused by the overlap of adjacent Bragg peaks, which suppresses the information contained in the powder diffraction data and consequently hampers the application of this technique to solve a complex structure¹⁵¹. The structure being refined here is a complicated three dimensional metal organic framework porous material with extra-framework cations inside the channels and water oxygen atoms that are highly disordered. Solving the structure with laboratory X-ray diffraction patterns is obviously not straightforward. Powder synchrotron X-ray diffraction with/or powder neutron diffraction would be of great assistance for the structure determination. With a high resolution synchrotron X-ray pattern, more peaks could be obtained making determination of the positions and occupancies of the potassium atoms more reliable. With the help of the neutron diffraction data, discriminating the occupancies and atomic site positions for nitrogen and oxygen atoms could be possible due to the difference of their neutron scattering lengths¹⁵². In addition, the scattering power of atoms in neutron diffraction does not have the angular dependence found in X-ray diffraction, resulting in more well defined diffraction peaks at high Bragg angle and more precise data for the refinement of

atomic positions and thermal displacement parameters. However, in this project we did not have the opportunity to examine the cation-exchanged samples by powder synchrotron X-ray diffraction. Neutron diffraction would have required fully deuterated samples, which would be costly to make both in financial terms and experimental time.

4.6.2 Single Crystal XRD Structure of K⁺-BIRM-1

At a late stage of writing this thesis, single crystal XRD data of K⁺-BIRM-1 were returned from the UK National Crystallographic Service after a year long queuing. The raw data was interpreted by Dr. Louise Male in the School of Chemistry at the University of Birmingham. The single crystal XRD results revealed that the framework was maintained after the ion exchange (Table 4.22, see Appendix 4 for more structure details), in agreement with the Rietveld refinement results. As with BIRM-1, the structure is still constructed by the corner sharing of ZnO₄ and CPO₃ tetrahedra linked by the organic ligands into a three dimensional porous structure (Figure 4.27). The potassium cations were successfully exchanged into the structure and distributed in both the large and the small channels. For the potassium cation in the large channel, it was found close to the organic ligand with a six-fold coordination environment with three framework oxygen atoms and three water oxygen atoms. For the one in the smaller channel, potassium cation was found close to the ZnO₄/CPO₃ inorganic chain with a six-fold coordination environment of four framework oxygen atoms and two water oxygen atoms. NH₄⁺ ions are distributed inside the smaller channels.

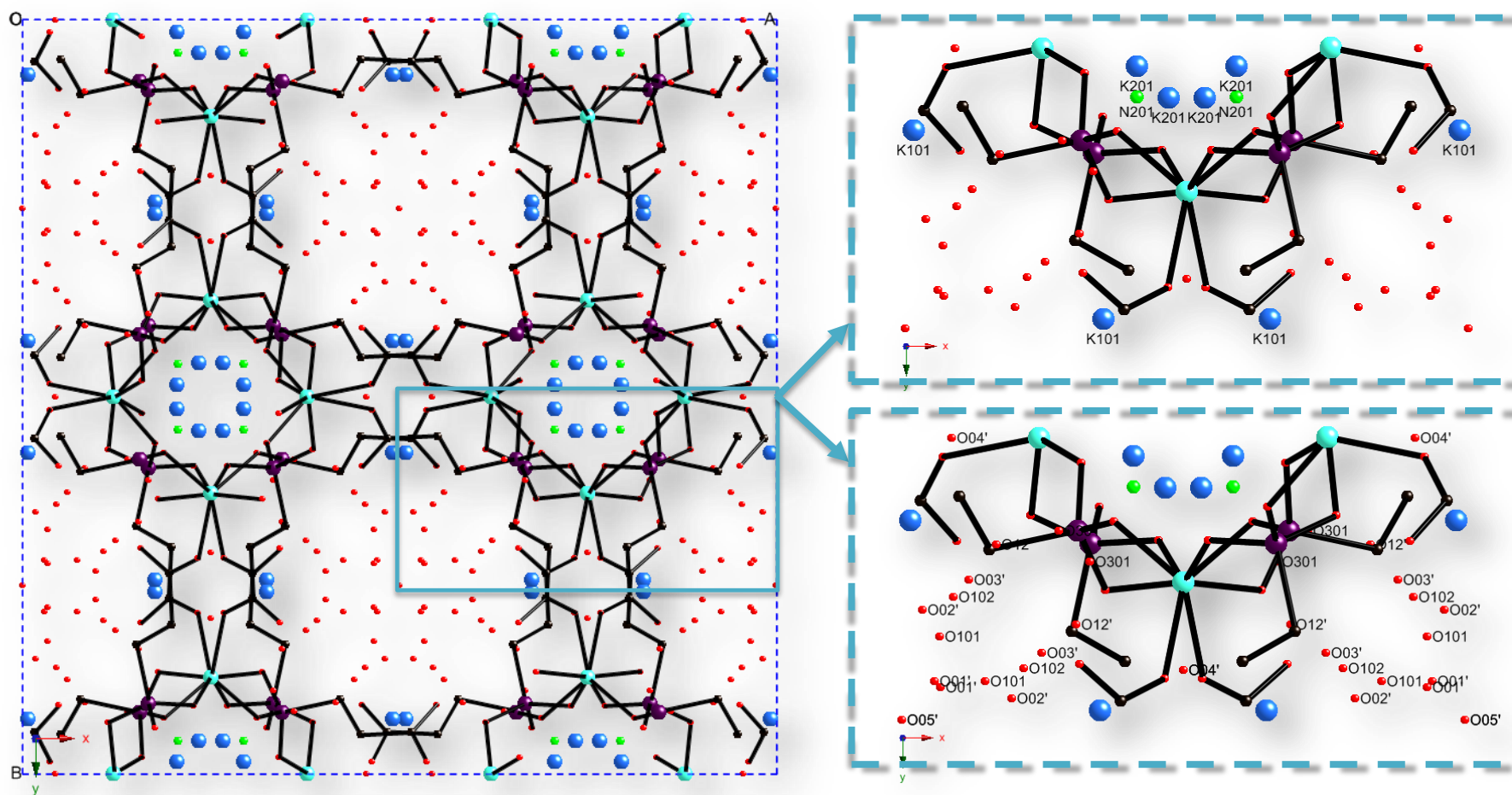


Fig. 4.27 Single crystal structure of K⁺-BIRM-1 viewed along the *z*-axis, illustrating the atomic positions of exchanged potassium atoms, ammonium nitrogen atoms and water oxygen atoms (right). Blue dashed lines indicate one unit cell (left); hydrogen atoms have been omitted for clarity; colour scheme: Zn – turquoise, P – purple, N – green, O – red, C – black and K – blue.

The structure contains 1.51 moles of potassium ions and 0.49 mole of ammonium ions for two moles of zinc atoms. The occupancy of the ammonium cation has been fixed at a value which ensures exact charge balancing within the structure. However when allowed to freely refine the occupancy of the ammonium cation was within 13% of this value. The structure also contains 5.97 water molecules per two zinc atoms, disordered over several sites and with some coordinating to the potassium cations and some being uncoordinated (Figure 4.28), and most of them are adjacent to the charge site of the structure (O5). The coordinated water molecule O(102)/O(12') is disordered over two positions with the occupancies fixed such that they add up exactly to the occupancy of K(101) (Figure 4.28a). It was not possible to locate hydrogen atom positions for the ammonium cation or for the water molecules. Thus it is not possible to tabulate the hydrogen bonding but it is to be expected that all the hydrogen bonding requirements in the structure are fulfilled¹³¹ (Table 4.23).

Table 4.22 Crystallographic data for K⁺-BIRM-1.

Empirical formula	(NH ₄) _{0.49} (K) _{1.51} [Zn ₂ (O ₃ PCH ₂ CH ₂ COO) ₂] 5.97H ₂ O
Formula weight	608.25
Crystal system	Tetragonal
Space group	<i>I</i> 4 ₁ / <i>acd</i>
<i>a</i> (Å)	22.153(9)
<i>c</i> (Å)	17.873(1)
Volume (Å ³)	8771(7)

Table 4.23 Selected interatomic distances for ammonium nitrogen atoms and water oxygen atoms.

Bond	Distance (Å)
N201-O3	2.8
O101-O5	2.8
O102-O5	2.8
O12'-O5	2.6

O01'-O5	2.9
O02'-O1	2.9
O03'-O5	3.3
O04'-O4	2.8
O05'-H3B	3.9
O301-O5	2.8

Note: atom distances were directly measured by Crystal Maker

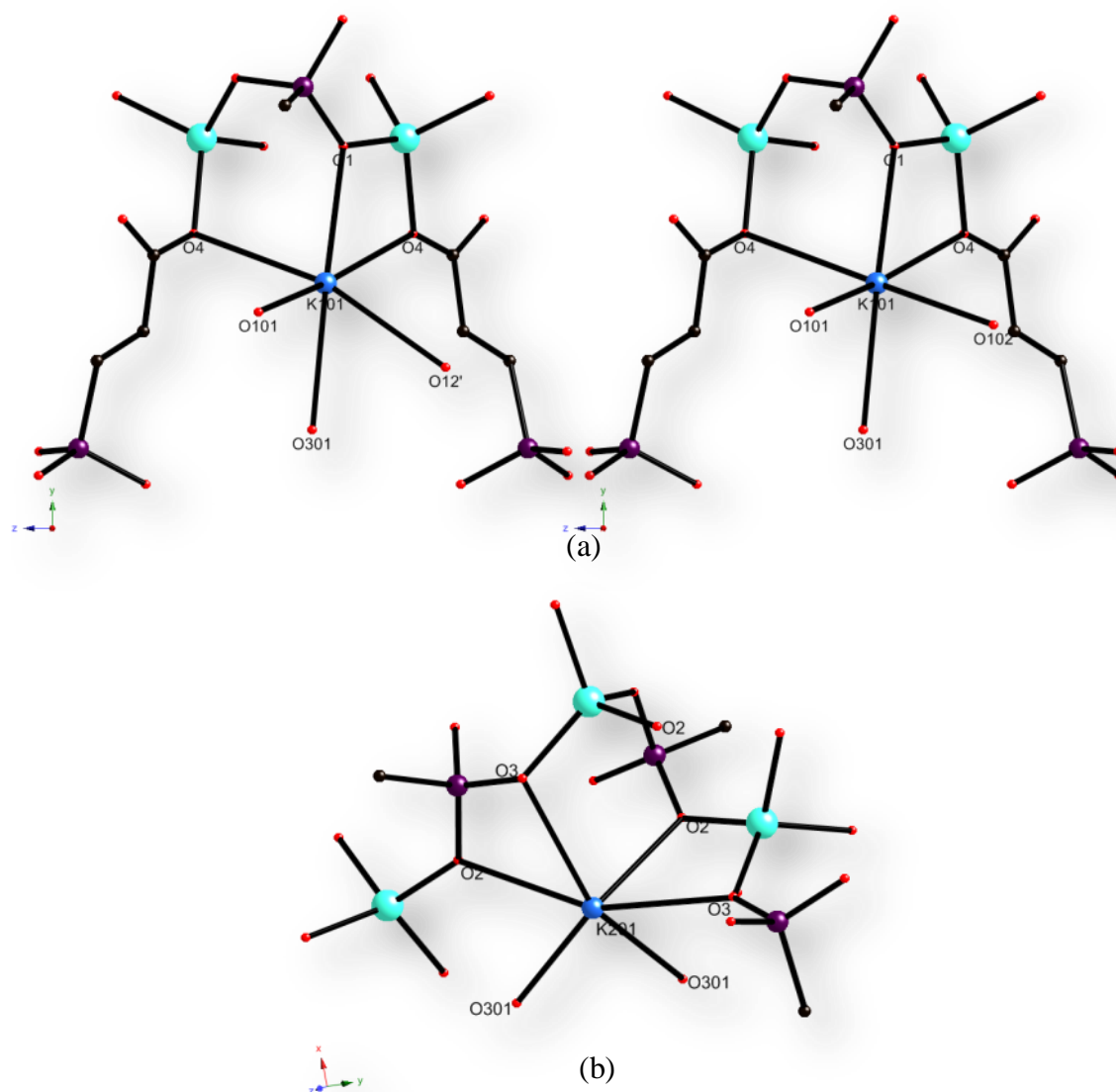


Fig. 4.28 (a) and (b) coordinations of potassium cations with framework oxygen atoms (O1 – O4) and free water oxygen atoms (O101, O102/O12', O301); hydrogen atoms and some water molecules have been omitted for clarity; colour scheme: Zn – turquoise, P – purple, K –blue, O – red and C – black.

4.6.3 Structure Comparison

Both the structures of K^+ -BIRM-1 refined from the powder XRD data bear close similarities to the single crystal structure (Figure 4.29).

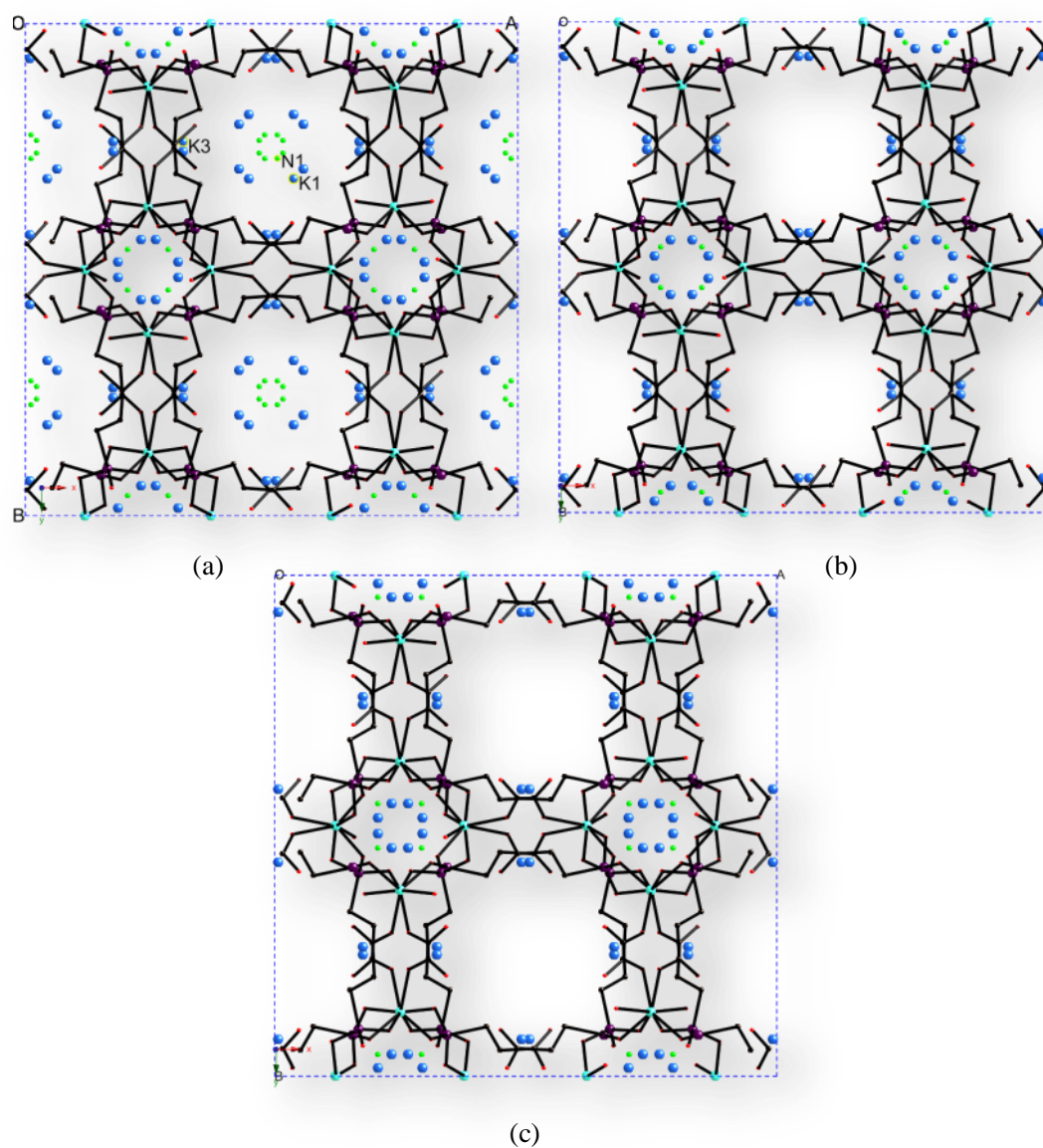


Fig. 4.29 (a, b) Rietveld refined structures from the first and second models, and (c) single crystal structure of K^+ -BIRM-1 viewed along the z-axis, illustrating the different potassium and nitrogen sites; hydrogen atoms and water molecules have been omitted for clarity; blue dashed lines indicated one unit cell (left); colour scheme: Zn – turquoise, P – purple, K – blue, N – green, O – red and C – black.

For the structure refined at the first attempt, the framework is almost the same as in the single crystal structure and most of the potassium ion and ammonium nitrogen ion positions are very similar. Differences arise in one of the nitrogen sites and one potassium ion site in the large channel. In the refined structure, besides the potassium site around the organic ligands (K3 in Figure 4.29), there are extra potassium (K1 in Figure 4.29) and nitrogen ion sites (N1 in Figure 4.29) in the large channel. The structure obtained from the second Rietveld refinement attempt is very similar to the single crystal structure. The only difference is the arrangement of the potassium ion and the ammonium ion sites inside the smaller channel, which vary slightly. The single crystal diffraction method can provide more detailed structure information but this is limited to only the examined crystal. For a structure with many potentially variable atom sites such as the exchanged metal sites and free water sites of our ion-exchanged material, the single crystal structure may not be entirely representative. By contrast, in the powder XRD method, many tiny crystals are examined to reveal general structure information for the material. When the single crystal structure of K^+ -BIRM-1 was refined against the powder XRD pattern (Figure 4.30 and 4.31), the potassium site positions and ammonium nitrogen site positions in the smaller pore moved slightly to positions similar to those originally obtained in the second Rietveld analysis. These small differences may reflect variations among crystals, but also confirm the validity of the refined structure.

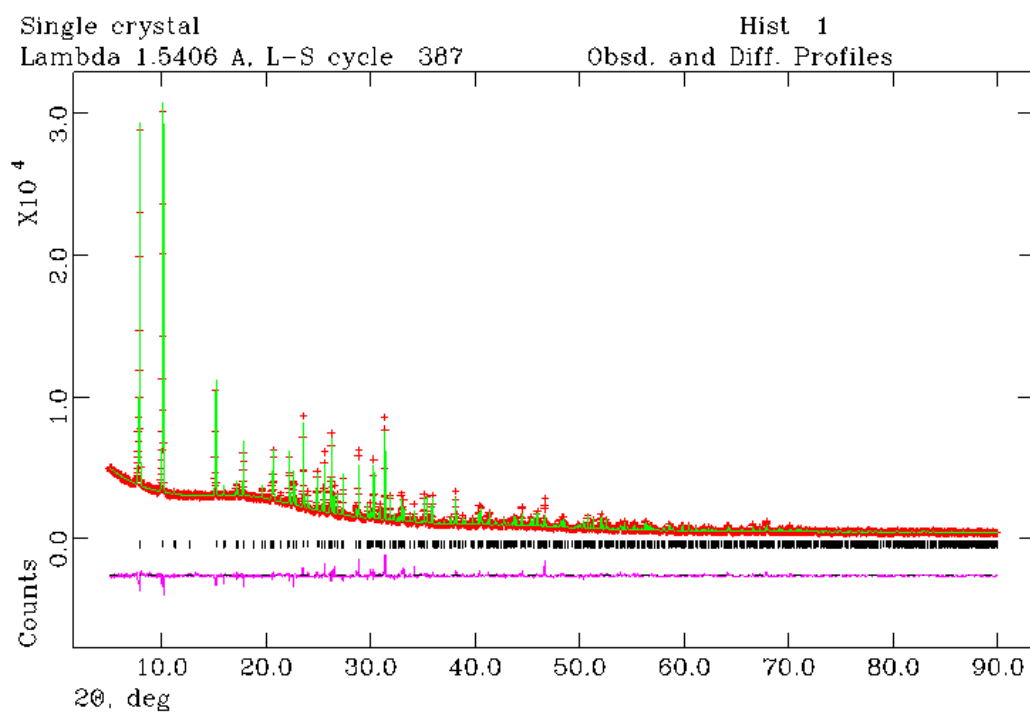


Fig. 4.30 Final observed (crosses), calculated (solid line), difference (below) and reflection positions (middle) for the final Rietveld refinement of K⁺-BIRM-1, using the single crystal structure model, against lab powder XRD data; $\chi^2 = 4.318$, $R_{wp} = 5.45\%$ and $R_p = 3.72\%$.

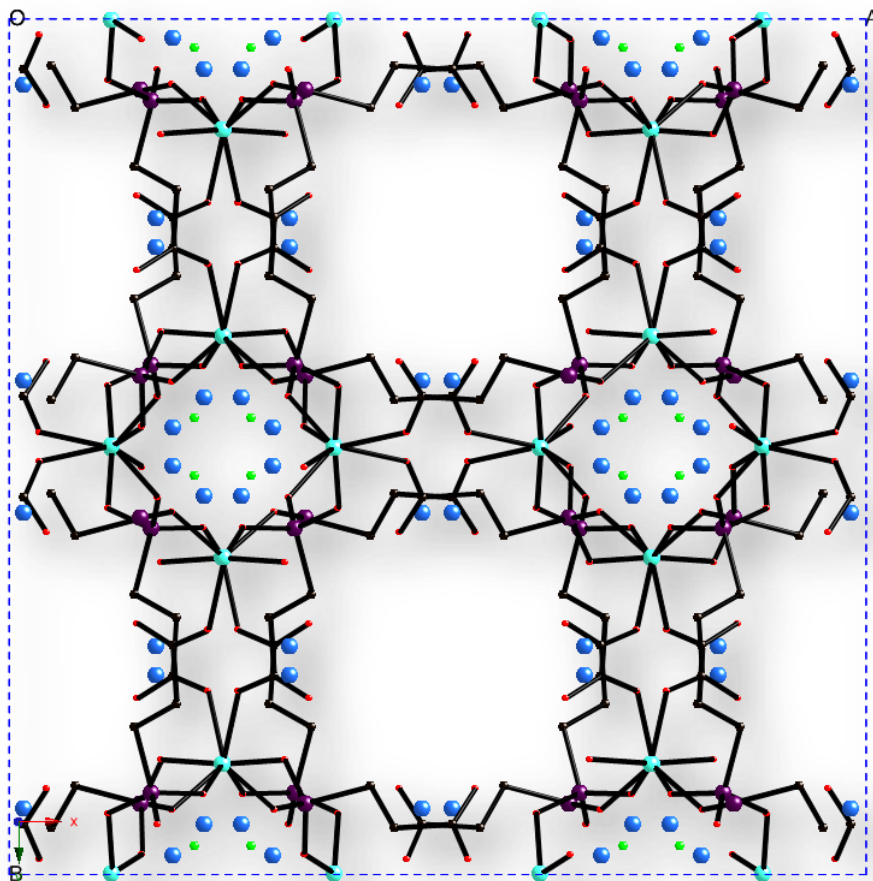


Fig. 4.31 Refined structure of K^+ -BIRM-1, using the single crystal structure model, against lab powder XRD data, viewed along the z -axis; hydrogen atoms have been omitted for clarity; colour scheme: Zn – turquoise, P – purple, K – blue, N – green, O – red and C – black.

4.6.4 Na^+ -BIRM-1 Structure Determination

For the sodium-exchanged product, due to the significant change in the XRD pattern, the crystal structure of BIRM-1 was not considered as an appropriate structure model to start a Rietveld refinement. Refinement with only a framework structure from the cobalt-exchanged product (detailed in Chapter 5) was initially carried out. However, due to the significant difference of the space group between these two exchanged products ($Pnma$ for Na^+ -BIRM-1 and $Ibca$ for Co^{2+} -BIRM-1), structure determination was not pursued. Constructing a suitable structure model for the refinement against

laboratory XRD data would be seriously compromised by problems in distinguishing Na, O, and N atoms, which all have similar scattering power, and was considered likely to be too unreliable.

4.7 Conclusion

The ion exchange properties of BIRM-1 have been studied and analyzed in detail by powder XRD, SEM/EDX, TGA and FTIR. These demonstrated that lithium, sodium and potassium ion-exchanged products had been successfully achieved with the structure maintained, suggesting that further ion exchange with other metal cations may be possible. The use of Rietveld refinement against laboratory powder X-ray diffraction data has been demonstrated in the determination of the K^+ -BIRM-1 structure. Although laboratory X-ray data is not ideal for solving a structure containing many light atoms, this refined structure is quite close to the single crystal structure obtained more recently. Due to the weak X-ray scattering power of the lithium ion, and the lack of a good structural model for Na^+ -BIRM-1, the structures of these two exchanged samples were not determined.

Chapter 5

Ion Exchange of BIRM-1 with Divalent Cations: Cobalt(II), Manganese(II) and Magnesium(II)

5.1 Introduction

Having successfully exchanged several alkali metal ions into the structure of BIRM-1, investigations into divalent cations were undertaken in this chapter. As Hoang *et al.*^{153, 154} and Hamaed *et al.*¹⁵⁵ reported, the transition metals in low oxidation states could function as ideal binding sites for molecular hydrogen through the Kubas interaction¹⁵⁶, thus ion exchange experiments with manganese (II) and cobalt (II) were studied. Further ion exchange attempts with another divalent cation, magnesium, were carried out as well for comparison. The spectroscopic, thermal properties and structure of these exchanged products were investigated.

5.2 Experimental

5.2.1 Ion Exchange with Cobalt(II), Magnesium and Manganese(II) Ions

Ion exchange experiments on BIRM-1 powders were performed on unground crystals by conventional methods. 1×10^{-3} mol BIRM-1 was mixed with 50 ml of 0.1 M cobalt, magnesium and manganese acetate aqueous solutions, respectively. After

stirring for 10 minutes, the pH values of the solutions were adjusted to around 5.50 with hydrochloric acid. Then the reaction systems were sealed in a flask and very slowly stirred for 24 hours at ambient temperature. Single crystal XRD data were obtained using a Bruker APEXII CCD diffractometer at the window of a Bruker FR591 rotating anode with Mo-K α ($\lambda_{\text{Mo-K}\alpha} = 0.71073 \text{ \AA}$) radiation at 120 K, and the structures were analyzed by Dr. Louise Male.

5.3 Cobalt(II)-Exchanged BIRM-1 (Co²⁺-BIRM-1)

Ion exchange attempts with divalent ions were initially performed with cobalt(II) ions, as this transition metal could provide good metal binding sites for gas adsorption^{84,157}, and its pink color could be an obvious indication of a successful ion exchange. The hydrated radius of cobalt ion (2.95 \AA)¹⁴³ is smaller than the pore diameter (7.6 \AA).

5.3.1 Laboratory Powder XRD

After ion exchange, the colour of the crystals had changed from white to light pink. Powder XRD patterns (Figure 5.1) indicated that the structure remained in highly crystalline form after the treatment, and showed clear differences from the XRD pattern of BIRM-1, analogous to those observed in Na⁺-BIRM-1.

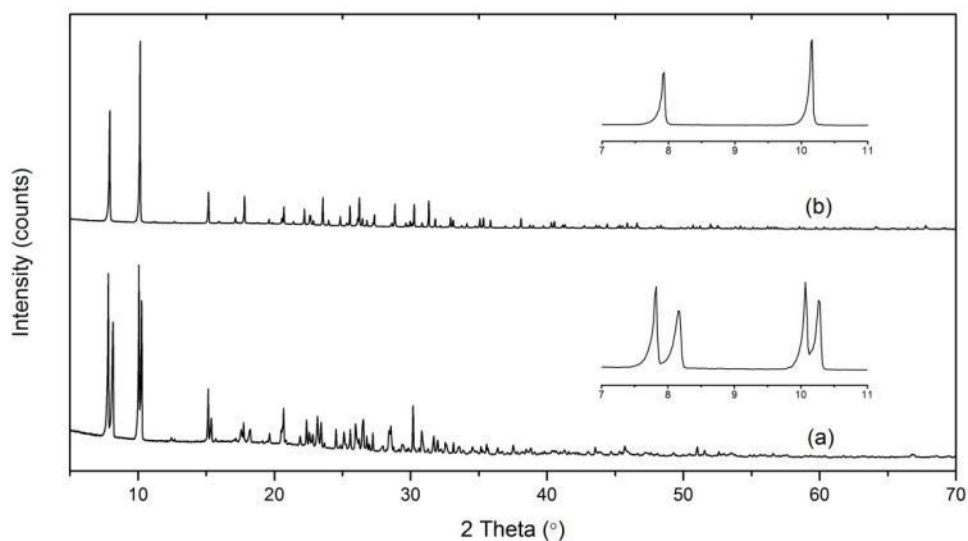


Fig. 5.1 (a) Powder XRD patterns of Co^{2+} -BIRM-1 and (b) BIRM-1, illustrating the peak splitting observed.

Peaks broadened and split in the same place and also extra peaks appeared after ion exchange, for which there were several possible explanations. Samples could contain both BIRM-1 and a new cobalt-exchanged phase which had different lattice parameters. Alternatively, an exchanged compound may have been formed, in which a small structural distortion occurred resulting in a lowering of symmetry that led to the splitting of peaks in the XRD patterns. A reduction in symmetry was then proved by indexing the powder X-ray diffraction pattern (Table 5.1).

Table 5.1 Lattice parameters of BIRM-1 and Co^{2+} -BIRM-1.

	BIRM-1	Co^{2+} -BIRM-1
Crystal System	Tetragonal	Orthorhombic
Space Group	$I4_1/acd$	$Ibca$
$a/\text{\AA}$	22.302(2)	18.1894(4)
$b/\text{\AA}$	22.302	21.5294(6)
$c/\text{\AA}$	17.738(1)	22.4930(5)
Volume/ \AA^3	8822.6(1)	8812.8(4)

5.3.2 SEM and EDX

The morphology of Co^{2+} -BIRM-1 was examined by SEM showing the phase to consist of needle-like crystals but crushed into small pieces after the ion exchange (Figure 5.2). The presence of the cobalt ion was investigated by EDX (Table 5.2). The results revealed that cobalt ions were contained in the examined crystals, indicating a successful ion exchange. The average molar ratios of Zn:P:Co calculated were 1:1:0.29, in good agreement with the theoretical value molar ratio value of Zn:P, and the degree of ion exchange rate therefore was estimated to be 60% as one cobalt ion replaces two ammonium ions.

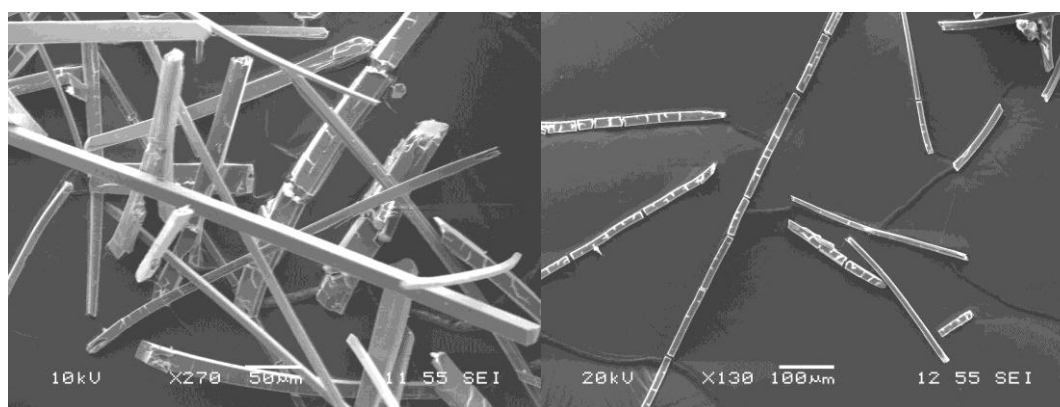


Fig.5.2 SEM images of Co^{2+} -BIRM-1.

Table 5.2 EDX results for Co^{2+} -BIRM-1 crystals.

	Zn	P	Co
	17.20	17.78	5.63
	17.57	18.62	4.03
	23.53	22.84	5.78
	18.05	18.39	4.09
	22.78	22.10	4.52
	21.57	21.21	5.38
	22.43	20.37	5.30
	20.04	19.65	3.51

Spectrum (Atomic %)	18.03	18.07	7.62
	19.33	20.05	6.35
	16.52	17.83	9.47
	18.91	17.22	8.54
	22.69	21.60	3.95
	20.13	17.20	5.73
	18.28	16.96	4.78
	18.87	17.15	4.79
	19.25	17.95	5.48
Std. Deviation	2.16	1.91	1.64
Mean	19.72	19.12	5.59
Molar Ratio	1.03	1	0.29

5.3.3 Thermal Stability

As is apparent from the TG curve (Figure 5.3), the cobalt-exchanged product revealed a total weight loss of 40% up to 900 °C. In the DTA trace, the endothermic peak at 120 °C was attributable to loss of water and emission of small amounts of NH₃ (Figure 5.4). Above this temperature the material kept on losing weight gradually and did not show very clear weight loss steps. At about 500 °C, one sharp and two shoulder exothermic peaks were observed which indicated collapse of the structure. Release of NH₃, H₂O and CO₂ were then detected by mass spectrometry. Eventually the residue reacted further with O₂, which generated a quite broad exothermic peak at 660 °C as a result of the CO₂ release step.

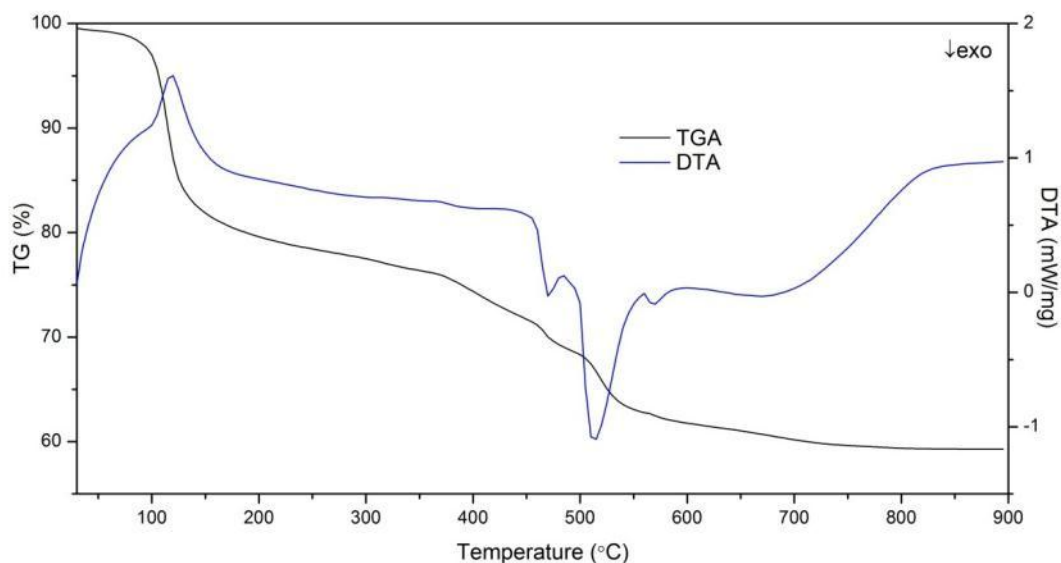


Fig. 5.3 TGA (black trace) and DTA (blue trace) of Co^{2+} -BIRM-1.

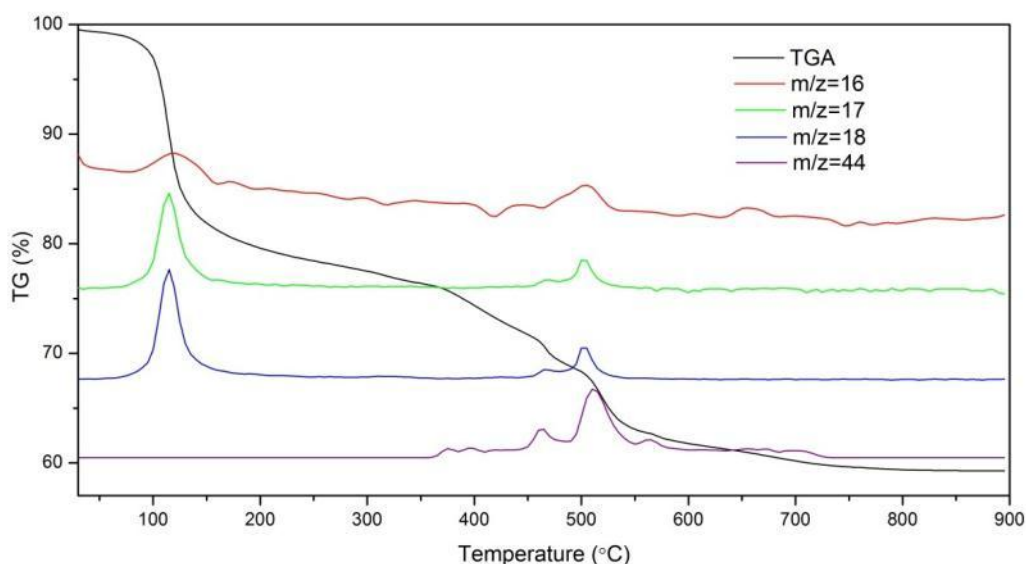


Fig. 5.4 TGA (black trace) of Co^{2+} -BIRM-1, and mass analyses of $m/z = 16$ (red trace), $m/z = 17$ (green trace), $m/z = 18$ (blue trace) and $m/z = 44$ (purple trace).

After heating, the material left in the crucible was identified by powder XRD as a mixture of $\text{Zn}_2\text{Co}(\text{PO}_4)_2$ ¹⁵⁸ with a small amount of $\text{Zn}_2\text{P}_2\text{O}_7$ ¹⁵⁹ (Table 5.3). Quantitative phase analysis (Figure 5.5) was carried out through Rietveld refinement of the structures in GSAS^{126, 127} suggesting the molar ratio of Zn:P:Co was about

1:1:0.42. As the bump was again observed at lower two-theta angles from the XRD pattern, this inconsistency compared with EDX results could be therefore explained by the presence of poorly crystalline material.

Table 5.3 Quantitative phase analysis results.

Phase	Weight Percentage (%)
$\text{Zn}_2\text{Co}(\text{PO}_4)_2$	86.32(5)
$\text{Zn}_2\text{P}_2\text{O}_7$	13.7(2)

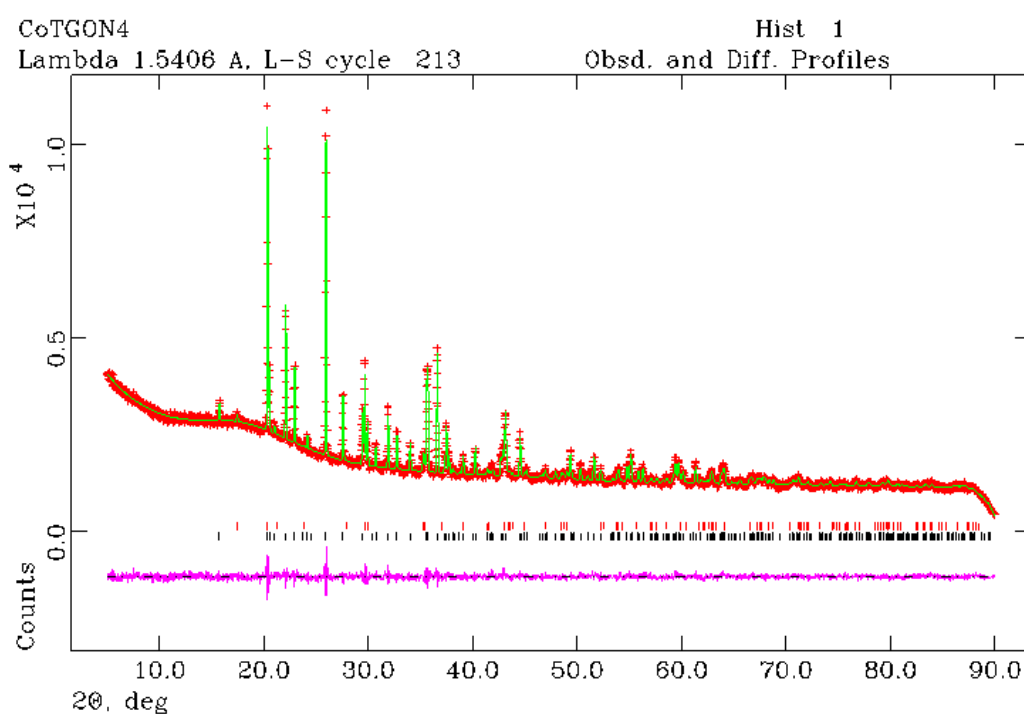


Fig. 5.5 Final observed (crosses), calculated (solid line), difference (below) and reflection positions [red top lines indicate peaks from $\text{Zn}_2\text{Co}(\text{PO}_4)_2$ and black lower lines indicate peaks from $\text{Zn}_2\text{P}_2\text{O}_7$] for the final Rietveld refinements against powder XRD data for Co^{2+} -BIRM-1 TGA products, $\chi^2 = 1.698$, $R_{\text{wp}} = 3.04\%$, $R_{\text{p}} = 2.31\%$.

5.3.4 Fourier Transform Infrared Spectroscopy

The FTIR spectrum for Co^{2+} -BIRM-1 was very much the same as seen for the alkali

metal-exchanged products and not very different from that of BIRM-1 (Table 5.4). The IR spectrum of BIRM-1 (Figure 5.6a) exhibited a very broad and overlapped peak at around 3200 and 3050 cm^{-1} due to stretching vibrations of O–H from the coordinated water molecules and N–H stretches, but the broad band occurring at around 3050 cm^{-1} almost vanished after ion exchange, which can be attributed to the decrease in N–H vibrations caused by the removal of the exchangeable ammonium cations (Figure 5.6b). The IR data thus give further indications that structure was sustained after ion exchange and that cobalt ions were introduced into the porous structure by exchanging with ammonium cations.

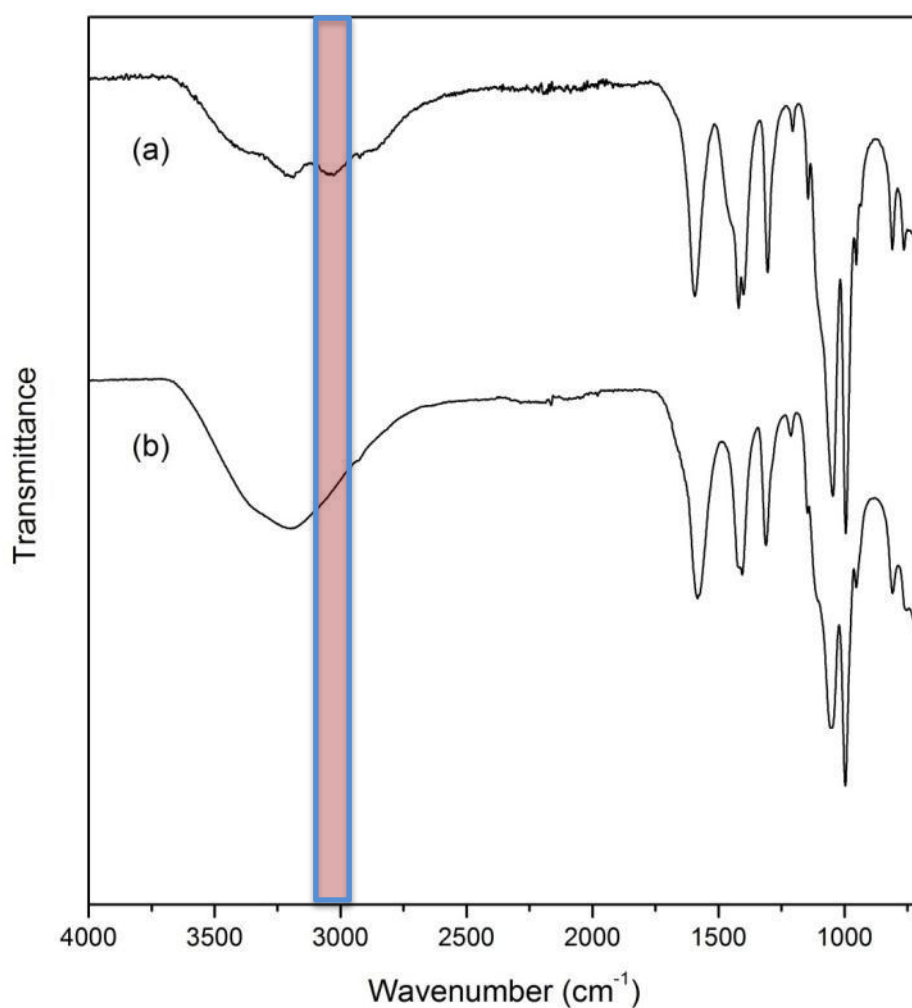


Fig. 5.6 FTIR spectra for (a) BIRM-1 and (b) Co^{2+} -BIRM-1; the pink area illustrates the peak

disappearing after ion exchange.

Table 5.4 Observed FTIR peaks and assignments for Co²⁺-BIRM-1.

Peak (cm ⁻¹)	Assignment
3200	O–H (H ₂ O)
1583	COO ⁻ (sym)
1312	C–O
1406	COO ⁻ (asym)
1422	P–C
1150–950	P–O

5.4 Manganese (II)-Exchanged BIRM-1 (Mn²⁺-BIRM-1)

Taking the findings of Hoang^{153, 154} and Hamaed¹⁵⁵ on the possibility of using Kubas ions as a binding site for hydrogen adsorption into account, exchange of an earlier transition series element, manganese, into BIRM-1 was attempted. The hydrated radius of the manganese(II) ion is 2.86 Å¹⁴³, again much smaller than the pore size of BIRM-1.

5.4.1 Laboratory Powder XRD

The powder XRD pattern again showed clear alterations after manganese-ion exchange, compared to the XRD pattern of BIRM-1 (Figure 5.7). Peaks appeared broadened and split showing evidence of a lower symmetry phase, which was similar to the sodium and cobalt-exchanged products. However, the extra peak observed at around 9 ° was consistent with the sodium-exchanged phase but not the cobalt phase representing a small structural difference, which was then verified by indexing the pattern (Table 5.5) in space group *Pban*.

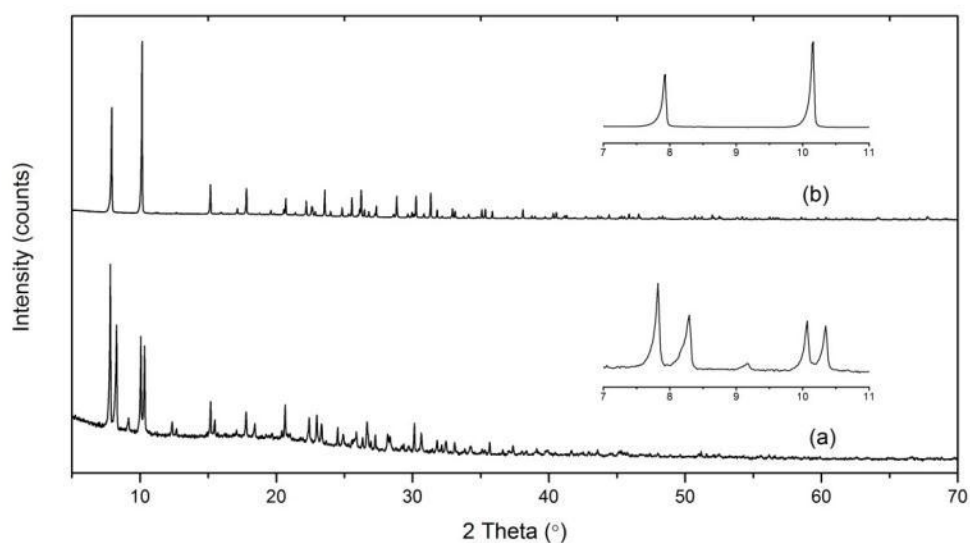


Fig. 5.7 (a) Powder XRD patterns of Mn^{2+} -BIRM-1 and (b) BIRM-1, illustrating the peak splitting and extra peak observed.

Table 5.5 Lattice parameters of BIRM-1 and Mn^{2+} -BIRM-1.

	BIRM-1	Mn^{2+} -BIRM-1
Crystal System	Tetragonal	Orthorhombic
Space Group	$I4_1/acd$	$Pbam$
$a/\text{\AA}$	22.302(2)	22.5522(5)
$b/\text{\AA}$	22.302	22.2562(4)
$c/\text{\AA}$	17.738(1)	18.4730(4)
Volume/ \AA^3	8822.6(1)	8855.5(3)

5.4.2 SEM and EDX

SEM with EDX were employed to scan the manganese-exchanged crystals to estimate the degree of ion exchange. The results revealed that ion exchange was successfully achieved in the needle-shaped crystals (Figure 5.8). The average molar ratio of Zn: P: Mn was 1.03: 1: 0.33 (Table 5.6). The molar ratio of Zn to P was very close to the theoretical value (1: 1), and the average molar ratio of Mn of Zn/P was about 0.33: 1. So the degree of ion exchange could be roughly estimated to be 66%.

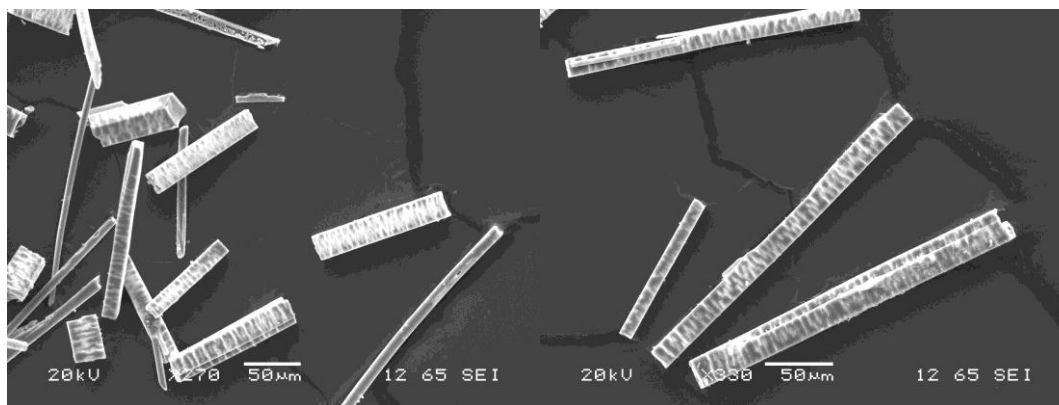


Fig. 5.8 Selected SEM images for Mn²⁺-BIRM-1.

Table 5.6 EDX results for Mn²⁺-BIRM-1 crystals.

	Zn	P	Mn
Spectrum (Atomic %)	17.15	15.73	4.57
	23.01	20.10	7.73
	15.51	13.86	4.41
	14.54	16.57	5.01
	18.47	19.38	5.66
	20.11	18.72	5.82
	23.07	21.66	6.50
	21.14	20.92	7.12
	13.60	15.90	5.04
	12.67	14.45	4.43
	19.82	21.02	7.12
	20.38	22.08	7.21
	24.83	23.84	8.14
	21.41	21.41	7.00
	24.29	23.23	8.52
	17.24	18.90	5.99
	21.34	21.32	7.20
Std. Deviation	3.60	2.96	1.28
Mean	19.33	19.36	6.32
Molar Ratio	1	1	0.33

5.4.3 Thermal Stability

TGA of the manganese-exchanged product disclosed a total weight loss of about 39.2% at 900 °C (Figure 5.9). From the DTA curve, an endothermic peak appeared at 140 °C,

which can be attributed to the removal of water in the structure accompanied by the release of a small amount of residual ammonia (Figure 5.10). This process began almost as soon as heating was initiated and occurred in one big weight loss step. At 510 °C, a sharp exothermic peak appeared in the DTA curve, which indicated the collapse of the structure and decomposition of the organic ligand groups.

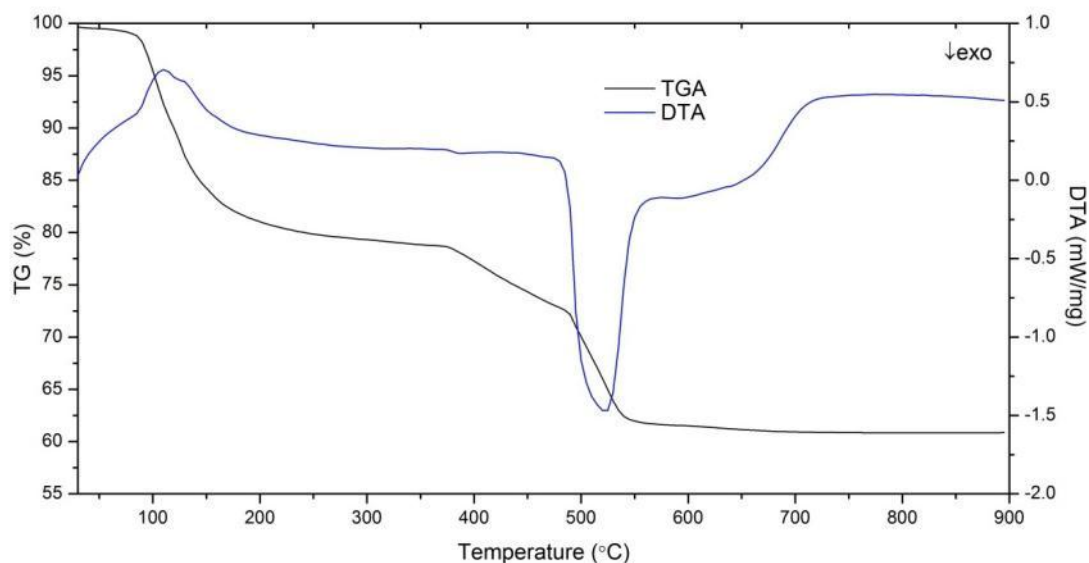


Fig. 5.9 TGA (black trace) and DTA (blue trace) of Mn^{2+} -BIRM-1.

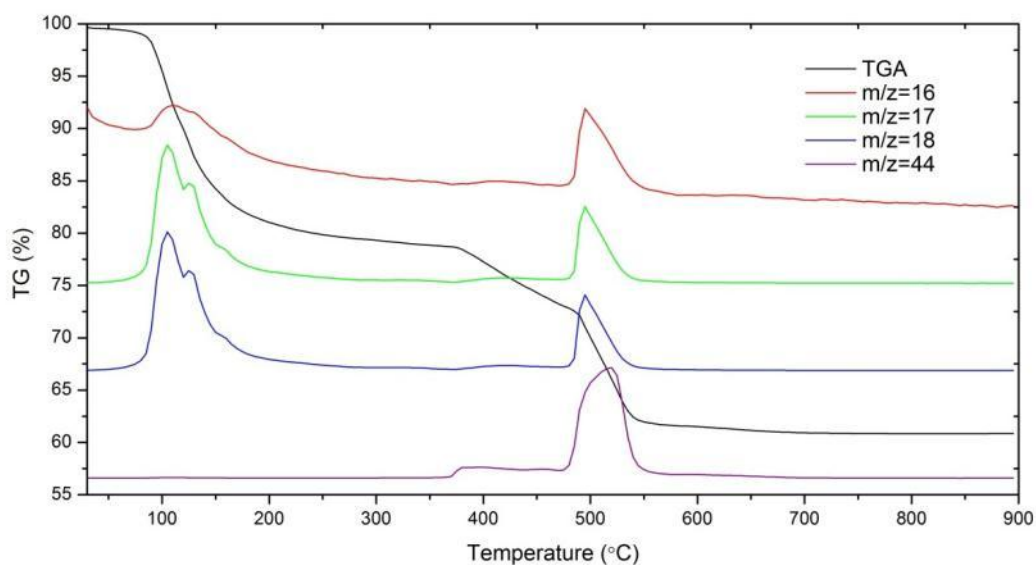


Fig. 5.10 TGA (black trace) of Mn^{2+} -BIRM-1, and mass analyses of $m/z = 16$ (red trace), $m/z = 17$ (green trace), $m/z = 18$ (blue trace) and $m/z = 44$ (purple trace).

The residual solid after heating was then examined by powder XRD. It has been identified as a mixture of $\text{Zn}_{2.25}\text{Mn}_{0.75}(\text{PO}_4)_2$ ¹⁶⁰ and $\text{Zn}_2\text{P}_2\text{O}_7$ ¹⁵⁹ (Table 5.7). Quantitative phase analysis revealed the molar ratio of Zn: P: Mn was 1:0.9:0.29 which varied slightly from the EDX result (Figure 5.11). Note the background suggests amorphous material was also present. The presence of manganese ions in the final TGA products may be taken as good evidence that manganese ions were exchanged into the structure of BIRM-1.

Table 5.7 Quantitative phase analysis results.

Phase	Weight Percentage (%)
$\text{Zn}_{2.25}\text{Mn}_{0.75}(\text{PO}_4)_2$	88.11(6)
$\text{Zn}_2\text{P}_2\text{O}_7$	11.9(1)

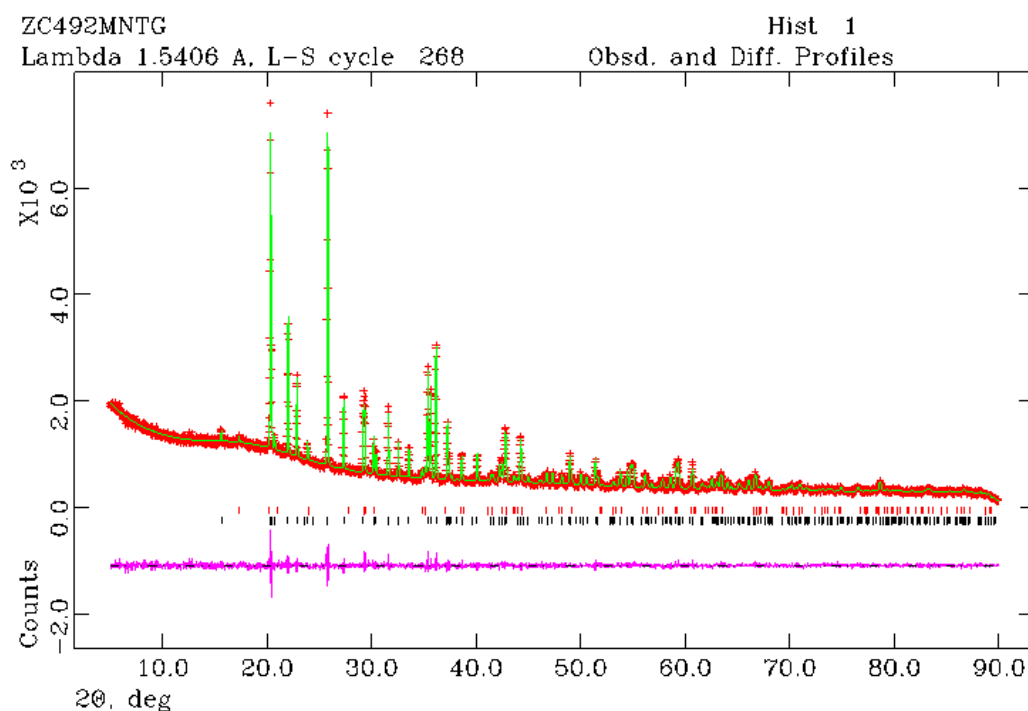


Fig. 5.11 Final observed (crosses), calculated (solid line), difference (below) and reflection positions [red top lines indicate peaks from $\text{Zn}_{2.25}\text{Mn}_{0.75}(\text{PO}_4)_2$ and black lower lines indicate peaks from $\text{Zn}_2\text{P}_2\text{O}_7$] for the final Rietveld refinements against powder XRD data for manganese ion-exchanged BIRM-1 TGA products, $\chi^2 = 1.435$, $R_{\text{wp}} = 4.53\%$, $R_p = 3.4\%$.

5.4.4 Fourier Transform Infrared Spectroscopy

The FTIR spectrum of Mn^{2+} -BIRM-1 contained clear information regarding the nature of the zinc carboxyethylphosphonate framework and was akin to those of the previous ion-exchanged products (Table 5.8). The main feature was again that the peak at about 3050 cm^{-1} arising from the stretching mode of the N–H bond which disappeared after exchange with manganese ions (Figure 5.12b), representing a decrease in the amount of ammonium ions inside the structure after ion-exchange.

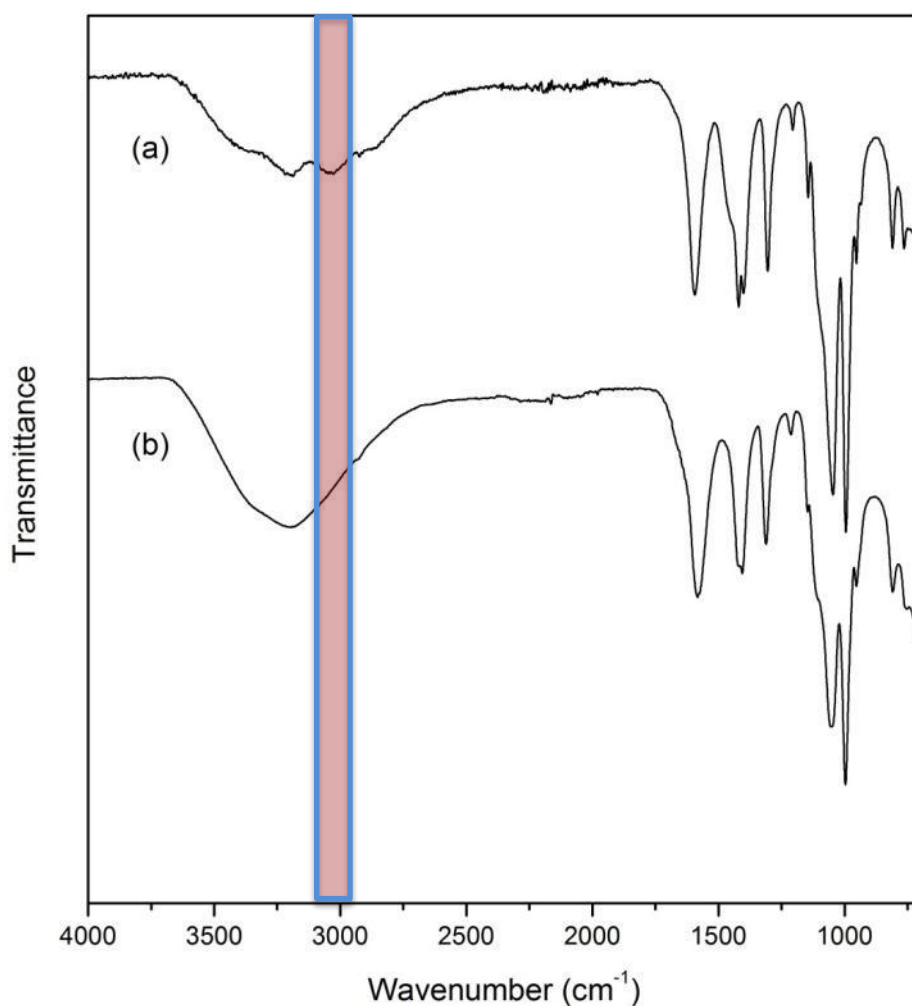


Fig. 5.12 FTIR spectra for (a) BIRM-1 and (b) Mn^{2+} -BIRM-1; the pink area illustrates the peak disappearing after ion exchange.

Table 5.8 Observed FTIR peaks and assignments for Mn²⁺-BIRM-1.

Peak (cm ⁻¹)	Assignment
3200	O–H (H ₂ O)
1587	COO ⁻ (sym)
1311	C–O
1403	COO ⁻ (asym)
1420	P–C
1150–950	P–O

5.5 Magnesium-Exchanged BIRM-1 (Mg²⁺-BIRM-1)

Following the success of the cobalt and manganese ion-exchange experiments, attempts were then carried out with magnesium ions. The hydrated radius of the magnesium ion is 2.99 Å¹⁴³, smaller than the pore size of BIRM-1.

5.5.1 Laboratory Powder XRD

The powder XRD pattern (Figure 5.13) confirmed the structure was maintained intact with good crystallinity after ion exchange. Peak splittings were again observed after magnesium ion exchange indicating a lower symmetry structure was obtained, similar to the XRD patterns of the cobalt- and manganese-exchanged products; this was verified by the indexing results (Table 5.9).

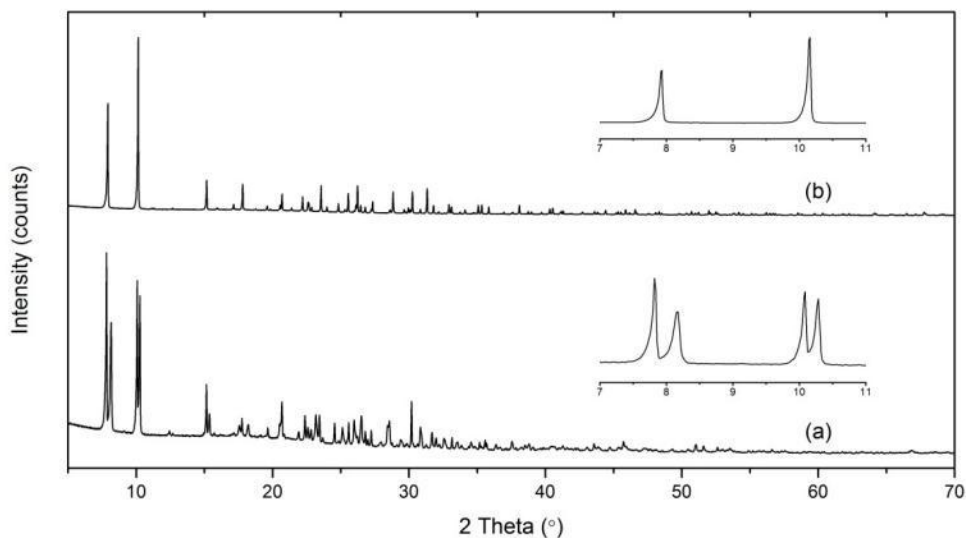


Fig. 5.13 (a) Powder XRD patterns of Mg^{2+} -BIRM-1 and (b) BIRM-1, illustrating the peak splitting observed.

Table 5.9 Lattice parameters of BIRM-1 and Mg^{2+} -BIRM-1.

	BIRM-1	Mg^{2+} -BIRM-1
Crystal System	Tetragonal	Orthorhombic
Space Group	$I4_1/acd$	$Ibca$
$a/\text{\AA}$	22.302(2)	18.1859(5)
$b/\text{\AA}$	22.302	21.5355(7)
$c/\text{\AA}$	17.738(1)	22.4777(6)
Volume/ \AA^3	8822.6(1)	8803.2(4)

5.5.2 SEM and EDX

SEM images showed the morphology of the exchanged products was maintained well after ion exchange (Figure 5.14), although slight damage on the surface of the needle-shaped crystals was apparent. The presence of the magnesium ions inside the examined crystals was then proved by EDX (Table 5.10), showing magnesium ions were contained inside the examined crystals. The average molar ratio of Zn:P:Mg was calculated to be 1:1:0.16, which was in good accordance with the theoretical Zn:P

value (1:1). Therefore the degree of ion exchange was estimated to be around 32%. This EDX result showed evidence for a successful ion exchange, albeit to a smaller degree than had been seen for the other divalent cations.

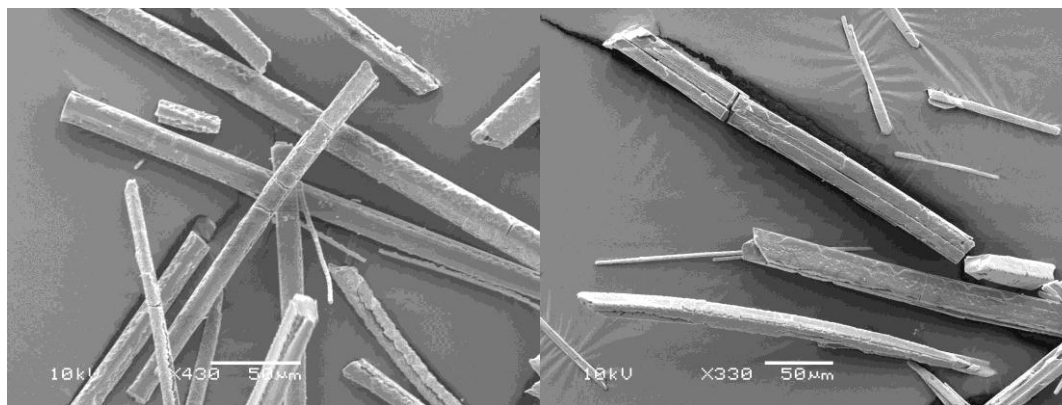


Fig 5.14 SEM images for Mg^{2+} -BIRM-1.

Table 5.10 EDX results for Mg^{2+} -BIRM-1 crystals.

	Zn	P	Mg
Spectrum (Atomic %)	24.72	22.25	2.41
	25.46	23.50	3.57
	25.55	24.32	3.21
	27.11	23.78	3.11
	19.27	21.21	3.33
	19.15	20.61	3.33
	20.05	22.14	3.77
	19.05	20.21	2.95
	17.05	17.66	3.66
	20.45	21.27	3.85
	21.14	22.19	3.14
	21.61	23.17	3.78
	22.16	19.91	3.65
	18.37	19.37	3.52
	19.92	20.34	3.29
	22.82	21.00	3.53
Std. Deviation	2.83	1.72	0.36
Mean	21.49	21.43	3.38
Molar Ratio	1	1	0.16

5.5.3 Thermal Stability

TGA of Mg^{2+} -BIRM-1 gave similar results to those of the cobalt and manganese-exchanged products. The magnesium-exchanged product showed a nearly continuous mass loss up to 600 °C in roughly two steps (Figure 5.15). DTA and mass spectrum curves suggest that the weight loss for the first step at about 140 °C corresponds to the removal of water as well as some ammonia from residual NH_4^+ ions (Figure 5.16). The appearance of the broad exothermic peak at about 530 °C, marked the decomposition of the coordination network and release of NH_3 , CO_2 and H_2O . After that there was almost no mass loss observed and the final weight loss was found to be 43.9%.

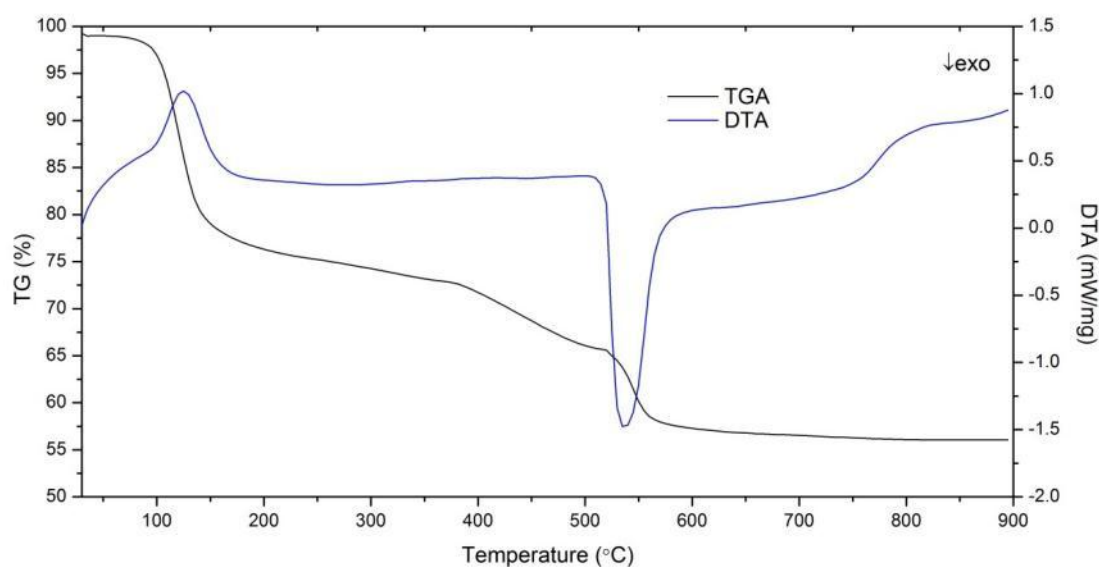


Fig. 5.15 TGA (black trace) and DTA (blue trace) of Mg^{2+} -BIRM-1.

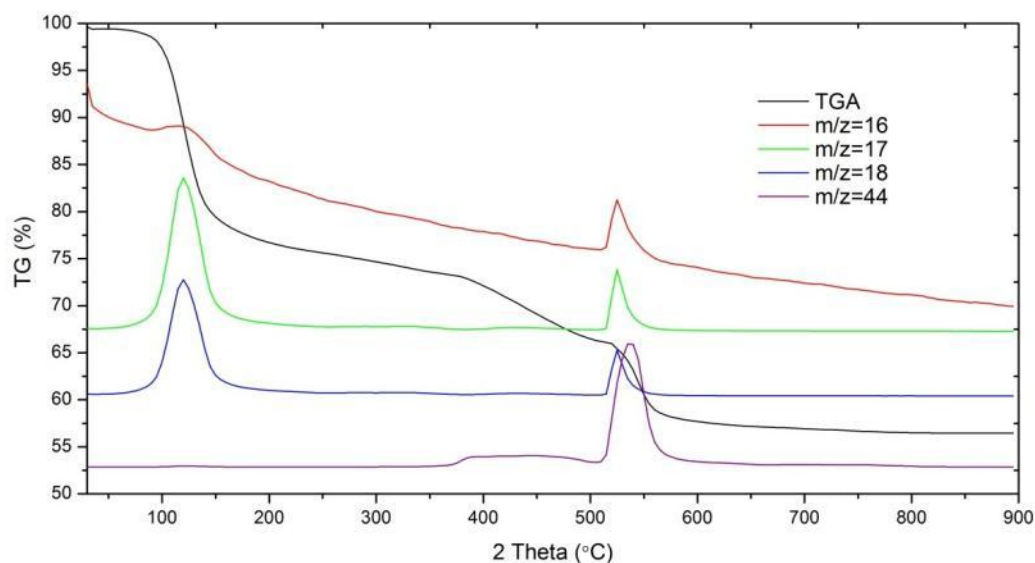


Fig. 5.16 TGA (black trace) of Mg^{2+} -BIRM-1, and mass analyses of $m/z = 16$ (red trace), $m/z = 17$ (green trace), $m/z = 18$ (blue trace) and $m/z = 44$ (purple trace).

The solid residue after heating was identified by powder XRD as a mixture of $\text{Zn}_2\text{Mg}(\text{PO}_4)_2$ ¹⁶¹ and two different $\text{Zn}_2\text{P}_2\text{O}_7$ phases^{159, 162} (Table 5.11 and Figure 5.17). Quantitative phase analysis found out that the molar ratio of Zn:P:Mg was 1:1:0.4. Again this magnesium content was inconsistent with the results obtained from EDX and can probably be assigned by the existence of a poorly crystalline phase mixed within the TGA residue.

Table 5.11 Quantitative phase analysis result.

Phase	Weight Percentage (%)
$\text{Zn}_2\text{Mg}(\text{PO}_4)_2$	82.11(4)
$\text{Zn}_2\text{P}_2\text{O}_7$ ¹⁶²	9.2(3)
$\text{Zn}_2\text{P}_2\text{O}_7$ ¹⁵⁹	8.7(1)

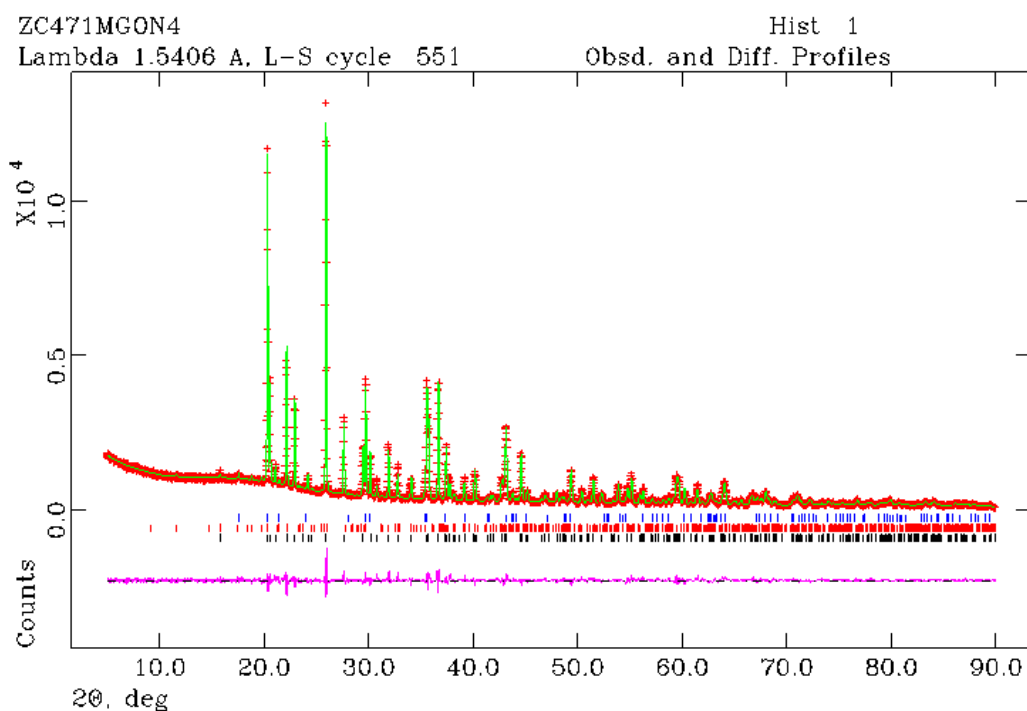


Fig. 5.17 Final observed (crosses), calculated (solid line), difference (below) and reflection positions [blue top lines indicate peaks from $\text{Zn}_2\text{Mg}(\text{PO}_4)_2$ and black/red lower lines indicate peaks from two $\text{Zn}_2\text{P}_2\text{O}_7$ phases] for the final Rietveld refinements against powder XRD data for magnesium-exchanged BIRM-1 TGA products; $\chi^2 = 2.819$, $R_{\text{wp}} = 6.90\%$, $R_p = 5.05\%$.

5.5.4 Fourier Transform Infrared Spectroscopy

FTIR spectra of Mg^{2+} -BIRM-1 again showed reduction in intensity of the N–H stretch vibrations occurring at around 3050 cm^{-1} after ion exchange, representing the replacement of ammonium ions by magnesium ion-exchange (Figure 5.18). The rest of the IR spectrum was qualitatively comparable to that of BIRM-1 (Table 5.12). This provides additional evidence for magnesium ion exchange.

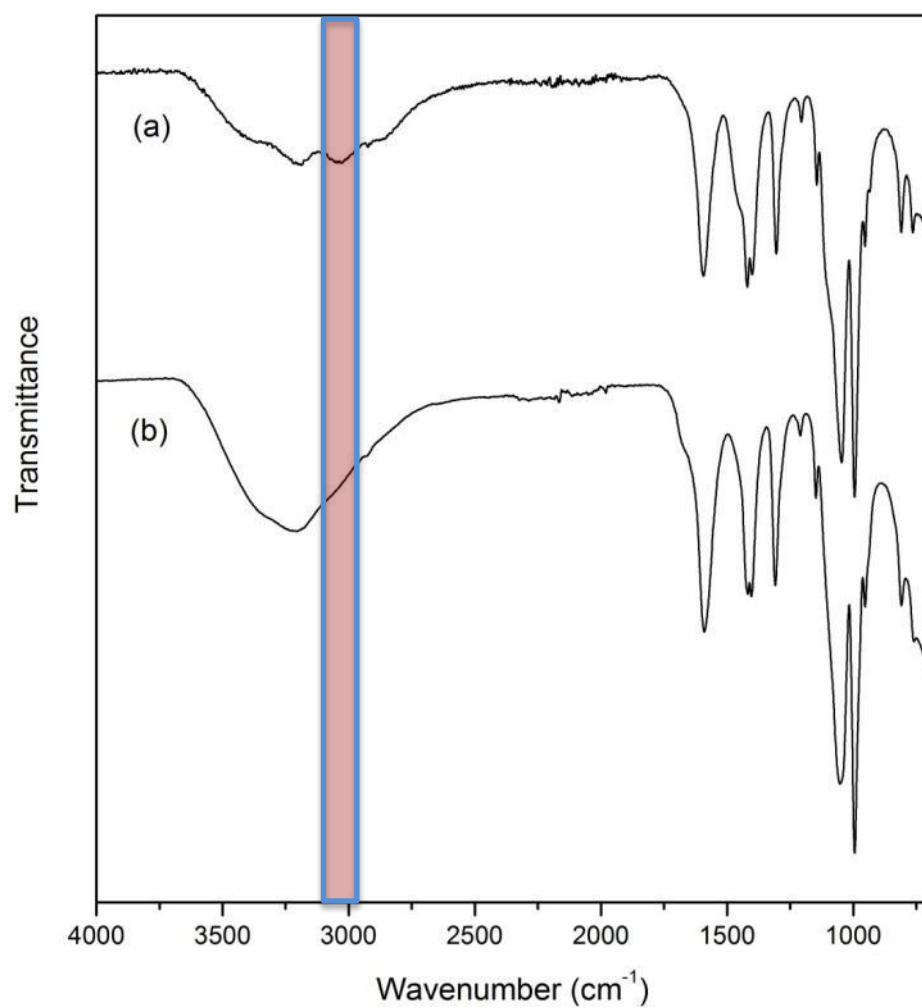


Fig. 5.18 FTIR spectra for (a) BIRM-1 and (b) Mg²⁺-BIRM-1; the pink area illustrates the peak disappearing after ion exchange.

Table 5.12 Observed FTIR peaks and assignments for Mg²⁺-BIRM-1.

Infrared shift	Assignment
3200	O-H (H ₂ O)
1590	COO ⁻ (sym)
1309	C-O
1404	COO ⁻ (asym)
1418	P-C
1150–950	P-O

5.6 Structure Determination of Co²⁺-BIRM-1

5.6.1 Structure Determination by Single Crystal X-ray Diffraction

An attempt to determine the structure of Co²⁺-BIRM-1 was made by single crystal XRD in early stages of this project (see Appendix 5 for full structure details). Although the spectroscopic evidence suggested the existence of cobalt ions in the structure, it was not possible to determine precisely atom types and refine the positions inside the channels, as the positions of water oxygen atoms, ammonium nitrogen atoms as well as the cobalt ions were very highly disordered. So only the zinc carboxyethylphosphonate network of the structure was successfully refined (Figure 5.19). Powder diffraction data indicated that the crystal system was orthorhombic rather than tetragonal, and it was concluded that it was the contents of the channels that caused this reduction in symmetry (Table 5.13). This partial structure solution nevertheless enabled us to attempt structure determination from powder XRD data.

Table 5.13 Lattice parameters of BIRM-1 and Co²⁺-BIRM-1.

	BIRM-1	Co ²⁺ -BIRM-1 [†]
Crystal System	Tetragonal	Orthorhombic
Space Group	<i>I4₁/acd</i>	<i>Ibca</i>
<i>a</i> /Å	22.302(2)	17.9820(6)
<i>b</i> /Å	22.302(2)	21.963(1)
<i>c</i> /Å	17.738(1)	22.227(1)
Volume/Å ³	8822.6(1)	8778.0(7)

[†]Data obtained from single crystal XRD structure analysis

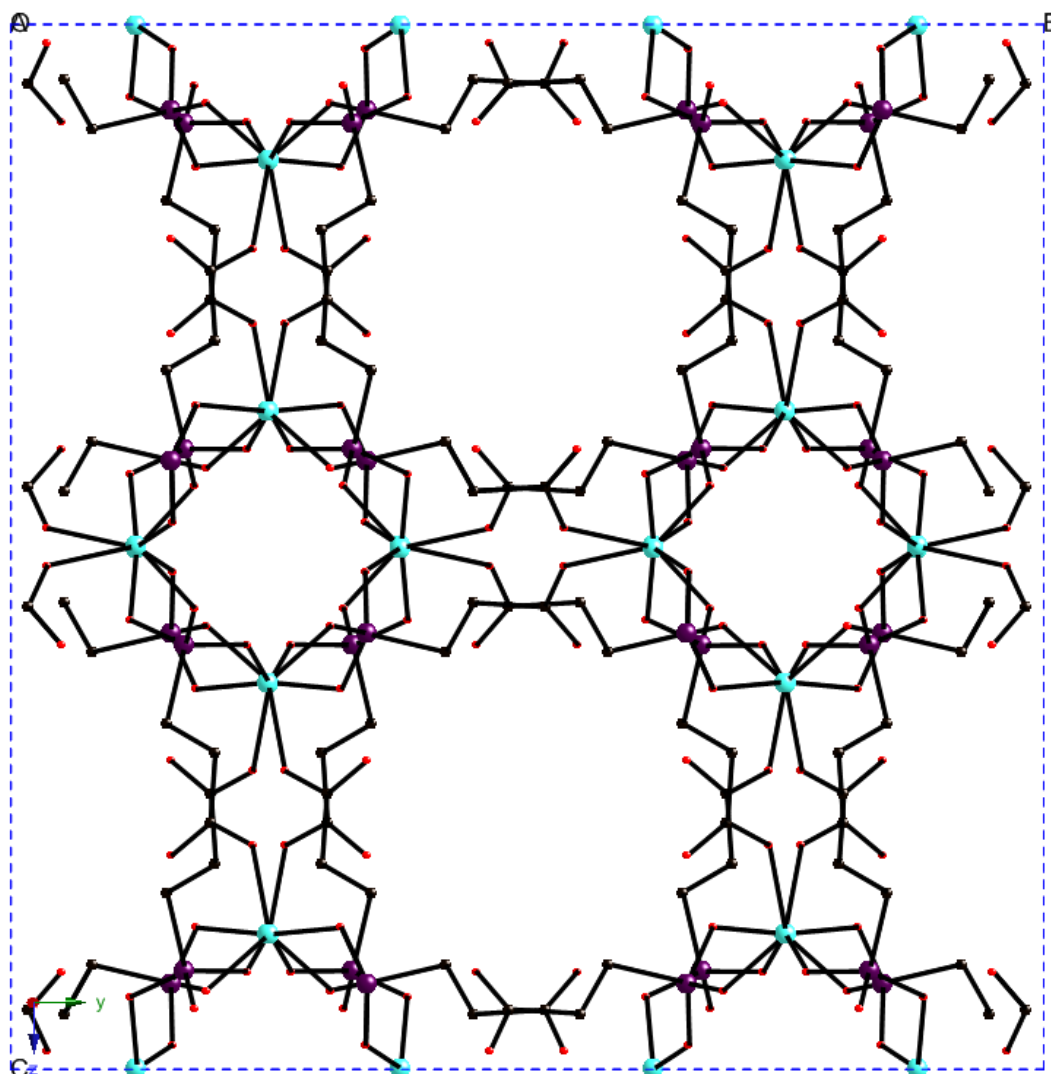


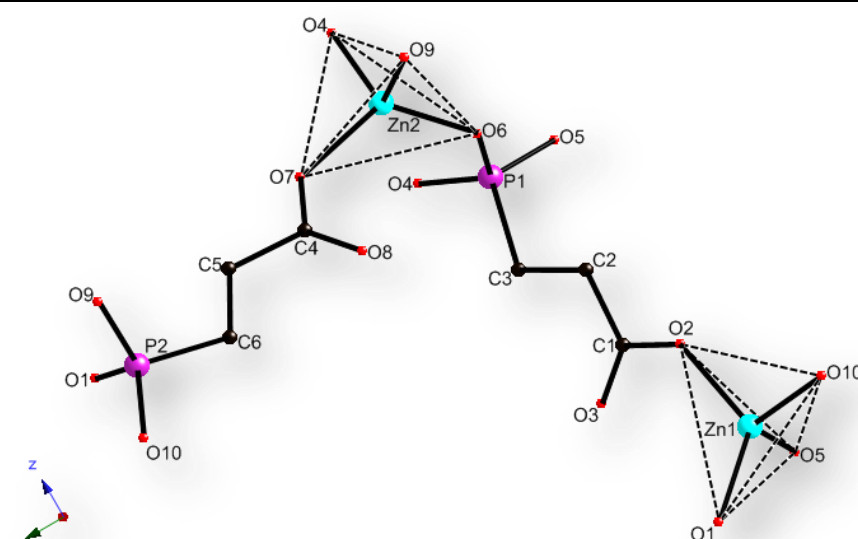
Fig. 5.19 Structural model for Co^{2+} -BIRM-1 viewed along the x -axis; hydrogen atoms have been omitted for clarity; colour scheme: Zn – turquoise, P – purple, O – red and C – black.

5.6.2 Structure Determination by Powder X-ray Diffraction

Confirmation that cobalt ions were exchanged into BIRM-1 led us attempt structural analysis through Rietveld refinement against laboratory powder X-ray diffraction data collected over 6 hours. As cobalt is a heavier element with much greater scattering power than that of oxygen and nitrogen, we attempted first to find the cobalt ion positions with the assistance of difference Fourier maps. The empty framework structure (Figure 5.19) obtained from the single crystal XRD was used as the starting

model for this refinement. The unit cell, background and profile parameters obtained from the previous Le Bail fit were imported directly into the refinement.

Table 5.14 Refinement parameters of bond/non-bonding length and bond angle restraints; colour scheme: Zn – turquoise, P – purple, O – red and C – black.



Bond	Distance (Å)	Bond	Distance (Å)	Bond Angle	Angle (°)
Zn1–O10	2.0	C4–C5	1.5	C1–O2–Zn1	124.3
Zn1–O5	2.0	C6–C5	1.5	O2–C1–O3	122.1
Zn1–O1	2.0	C6–P2	1.8	O3–C1–C2	123.1
Zn1–O2	2.0	P2–O10	1.5	O2–C1–C2	114.7
C1–O2	1.3	P2–O1	1.5	C1–C2–C3	115.6
C1–O3	1.2	P2–O9	1.5	C2–C3–P1	111.8
C1–C2	1.5	O6–O7	3.4	Zn2–O7–C4	121.0
C2–C3	1.5	O4–O7	3.0	O7–C4–O8	125.7
C3–P1	1.8	O4–O6	3.2	O7–C4–C5	112.3
O4–P1	1.5	O9–O4	3.2	O8–C4–C5	121.8
O5–P1	1.5	O9–O7	3.2	C4–C5–C6	116.2
O6–P1	1.5	O9–O6	3.1	C5–C6–P2	110.8
Zn2–O6	2.0	O10–O5	3.2		
Zn2–O9	2.0	O10–O2	2.9		
Zn2–O4	2.0	O10–O1	3.2		
Zn2–O7	2.0	O2–O1	3.4		
C4–O7	1.2	O5–O1	3.1		
C4–O8	1.2	O2–O5	3.2		

Without restraint, the framework was found to be significantly distorted after only a few cycles of least squares refinements and the light atoms drifted away from reasonable locations. Unlike the refinement for K⁺-BIRM-1, due to the absence of

significant levels of electron density inside the channels, applying only soft bond distance restraints was not adequate to maintain the structure. As a consequence soft angle restraints for the organic ligand and selected non-bonding distance restraints (Table 5.14) were added. With these restraints a reasonable framework structure could be produced with $R_{wp} = 20.69\%$ and $R_p = 16.53\%$, which was very slightly distorted compared with the structure obtained from the single crystal XRD (Figure 5.20).

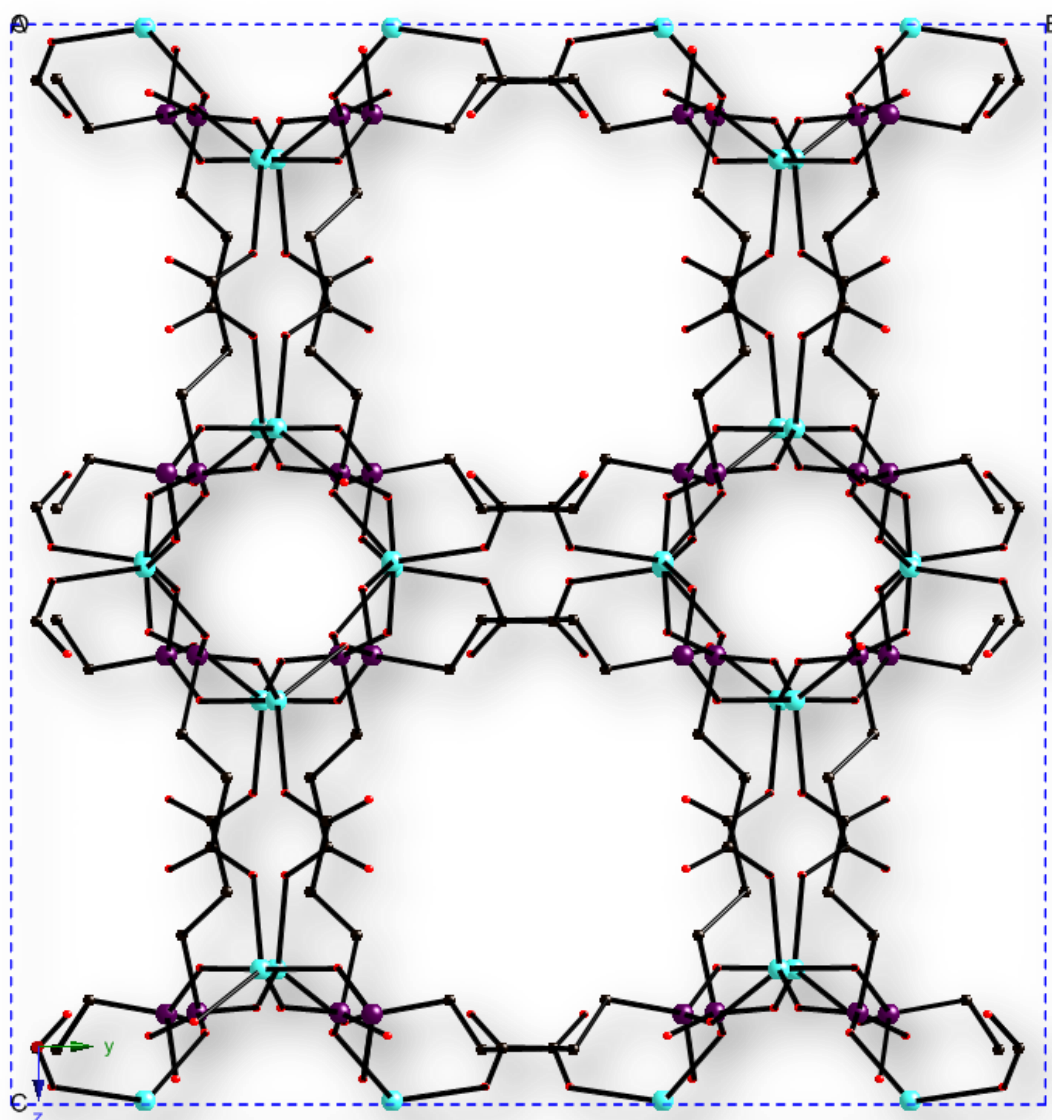


Fig. 5.20 Refined structural model for Co²⁺-BIRM-1 with soft restraints, viewed along the x -axis; hydrogen atoms have been omitted for clarity; colour scheme: Zn – turquoise, P – purple, O – red and C – black.

Difference Fourier maps were then calculated to find the positions of the extra framework atoms. As the scattering power of cobalt in X-ray diffraction is much greater than that of water oxygen or ammonium nitrogen atoms, it was hoped to find positions with higher electron density that could be distinguished from the water oxygen atoms and ammonium nitrogen atoms. Of the forty most intense electron density difference peaks, twenty positions turned out to result from misfit or noise around the framework atoms. Thus these positions were not considered as exchanged cobalt ion sites. For the rest of the positions, with the assistance of interatomic distances¹⁶³ (Table 5.15), if the distance of the position to the closest atom from the framework *e.g.* oxygen was shorter than 2 Å, it could not be a cobalt, water oxygen or ammonium nitrogen atom. If the distance was between 2 Å and 2.8 Å, then this site could probably be attributed to a missing cobalt site. If the distance was longer than 2.8 Å, any of these three types of atoms could occupy this site. With the categorization of the interatomic distance, twelve hypothetical sites were then considered for addition to the refinement (Table 5.16).

The above method is suitable to discern incorrect positions from possible real sites, but it does not definitively draw a dividing line between cobalt atoms and oxygen/nitrogen atoms. Thus in the subsequent refinement, on including these twelve sites in the model, they were all assumed to be cobalt atoms in the first instance. When the occupancies of several sites refined to negative values after only a few least squares cycles, these sites were considered more likely to be oxygen or nitrogen sites, and were included as oxygen. If the occupancies of certain of these refined to be higher than one, then these sites could be occupied only by cobalt ions. When this procedure was exhausted, the element types for eight hypothetical sites had been

allocated the remaining four being disregarded owing to negative occupancies after both refinements (Table 5.17).

Table 5.15 Interatomic distances, generated from ionic radii of each element.

Bond Type	Distance (Å)
$d_{\text{Co-O}}$	2.1
$d_{\text{Co-C}}$	0.9
$d_{\text{O-O}}$	2.7
$d_{\text{O-C}}$	1.5
$d_{\text{N-O}}$	2.8
$d_{\text{N-C}}$	1.6

Table 5.16 Calculated atomic positions for extra framework sites inside the structure, generated from difference Fourier maps.

Position	Counter Height	Site	Coordination (x, y, z)	Distance (Å) [†]
1	31.82	16f	0.1150, 0.2534, 0.3739	$d_{\text{Zn1}} = 0.09$
2	18.364	16f	0.2392, 0.3157, 0.0857	$d_{\text{P1}} = 0.08$
3	16.874	16f	0.0024, 0.1512, 0.4156	$d_{\text{P2}} = 0.01$
4	16.775	16f	0.0025, 0.1512, 0.4155	$d_{\text{P2}} = 0.01$
5	7.569	16f	0.0581, 0.1857, 0.3730	$d_{\text{O10}} = 0.10$
6	7.351	16f	0.0716, 0.3141, 0.4215	$d_{\text{O1}} = 0.19$
7	7.037	16f	0.1624, 0.3073, 0.0658	$d_{\text{O6}} = 0.11$
8	6.93	16f	0.1989, 0.1265, 0.4349	$d_{\text{O4}} = 0.20$
9	6.392	16f	0.2062, 0.2363, 0.4063	$d_{\text{O5}} = 0.13$
10	6.27	16f	0.1165, 0.2744, 0.1269	$d_{\text{O6}} = 1.80$
11	6.216	16f	0.0436, 0.1553, 0.4791	$d_{\text{O9}} = 0.18$
12	5.905	16f	0.1355, 0.3876, 0.4958	-
13	5.493	16f	0.0475, 0.4341, 0.0869	$d_{\text{O8}} = 0.26$
14	5.406	16f	0.2061, 0.3429, 0.2806	$d_{\text{O3}} = 0.09$
15	5.24	16f	0.1283, 0.4486, 0.0155	$d_{\text{O7}} = 0.24$
16	5.183	16f	0.2080, 0.3334, 0.1546	$d_{\text{C3}} = 0.12$
17	5.124	16f	0.1220, 0.2617, 0.2957	$d_{\text{O2}} = 0.19$
18	4.791	16f	0.1655, 0.2992, 0.2616	$d_{\text{C1}} = 0.16$
19	4.628	16f	0.0339, 0.4168, 0.4027	$d_{\text{C6}} = 0.18$
20	4.504	16f	0.0842, 0.4699, 0.0520	$d_{\text{C4}} = 0.11$
21	4.014	16f	0.1589, 0.2774, 0.2007	$d_{\text{C2}} = 0.30$
22	3.855	16f	0.2471, 0.1929, 0.0946	$d_{\text{O5}} = 1.67$
23	3.519	16f	0.2149, 0.1471, 0.0562	-
24	3.401	16f	0.0854, 0.4554, 0.4497	$d_{\text{O6}} = 1.57$

25	3.29	16f	0.1391, 0.2489, 0.0374	$d_{C5} = 0.02$
26	3.102	16f	0.2320, 0.3374, 0.4115	-
27	2.897	16f	0.1146, 0.1919, 0.0393	-
28	2.726	16f	0.0413, 0.2349, 0.2181	-
29	2.598	16f	0.1541, 0.1185, 0.1863	-
30	2.597	16f	0.1280, 0.1523, 0.4409	$d_{O4} = 1.42$
31	2.595	16f	0.1353, 0.0741, 0.0174	-
32	2.591	16f	0.1250, 0.3065, 0.4801	$d_{O1} = 1.61$
33	2.538	16f	0.1675, 0.1062, 0.1107	-
34	2.435	16f	0.2153, 0.0241, 0.0609	-
35	2.426	16f	0.0694, 0.4160, 0.0003	$d_{O7} = 1.48$
36	2.409	16f	0.1908, 0.2500, 0.1140	$d_{O6} = 1.80$
37	2.34	16f	0.2194, 0.1601, 0.3600	$d_{C3} = 1.48$
38	2.312	8c	0.0615, 0.5000, 0.2500	-
39	2.294	16f	0.0022, 0.0008, 0.0005	-
40	2.285	16f	0.1159, 0.2395, 0.1732	-

[†] Distance to the closest framework atom

Table 5.17 Extra framework site decisions, derived from refined occupancies.

Position	Distance (Å) [†]	Assumption	Refine as Co	Refine as O	Decision
12	$d_{C5} = 2.0$ $d_{O1} = 2.4$	Co	Negative value	Negative value	Disregard
23	$d_{O5} = 2.9$	N/O/Co	0.22	0.68	O [‡]
26	$d_{O5} = 2.2$	Co	Negative value	Negative value	Disregard
27	$d_{O1} = 2.7$	N/O/Co	0.25	0.65	O
28	$d_{O2} = 2.2$	Co	0.22	0.55	Co
29	$d_{O3} = 2.8$	N/O/Co	0.46	1.31	Co
31	$d_{C5} = 1.9$ $d_{O7} = 2.6$	N/O/Co	0.03	0.13	O
33	$d_{O3} = 3.5$	N/O/Co	0.03	0.12	O
34	$d_{O7} = 2.7$	N/O/Co	0.4	1.06	Co
38	$d_{O3} = 3.4$	N/O/Co	0.57	1.58	Co
39	$d_{C4} = 2.0$ $d_{O8} = 2.2$	Co	Negative value	Negative value	Disregard
40	$d_{C2} = 1.5$ $d_{O2} = 2.7$	O/N/Co	Negative value	Negative value	Disregard

[†] Distance to the closest framework atom; [‡] it was impossible to distinguish nitrogen and oxygen atoms in this refinement, so all the non-cobalt atoms were assumed to be oxygen in the refinement as they were more abundant in the structure.

Then following the same difference Fourier map result used above, sixty other sites were then generated subsequently for searching the water oxygen positions. By

analysis of the interatomic distances (Table 5.15), only twenty-six positions were considered to be water oxygen locations, and four positions were possibly cobalt sites. The intensities of these four cobalt sites were relatively small, so if these positions were real cobalt sites, the occupancy of such sites would be very low; consequently these locations were not included in the following refinements. With the previous eight sites together, four cobalt positions and thirty water oxygen positions were finally added to the refinement.

Taking into account the EDX results, the overall occupancy of the four cobalt sites was constrained to be equivalent to 0.6 cobalt atoms per formula unit in order to keep the molar ratio of Zn:Co to 1:0.3. Then oxygen atoms with the occupancy of 0.1 were inserted at each of thirty positions. All the isotropic thermal displacement parameters of these newly added thirty-four sites were set to be 0.025 and the occupancies were damped and refined simultaneously. Sites that refined to negative or near zero occupancy were then eliminated, and the framework was included in the refinement. After a number of least squares cycles, a reasonable fit could be achieved with $\chi^2 = 7.737$, $R_{wp} = 5.83\%$ and $R_p = 4.16\%$. Details on the atomic positions, distances and angles can be found in Figures 5.21–5.22 and Tables 5.18–5.21.

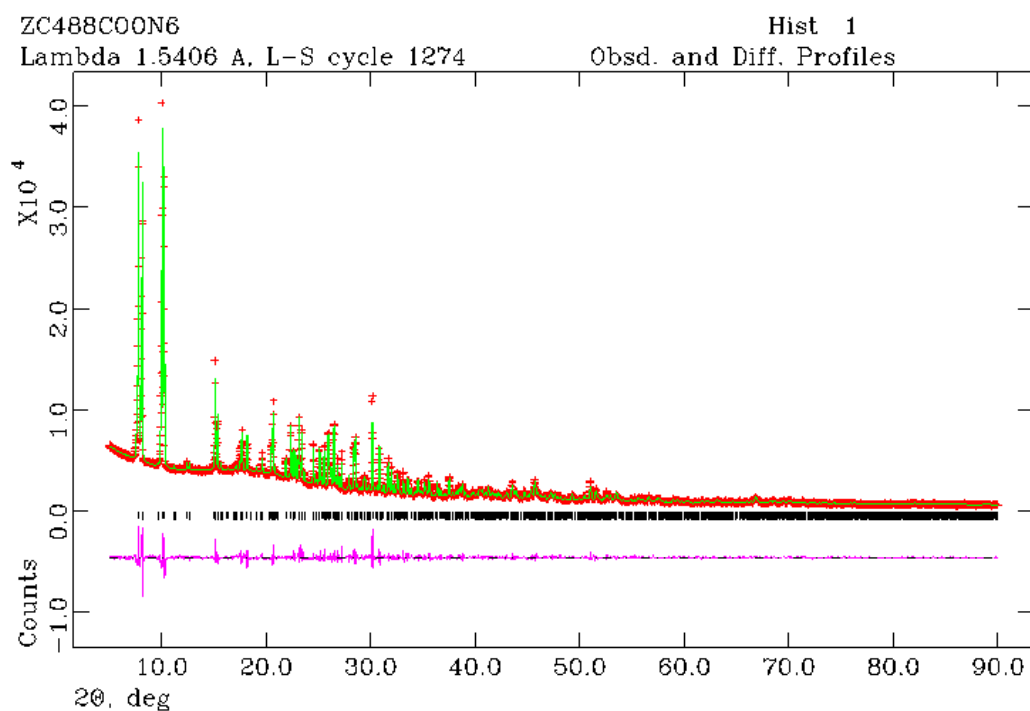


Fig. 5.21 Final observed (crosses) and calculated (solid line) powder X-ray diffraction patterns, with difference (below) and reflection positions (middle), for the final Rietveld refinement of Co^{2+} -BIRM-1; $\chi^2 = 7.737$, $R_{\text{wp}} = 5.83\%$ and $R_p = 4.16\%$.

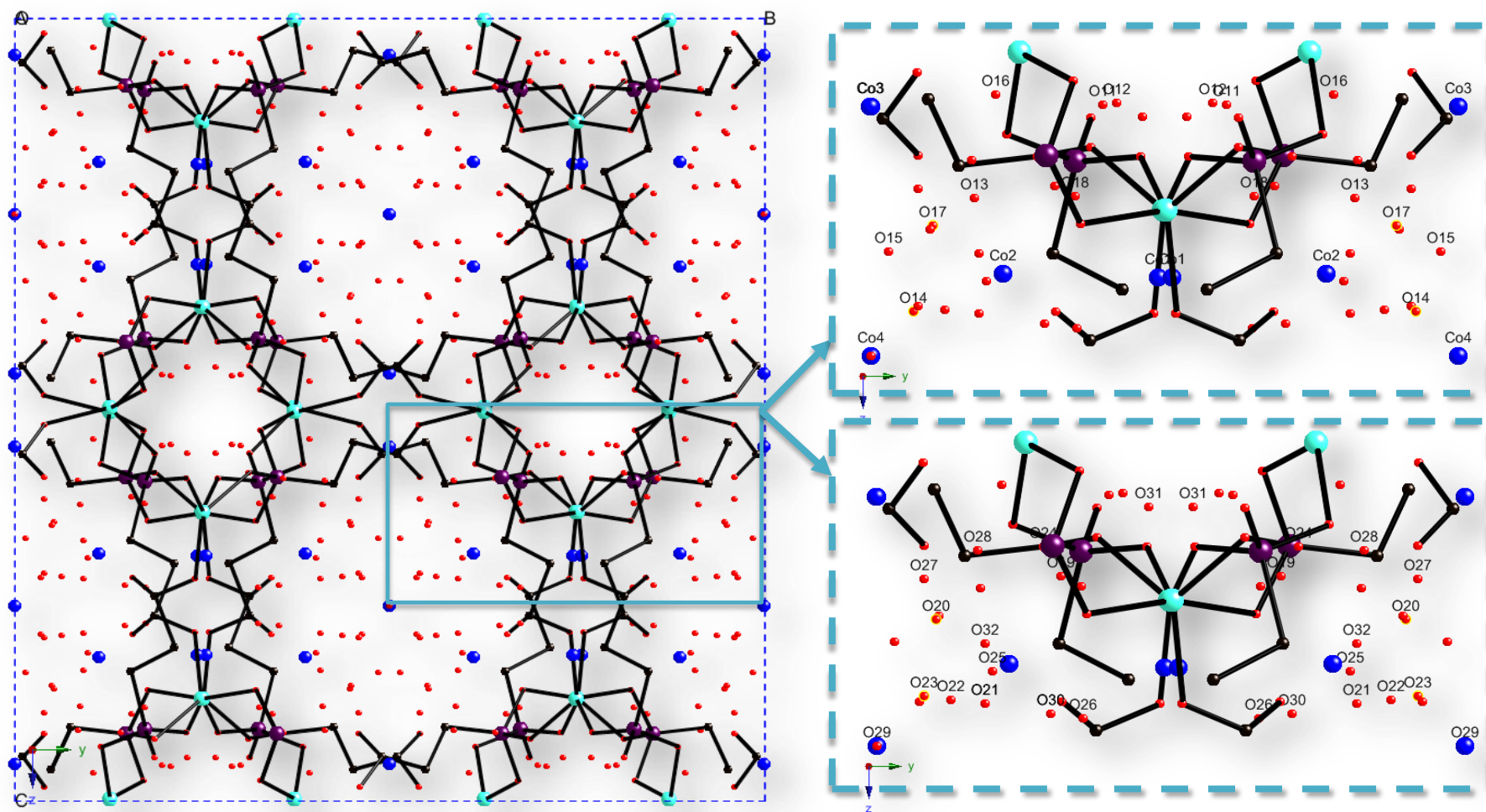


Fig. 5.22 Refined structure of Co^{2+} -BIRM-1 viewed along the z -axis, illustrating the atomic positions of exchanged cobalt atoms and water oxygen atoms (right). Blue dashed lines indicate one unit cell (left); colour scheme: Zn – turquoise, P – purple, N – green, O – red, C – black and Co – blue.

Table 5.18 Refined atomic positions for Co²⁺-BIRM-1; framework hydrogen atoms were placed geometrically after the refinement was complete.

Atom	Mult.	<i>x</i>	<i>y</i>	<i>z</i>	Occupancy	<i>U</i> _{iso}
C1	16	0.650(3)	0.313(2)	0.237(2)	1	0.045(2)
C2	16	0.683(2)	0.286(2)	0.304(2)	1	0.047(2)
H21	16	0.7204	0.2532	0.2980	1	-
H22	16	0.6418	0.2695	0.3294	1	-
C3	16	0.718(2)	0.345(2)	0.334(2)	1	0.040(2)
H31	16	0.7606	0.3595	0.3093	1	-
H32	16	0.6803	0.3794	0.3356	1	-
C4	16	0.594(3)	0.490(2)	0.443(2)	1	0.046(2)
C5	16	0.554(3)	0.548(2)	0.459(2)	1	0.053(1)
H51	16	0.5886	0.5782	0.4789	1	-
H52	16	0.5125	0.5389	0.4866	1	-
C6	16	0.527(2)	0.575(2)	0.405(2)	1	0.043(2)
H61	16	0.5673	0.5746	0.3752	1	-
H62	16	0.4853	0.5484	0.3907	1	-
O1	16	0.570(2)	0.687(1)	0.420(1)	1	0.040(1)
O2	16	0.626(2)	0.260(1)	0.216(1)	1	0.065(2)
O3	16	0.703(2)	0.343(1)	0.214(1)	1	0.064(2)
O4	16	0.786(1)	0.384(1)	0.430(1)	1	0.043(2)
O5	16	0.797(2)	0.271(1)	0.413(1)	1	0.043(1)
O6	16	0.675(2)	0.313(1)	0.444(1)	1	0.043(1)
O7	16	0.622(2)	0.461(1)	0.481(1)	1	0.061(2)
O8	16	0.556(2)	0.460(1)	0.413(1)	1	0.063(2)
O9	16	0.456(2)	0.672(1)	0.474(1)	1	0.047(1)
O10	16	0.453(2)	0.678(1)	0.358(1)	1	0.047(1)
P1	16	0.7485(9)	0.3259(7)	0.4086(7)	1	0.036(4)
P2	16	0.4958(9)	0.6497(7)	0.4137(7)	1	0.039(4)
Zn1	16	0.6122(4)	0.2511(4)	0.1312(3)	1	0.040(2)
Zn2	16	0.6389(4)	0.3734(4)	0.5026(4)	1	0.039(2)
Co1	16	0.068(3)	0.244(3)	0.186(3)	0.094(4)	0.025
Co2	16	0.156(2)	0.112(1)	0.183(1)	0.196(5)	0.025
Co3	16	0.230(2)	-0.999(1)	0.047(2)	0.168(4)	0.025
Co4	8	0.196(2)	0.5	0.25	0.284(8)	0.025
O11	16	0.204(2)	0.198(2)	0.045(2)	0.70(3)	0.025
O12	16	0.085(2)	0.209(2)	0.044(2)	0.67(3)	0.025
O13	16	0.202(3)	0.088(2)	0.122(2)	0.63(3)	0.025
O14	16	0.328(4)	0.036(3)	0.214(3)	0.40(3)	0.025
O15	16	0.182(2)	0.015(2)	0.335(2)	0.68(3)	0.025
O16	16	0.245(4)	0.394(2)	0.463(2)	0.48(2)	0.025
O17	16	0.214(3)	0.447(2)	0.356(2)	0.58(2)	0.025
O18	16	0.023(3)	0.326(2)	0.120(3)	0.51(2)	0.025
O19	16	0.063(6)	0.156(5)	0.112(5)	0.25(2)	0.025
O20	16	0.116(4)	0.050(3)	0.353(3)	0.43(2)	0.025

O21	16	0.094(3)	0.092(2)	0.285(3)	0.52(2)	0.025
O22	16	0.071(3)	0.437(2)	0.212(2)	0.61(2)	0.025
O23	16	0.169(6)	0.040(5)	0.209(6)	0.28(3)	0.025
O24	16	0.257(3)	0.141(2)	0.087(2)	0.59(2)	0.025
O25	16	0.047(3)	0.098(3)	0.189(3)	0.52(2)	0.025
O26	16	0.056(2)	0.175(2)	0.227(2)	0.69(2)	0.025
O27	16	0.192(4)	0.040(4)	0.113(4)	0.38(3)	0.025
O28	16	0.090(2)	0.086(2)	0.090(2)	0.73(2)	0.025
O29	8	0.963(8)	0.5	0.25	0.24(4)	0.025
O30	16	0.023(4)	0.147(4)	0.276(4)	0.34(2)	0.025
O31	16	0.995(3)	0.269(1)	0.0550(9)	1	0.025
O32	16	0.225(3)	0.092(2)	0.333(2)	0.44(2)	0.025

Table 5.19 Selected bond distances for the Co²⁺-BIRM-1 framework.

Bond	Distance (Å)	Bond	Distance (Å)
C1–O3	1.28(5)	P2–O10	1.600(27)
C1–O2	1.33(4)	P1–O4	1.515(26)
C1–C2	1.72(5)	P1–O5	1.487(26)
C2–C3	1.57(5)	P1–O6	1.578(29)
C3–P1	1.83(4)	Zn2–O4	2.049(26)
C4–O7	1.17(5)	Zn2–O6	1.969(26)
C4–O8	1.17(5)	Zn2–O7	1.964(27)
C4–C5	1.50(5)	Zn2–O9	2.045(26)
C5–C6	1.43(5)	Zn1–O1	1.920(28)
C6–P2	1.72(4)	Zn1–O2	1.923(24)
P2–O1	1.581(29)	Zn1–O5	1.973(27)
P2–O9	1.619(26)	Zn1–O10	1.989(26)

Table 5.20 Selected bond angles for Co²⁺-BIRM-1.

Bond Angle	Angle (°)	Bond Angle	Angle (°)
O2–Zn1–O10	91.6(13)	O6–P1–C3	104.2(19)
O2–Zn1–O1	125.2(14)	O5–P1–C3	115.1(21)
O10–Zn1–O1	112.5(11)	O4–P1–C3	104.3(20)
O2–Zn1–O5	114.2(13)	O1–P2–O9	99.0(18)
O10–Zn1–O5	112.1(12)	O1–P2–O10	106.8(16)
O1–Zn1–O5	101.4(12)	O9–P2–O10	109.5(18)
O9–Zn2–O6	97.9(12)	O1–P2–C6	102.0(20)
O9–Zn2–O7	112.9(13)	O9–P2–C6	121.1(19)
O6–Zn2–O7	121.5(13)	O10–P2–C6	115.5(21)
O9–Zn2–O4	115.5(12)	O3–C1–O2	122(4)
O6–Zn2–O4	110.2(12)	O3–C1–C2	105(4)
O7–Zn2–O4	99.8(12)	O2–C1–C2	98((4))
P1–O4–Zn2	116.2(18)	C1–C2–C3	103.5(35)

C1–O2–Zn1	119.4(33)	C2–C3–P1	109.1(32)
C4–O7–Zn2	139(4)	O7–C4–O8	113(5)
P2–O1–Zn1	129.78	O7–C4–C5	119(5)
P2–O9–Zn2	117.0(18)	O8–C4–C5	108(5)
P2–O10–Zn1	119.4(18)	C6–C5–C4	108(4)
O6–P1–O5	109.6(20)	C5–C6–P2	113(4)
O6–P1–O4	111.3(18)	P1–O5–Zn1	131.2(21)
O5–P1–O4	112.1(19)	P1–O6–Zn2	120.3(18)

Table 5.21 Selected interatomic distances for cobalt atoms (within 0–3 Å).

Bond	Distance (Å)
Co1–C2	2.28(6)
Co1–O2	2.47(6)
Co1–C1	2.72(6)
Co2–O3	2.821(30)
Co3–O4	2.562(31)
Co3–O7	2.59(4)
Co3–O7	2.90(4)

5.6.3 Discussion

Rietveld refinement against laboratory powder XRD data was used with difference Fourier maps to examine the structure of Co²⁺-BIRM-1, a newly formed cation-exchanged metal organic framework material (Table 5.22). Lattice parameters, background and profile parameters were first fitted with the Le Bail method, then transferred into the structure refinement, and finally the cobalt ion sites were included in the model.

Table 5.22 Experimental parameters and crystallographic data for Co²⁺-BIRM-1.

X-ray facility	Bruker D8, in transmission geometry
Wavelength (Å)	1.54056
Temperature	Ambient temperature
Profile range (°, 2θ)	5 – 90
Step size (2θ)	0.0197
Chemical formula	C ₃ Co _{0.6} N _{0.2} O _{10.8} PZn
Chemical formula weight	322.88
Space group	<i>Ibca</i>

a (Å)	18.1989(5)
b (Å)	21.5312 (6)
c (Å)	22.4941 (6)
V (Å ³)	8814.2 (4)
Background parameters	22
Profile parameters	8
R_{wp}	5.72%
R_p	4.08%
χ^2	7.434

By ignoring scattering density in the channels, including the heaviest atoms (cobalt) the initial framework model derived from single crystal studies that was applied in this refinement was over-simplified to be used as a starting model. With only the zinc carboxyethylphosphonate framework, the refinement was unstable in the early stages, thus geometrical restraints on the variation of bond distances, bond angles and even non-bonding distances had to be applied to avoid structure distortion beyond chemically sensible limits. When the framework only refinement reached a stable point, R_{wp} only converged to a value of 20.69%. Therefore it was highly likely that incorrect positions would be generated together with the real ones when calculating difference Fourier maps to locate the extra framework atoms. Interatomic distances and refinement of occupancies were then employed to identify reasonable atom sites as well as determine element types. After adding the possible cobalt sites and water oxygen sites, the refinement of this new model proceeded smoothly with the structure soft restraints released in the final refinement. Bond lengths and bond angles of the structure converged to reasonable values and the exchanged cobalt cations were located in chemically sensible positions. The interatomic distances of the cobalt cations to the closest framework atoms (Table 5.21) were in the range of the coordination distances of Co^{2+} (2.3 Å – 2.8 Å) in the compilation of extra-framework sites in zeolite¹⁴⁸. Due to the unreliability of the free water oxygen sites positions, the coordination environment of the exchanged cobalt cations were not further discussed.

The attempt to refine of this structure is not very satisfactory due to the limitation of the laboratory XRD data. As apparent from the refined structure (Figure 5.22), cobalt ions were distributed over several sites and mostly concentrated in the larger channel. Taking the similarities in scattering power and ionic radii of oxygen and nitrogen atoms into account, it was considered to be almost impossible to distinguish water oxygen atoms from ammonium nitrogen atoms with only laboratory powder XRD data in this refinement, thus the rest of the atoms inside the channel were all refined as oxygen, and their site positions was also believed not very reliable due to the disordered positions and very low scattering power. Because it was difficult to account for all the ions or water oxygen atoms inside the channels, there was contrast generated between the low and medium angle diffraction intensities in the refinement caused by missing extra-framework atoms, making it difficult to determine the structure of cobalt-exchanged BIRM-1 determined precisely. The rather low isotropic temperature parameter applied to the newly added cobalt and oxygen atoms in the refinement was an endeavour to compensate for this deficiency of the structure, but this was not entirely effective.

5.7 Structure Determination of Mg^{2+} -BIRM-1

Since Mg^{2+} -BIRM-1 had a very similar XRD pattern to that of Co^{2+} -BIRM-1 as well as the same space group, the structure determination of magnesium-exchanged BIRM-1 was therefore carried out with the same methodology. The starting structure model was the same used in the above Co^{2+} -BIRM-1 refinement, and similar bond/non-bonding distance and angle restraints were applied to help the refinement reach a reasonable fit with $R_{\text{wp}} = 15.72\%$. Then difference Fourier maps were initially calculated to investigate the extra framework atom positions inside the channels.

However, due to the magnesium and oxygen ions having the same number of electrons and their relatively weak scattering power for X-rays, the very low magnesium content (16%, from EDX result) and the presence of lots of disordered water molecules inside the structure, using the refined occupancies to distinguish them was not as effective as it was for Co^{2+} -BIRM-1. Although interatomic distance may provide some suggestions to distinguish the magnesium ions from water oxygen, too much uncertainty remained to determine the final structure. In view of this, further structure refinement attempts for Mg^{2+} -BIRM-1 were not carried out in this project.

Nevertheless, in the final stages of writing up my thesis, the single crystal X-ray diffraction data for Mg^{2+} -BIRM-1 collected by the UK National Crystallographic Service in Southampton was finally returned to us. The raw data was refined by Dr. Louise Male and the structure clearly indicates successful ion exchange (Figure 5.23 and Table 5.23). The zinc carboxyethylphosphonate network after ion exchange remains intact: the structure still has a three dimensional framework with channels. The phosphorus atom is tetrahedral in coordination with three oxygen atoms and one carbon atom. The zinc atom is coordinated by four oxygen atoms, one of which is from the carboxylate group of the organic ligand and shares other three oxygen atoms with three different CPO_3 groups. The structure contains 0.50 magnesium cations for every two zinc atoms with six-fold coordination of six water molecules (Figure 5.24, O101–O106) and located only inside the large channels around the framework. The remaining charge on the framework is balanced by the presence of one ammonium cation per two zinc atoms distributed in the small channel (Figure 5.24, N201). The occupancy of the magnesium cation was refined as 0.52 but was fixed at exactly 0.50 because of the proximity, via symmetry, of magnesium

cations to one another. The occupancy of the ammonium cation refined to 0.99 but was fixed at 1 to balance the charge of the magnesium cation. Also the structure also contains 4.40 uncoordinated water molecules per two zinc atoms, disordered over several sites. Several of them are around the structure charge sites (O5 and O10), others were distributed to sites nearby the framework oxygen atoms. However, the occupancies of O(301) and O(31') were fixed as it was not possible to refine them successfully. Although the framework remains similar to that of BIRM-1, the crystal system of this framework is lowered to an orthorhombic cell which confirms the previous indexing of powder XRD data (see Appendix 6 for more structure details). It was not possible to locate hydrogen atom positions, and thus find out the hydrogen bonding for the ammonium cations, the uncoordinated or magnesium-coordinated water molecules. It is to be expected that all hydrogen bonding requirements in the structure are fulfilled¹³¹ (Table 5.24).

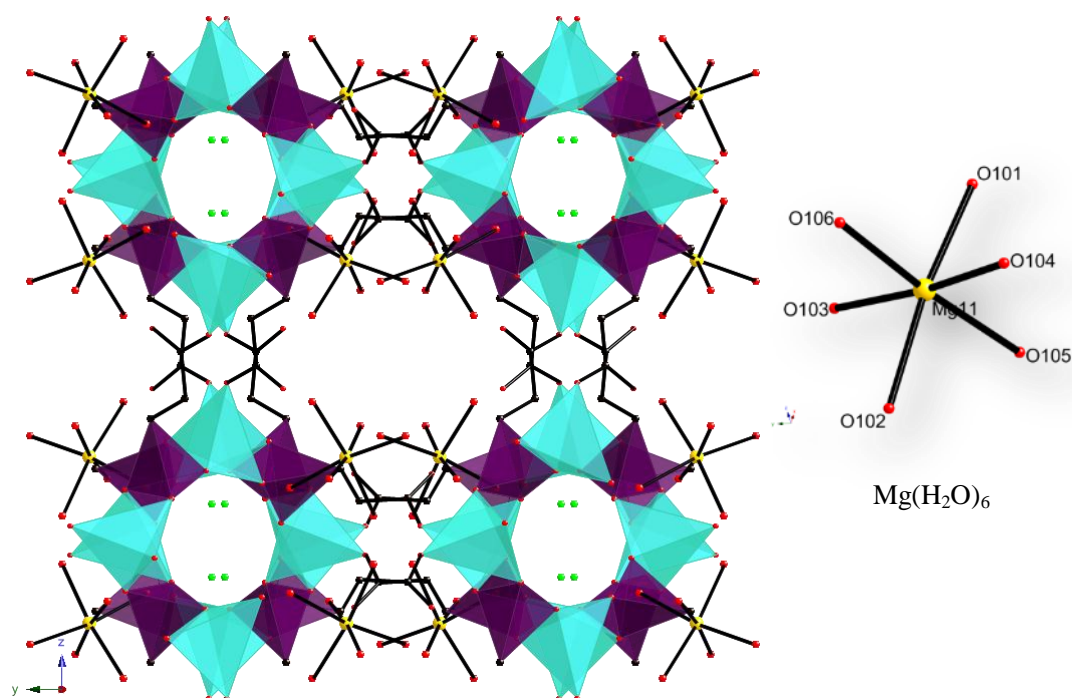


Fig. 5.23 Polyhedral view of the structure of Mg²⁺-BIRM-1 viewed along the *x*-axis, showing a three dimensional channel network; channels are filled with water molecules, Mg(H₂O)₆ octahedra are located inside the large channels and the NH₄ molecules are located inside the

smaller channels; hydrogen atoms and internal water molecules have been omitted for clarity; colour scheme: ZnO_4 – turquoise tetrahedra, CPO_3 – purple tetrahedra, Mg – yellow, O – red, N – green and C – black.

Table 5.23 Crystallographic data for Mg^{2+} -BIRM-1.

Empirical formula	$(\text{NH}_4)[\text{Mg}(\text{H}_2\text{O})_6]_{0.5}[\text{Zn}_2(\text{O}_3\text{PCH}_2\text{CH}_2\text{COO})_2] \cdot 4.40\text{H}_2\text{O}$
Formula weight	596.34
Crystal system	Orthorhombic
Space group	<i>Ibca</i>
<i>a</i> (Å)	18.1497(9)
<i>b</i> (Å)	21.5905(1)
<i>c</i> (Å)	22.4538(1)
Volume (Å ³)	8798.8(9)

Table 5.24 Selected interatomic distances for ammonium nitrogen atoms and non-framework water oxygen atoms.

Bond	Distance (Å)
N201–O2	2.7
O101–O5	2.8
O102–O10	2.6
O103–O8	2.8
O104–O7	2.8
O105–O10	2.6
O106–O4	2.6
O301–O7	2.7
O401–O5	2.8
O601–O3	2.8
O701–O9	2.6
O702–O3	3.0
O801–O9	2.9
O901–O9	2.6
O01'–O10	2.9
O02'–O5	3.4
O03'–O5	2.4
O31'–O1	2.5

Note: atom distances were directly measured by Crystal Maker

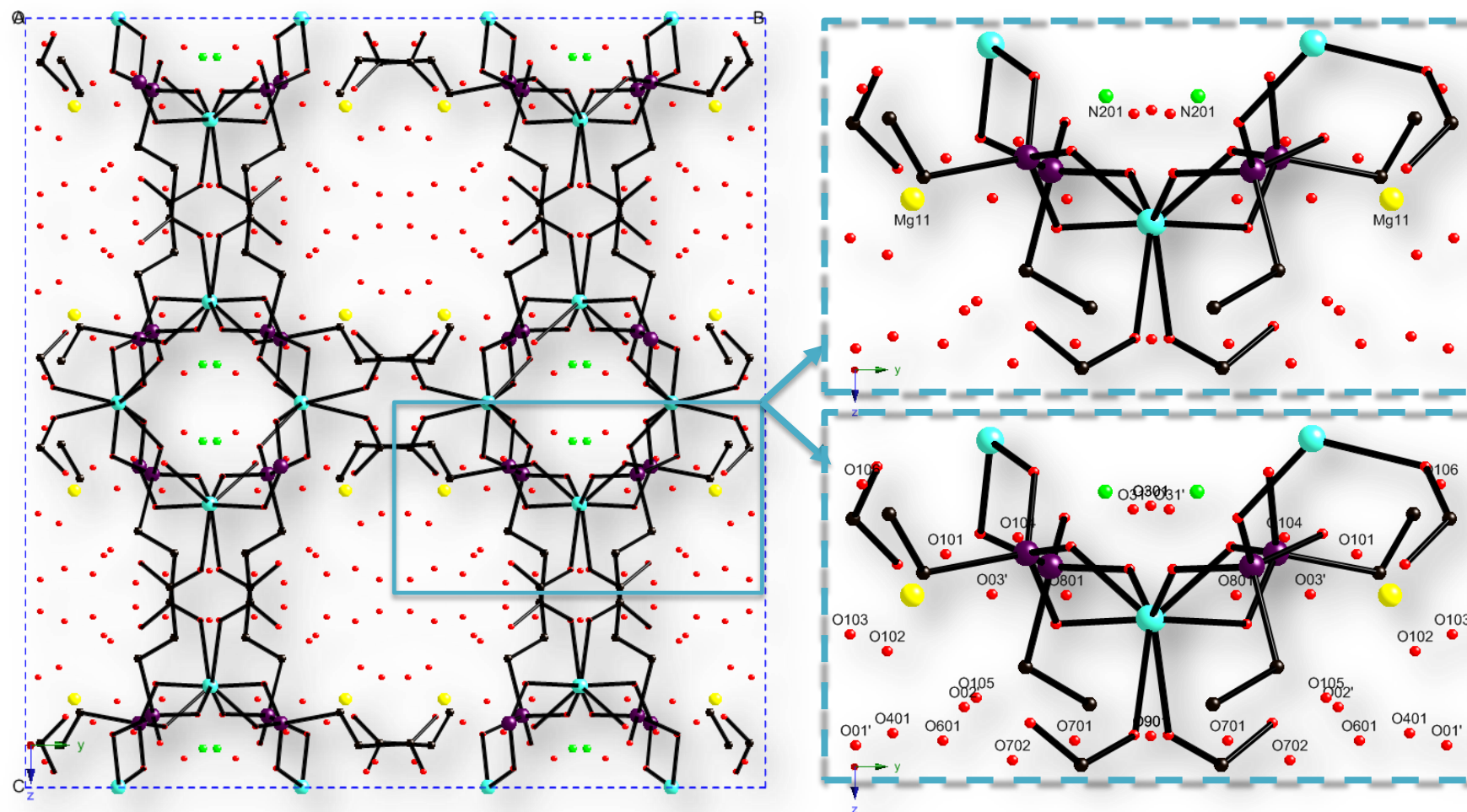


Fig. 5.24 Single crystal structure of Mg²⁺-BIRM-1 viewed along the z-axis, illustrating the atomic positions of exchanged magnesium atoms, ammonium nitrogen atoms and water oxygen atoms (right). Blue dashed lines indicate one unit cell (left); hydrogen atoms have been omitted for clarity; colour scheme: Zn – turquoise, P – purple, N – green, O – red, C – black and Mg – yellow.

5.8 Structure Determination of Mn^{2+} -BIRM-1

For Mn^{2+} -BIRM-1, although the XRD pattern was similar to those of Co^{2+} -BIRM-1 and Mg^{2+} -BIRM-1, there were some extra peaks and the space group was different. Owing to time limitations structural investigation of Mn^{2+} -BIRM-1 was not carried out in this project.

5.9 Conclusion

The synthesis and characterization of Co^{2+} -BIRM-1, Mn^{2+} -BIRM-1 and Mg^{2+} -BIRM-1 have been carried out with powder XRD, SEM & EDX, TGA, and FTIR measurements. Structures for Co^{2+} -BIRM-1 and Mg^{2+} -BIRM-1 were determined using Rietveld refinement of powder data and single crystal XRD methods, respectively, and demonstrated that ion exchange had been achieved and the frameworks were maintained with a reduced symmetry after ion exchange. So far, six different metal cation-exchanged BIRM-1 phases have been prepared and three structures have been determined. Hence the potential for BIRM-1 as an ion-exchangeable material has been substantiated, and the structures should provide an important basis for understanding the properties of the materials as well as promoting further investigations with better quality diffraction data.

Chapter 6

Hydrogen Uptake Attempts and De/Rehydration Investigations

6.1 Introduction

Metal organic frameworks as hydrogen physisorption materials have been the subject of great interest in recent years⁸⁴. In physisorption materials, the hydrogen molecule with just two electrons forms a very weak Van der Waals bond with the surface of the MOFs, which results in a low interaction energy (between 4 and 10 kJ/mol)⁸⁷. Although a high and rapid reversible hydrogen uptake can be achieved through physisorption, very low temperature (77 K) is unfortunately required for sufficient uptake⁹². Two main strategies have been investigated recently for enhancing hydrogen storage within metal organic frameworks under more moderate conditions. One is to enhance the surface area within a framework. It is widely recognized that a high surface area correlates almost linearly with the overall hydrogen uptake in a homogeneous, physisorption system⁹⁴⁻⁹⁶, but it is unlikely to result in an increase in the temperature required. Hence other approach is to create more attractive surface sites within the MOFs by using the strong metal hydrogen interactions between unsaturated metal centres and hydrogen to enhance hydrogen uptake. This is thought to be very a promising way to increase the hydrogen uptake capability at higher

temperature and lower pressure^{101, 102, 134, 135}.

In common with other MOFs, BIRM-1 has a low molecular mass and a three-dimensional porous framework structure, but unlike most has the advantage of containing exchangeable ammonium cations within the pores. The ability to undergo ion exchange is of interest in its own right, but also enables fine tuning of the properties of this material. After ion exchange, this compound may provide better binding sites for hydrogen molecules inside the structure to afford non-dissociative hydrogen binding between unsaturated metal centres and hydrogen molecules, which can significantly enhance the weak physisorption interaction⁸⁴. Since BIRM-1 and six different metal cation-exchanged phases have been successfully identified from the analyses in the preceding chapters, the cation-exchanged forms of BIRM-1 were clearly of interest in this context. However due to the very low hydrogen uptake, pore performances after evacuation and rehydration were investigated consequently.

6.2 Experimental

6.2.1 Hydrogen Uptake Measurement

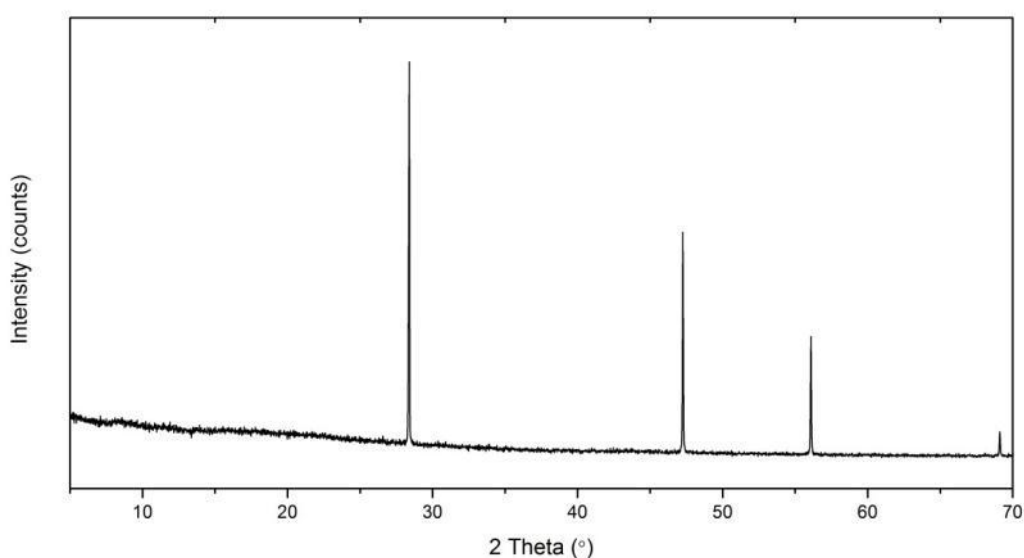
The hydrogen adsorption capacity of K⁺-BIRM-1 was investigated on a Hiden constant pressure thermogravimetric analyzer (IGA). Around 200 mg K⁺-BIRM-1 was loaded into a glass sample bulb and the sample degassed (Table 6.1). Then the sample was cooled to 77 K. Pressure–composition isotherms were determined from 0 to 20 bar. The purity of the hydrogen source was 99.995%, and a liquid nitrogen trap was used on the hydrogen gas inlet stream.

Table 6.1 Degassing procedures for the hydrogen uptake attempts with K⁺-BIRM-1.

	Procedure
Attempt I	Degassed at 100 °C for 2500 minutes then at 200 °C for 1300 minutes
Attempt II	Degassed under vacuum at room temperature for 1400 minutes

6.2.2 Dehydration and Rehydration Attempts

Dehydration of as-synthesized and ion-exchanged BIRM-1 products was mainly carried out with ground powder between 50 °C and 150 °C. Sample powder was attempted in a thin layer on a watch glass and dried in a pre-heated oven for 5 hours. After dehydration, the as-synthesized samples were soaked in deionized water (pH = 5.4, adjusted by HCl) for 12 hours to form rehydrated materials. In order to estimate the degree of structure recovery after rehydration, XRD measurements were made with the presence of high purity silicon powder (Acros Organic, 99+%, 325 mesh) as an internal standard (Figure 6.1). The mass ratio of silicon to examined product was 1:2.

**Fig.6.1** Powder XRD pattern of high purity silicon.

Backgrounds of these silicon mixed XRD patterns for each normal/rehydration samples group were subtract and the intensities were normalized. All the XRD measurements for each individual group were examined by Bruker D8 advance X-ray diffractometer on the same day with an interval of 30 minutes. The estimates of structure recovery were via the peak areas from the normalized XRD patterns using Equation 6.1. This ratio expressed as a percentage was then labeled relative crystallinity of rehydrated phase.

$$\text{Relative crystallinity of rehydrated phase} = \frac{A_r}{A_n} \times 100\% \quad (\text{Equation 6.1})$$

where:

A_r = Peak area from the XRD pattern of rehydrated phase, and

A_n = Peak area from the XRD pattern of phase before dehydration.

6.2.3 Organic Solvent Treatment of K⁺-BIRM-1

Further attempts to remove water molecules from the pores were carried out by soaking K⁺-BIRM-1 in anhydrous methanol, anhydrous dichloromethane (purified by Innovative Technology, Pure Solv PS-MD-4-EN Solvent Purification System), absolute ethanol (Fisher Scientific, 99.99% purity) and chloroform (Fisher Scientific, 99.9% purity), respectively, at room temperature for 2 days, making an effort to allow internal solvent molecules to be exchanged by the organic solvents. The wet samples were dried at room temperature for 24 hours and further evacuated at room temperature. Fourier transform infrared spectra were recorded from 4000 cm⁻¹ to 650 cm⁻¹ on a Perkin-Elmer FTIR System 1000 spectrometer to examine the presence of water (O–H) before and after the dehydration treatments.

6.3 Hydrogen Uptake Attempts with K⁺-BIRM-1

K⁺-BIRM-1 was the first compound to be measured isothermally on a constant pressure gravimetric analyzer system due to a plateau observed (from 200 °C to 350 °C) after losing coordinated water and ammonia on the TGA curve (Figure 6.2) suggesting a stable dehydrated phase.

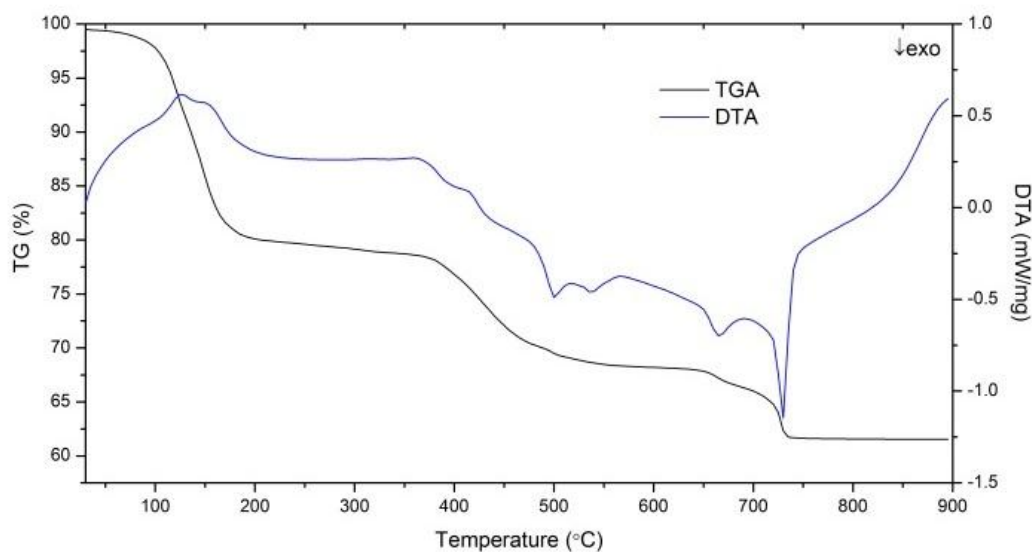


Fig. 6.2 TGA (black trace) and DTA (blue trace) of K⁺-BIRM-1.

At the beginning of this attempt, the sample was initially degassed at 100 °C for 2500 minutes under vacuum. As the mass did not stabilize, the temperature was raised to 200 °C till the variation in mass was minimal (about 1300 minutes). After that the sample was cooled down to 77 K and the hydrogen uptake was measured at pressures from 0 to 20 bar.

As apparent from the adsorption isotherm (Figure 6.3), a very low hydrogen uptake was observed with the values barely outside the error of the IGA machine. Since the structure was confirmed to be maintained after the potassium ion exchange, the low hydrogen uptake values observed here suggested that the material had lost

porosity after removal of the water molecules in the degas procedure. The XRD pattern after examination then confirmed this assumption (Figure 6.4).

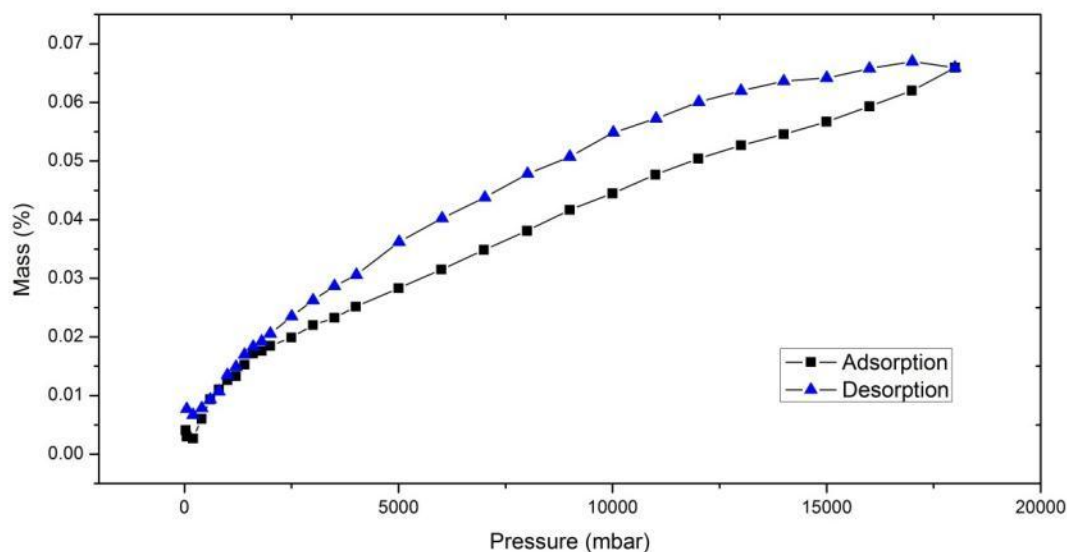


Fig. 6.3 Hydrogen adsorption isotherms for K^+ -BIRM-1 degassed under vacuum at 100 °C.

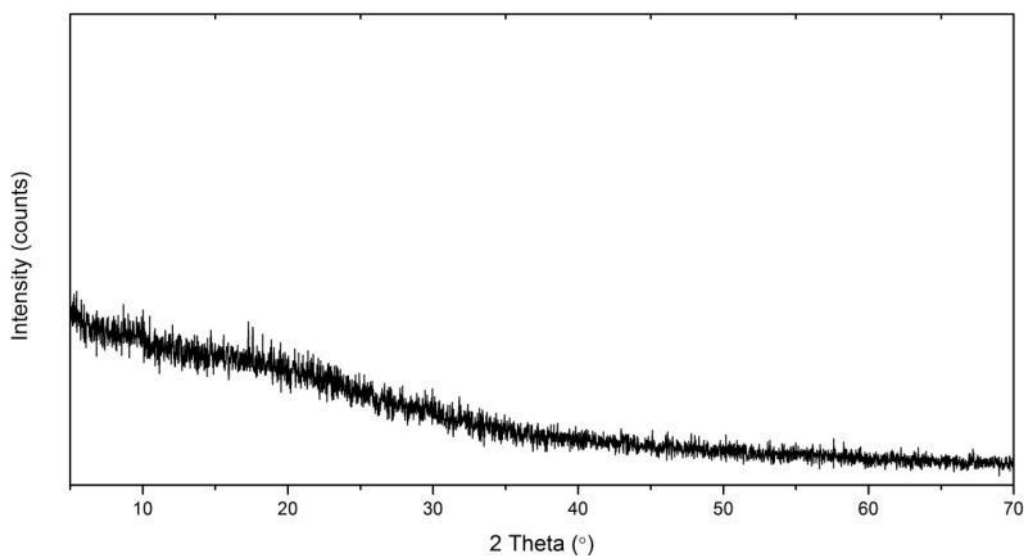


Fig. 6.4 Powder XRD pattern of K^+ -BIRM-1 after hydrogen uptake examination, degassed under vacuum at 100 °C.

Because of the low uptake observed, it was thought that the framework was possibly damaged under the degas conditions. Thus before the next hydrogen uptake

was carried out, an attempt to remove intrapore water under vacuum at room temperature was performed in the hope of avoiding thermal degradation of the product and consequently loss of porosity. After about 1400 minutes degassing, when no further mass change was detected, hydrogen adsorption was examined. Again there was no significant hydrogen adsorbed by K^+ -BIRM-1 (Figure 6.5).

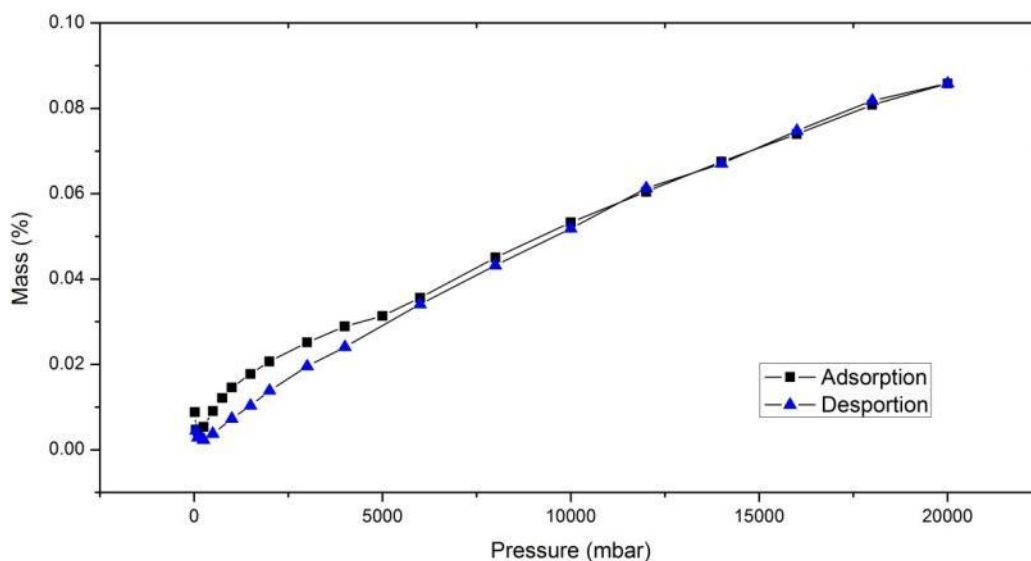


Fig. 6.5 Hydrogen adsorption isotherms for K^+ -BIRM-1 vacuum degassed at room temperature.

The powder XRD pattern after the examination (Figure 6.6) showed only two very broad peaks, indicating the structure had lost its crystallinity after degas and explaining the low hydrogen uptake. This degas process was then simulated in the lab. The XRD pattern of the dehydrated product showed the same result, leading to the conclusion that the very low hydrogen uptake was caused by loss of porosity during the degas treatment.

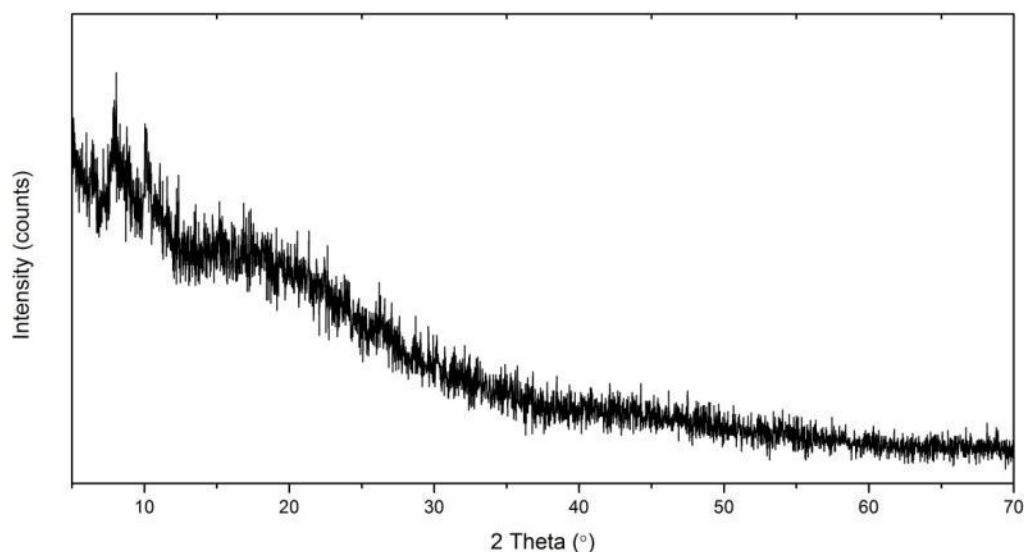


Fig. 6.6 Powder XRD pattern of K^+ -BIRM-1 after the hydrogen uptake examination, vacuum degassed at room temperature.

6.4 Dehydration and Rehydration Attempts with K^+ -BIRM-1

The above hydrogen uptake results revealed that the removal of the water molecules inside the structure result in a collapse of the K^+ -BIRM-1 framework and no significant hydrogen uptake. Further dehydration examinations of K^+ -BIRM-1 were carried out at various temperatures. Samples of K^+ -BIRM-1 were heated in a oven at 50 °C, 80 °C, 100 °C, 120 °C and 150 °C, respectively, for 5 hours to allow dehydration. After being heated at 50 °C for 5 hours, the XRD pattern was maintained (Figure 6.7), but O–H stretches at about 3400 cm^{-1} were still observed in the IR spectrum (Figure 6.8), indicating the dehydration was not complete.

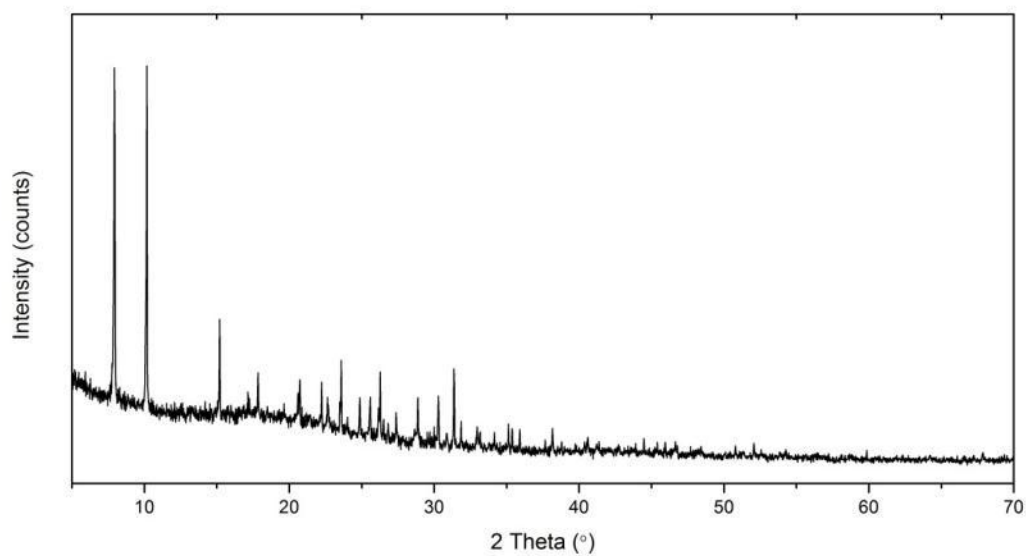


Fig. 6.7 Powder XRD pattern of K⁺-BIRM-1 after dehydration at 50 °C for 5 hours.

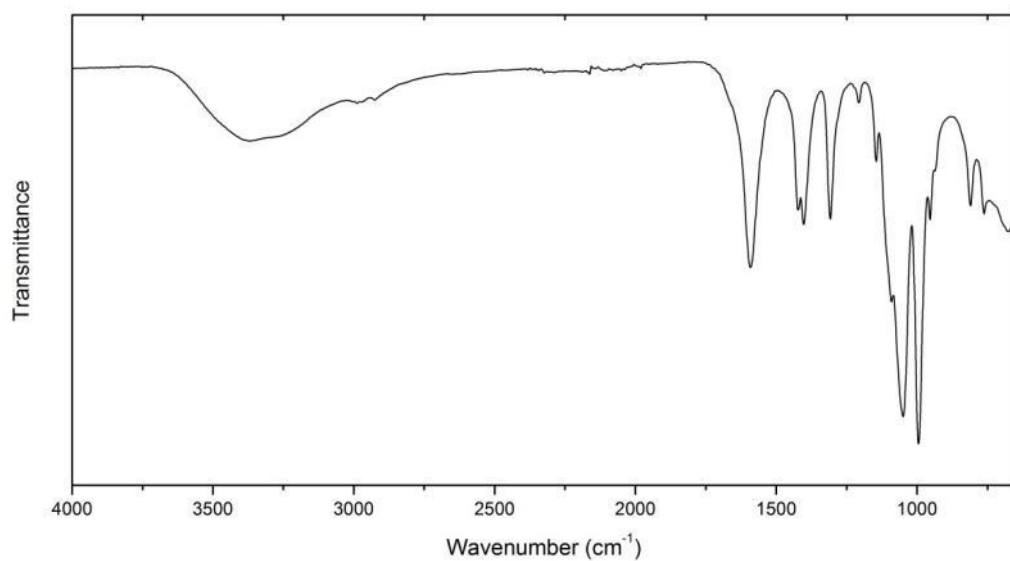


Fig. 6.8 FTIR spectrum of K⁺-BIRM-1 after dehydration at 50 °C for 5 hours.

However, with dehydration temperatures of 80 °C and higher, no peaks were observed from the XRD patterns (Figure 6.9) after the dehydration treatment, suggesting that the framework structure may no longer be retained intact. Nevertheless, TGA data of K⁺-BIRM-1 (Figure 6.2) suggested that total breakdown of

the framework did not occur until the temperature reached around 500 °C. To explore this apparent contradiction further, rehydration investigations of the dehydrated K^+ -BIRM-1 were carried out.

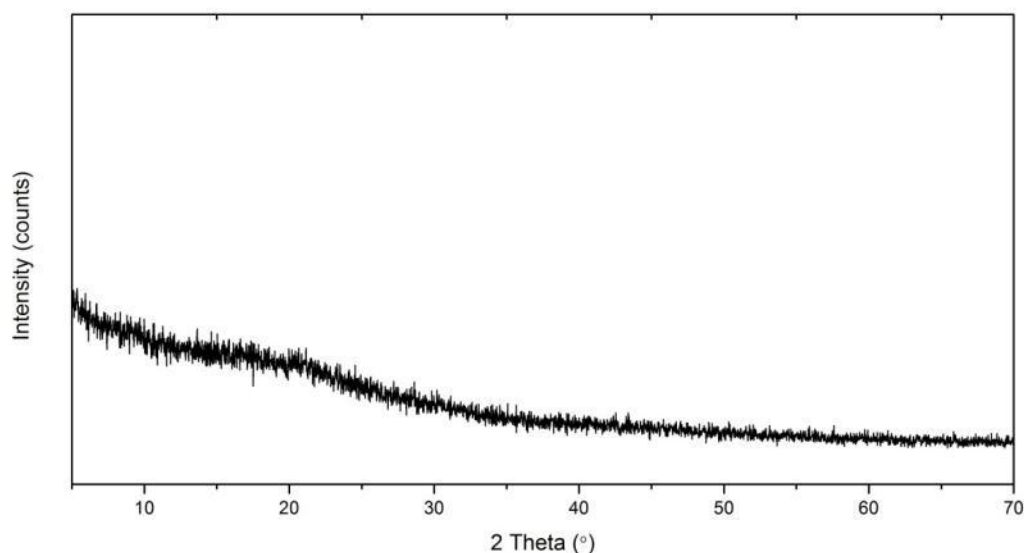


Fig. 6.9 Powder XRD pattern of K^+ -BIRM-1 after being dehydrated at 80 °C for 5 hours.

The dehydrated products were stirred with deionized water (pH was adjusted to around 5.40 by HCl) overnight. As can be seen in Figure 6.10, peaks returned to the XRD patterns after the rehydration attempts. This is consistent with the suggestion that after the K^+ -BIRM-1 had been heated for a couple of hours, removing water molecules from the channels the structure became distorted, leaving atoms arranged in a random way with no long-range order present and no peaks in the XRD pattern. After being rehydrated with water, the structure recovered, and the atoms were arranged in a regular pattern again.

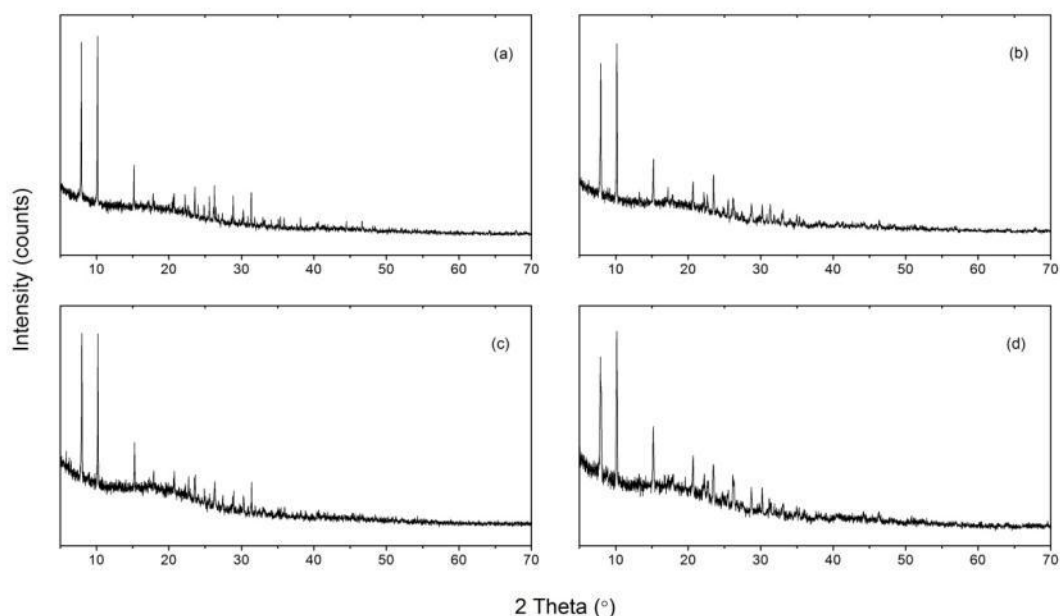


Fig. 6.10 Powder XRD patterns of rehydrated K⁺-BIRM-1 after dehydration at (a) 80 °C, (b) 100 °C, (c) 120 °C and (d) 150 °C for 5 hours.

The dehydrated (at 100 °C) K⁺-BIRM-1 was further examined by FTIR, before and after rehydration (Figure 6.11). The spectra exhibited clear information regarding the nature of the zinc carboxyethylphosphonate framework. The band at around 1600 cm⁻¹ is representing the symmetric vibrations the carboxyl group occurs. The strong band at 1400 cm⁻¹ is likely due to the asymmetric vibrations of the carboxyl group with a possible contribution of the P–C stretching mode. The stretching band of the C–O group was observed as a peak at around 1300 cm⁻¹. And the P–O stretching modes were seen as a series of sharp bands in the region 1150–950 cm⁻¹. However, after heating, the very broad peak at around 3200 cm⁻¹ representing the O–H stretches disappeared from the spectrum. Then after being rehydrated with water, this broad peak appeared again and the spectrum was virtually the same as the original pattern (Figure 4.6 in Chapter 4). These spectra corroborate the XRD analysis, that after dehydration, the bonds forming the framework structure were still broadly intact, but

the framework itself no longer exhibited long-range order after removing the internal water. FTIR spectra for products treated at different temperatures were similar.

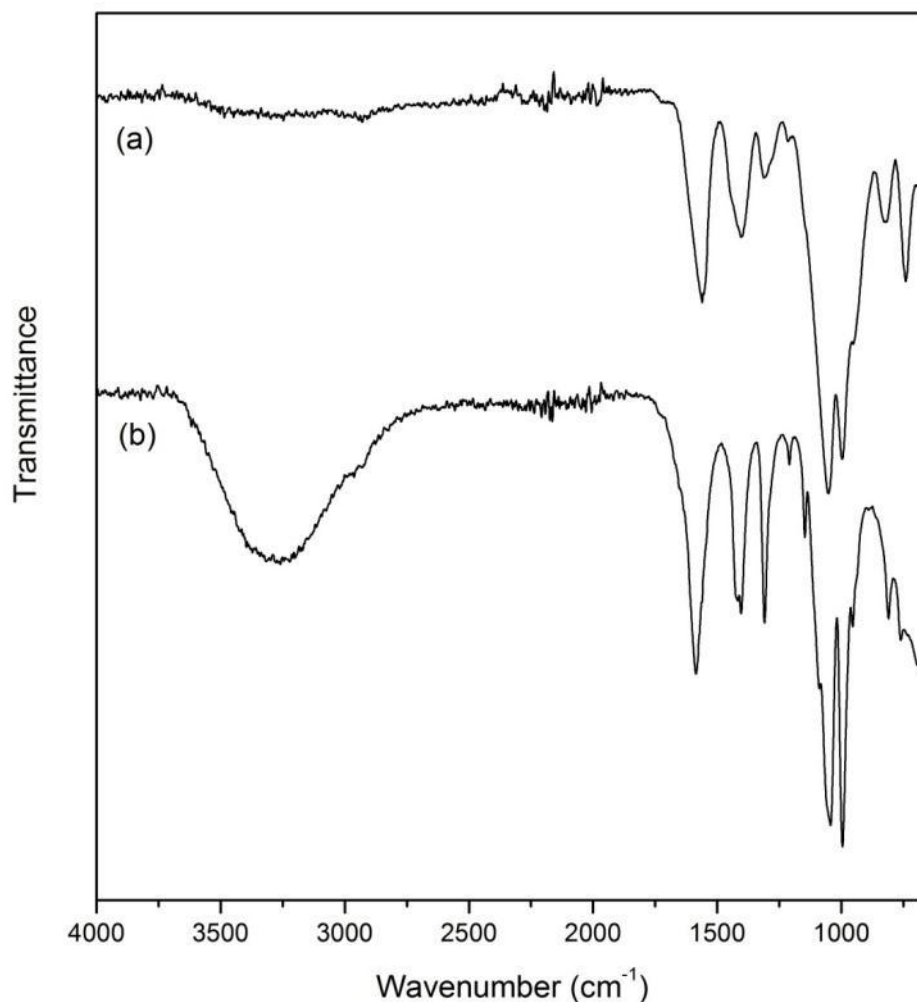


Fig. 6.11 FTIR spectra of dehydrated (100 °C) K⁺-BIRM-1 before (a) and (b) after rehydration.

6.5 Dehydration and Rehydration Attempts with BIRM-1 and Other Ion-Exchanged Forms

Since the structural transformation of K⁺-BIRM-1 on dehydration was shown to be at least partly reversible, the dehydration and rehydration properties of BIRM-1 and the

other ion-exchanged products were investigated. Samples were dried at 100 °C for 5 hours, then these dehydrated products were soaked with deionized water acidified with HCl (pH = 5.4) for 12 hours to allow rehydration.

Again, no peaks were observed in the XRD patterns of all the dehydrated samples, indicating that long-range order was not retained. After the rehydration, FTIR spectra of all the samples showed the reappearance of the broad O–H band. (See Appendix 7.1 for all dehydration/rehydration infrared spectra.) Analogous to the rehydrated K⁺-BIRM-1 (Figure 6.12b), the XRD patterns of rehydrated BIRM-1, Mn²⁺-BIRM-1, Mg²⁺-BIRM-1 and Na⁺-BIRM-1 reappeared (Figure 6.13b–6.16b), indicating the structures recovered to a certain degree. The main characteristic peaks occurred at almost the same two theta angles, but with much broadened peak shapes and lower intensities, and the medium angle diffraction peaks had almost disappeared. Both the increased full width half maximum (FWHM) and the relative crystallinity values (Table 6.2–6.3), indicated that the structures were only partly recovered in some cases.

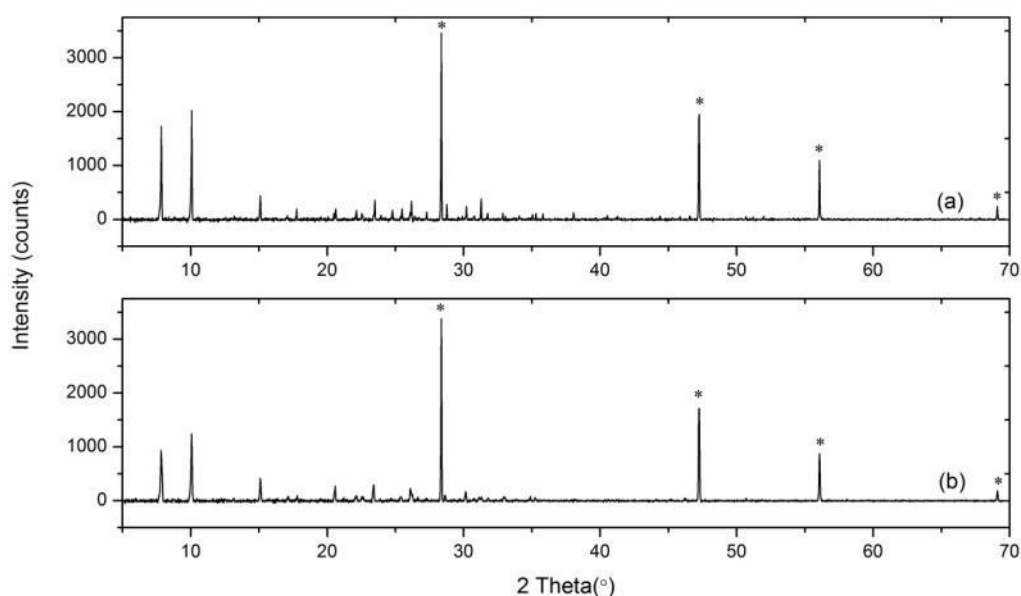


Fig. 6.12 Powder XRD patterns of (a) K⁺-BIRM-1 and (b) rehydrated K⁺-BIRM-1; Bragg peak positions marked with (*) originated from silicon.

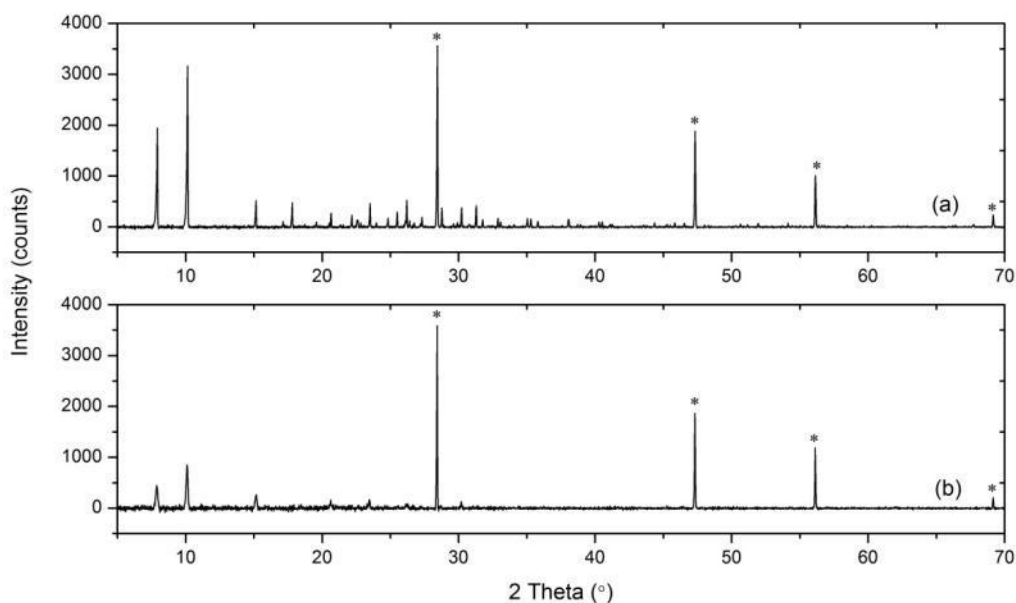


Fig. 6.13 Powder XRD patterns of (a) BIRM-1 and (b) rehydrated BIRM-1; Bragg peak positions marked with (*) originated from silicon.

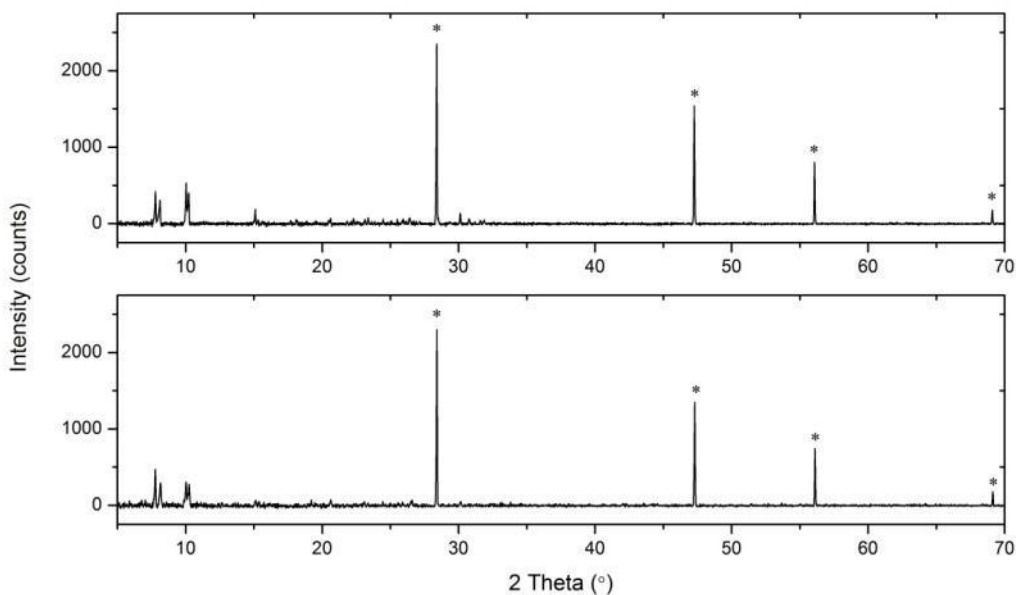


Fig. 6.14 Powder XRD patterns of (a) Mg²⁺-BIRM-1 and (b) rehydrated Mg²⁺-BIRM-1; Bragg peak positions marked with (*) originated from silicon.

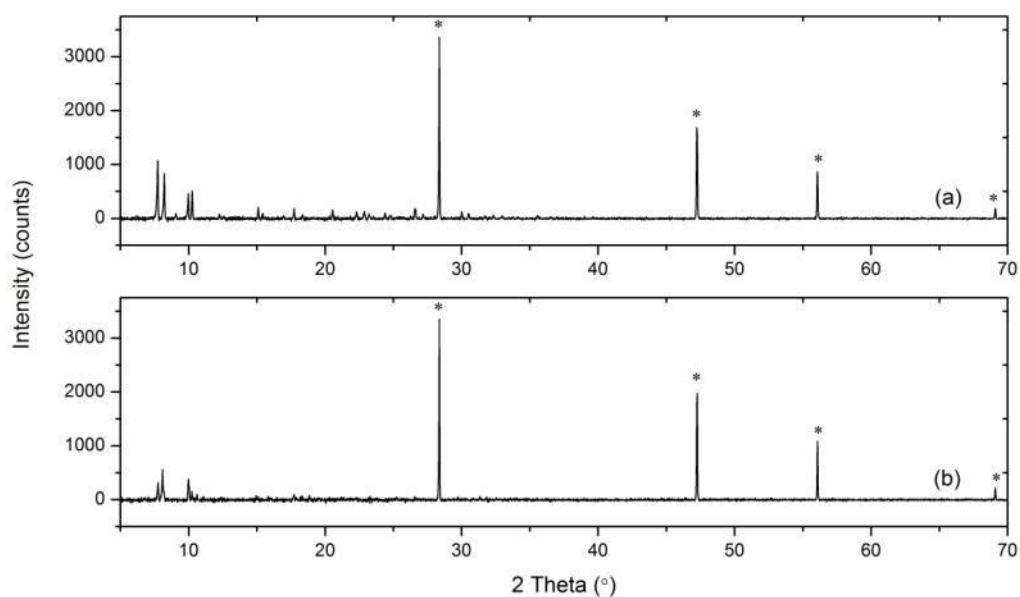


Fig. 6.15 Powder XRD patterns of (a) Mn^{2+} -BIRM-1 and (b) rehydrated Mn^{2+} -BIRM-1; Bragg peak positions marked with (*) originated from silicon.

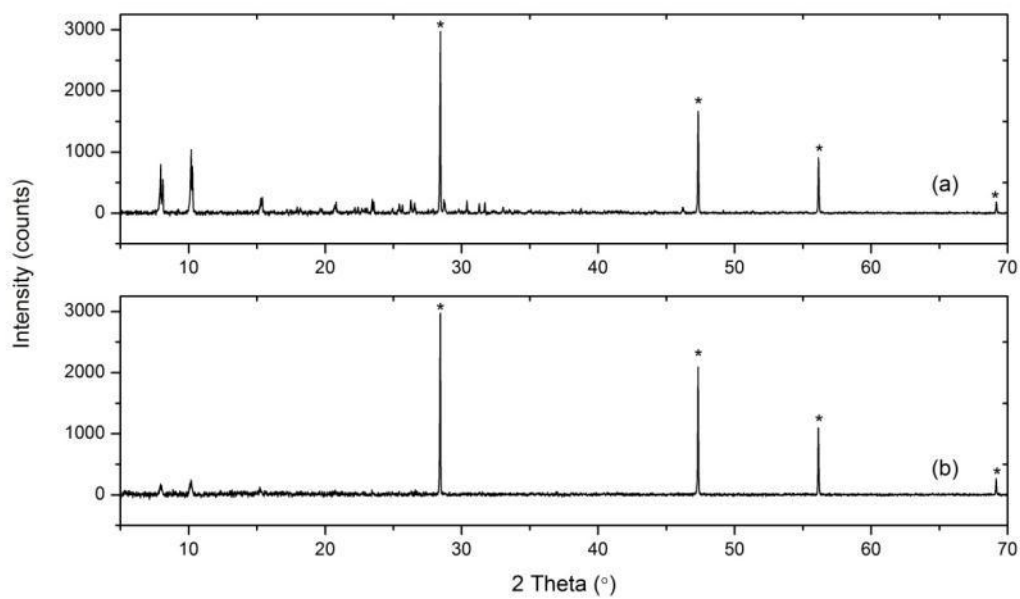


Fig. 6.16 Powder XRD patterns of (a) Na^+ -BIRM-1 and (b) rehydrated Na^+ -BIRM-1; Bragg peak positions marked with (*) originated from silicon.

Table 6.2 FWHM and selected peak areas of as-synthesized and rehydrated BIRM-1 materials.

Sample Name	2 Theta (°)	FWHM(°)	Area	Sample Name	2 Theta (°)	FWHM (°)	Area
BIRM-1	7.906	0.072(4)	10615	Mg ²⁺ -BIRM-1	7.774	0.09(2)	4479
	10.133	0.059(3)	15241		8.090	0.15(2)	2855
BIRM-1(R) [†]	7.878	0.20(2)	5413		10.028	0.09(2)	3346
	10.102	0.15(1)	7494		10.205	0.11(2)	2741
K ⁺ -BIRM-1	7.847	0.072(4)	8973	Mg ²⁺ -BIRM-1(R) [†]	7.761	0.10(2)	3831
	10.076	0.063(3)	8873		8.127	0.19(4)	3655
K ⁺ -BIRM-1(R) [†]	7.845	0.135(6)	8414		10.024	0.13(3)	2681
	10.068	0.097(6)	8095		10.244	0.14(4)	2162
Mn ²⁺ -BIRM-1	7.719	0.09(1)	6022	Na ⁺ -BIRM-1	7.935	0.08(2)	4392
	8.215	0.081(9)	5481		8.104	0.07(2)	3194
	9.965	0.09(1)	2862		10.172	0.09(2)	6500
	10.259	0.09(1)	3271		10.287	0.053(9)	3403
Mn ²⁺ -BIRM-1(R) [†]	7.741	0.08(1)	2234	Na ⁺ -BIRM-1(R) [†]	7.926	0.08(3)	703
	8.086	0.11(1)	4596		8.029	0.06(6)	412
	9.996	0.11(1)	4318		10.093	0.07(6)	618
	10.257	0.11(4)	1647		10.192	0.08(7)	1048

[†]After rehydration**Table 6.3** Recoverability estimations of rehydrated materials.

	BIRM-1	K ⁺ -BIRM-1	Mn ²⁺ -BIRM-1	Mg ²⁺ -BIRM-1	Na ⁺ -BIRM-1
Original Peak Area	25856	17846	17636	13421	17489
After rehydration	12907	16509	12795	12329	2781
Recoverability	49.9%	92.5%	72.6%	91.9%	15.9%

Clearly, after rehydration, the materials did not return entirely to their original condition. The peak broadening observed most likely indicates a lowering in the degree of long range order, caused either by a reduction in crystallite (or domain) size or, perhaps more likely, some residual lattice strain. A third possibility would be some compositional variation: different amounts of water present in different parts of the sample might lead to a distribution of lattice parameters and in this case also additional lattice strain.

For two samples more significant changes were observed on rehydration. As apparent from the XRD pattern of Li^+ -BIRM-1 (Figure 6.17), peak splitting was observed after the rehydration, similar to that observed in the divalent ion exchanged materials, indicating a lowering of symmetry (Table 6.4).

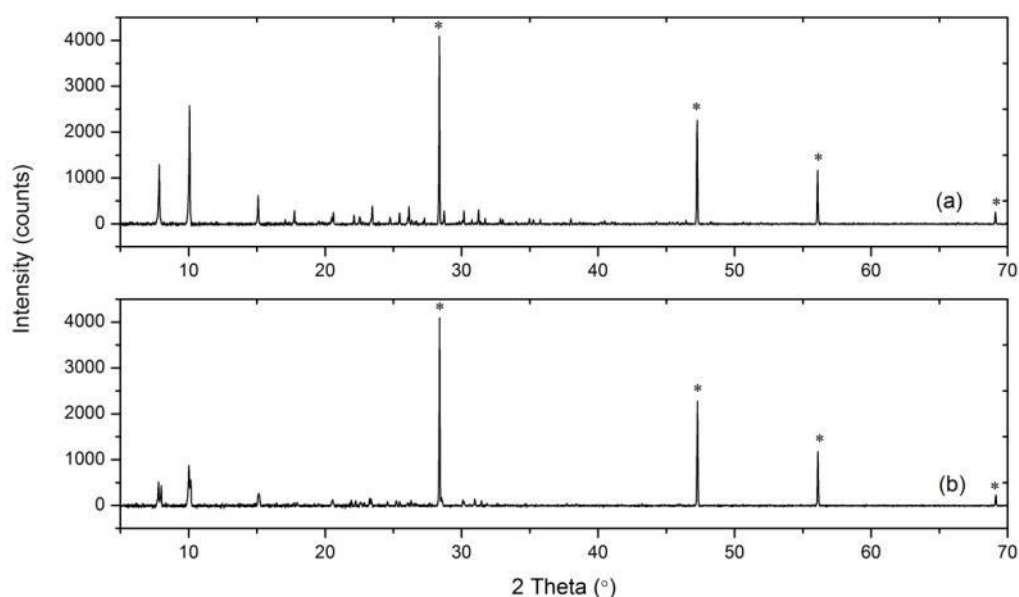


Fig. 6.17 Powder XRD patterns of (a) Li^+ -BIRM-1 and (b) rehydrated Li^+ -BIRM-1; Bragg peak positions marked with (*) originated from silicon.

For the Co^{2+} -BIRM-1, after rehydration a quite different set of peaks was observed (Figure 6.18), which could be indexed to a monoclinic cell (Table 6.4).

These changes in the XRD pattern may indicate a more significant change in structure on rehydration.

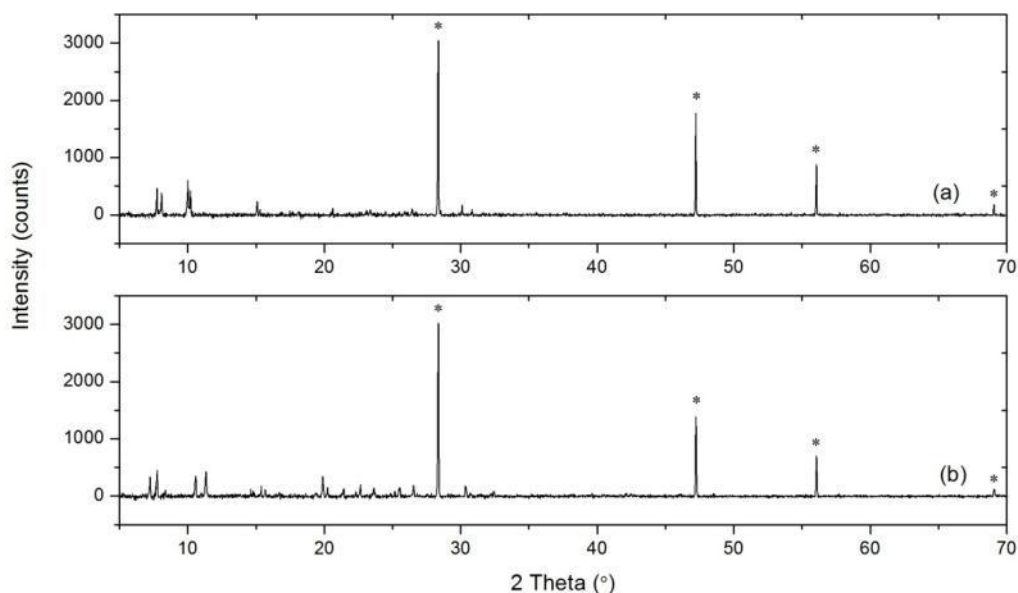


Fig. 6.18 Powder XRD patterns of (a) Co²⁺-BIRM-1 and (b) rehydrated Co²⁺-BIRM-1; Bragg peak positions marked with (*) originated from silicon.

Table 6.4 Lattice parameters of rehydrated Li⁺-BIRM-1 and Co²⁺-BIRM-1.

	Li ⁺ -BIRM-1(R)	Co ²⁺ -BIRM-1(R)
Crystal System	Orthorhombic	Monoclinic
Space group	<i>Pmna</i>	<i>P2₁/m</i>
<i>a</i> /Å	13.694(5)	26.75(2)
<i>b</i> /Å	24.27(1)	11.557(7)
<i>c</i> /Å	25.54(1)	24.47(2)
β /°	90	111.700 (5)
Volume/ Å ³	8490(6)	7027(8)
FOM [†] (M20)	4.8	5.0

[†]Figure of Merit

6.6 Evacuation Attempts with Organic Solvent Treated K⁺-BIRM-1

Degassing is an essential stage to facilitate gas storage. However, based on the above experiments, it proved difficult to sustain the structure, in particular the porosity, on

dehydration either for BIRM-1 or its ion-exchanged forms. Further attempts were therefore made to find a process to evacuate the material while maintaining the porosity of the structure.

Cheng *et al.*¹⁶⁴ reported a new way to tune the pore performance of a flexible material. They used an ethanol treatment on a layered flexible MOF, in which the presence of ethanol molecules influenced the connections between water molecules and framework, resulting in easier dehydration under vacuum at room temperature, with the basic structure remaining due to a trace of ethanol included in the pores. The following dehydration attempts were therefore carried out under vacuum after samples were immersed in methanol, ethanol, dichloromethane and chloroform for 2 days, in order to introduce these solvents into the channels and then remove them with internal solvent under milder conditions.

After mixing with the organic solvents for 2 days, there were no significant modifications in the XRD patterns (Figures 6.19a–6.22a) indicating the structure was maintained. Slight differences in relative peak intensities of the first two peaks occurring for dichloromethane and chloroform treated K^+ -BIRM-1 were probably caused by the presence of these organic molecules inside the lattice structure.

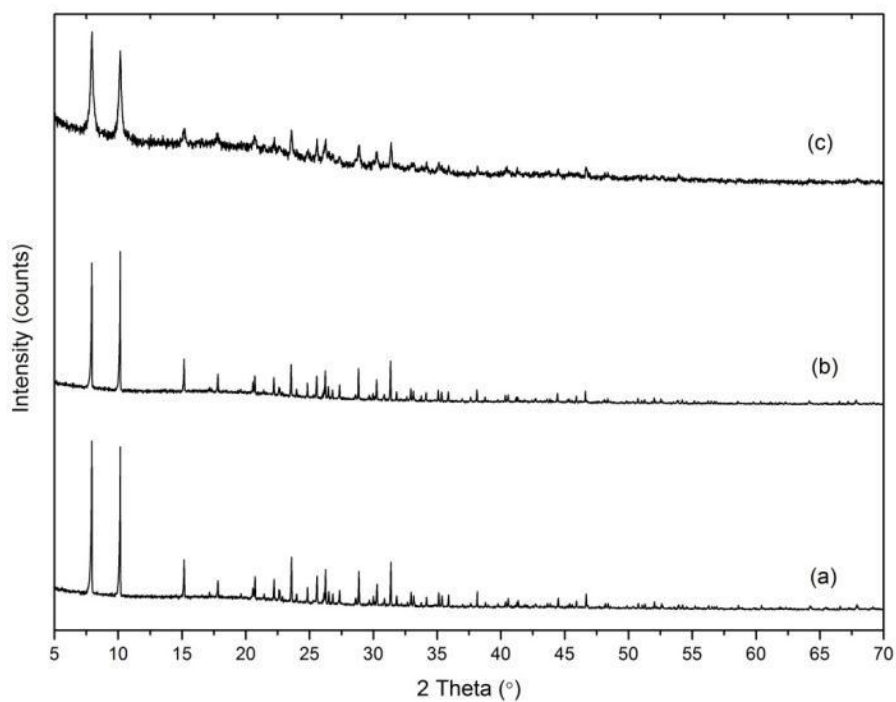


Fig. 6.19 Powder XRD patterns of (a) dichloromethane treated K^+ -BIRM-1, (b) after 5 hours evacuation and (c) after 15 hours evacuation.

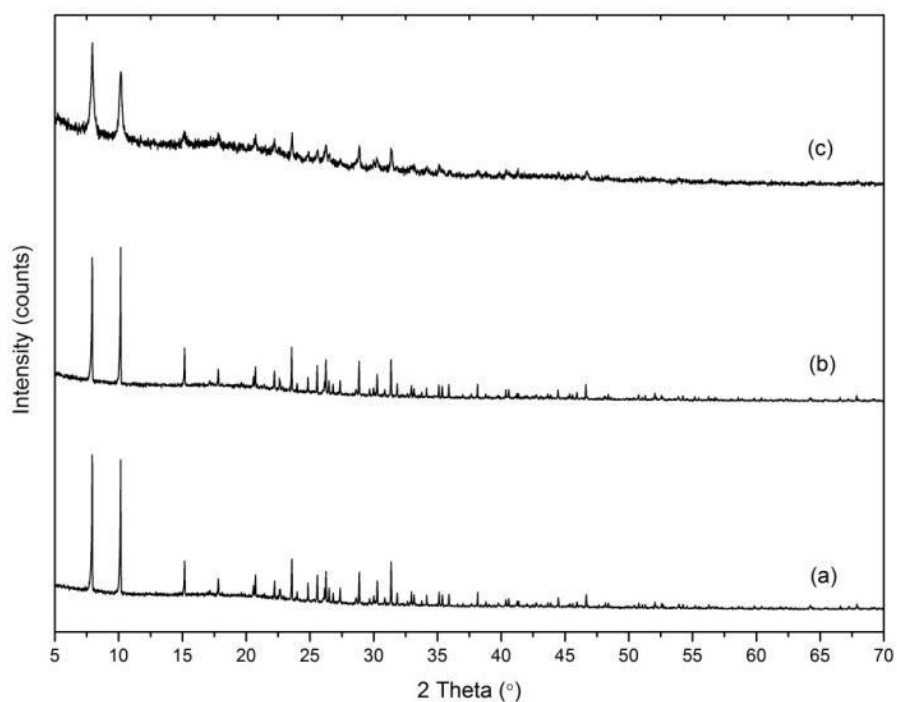


Fig. 6.20 Powder XRD patterns of (a) chloroform treated K^+ -BIRM-1, (b) after 5 hours evacuation and (c) after 15 hours evacuation.

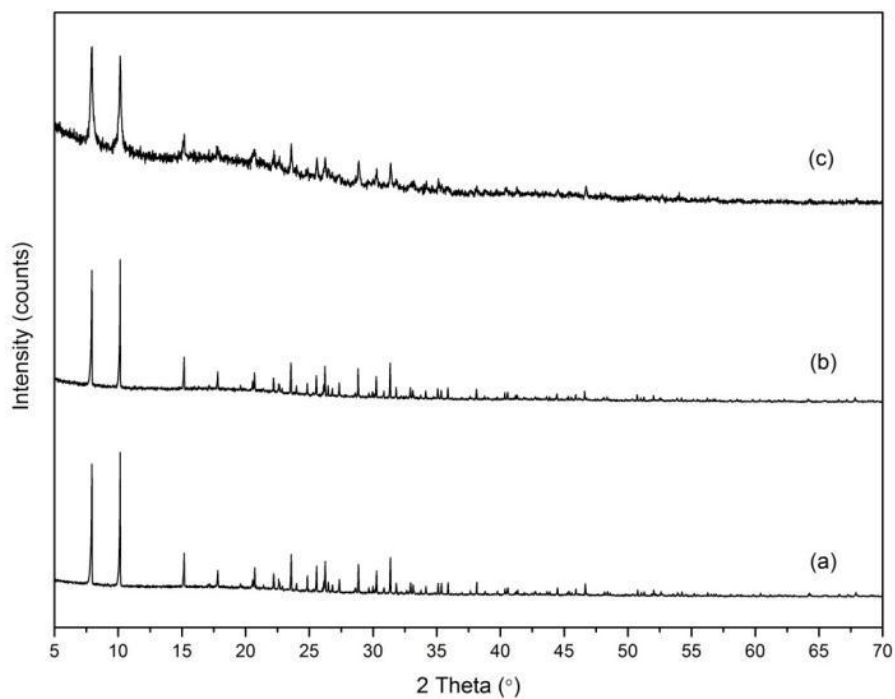


Fig. 6.21 Powder XRD patterns of (a) methanol treated K^+ -BIRM-1, (b) after 5 hours evacuation and (c) after 15 hours evacuation.

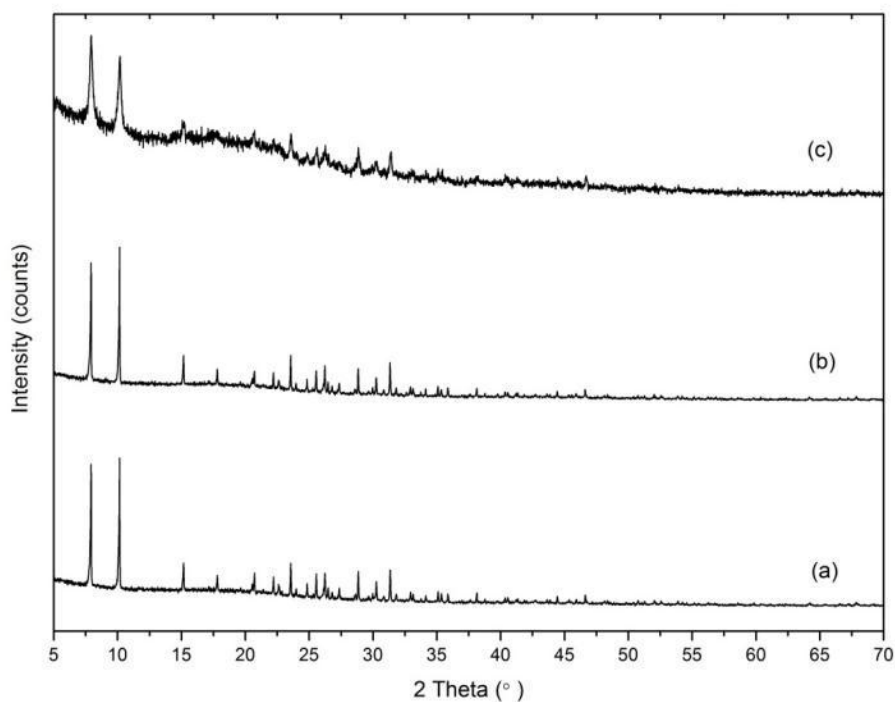


Fig. 6.22 Powder XRD patterns of (a) ethanol treated K^+ -BIRM-1, (b) after 5 hours evacuation and (c) after 15 hours evacuation.

After evacuation at room temperature for 5 hours, XRD patterns of the products indicated that they remained intact (Figures 6.19b–6.22b). The relative intensities for the XRD patterns of chloroform and dichloromethane treated K^+ -BIRM-1 more closely resembled their original forms, which possibly revealed the removal of these organic molecules. The O–H vibrations were still detected as a broad band in the FTIR spectra (Figure 6.23; see Appendix 7.2 for all other FTIR spectra before and after evacuation). After another 10 hours evacuation, the XRD patterns (Figures 6.19c–6.22c) indicated that the structures were significantly deformed with the (further) removal of the internal water, and much weaker broad band representing the O–H vibration still observed in the FTIR spectrum (Figure 6.23).

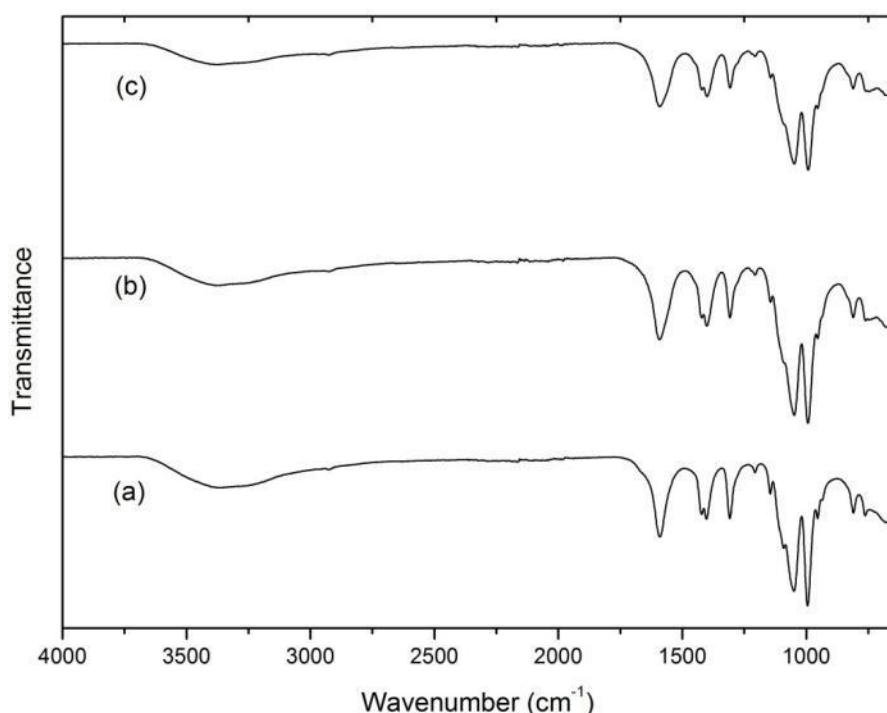


Fig. 6.23 FTIR spectra of (a) ethanol treated K^+ -BIRM-1, (b) after 5 hours evacuation and (c) after 15 hours evacuation.

For the chloroform and dichloromethane treated K^+ -BIRM-1, the XRD patterns were slightly modified in relative peak intensities of the first two peaks after

the solvent treatment, and these alterations then disappeared subsequently with further evacuation, representing the removal of the organic molecules. After the 5 hours dehydration, the O–H vibrations were not eliminated, but the intensity of the O–H peak was reduced after 10 further hours of evacuation. This suggests that the organic treatment did not actually help to remove the internal water, with prolonged evacuation required.

Although the XRD pattern did not show obvious evidence for the introduction of the ethanol and methanol molecules into the lattice, it was possible that the O–H vibration band from the FTIR spectra was produced by overlapping bands from water and ethanol/methanol molecules. But as the presence of the O–H vibration still could be observed even after 15 hours evacuation, ethanol and methanol were not helpful in making the dehydration of the material easier. Thus it can be concluded that although a certain amount of the organic solvent may have been introduced to the structure, the result was not an easier and faster dehydration after this treatment. It is likely that, if the dehydration attempts resumed for a longer time, the O–H vibration would be eliminated from FTIR spectra and no peaks would remain in the XRD patterns, as removal of the internal solvent distorted the framework. Due to these undesirable results occurred in the non-thermal dehydration investigations of K^+ -BIRM-1 and the tight deadline of this project, attempts on BIRM-1 and other ion-exchanged materials were therefore not carried out.

Confronted with these disappointing results, maintaining the flexible structure network which defines the accessible porosity during the dehydration by directly heating or reducing the system pressure was proved to be really challenging. And the

removal of the internal solvent will probably generate a surface tension, which drove the pores to collapse and elicited the deformation of the structure. However, Nelson *et al.*¹⁶⁵, Ma *et al.*¹⁶⁶ and Park *et al.*¹⁶⁷ demonstrated potential solutions to this problem. They suggested the accessible internal surface area of certain MOFs that collapse on thermal evacuation or with highly flexible structures would be significantly increased when activated the dehydration treatments with supercritical carbon dioxide or freeze drying. These methods rely on the internal water in the MOFs being replaced by supercritical carbon dioxide which can be removed by depressurization under milder conditions, or by a solvent such as benzene that can be removed by freeze drying, to leave the empty porous materials without crossing the liquid gas phase boundary, thus eliminating the surface tension inducing pore collapse. This seems to be a possible route to overcome the drawbacks that currently occur on the dehydration of our materials, but unfortunately no further attempts at improving this process were possible owing to time constraints. Further research is therefore required.

6.7 Conclusion

Dehydration and rehydration investigations illustrated the structural flexibility of both BIRM-1 and the ion-exchanged compounds. If the internal water was removed from the structure, the long-range order was hugely diminished or completely lost. Hence the compounds did not retain any porosity and were unsuitable for gas storage. However, rather than an irreversible collapse of the framework, it was found that when the samples were rehydrated, the structure could be recovered to a certain extent. Degassing is necessary to facilitate gas storage by creating space in the porous structure by the removal of internal water molecules as well as providing access to the additional open binding sites, but currently normal degas methods have turned out not

to be helpful in preserving porosity. If a method can be discovered for improving the pore retention during dehydration, such as using supercritical fluid or freeze drying methods, gas storage may still be possible in such a three dimensional ion-exchangeable porous material.

Chapter 7

Conclusion and Future Work

As a result of this project, a suitable and reproducible method has been obtained for the synthesis of a three dimensional porous zinc carboxyethylphosphonate material BIRM-1, which has been shown to be an excellent host material for ion-exchanging with various types of metal cations and to have a very flexible structure.

A highly crystalline BIRM-1 material was synthesized by using a mixture of urea (pH controller) and tetraethylammonium bromide (mineralizer) as the reaction medium for a reaction between zinc nitrate and 2-carboxyethylphosphonic acid under hydrothermal conditions. During the synthesis optimization process, three other zinc carboxyethylphosphonates with different pore size and framework topologies were also isolated (Figure 7.1). These phases can all be prepared from the same synthesis mixture with minor adjustments to the reagent mole ratios, the reaction temperature or the reaction time. BIRM-1 is the one with the largest pore size, providing potential access to its high internal surface area and has attracted the most interest. Compared to most other zeolites and porous metal organic frameworks, this material has relatively low density obtained by choosing 2-carboxyethylphosphonate acid as the organic ligand, which could be benefit in gas storage applications. Although metal phosphonates, or other MOFs, seldom exhibit any ion exchange capacity, BIRM-1 has

the advantage of containing ammonium cations within the pores, derived from the hydrolysed urea, which are present to charge balance the deprotonated carboxylic acid groups, and can undergo ion exchange with certain metal cations such as Li^+ , Na^+ , K^+ , Mg^{2+} , Mn^{2+} and Co^{2+} . The ability to undergo ion exchange is of interest in its own right, but also enables fine-tuning of the properties of this material.

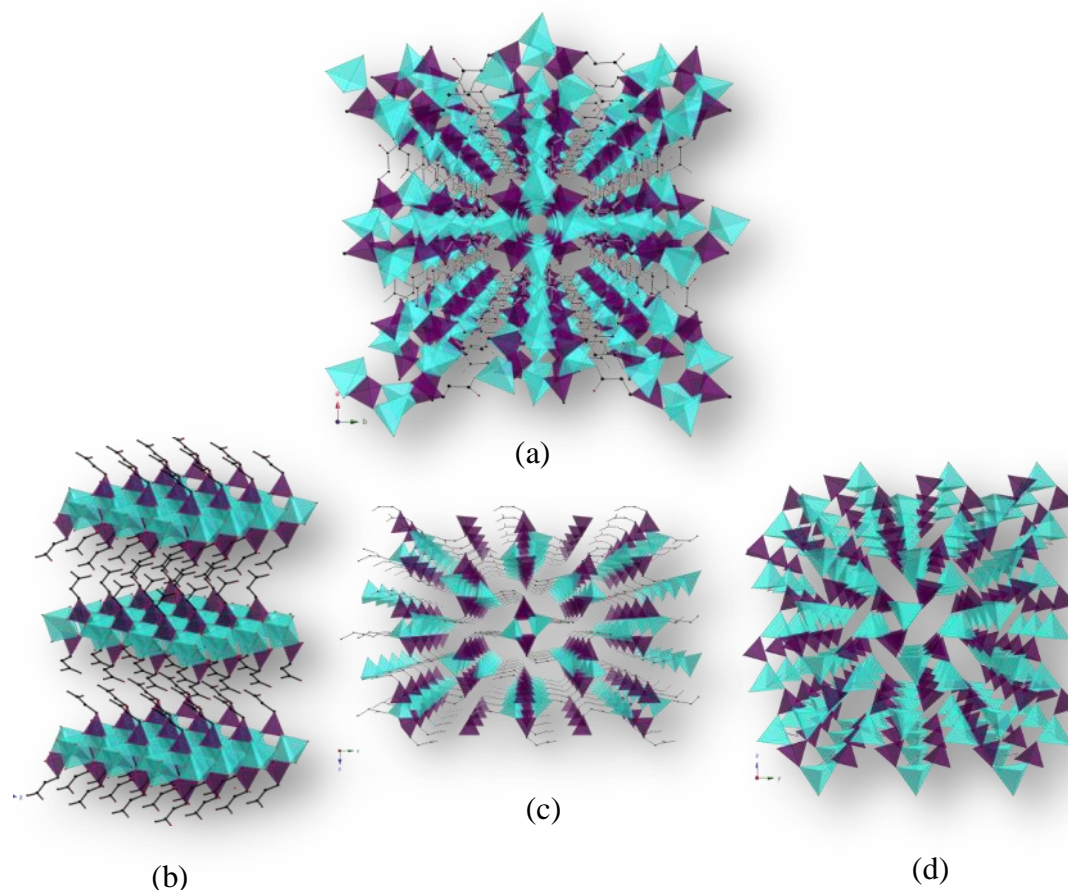


Fig.7.1 Crystal structures of (a) BIRM-1 and (b), (c), (d) three other zinc carboxyethylphosphonates synthesized from the same reagents under different conditions; hydrogen atoms, ammonium nitrogen atoms and internal oxygen atoms have been omitted for clarity; colour scheme: ZnO_4 – turquoise tetrahedra, CPO_3 – purple tetrahedra, O – red, and C – black.

By adjusting the pH value of the ion exchange solution to the same value as the final solution in the BIRM-1 synthesis reaction, the framework structure appeared to be well maintained after ion exchange. The results from XRD, SEM/EDX,

TG-DTA and FTIR of these recovered solids indicated that ion exchange has been successfully achieved and the metal cations were located inside the crystal structure. For K^+ -BIRM-1 and Mg^{2+} -BIRM-1, these were also backed up by the results from single crystal X-ray diffraction structure analysis.

Before any structure solutions were obtained from single crystal X-ray diffraction, endeavours were dedicated to determining the structures of K^+ -BIRM-1 and Co^{2+} -BIRM-1 through Rietveld refinement against powder XRD data. For the structure of K^+ -BIRM-1, the starting model employed was that of BIRM-1. The whole refinement strategy was based on the premise that the exchanged potassium ions will share the locations ammonium nitrogen atoms in BIRM-1, and then the use of difference Fourier maps to find other oxygen atoms. The amount of the potassium ions contained inside the structure was directly adopted from the EDX results and several occupancy constraints and bond length and angle restraints were also applied during the refinement procedures to allow a chemically sensible framework to be achieved. The agreement between the experimental and calculated profiles was satisfactory and one of the refined structures had a very similar structure to the single crystal structure solution. Nevertheless, the positions for the light atoms such as oxygen and nitrogen atoms may be not very reliable and could essentially be occupied by potassium ions with lower occupancies and the reverse is also possible. For Co^{2+} -BIRM-1, the structure model was adopted from an unfinished single crystal XRD structure of the cobalt-exchanged product generated in the early stage of this project, which only provided information on the structure framework. Hence all site positions of the cobalt ions as well as the solvent water molecules were predicted with the assistance of difference Fourier maps, and the element types were estimated by the

examination of the interatomic distances. Although the bond lengths and bond angles of the structure can be converged to reasonable values, the site positions for the exchanged metal ions and the solvent atoms were still very difficult to locate very precisely with current data.

The structure being refined with Rietveld refinement in this project is a complicated three dimensional porous MOF with extra-framework cations inside the channels and highly disordered internal solvent molecules. All these cannot be refined completely satisfactorily. The endeavours presented in this thesis are not a complete structural solution for those exchanged products but best attempts with all the data we currently have and appropriate strategies contributing to the structure determination. Although these structure determinations may not be totally accurate, the potential for BIRM-1 as an ion-exchangeable material has been substantiated. These structures should provide an important basis for understanding the properties of BIRM-1 as well as promoting further investigations with better quality diffraction data. Due to the very light exchanged cation (Li^+) and lack of the structure models for further refinement of Na^+ -BIRM-1 and Mn^{2+} -BIRM-1, structure determinations with powder XRD for these three exchanged products were not carried out in the project.

Single crystal structures of K^+ -BIRM-1 and Mg^{2+} -BIRM-1 (Figure 7.2a and b) were obtained in the very late stage of writing this thesis. The structure framework of K^+ -BIRM-1 was maintained well after the ion exchange and the tetragonal symmetry was maintained, with 0.77 moles of potassium ions and 0.23 moles of ammonium ions for one mole of zinc atoms. Those potassium ions were distributed in both the large and the small channels. For Mg^{2+} -BIRM-1, consistent with the indexing result, the

symmetry of the crystal system was lowered from tetragonal to orthorhombic. The structure contains 0.50 magnesium ions for every two zinc atoms which are coordinated by six water molecules and located only inside the large channels. Then this charge inside the structure is balanced by the presence of one ammonium cation per two zinc atoms distributed in the small channel. Both of these structures are very distinct evidence to demonstrate the success of the ion exchange, which makes it very reasonable to believe that other ion exchange attempts with Li^+ , Na^+ , Co^{2+} and Mn^{2+} were achieved as well.

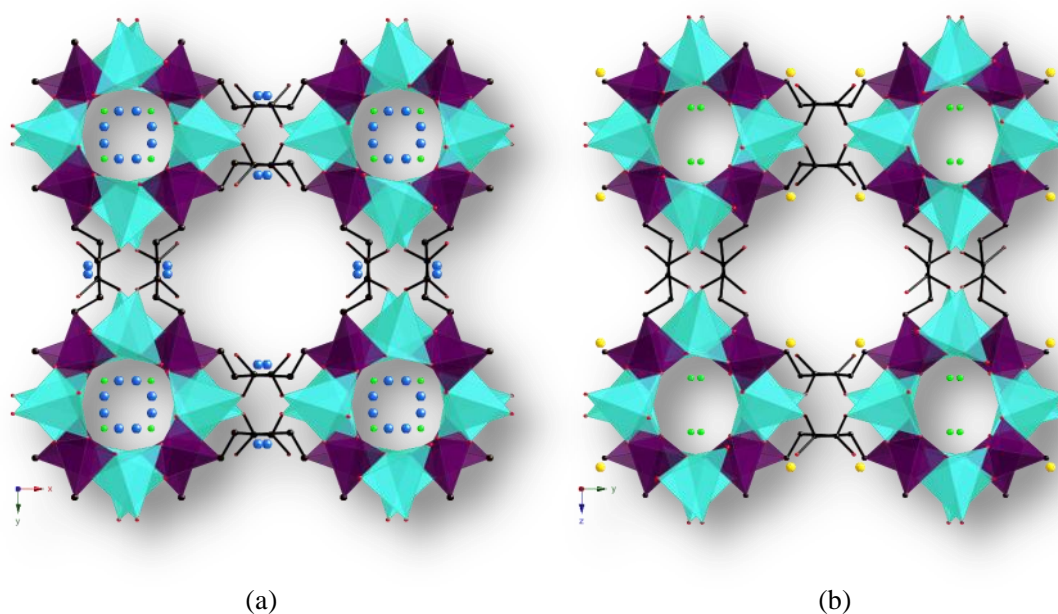


Fig. 7.2 Polyhedral view of the structure of (a) K^+ -BIRM-1 and (b) Mg^{2+} -BIRM-1, illustrating a successful ion exchange with potassium ions and magnesium ions; hydrogen atoms and internal oxygen atoms have been omitted for clarity; colour scheme: ZnO_4 – turquoise tetrahedra, CPO_3 – purple tetrahedra, K – blue, Mg – yellow, O – red, N – green and C – black.

Dehydration and rehydration investigations on both BIRM-1 and the ion-exchanged compounds illustrated a very interesting structural flexibility. If the internal solvent was removed from the structure by either heating or evacuation, the long-range order of the crystal was hugely diminished or completely lost. Hence the

compounds did not retain any porosity and were unsuitable for gas storage. However, rather than an irreversible collapse of the framework, it was found that when the samples were rehydrated, the frameworks could be recovered to a certain extent. Dehydration is necessary to facilitate gas storage by creating space in the porous structure as well as providing access to the additional open binding sites, but currently normal dehydration methods have turned out not to be helpful in preserving porosity and facilitating hydrogen physisorption. If a method can be discovered for improving the pore retention during dehydration, gas storage may still be possible in such a three dimensional ion-exchangeable porous material.

Future Work

There are several possible avenues of work that could be further explored following the work presented in this thesis. One important area is to find a way to dehydrate the BIRM-1 and its exchanged derivatives without losing the porous structure. Methods such as supercritical fluid or freeze drying are worth trying. Crystallographic and spectroscopic methods such as synchrotron and neutron diffraction can be employed to determine the unsolved structures of the exchanged products and locate the guest species within the porous structure with these newly obtained single crystal structures. Further insights gained into the applications of the flexibility of BIRM-1 and exchanged materials might also prove interesting. Ion-exchange attempts with different types of metal cations, and the synthesis of novel phosphonate based MOFs with more rigid ligands are also possibilities.

Reference

1. Z. Q. Wang and S. M. Cohen, *Chem. Soc. Rev.*, 2009, **38**, 1315-1329.
2. K. L. Mulfort, O. K. Farha, C. L. Stern, A. A. Sarjeant and J. T. Hupp, *J. Am. Chem. Soc.*, 2009, **131**, 3866-3868.
3. F. Nouar, J. Eckert, J. F. Eubank, P. Forster and M. Eddaoudi, *J. Am. Chem. Soc.*, 2009, **131**, 2864-2870.
4. M. Dinca, A. Dailly and J. R. Long, *Chem.-Eur. J.*, 2008, **14**, 10280-10285.
5. J. L. C. Rowsell and O. M. Yaghi, *Microporous Mesoporous Mater.*, 2004, **73**, 3-14.
6. G. Ferey, F. Millange, M. Morcrette, C. Serre, M. L. Doublet, J. M. Greneche and J. M. Tarascon, *Angew. Chem. Int. Ed.*, 2007, **46**, 3259-3263.
7. J.-R. Li, R. J. Kuppler and H.-C. Zhou, *Chem. Soc. Rev.*, 2009, **38**, 1477-1504.
8. M. Eddaoudi, D. B. Moler, H. L. Li, B. L. Chen, T. M. Reineke, M. O'Keeffe and O. M. Yaghi, *Acc. Chem. Res.*, 2001, **34**, 319-330.
9. A. U. Czaja, N. Trukhan and U. Mueller, *Chem. Soc. Rev.*, 2009, **38**, 1284-1293.
10. R. J. Kuppler, D. J. Timmons, Q.-R. Fang, J.-R. Li, T. A. Makal, M. D. Young, D. Yuan, D. Zhao, W. Zhuang and H.-C. Zhou, *Coord. Chem. Rev.*, 2009, **253**, 3042-3066.
11. N. Stock and S. Biswas, *Chem. Rev. (Washington, DC, U. S.)*, 2012, **112**, 933-969.
12. R. Robson, *Dalton Trans.*, 2008, 5113-5131.
13. J. L. C. Rowsell, A. R. Millward, K. S. Park and O. M. Yaghi, *J. Am. Chem. Soc.*, 2004, **126**, 5666-5667.
14. B. F. Hoskins and R. Robson, *J. Am. Chem. Soc.*, 1989, **111**, 5962-5964.
15. B. F. Hoskins and R. Robson, *J. Am. Chem. Soc.*, 1990, **112**, 1546-1554.
16. D. J. Tranchemontagne, J. L. Mendoza-Cortes, M. O'Keeffe and O. M. Yaghi, *Chem. Soc. Rev.*, 2009, **38**, 1257-1283.
17. B. Yilmaz, N. Trukhan and U. Muller, *Chin. J. Catal.*, 2012, **33**, 3-10.
18. K. M. Thomas, *Catal. Today*, 2007, **120**, 389-398.

19. U. Mueller, M. Schubert, F. Teich, H. Puetter, K. Schierle-Arndt and J. Pastre, *J. Mater. Chem.*, 2006, **16**, 626-636.
20. O. M. Yaghi, G. M. Li and H. L. Li, *Nature*, 1995, **378**, 703-706.
21. M. Kondo, T. Yoshitomi, K. Seki, H. Matsuzaka and S. Kitagawa, *Angew. Chem. Int. Ed.*, 1997, **36**, 1725-1727.
22. H. Li, M. Eddaoudi, M. O'Keeffe and O. M. Yaghi, *Nature*, 1999, **402**, 276-279.
23. O. M. Yaghi, M. O'Keeffe, N. W. Ockwig, H. K. Chae, M. Eddaoudi and J. Kim, *Nature*, 2003, **423**, 705-714.
24. M. O'Keeffe, *Chem. Soc. Rev.*, 2009, **38**, 1215-1217.
25. M. Eddaoudi, J. Kim, N. Rosi, D. Vodak, J. Wachter, M. O'Keeffe and O. M. Yaghi, *Science*, 2002, **295**, 469-472.
26. K. Sanderson, *Nature*, 2007, **448**, 746-748.
27. C. Serre, F. Millange, C. Thouvenot, M. Nogues, G. Marsolier, D. Louer and G. Férey, *J. Am. Chem. Soc.*, 2002, **124**, 13519-13526.
28. C. Serre, C. Mellot-Draznieks, S. Surblé, N. Audebrand, Y. Filinchuk and G. Férey, *Science*, 2007, **315**, 1828-1831.
29. C. Serre, S. Surble, C. Mellot-Draznieks, Y. Filinchuk and G. Férey, *Dalton Trans.*, 2008, 5462-5464.
30. K. Seki and W. Mori, *J. Phys. Chem. B*, 2002, **106**, 1380-1385.
31. D. N. Dybtsev, H. Chun and K. Kim, *Angew. Chem. Int. Ed.*, 2004, **43**, 5033-5036.
32. A. D. Burrows, *CrystEngComm*, 2011, **13**, 3623-3642.
33. Y.-S. Bae, K. L. Mulfort, H. Frost, P. Ryan, S. Punathanam, L. J. Broadbelt, J. T. Hupp and R. Q. Snurr, *Langmuir*, 2008, **24**, 8592-8598.
34. K. S. Park, Z. Ni, A. P. Cote, J. Y. Choi, R. Huang, F. J. Uribe-Romo, H. K. Chae, M. O'Keeffe and O. M. Yaghi, *Proc. Natl. Acad. Sci. U. S. A.*, 2006, **103**, 10186-10191.
35. R. Banerjee, A. Phan, B. Wang, C. Knobler, H. Furukawa, M. O'Keeffe and O. M. Yaghi, *Science*, 2008, **319**, 939-943.
36. W. Morris, B. Leung, H. Furukawa, O. K. Yaghi, N. He, H. Hayashi, Y. Houndonougbo, M. Asta, B. B. Laird and O. M. Yaghi, *J. Am. Chem. Soc.*, 2010, **132**, 11006-11008.
37. G. Férey, *Chem. Soc. Rev.*, 2008, **37**, 191-214.
38. K. Byrappa and M. Yoshimura, in *Handbook of Hydrothermal Technology*, William Andrew Publishing, Norwich, NY, 2001, pp. 1-52.
39. K. J. Gagnon, H. P. Perry and A. Clearfield, *Chem. Rev. (Washington, DC, U. S.)*, 2012, **112**, 1034-1054.
40. G. Férey, C. Mellot-Draznieks, C. Serre, F. Millange, J. Dutour, S. Surble and I. Margiolaki, *Science*, 2005, **309**, 2040-2042.

41. H. K. Chae, D. Y. Siberio-Perez, J. Kim, Y. Go, M. Eddaoudi, A. J. Matzger, M. O'Keeffe and O. M. Yaghi, *Nature*, 2004, **427**, 523-527.
42. H. Furukawa, N. Ko, Y. B. Go, N. Aratani, S. B. Choi, E. Choi, A. O. Yazaydin, R. Q. Snurr, M. O'Keeffe, J. Kim and O. M. Yaghi, *Science*, 2010, **329**, 424-428.
43. H. X. Deng, C. J. Doonan, H. Furukawa, R. B. Ferreira, J. Towne, C. B. Knobler, B. Wang and O. M. Yaghi, *Science*, 2010, **327**, 846-850.
44. H. Chun, D. N. Dybtsev, H. Kim and K. Kim, *Chem.-Eur. J.*, 2005, **11**, 3521-3529.
45. T. Fukushima, S. Horike, Y. Inubushi, K. Nakagawa, Y. Kubota, M. Takata and S. Kitagawa, *Angew. Chem. Int. Ed.*, 2010, **49**, 4820-4824.
46. T. Loiseau, C. Serre, C. Huguenard, G. Fink, F. Taulelle, M. Henry, T. Bataille and G. Ferey, *Chem.-Eur. J.*, 2004, **10**, 1373-1382.
47. C. Volkringer, T. Loiseau and G. Ferey, *Solid State Sci.*, 2009, **11**, 29-35.
48. S. Surble, C. Serre, C. Mellot-Draznieks, F. Millange and G. Ferey, *Chem. Commun. (Cambridge, U. K.)*, 2006, 284-286.
49. G. K. H. Shimizu, R. Vaidhyanathan and J. M. Taylor, *Chem. Soc. Rev.*, 2009, **38**, 1430-1449.
50. F. Fredoueil, M. Evain, D. Massiot, M. Bujoli-Doeuff and B. Bujoli, *J. Mater. Chem.*, 2001, **11**, 1106-1110.
51. B. L. Zhang and A. Clearfield, *J. Am. Chem. Soc.*, 1997, **119**, 2751-2752.
52. J. L. Snover, H. Byrd, E. P. Suponeva, E. Vicenzi and M. E. Thompson, *Chem. Mater.*, 1996, **8**, 1490-1499.
53. G. Alberti, R. Vivani, F. Marmottini and P. Zappelli, *J. Porous Mater.*, 1998, **5**, 205-220.
54. G. Alberti, U. Costantino, F. Marmottini, R. Vivani and P. Zappelli, *Angew. Chem. Int. Ed.*, 1993, **32**, 1357-1359.
55. J. Le Bideau, C. Payen, P. Palvadeau and B. Bujoli, *Inorg. Chem.*, 1994, **33**, 4885-4890.
56. K. Maeda, *Microporous Mesoporous Mater.*, 2004, **73**, 47-55.
57. K. Maeda, Y. Kiyozumi and F. Mizukami, *Angew. Chem. Int. Ed.*, 1994, **33**, 2335-2337.
58. K. Maeda, J. Akimoto, Y. Kiyozumi and F. Mizukami, *Angew. Chem. Int. Ed.*, 1995, **34**, 1199-1201.
59. K. Maeda, J. Akimoto, Y. Kiyozumi and F. Mizukami, *Journal of the Chemical Society-Chemical Communications*, 1995, 1033-1034.
60. D. L. Lohse and S. C. Sevov, *Angew. Chem. Int. Ed.*, 1997, **36**, 1619-1621.
61. C. A. Merrill and A. K. Cheetham, *Inorg. Chem.*, 2005, **44**, 5273-5277.
62. C. A. Merrill and A. K. Cheetham, *Inorg. Chem.*, 2007, **46**, 278-284.

63. R. B. Fu, X. T. Wu, S. M. Hu, J. J. Zhang, Z. Y. Fu and W. X. Du, *Polyhedron*, 2003, **22**, 2739-2744.
64. W. Ouellette, M. H. Yu, C. J. O'Connor and J. Zubieta, *Inorg. Chem.*, 2006, **45**, 3224-3239.
65. M. P. Attfield, Z. Yuan, H. G. Harvey and W. Clegg, *Inorg. Chem.*, 2010, **49**, 2656-2666.
66. R. LaDuca, D. Rose, J. R. D. DeBord, R. C. Haushalter, C. J. Oconnor and J. Zubieta, *J. Solid State Chem.*, 1996, **123**, 408-412.
67. J. A. Groves, S. R. Miller, S. J. Warrender, C. Mellot-Draznieks, P. Lightfoot and P. A. Wright, *Chem. Commun. (Cambridge, U. K.)*, 2006, 3305-3307.
68. M. T. Wharmby, J. P. S. Mowat, S. P. Thompson and P. A. Wright, *J. Am. Chem. Soc.*, 2011, **133**, 1266-1269.
69. J. A. Groves, N. F. Stephens, P. A. Wright and P. Lightfoot, *Solid State Sci.*, 2006, **8**, 397-403.
70. S. R. Miller, G. M. Pearce, P. A. Wright, F. Bonino, S. Chavan, S. Bordiga, I. Margiolaki, N. Guillou, G. Ferey, S. Bourrelly and P. L. Llewellyn, *J. Am. Chem. Soc.*, 2008, **130**, 15967-15981.
71. J. P. S. Mowat, J. A. Groves, M. T. Wharmby, S. R. Miller, Y. Li, P. Lightfoot and P. A. Wright, *J. Solid State Chem.*, 2009, **182**, 2769-2778.
72. M. T. Wharmby, S. R. Miller, J. A. Groves, I. Margiolaki, S. E. Ashbrook and P. A. Wright, *Dalton Trans.*, 2010, **39**, 6389-6391.
73. G. B. Hix, A. Turner, B. M. Kariuki, M. Tremayne and E. J. MacLean, *J. Mater. Chem.*, 2002, **12**, 3220-3227.
74. G. B. Hix, A. Turner, L. Vahter and B. M. Kariuki, *Microporous Mesoporous Mater.*, 2007, **99**, 62-69.
75. A. Turner, P. A. Jaffres, E. J. MacLean, D. Villemin, V. McKee and G. B. Hix, *Dalton Trans.*, 2003, 1314-1319.
76. S. Lodhia, A. Turner, M. Papadaki, K. D. Demadis and G. B. Hix, *Cryst. Growth Des.*, 2009, **9**, 1811-1822.
77. S. Drumel, P. Janvier, P. Barboux, M. Bujolidoeuff and B. Bujoli, *Inorg. Chem.*, 1995, **34**, 148-156.
78. N. Stock, S. A. Frey, G. D. Stucky and A. K. Cheetham, *Journal of the Chemical Society-Dalton Transactions*, 2000, 4292-4296.
79. A. Cabeza, M. A. G. Aranda and S. Bruque, *J. Mater. Chem.*, 1998, **8**, 2479-2485.
80. S. Ayyappan, G. D. de Delgado, A. K. Cheetham, G. Ferey and C. N. R. Rao, *Journal of the Chemical Society-Dalton Transactions*, 1999, 2905-2907.
81. Z. Chen, Y. Zhou, L. Weng and D. Zhao, *Cryst. Growth Des.*, 2008, **8**, 4045-4053.

82. J.-T. Li, D.-K. Cao, B. Liu, Y.-Z. Li and L.-M. Zheng, *Cryst. Growth Des.*, 2008, **8**, 2950-2953.
83. R. Zou, A. I. Abdel-Fattah, H. Xu, Y. Zhao and D. D. Hickmott, *CrystEngComm*, 2010, **12**, 1337-1353.
84. M. Dinca and J. R. Long, *Angew. Chem. Int. Ed.*, 2008, **47**, 6766-6779.
85. N. L. Rosi, J. Eckert, M. Eddaoudi, D. T. Vodak, J. Kim, M. O'Keeffe and O. M. Yaghi, *Science*, 2003, **300**, 1127-1129.
86. P. B énard and R. Chahine, in *Solid-State Hydrogen Storage: Materials and Chemistry*, ed. G. Walker, Woodhead Publ Ltd, Cambridge, 2008, pp. 288-291.
87. A. Mavrandonakis, E. Tylianakis, A. K. Stubos and G. E. Froudakis, *J. Phys. Chem. C*, 2008, **112**, 7290-7294.
88. H. Furukawa, M. A. Miller and O. M. Yaghi, *J. Mater. Chem.*, 2007, **17**, 3197-3204.
89. D. Saha, Z. Wei and S. Deng, *Int. J. Hydrogen Energy*, 2008, **33**, 7479-7488.
90. O. M. Yaghi, *DOE Hydrogen and Fuel Cells Program 2011 Annual Progress Report*, 2011, 474-478.
91. U. S. Department of Energy, Targets for on-board hydrogen storage systems: Current R&D focus is on 2015 targets with potential to meet ultimate targets (http://www1.eere.energy.gov/hydrogenandfuelcells/storage/current_technology.html) (accessed May 2012).
92. L. J. Murray, M. Dinca and J. R. Long, *Chem. Soc. Rev.*, 2009, **38**, 1294-1314.
93. S. Ma and H.-C. Zhou, *Chem. Commun. (Cambridge, U. K.)*, 2010, **46**, 44-53.
94. H. Kabbour, T. F. Baumann, J. H. Satcher, Jr., A. Saulnier and C. C. Ahn, *Chem. Mater.*, 2006, **18**, 6085-6087.
95. K. M. Thomas, *Dalton Trans.*, 2009, 1487-1505.
96. A. G. Wong-Foy, A. J. Matzger and O. M. Yaghi, *J. Am. Chem. Soc.*, 2006, **128**, 3494-3495.
97. M. Dinca and J. R. Long, *J. Am. Chem. Soc.*, 2005, **127**, 9376-9377.
98. S. Q. Ma, D. F. Sun, M. Ambrogio, J. A. Fillinger, S. Parkin and H. C. Zhou, *J. Am. Chem. Soc.*, 2007, **129**, 1858-1859.
99. Q. Y. Wang and J. K. Johnson, *J. Chem. Phys.*, 1999, **110**, 577-586.
100. J. Luo, H. Xu, Y. Liu, Y. Zhao, L. L. Daemen, C. Brown, T. V. Timofeeva, S. Ma and H.-C. Zhou, *J. Am. Chem. Soc.*, 2008, **130**, 9626-9627.
101. S. S. Kaye and J. R. Long, *J. Am. Chem. Soc.*, 2005, **127**, 6506-6507.
102. B. Chen, X. Zhao, A. Putkham, K. Hong, E. B. Lobkovsky, E. J. Hurtado, A. J. Fletcher and K. M. Thomas, *J. Am. Chem. Soc.*, 2008, **130**, 6411-6423.
103. M. Dinca, A. Dailly, Y. Liu, C. M. Brown, D. A. Neumann and J. R. Long, *J. Am. Chem. Soc.*, 2006, **128**, 16876-16883.

104. Y. G. Lee, H. R. Moon, Y. E. Cheon and M. P. Suh, *Angew. Chem. Int. Ed.*, 2008, **47**, 7741-7745.
105. J. Sculley, D. Q. Yuan and H. C. Zhou, *Energy Environ. Sci.*, 2011, **4**, 2721-2735.
106. S. Horike, M. Dinca, K. Tamaki and J. R. Long, *J. Am. Chem. Soc.*, 2008, **130**, 5854-5855.
107. Y. K. Hwang, D.-Y. Hong, J.-S. Chang, S. H. Jhung, Y.-K. Seo, J. Kim, A. Vimont, M. Daturi, C. Serre and G. Ferey, *Angew. Chem. Int. Ed.*, 2008, **47**, 4144-4148.
108. P. Horcajada, C. Serre, M. Vallet-Regi, M. Sebban, F. Taulelle and G. Ferey, *Angew. Chem. Int. Ed.*, 2006, **45**, 5974-5978.
109. C. Biswas, P. Mukherjee, M. G. B. Drew, C. J. Gomez-Garcia, J. M. Clemente-Juan and A. Ghosh, *Inorg. Chem.*, 2007, **46**, 10771-10780.
110. Q.-X. Jia, Y.-Q. Wang, Q. Yue, Q.-L. Wang and E.-Q. Gao, *Chem. Commun. (Cambridge, U. K.)*, 2008, 4894-4896.
111. B. Chen, L. Wang, F. Zapata, G. Qian and E. B. Lobkovsky, *J. Am. Chem. Soc.*, 2008, **130**, 6718-6719.
112. L.-G. Qiu, Z.-Q. Li, Y. Wu, W. Wang, T. Xu and X. Jiang, *Chem. Commun. (Cambridge, U. K.)*, 2008, 3642-3644.
113. V. J. Inglezakis, *J. Colloid Interface Sci.*, 2005, **281**, 68-79.
114. V. K. Pecharsky and P. Y. Zavalij, *Fundamentals of powder diffraction and structural characterization of materials*, 2nd edn., Springer, New York, 2009.
115. R. J. D. Tilley, *Crystals and crystal structures*, John Wiley, Hoboken, NJ, 2006.
116. C. Hammond, *The basics of crystallography and diffraction*, Oxford University Press, Oxford; New York, 2009.
117. W. I. F. David, *Structure determination from powder diffraction data*, Oxford University Press, Oxford ; New York, 2002.
118. M. F. C. Ladd and R. A. Palmer, *Structure determination by X-ray crystallography*, 3rd edn., Plenum Press, New York, 1993.
119. R. L. Snyder, J. Fiala and H. J. Bunge, *Defect and microstructure analysis by diffraction*, Oxford University Press, Oxford ; New York, 1999.
120. R. Shirley, *The CRYSFIRE System for Automatic Powder Indexing: User's Manual*, The Lattice Press, 41 Guilford Park Avenue, Guilford, Surry, GU42 47NL, England, 2000.
121. D. Taupin, *J. Appl. Crystallogr.*, 1973, **6**, 380-385.
122. A. Boultif and D. Louer, *J. Appl. Crystallogr.*, 1991, **24**, 987-993.
123. P. E. Werner, L. Eriksson and M. Westdahl, *J. Appl. Crystallogr.*, 1985, **18**, 367-370.
124. J. Laugier and B. Bochu, *LMGP Suite of Programs*, Laboratoire des Matériaux et du Génie Physique, France, 2002.

125. A. Le Bail, *Powder Diffr.*, 2005, **20**, 316-326.
126. A. C. Larson and R. B. Von Dreele, "*General Structure Analysis System (GSAS)*", *Los Alamos National Laboratory Report LAUR*, 1994, 86-748
127. B. H. Toby, *J. Appl. Crystallogr.*, 2001, **34**, 210-213.
128. M. Savonnet, E. Kockrick, A. Camarata, D. Bazer-Bachi, N. Bats, V. Lecocq, C. Pinel and D. Farrusseng, *New J. Chem.*, 2011, **35**, 1892-1897.
129. L. B. McCusker, R. B. Von Dreele, D. E. Cox, D. Louer and P. Scardi, *J. Appl. Crystallogr.*, 1999, **32**, 36-50.
130. PDF-4 full file relational database, ed. K. Soorya, International Centre for Diffraction Data, Newtown Square, PA, USA, 2011.
131. T. Steiner, *Angewandte Chemie International Edition*, 2002, **41**, 48-76.
132. G. B. Hix, B. M. Kariuki, S. Kitchin and M. Tremayne, *Inorg. Chem.*, 2001, **40**, 1477-1481.
133. G. B. Hix, D. S. Wragg, P. A. Wright and R. E. Morris, *Journal of the Chemical Society-Dalton Transactions*, 1998, 3359-3361.
134. H. W. Langmi, A. Walton, M. M. Al-Mamouri, S. R. Johnson, D. Book, J. D. Speight, P. P. Edwards, I. Gameson, P. A. Anderson and I. R. Harris, *J. Alloys Compd.*, 2003, **356**, 710-715.
135. H. W. Langmi, D. Book, A. Walton, S. R. Johnson, M. M. Al-Mamouri, J. D. Speight, P. P. Edwards, I. R. Harris and P. A. Anderson, *J. Alloys Compd.*, 2005, **404**, 637-642.
136. P. Kumar, C. Y. Sung, O. Muraza, M. Cococcioni, S. Al Hashimi, A. McCormick and M. Tsapatsis, *Microporous Mesoporous Mater.*, 2011, **146**, 127-133.
137. P. Horcajada, S. Surble, C. Serre, D.-Y. Hong, Y.-K. Seo, J.-S. Chang, J.-M. Greneche, I. Margiolaki and G. Ferey, *Chem. Commun. (Cambridge, U. K.)*, 2007, 2820-2822.
138. S. Bordiga, L. Regli, F. Bonino, E. Groppo, C. Lamberti, B. Xiao, P. S. Wheatley, R. E. Morris and A. Zecchina, *Phys. Chem. Chem. Phys.*, 2007, **9**, 2676-2685.
139. R. Custelcean and B. A. Moyer, *Eur. J. Inorg. Chem.*, 2007, 1321-1340.
140. S. Qiu and G. Zhu, *Coord. Chem. Rev.*, 2009, **253**, 2891-2911.
141. J. M. Taylor, R. K. Mah, I. L. Moudrakovski, C. I. Ratcliffe, R. Vaidhyanathan and G. K. H. Shimizu, *J. Am. Chem. Soc.*, 2010, **132**, 14055-14057.
142. C. Duan, M. Wei, D. Guo, C. He and Q. Meng, *J. Am. Chem. Soc.*, 2010, **132**, 3321-3330.
143. Y. Marcus, *Journal of the Chemical Society-Faraday Transactions*, 1991, **87**, 2995-2999.
144. S. V. Priya, J. H. Mabel, S. Gopalakrishnan, M. Palanichamy and V. Murugesan, *J. Porous Mater.*, 2009, **16**, 419-427.
145. P. Castaldi, L. Santona, S. Enzo and P. Melis, *J. Hazard. Mater.*, 2008, **156**, 428-434.

146. R. Wei, M. Guo and J. Wang, *Chin. J. Chem. Eng.*, 2009, **17**, 58-63.
147. S. H. Yang, G. S. B. Martin, J. J. Titman, A. J. Blake, D. R. Allan, N. R. Champness and M. Schroder, *Inorg. Chem.*, 2011, **50**, 9374-9384.
148. S. L. Rock, *J. Am. Oil Chem. Soc.*, 1983, **60**, 1019-1020.
149. W. I. F. David, *Structure determination from powder diffraction data*, Oxford University Press, Oxford; New York, 2002.
150. W. I. F. David and K. Shankland, *Acta Crystallographica Section A*, 2008, **64**, 52-64.
151. M. Brunelli, J. P. Wright, G. R. M. Vaughan, A. J. Mora and A. N. Fitch, *Angew. Chem. Int. Ed.*, 2003, **42**, 2029-2032.
152. V. F. Sears, *Neutron News*, 1992, **3**, 26-37.
153. T. K. A. Hoang and D. M. Antonelli, *Adv. Mater. (Weinheim, Ger.)*, 2009, **21**, 1787-1800.
154. T. K. A. Hoang, M. I. Webb, H. V. Mai, A. Hamaed, C. J. Walsby, M. Trudeau and D. M. Antonelli, *J. Am. Chem. Soc.*, 2010, **132**, 11792-11798.
155. A. Hamaed, T. K. A. Hoang, G. Moula, R. Aroca, M. L. Trudeau and D. M. Antonelli, *J. Am. Chem. Soc.*, 2011, **133**, 15434-15443.
156. G. J. Kubas, *J. Organomet. Chem.*, 2001, **635**, 37-68.
157. J. A. Botas, G. Calleja, M. Sanchez-Sanchez and M. Gisela Orcajo, *Langmuir*, 2010, **26**, 5300-5303.
158. A. Nord, *Acta Crystallographica Section B*, 1984, **40**, 191-194.
159. C. Calvo, *Can. J. Chem.*, 1965, **43**, 1147-1153.
160. A. G. Nord and T. Stefanidis, *Polyhedron*, 1982, **1**, 349-353.
161. A. G. Nord, *Mater. Res. Bull.*, 1977, **12**, 563-568.
162. O. V. Karimova, O. V. Yakubovich and V. S. Urusov, *Vestnik Moskovskogo Universiteta, Geologiya*, 1997, **52**, 35-45.
163. R. Shannon, *Acta Crystallographica Section A*, 1976, **32**, 751-767.
164. Y. Cheng, H. Kajiro, H. Noguchi, A. Kondo, T. Ohba, Y. Hattori, K. Kaneko and H. Kanoh, *Langmuir*, 2011, **27**, 6905-6909.
165. A. P. Nelson, O. K. Farha, K. L. Mulfort and J. T. Hupp, *J. Am. Chem. Soc.*, 2009, **131**, 458-460.
166. L. Ma, A. Jin, Z. Xie and W. Lin, *Angew. Chem. Int. Ed.*, 2009, **48**, 9905-9908.
167. H. J. Park, D. W. Lim, W. S. Yang, T. R. Oh and M. P. Suh, *Chem.-Eur. J.*, 2011, **17**, 7251-7260.

Appendix

Appendix 1 Crystallographic Data of BIRM-1

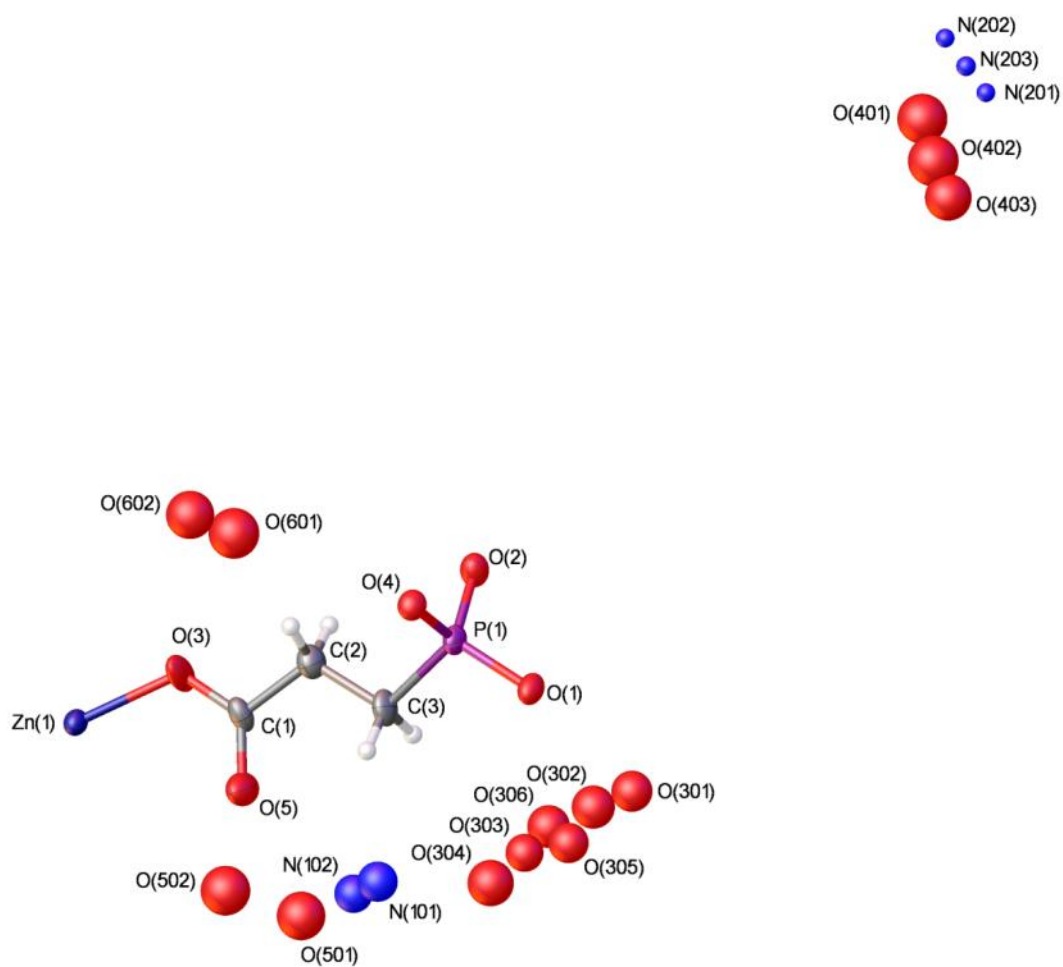


Fig. A1.1 The asymmetric unit of BIRM-1 with ellipsoids drawn at the 50 % probability level.

Table A1.1 Atomic coordinates ($\times 10^4$), occupancies and equivalent isotropic displacement parameters ($\times 10^3$) for BIRM-1, U_{eq} is defined as one third of the trace of the orthogonalized U_{ij} tensor.

Atom	Mult.	<i>x</i>	<i>y</i>	<i>z</i>	Occupancy	U_{eq}
C(1)	32	3057(3)	2338(3)	1694(4)	1	27(2)
C(2)	32	3031(3)	3018(3)	1788(4)	1	32(2)
C(3)	32	3495(3)	3285(3)	2308(4)	1	29(2)
O(1)	32	3853(2)	4313(2)	2956(3)	1	28(1)
O(2)	32	3270(2)	4381(2)	1739(3)	1	32(1)
O(3)	32	2658(3)	2133(2)	1256(3)	1	50(2)
O(4)	32	2738(2)	4093(2)	2917(3)	1	26(1)
O(5)	32	3410(3)	2026(2)	2047(4)	1	47(2)
P(1)	32	3333(1)	4061(1)	2498(1)	1	24(1)
Zn(1)	32	2497(1)	1281(1)	1143(1)	1	23(1)
N(101)	32	4672(14)	2285(15)	2062(18)	0.25	46(8)
N(102)	32	4684(14)	2062(15)	1919(17)	0.25	42(7)
N(201)	16	2923(6)	9577(6)	1250	0.35	10(4)
N(202)	32	2683(11)	9473(11)	425(15)	0.18	10(5)
N(203)	32	2803(13)	9528(14)	859(17)	0.15	11(6)
O(301)	32	5098(12)	4285(15)	2733(14)	0.25	48(6)
O(302)	32	5047(16)	3970(20)	2630(20)	0.20	53(9)
O(303)	32	4776(13)	3473(16)	3219(17)	0.20	41(7)
O(304)	32	4840(20)	3110(20)	3120(20)	0.15	61(12)
O(305)	32	4980(30)	3740(30)	3090(40)	0.10	46(16)
O(306)	32	4920(30)	3640(30)	2710(40)	0.10	52(17)
O(401)	32	3272(10)	8829(9)	-56(13)	0.38	71(6)
O(402)	32	3455(17)	8744(15)	320(20)	0.27	73(9)
O(403)	32	3680(30)	8680(20)	540(30)	0.15	62(15)
O(501)	32	3972(13)	1974(13)	3482(16)	0.25	67(7)
O(502)	32	3400(20)	1710(20)	3570(30)	0.15	70(13)
O(601)	16	2500	2905(13)	0	0.40	73(7)
O(602)	32	2110(40)	2790(30)	140(40)	0.10	66(19)

Note: The occupancies of non-framework atoms are all fixed during the refinement.

Table A1.2 Bond lengths [Å] for BIRM-1.

Bond	Bond Length	Bond	Bond Length
C(1)-O(5)	1.222(9)	O(1)-Zn(1) ^[a]	1.958(5)
C(1)-O(3)	1.268(8)	O(2)-P(1)	1.531(5)
C(1)-C(2)	1.527(9)	O(2)-Zn(1) ^[b]	1.920(5)
C(2)-C(3)	1.509(9)	O(3)-Zn(1)	1.943(5)
C(2)-H(2A)	0.99	O(4)-P(1)	1.524(5)
C(2)-H(2B)	0.99	O(4)-Zn(1) ^[c]	1.936(5)
C(3)-P(1)	1.799(7)	Zn(1)-O(2) ^[d]	1.920(5)
C(3)-H(3A)	0.99	Zn(1)-O(4) ^[c]	1.936(5)
C(3)-H(3B)	0.99	Zn(1)-O(1) ^[e]	1.958(4)
O(1)-P(1)	1.524(5)		

Note: Symmetry transformations used to generate equivalent atoms: [a] $y+1/4, x+1/4, z+1/4$; [b] $y+1/4, -x+3/4, -z+1/4$; [c] $-x+1/2, -y+1/2, -z+1/2$; [d] $-y+3/4, x-1/4, -z+1/4$; [e] $y-1/4, x-1/4, z-1/4$.

Table A1.3 Bond angles [°] for BIRM-1.

Bond Angle	Angle	Bond Angle	Angle
O(5)-C(1)-O(3)	124.2(6)	P(1)-O(2)-Zn(1) ^[b]	126.4(3)
O(5)-C(1)-C(2)	122.3(6)	C(1)-O(3)-Zn(1)	123.1(5)
O(3)-C(1)-C(2)	113.4(6)	P(1)-O(4)-Zn(1) ^[c]	129.3(3)
C(3)-C(2)-C(1)	115.6(6)	O(1)-P(1)-O(4)	112.7(3)
C(3)-C(2)-H(2A)	108.4	O(1)-P(1)-O(2)	111.5(3)
C(1)-C(2)-H(2A)	108.4	O(4)-P(1)-O(2)	109.0(3)
C(3)-C(2)-H(2B)	108.4	O(1)-P(1)-C(3)	107.6(3)
C(1)-C(2)-H(2B)	108.4	O(4)-P(1)-C(3)	108.2(3)
H(2A)-C(2)-H(2B)	107.4	O(2)-P(1)-C(3)	107.6(3)
C(2)-C(3)-P(1)	110.9(5)	O(2) ^[d] -Zn(1)-O(4) ^[c]	104.05(19)
C(2)-C(3)-H(3A)	109.5	O(2) ^[d] -Zn(1)-O(3)	118.9(3)
P(1)-C(3)-H(3A)	109.5	O(4) ^[c] -Zn(1)-O(3)	112.5(2)
C(2)-C(3)-H(3B)	109.5	O(2) ^[d] -Zn(1)-O(1) ^[e]	113.0(2)
P(1)-C(3)-H(3B)	109.5	O(4) ^[c] -Zn(1)-O(1) ^[e]	111.21(19)
H(3A)-C(3)-H(3B)	108	O(3)-Zn(1)-O(1) ^[e]	97.3(2)
P(1)-O(1)-Zn(1) ^[a]	123.9(3)		

Note: Symmetry transformations used to generate equivalent atoms: [a] $y+1/4, x+1/4, z+1/4$; [b] $y+1/4, -x+3/4, -z+1/4$; [c] $-x+1/2, -y+1/2, -z+1/2$; [d] $-y+3/4, x-1/4, -z+1/4$; [e] $y-1/4, x-1/4, z-1/4$.

Table A1.4 Anisotropic displacement parameters ($\text{\AA}^2 \times 10^3$) for BIRM-1.

	U^{11}	U^{22}	U^{33}	U^{23}	U^{13}	U^{12}
C(1)	41(4)	17(3)	23(3)	1(3)	2(3)	-7(3)
C(2)	35(4)	24(3)	36(4)	-5(3)	-2(3)	-2(3)
C(3)	36(4)	20(3)	32(4)	-10(3)	0(3)	-6(3)
O(1)	24(2)	23(2)	38(3)	-10(2)	-5(2)	0(2)
O(2)	37(3)	28(3)	30(3)	0(2)	-7(2)	-7(2)
O(3)	76(4)	19(2)	53(3)	-2(2)	-36(3)	-12(3)
O(4)	25(2)	25(2)	27(2)	-4(2)	0(2)	0(2)
O(5)	47(3)	25(3)	69(4)	-11(3)	-24(3)	3(2)
P(1)	24(1)	19(1)	29(1)	-6(1)	-4(1)	-3(1)
Zn(1)	21(1)	18(1)	31(1)	-3(1)	-6(1)	-1(1)

Table A1.5 Hydrogen coordinates ($\times 10^4$) and isotropic displacement parameters ($\text{\AA}^2 \times 10^3$) for BIRM-1

Atom	x	y	z	U_{eq}
H(2A)	3076	3205	1285	38
H(2B)	2628	3127	1980	38
H(3A)	3896	3252	2073	35
H(3B)	3501	3058	2787	35

Table A1.6 Torsion angles ($^\circ$) for BIRM-1

Bond	Angle	Bond	Angle
O(5)-C(1)-C(2)-C(3)	3.7(10)	Zn(1) ^[b] -O(2)-P(1)-O(1)	2.4(5)
O(3)-C(1)-C(2)-C(3)	179.7(7)	Zn(1) ^[b] -O(2)-P(1)-O(4)	127.4(4)
C(1)-C(2)-C(3)-P(1)	-169.8(5)	Zn(1) ^[b] -O(2)-P(1)-C(3)	-115.5(4)
O(5)-C(1)-O(3)-Zn(1)	5.6(11)	C(2)-C(3)-P(1)-O(1)	-174.2(5)
C(2)-C(1)-O(3)-Zn(1)	-170.3(5)	C(2)-C(3)-P(1)-O(4)	63.7(6)
Zn(1) ^[a] -O(1)-P(1)-O(4)	-35.0(4)	C(2)-C(3)-P(1)-O(2)	-53.9(6)
Zn(1) ^[a] -O(1)-P(1)-O(2)	88.0(4)	C(1)-O(3)-Zn(1)-O(2) ^[d]	-62.4(7)
Zn(1) ^[a] -O(1)-P(1)-C(3)	-154.2(3)	C(1)-O(3)-Zn(1)-O(4) ^[c]	59.6(7)
Zn(1) ^[c] -O(4)-P(1)-O(1)	-61.6(4)	C(1)-O(3)-Zn(1)-O(1) ^[e]	176.2(6)
Zn(1) ^[c] -O(4)-P(1)-O(2)	174.0(3)	Zn(1) ^[c] -O(4)-P(1)-C(3)	57.3(4)

Note: Symmetry transformations used to generate equivalent atoms: [a] $y+1/4, x+1/4, z+1/4$; [b] $y+1/4, -x+3/4, -z+1/4$; [c] $-x+1/2, -y+1/2, -z+1/2$; [d] $-y+3/4, x-1/4, -z+1/4$; [e] $y-1/4, x-1/4, z-1/4$.

Appendix 2 Index Details

2.1 K⁺-BIRM-1

After indexing by the Crysfire, the Unit cell parameters were then determined by Chekcell: $a = 22.201(3) \text{ \AA}$, $c = 17.8576(1) \text{ \AA}$, $I4_1/acd$, FOM (M20) = 21.13. Then this cell was refined by model-less Le Bail fitting in the programme of GSAS (Figure A2.1) and gives out the final unit cell parameters: $a = 22.1937(2)$, $c = 17.8525(1)$, $I4_1/acd$.

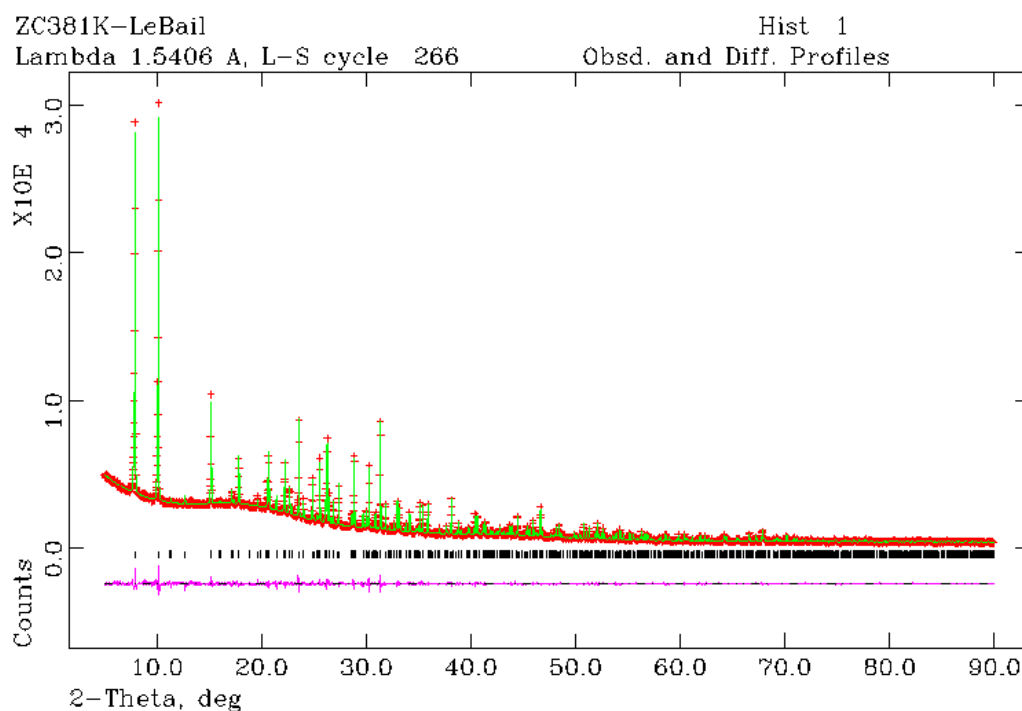


Fig. A2.1 Final observed (crossed), calculated (solid line), difference (below) and reflection positions for structure less Le Bail refinements against powder XRD data for potassium-exchanged BIRM-1 product, $\chi^2 = 1.937$, $R_{wp} = 3.65\%$, $R_p = 2.67\%$.

2.2 Li⁺-BIRM-1

After indexing by the Crysfire, the Unit cell parameters were then determined by Chekcell: $a = 22.228(7)$ Å, $c = 17.9179(4)$ Å, $I4_1/acd$, FOM (M20) = 18.59. Then this cell was refined by model-less Le Bail fitting in the programme of GSAS (Figure A2.2) and gives out the final unit cell parameters: $a = 22.2099(4)$, $c = 17.9155(3)$, $I4_1/acd$.

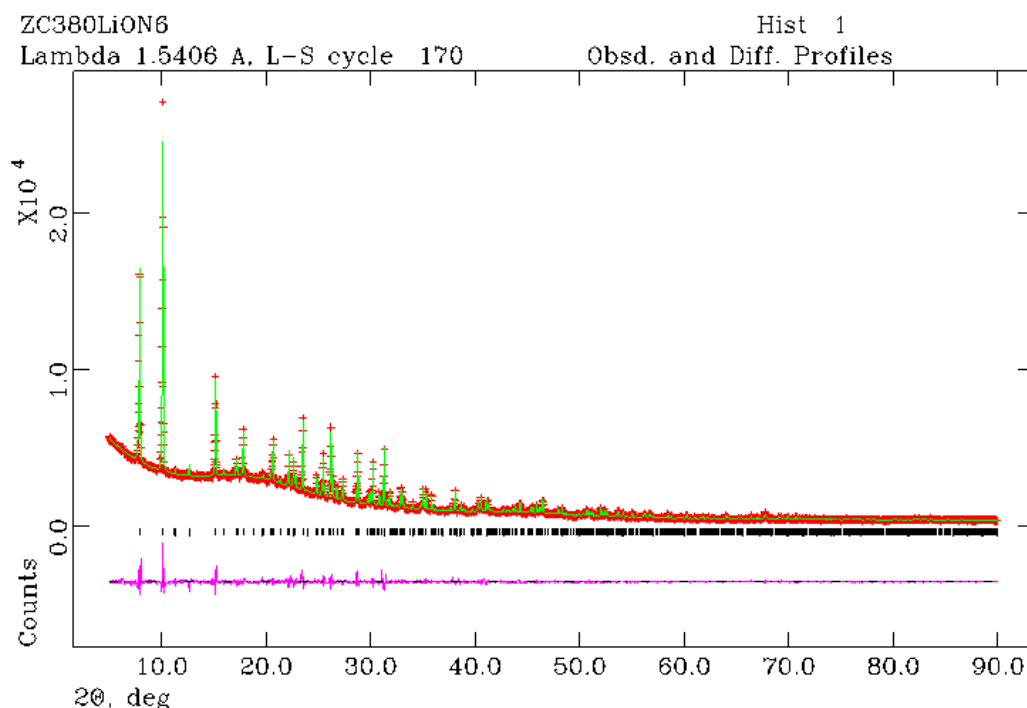


Fig. A2.2 Final observed (crossed), calculated (solid line), difference (below) and reflection positions for structure less Le Bail refinements against powder XRD data for lithium-exchanged BIRM-1 product, $\chi^2 = 3.257$, $R_{wp} = 4.62\%$, $R_p = 3.12\%$.

2.3 Na⁺-BIRM-1

After indexing by the Crysfire, the Unit cell parameters were then determined by Chekcell: $a = 22.20(1) \text{ \AA}$, $b = 21.517(9) \text{ \AA}$, $c = 18.06(1) \text{ \AA}$, $Pnma$, FOM (M20) = 21.4. Then this cell was refined by model-less Le Bail fitting in the programme of GSAS (Figure A2.3) and gives out the final unit cell parameters: $a = 22.2150(5)$, $b = 21.5250(5)$, $c = 18.0773(3)$, $Pnma$.

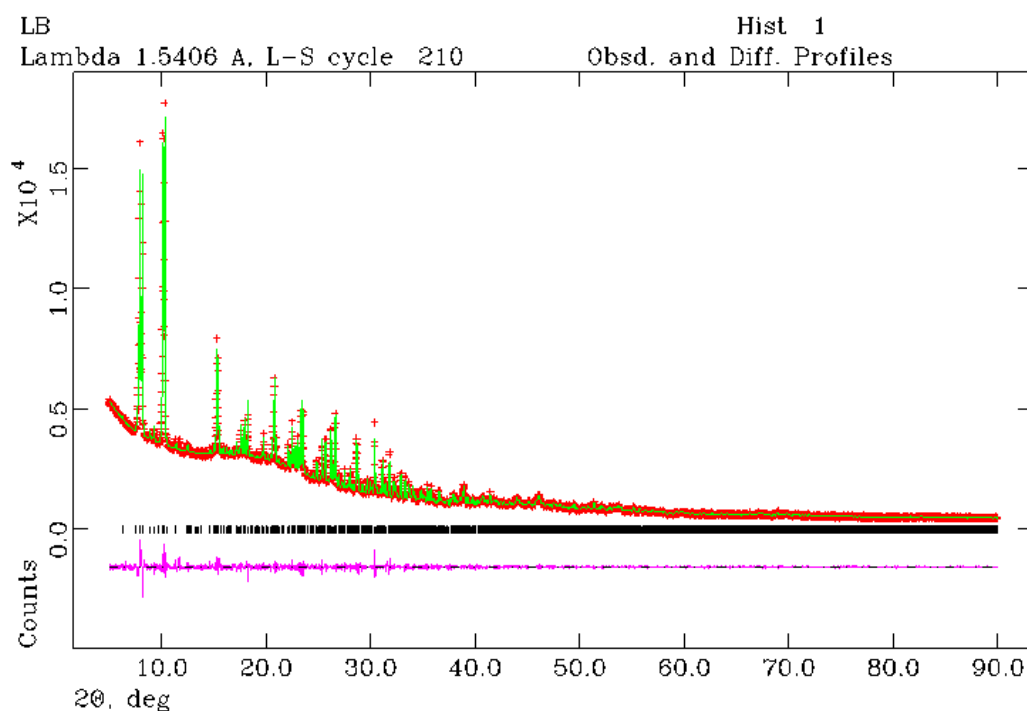


Fig. A2.3 Final observed (crossed), calculated (solid line), difference (below) and reflection positions for structure less Le Bail refinements against powder XRD data for sodium-exchanged BIRM-1 product, $\chi^2 = 1.792$, $R_{wp} = 3.37\%$, $R_p = 2.47\%$.

2.4 Co²⁺-BIRM-1

After indexing by the Crysfire, the Unit cell parameters were then determined by Chekcell: $a = 18.237(4)$ $b = 21.604(6)$ Å, $c = 22.540(5)$ Å, $Ibca$, FOM (M20) = 9.2. Then this cell was refined by model-less Le Bail fitting in the programme of GSAS (Figure A2.4) and gives out the final unit cell parameters: $a = 18.1984(4)$ $b = 21.5299(6)$, $c = 22.4930(5)$, $Ibca$.

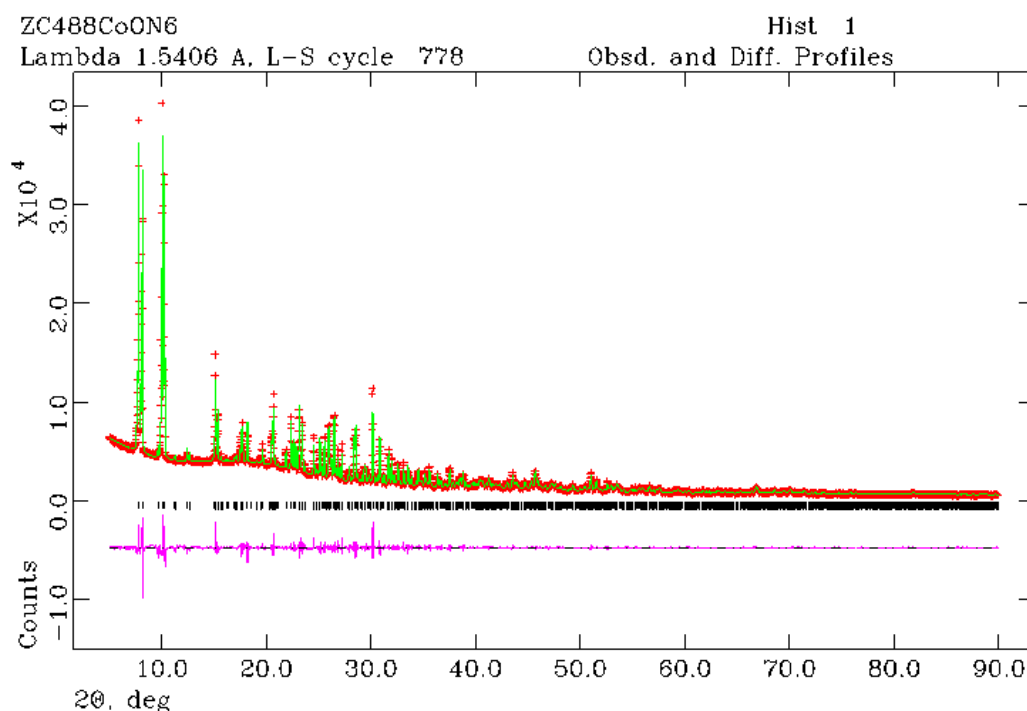


Fig. A2.4 Final observed (crossed), calculated (solid line), difference (below) and reflection positions for structure less Le Bail refinements against powder XRD data for Co²⁺-BIRM-1, $\chi^2 = 6.306$, $R_{wp} = 5.28\%$, $R_p = 3.60\%$.

2.5 Mn²⁺-BIRM-1

After indexing by the Crysfire, the Unit cell parameters were then determined by Chekcell: $a = 22.525(8)$ $b = 21.258(7)$ Å, $c = 18.448(5)$ Å, P_{ban} , FOM (M20) = 27. Then this cell was refined by model-less Le Bail fitting in the programme of GSAS (Figure A2.5) and gives out the final unit cell parameters: $a = 22.5522(5)$ $b = 21.2562(4)$, $c = 18.4730(4)$, P_{ban} .

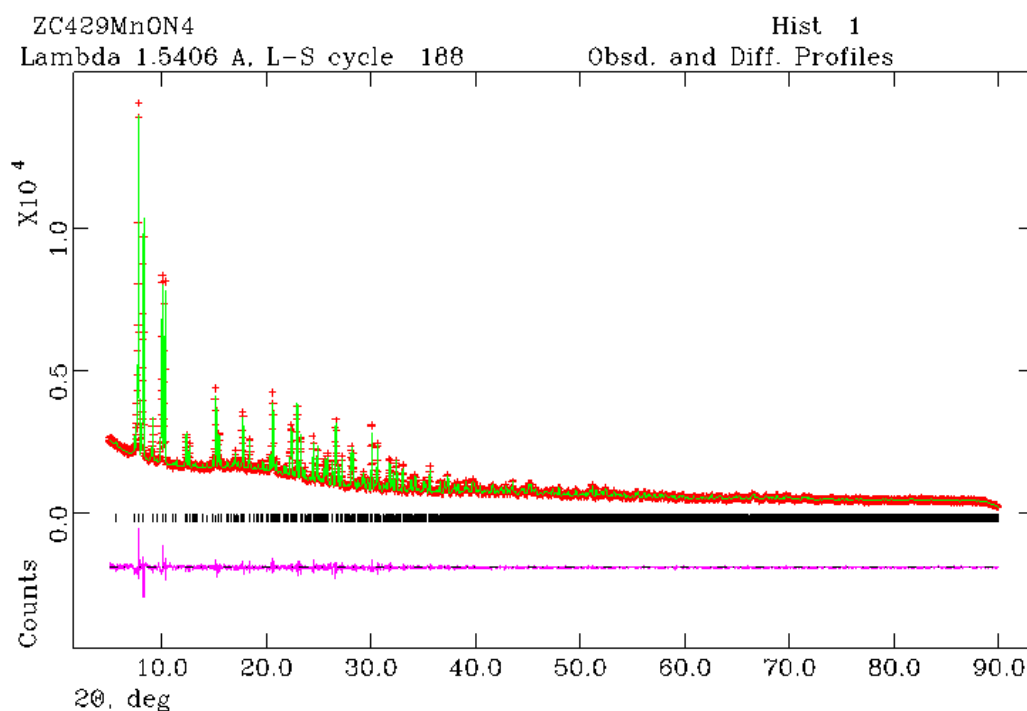


Fig. A2.5 Final observed (crossed), calculated (solid line), difference (below) and reflection positions for structure less Le Bail refinements against powder XRD data for Mn²⁺-BIRM-1, $\chi^2 = 1.637$, $R_{wp} = 4.06\%$, $R_p = 3.09\%$.

2.6 Mg²⁺-BIRM-1

After indexing by the Crysfire, the Unit cell parameters were then determined by Chekcell: $a = 18.203(3)$ $b = 21.585(4)$ Å, $c = 22.503(4)$ Å, *Ibca*, FOM (M20) = 13.88. Then this cell was refined by model-less Le Bail fitting in the programme of GSAS (Figure A2.6) and gives out the final unit cell parameters: $a = 18.1880(4)$ $b = 21.5354(6)$, $c = 22.4793(6)$, *Ibca*.

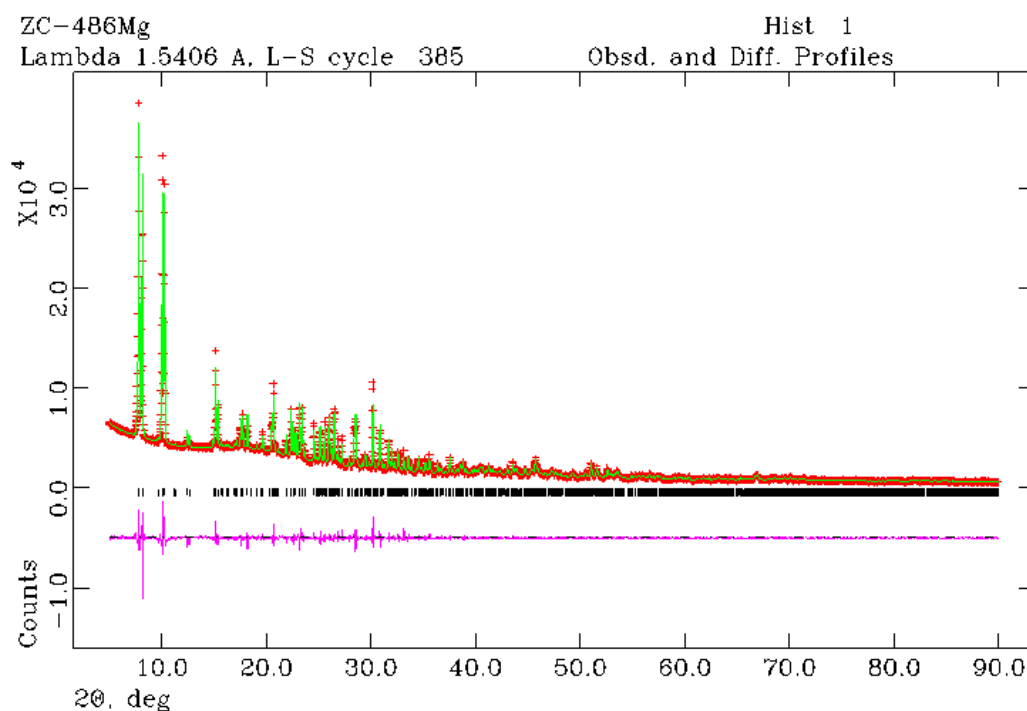


Fig. A2.6 Final observed (crossed), calculated (solid line), difference (below) and reflection positions for structure less Le Bail refinements against powder XRD data for Mg²⁺-BIRM-1, $\chi^2 = 5.441$, $R_{wp} = 4.93\%$, $R_p = 3.38\%$.

Appendix 3 Flame Photometry

3.1 Li⁺-BIRM-1

3.1.1 Li⁺-BIRM-1 Sample Solution Preparation

0.05 g lithium-exchanged products from three different exchanged samples were dissolved in 100 ml for volumetric flask with the help of 1.5 ml of HNO₃ (1M).

3.1.2 Lithium ion Content Calculation

Lithium ion concentrations of the three exchanged sample can be obtained from the standard curve. Then the exchange rate can be calculated from the equation (Equation A3.1). So for the Li-exchanged product, the exchange rate is approximately 55% (Table A3.1).

$$\frac{\text{Calculated Li mass}}{\text{Mass of Li}^+\text{-BIRM-1}} = \frac{A_r \text{ of Lithium}}{M_r \text{ of Li}^+\text{-BIRM-1}} \quad (\text{Equation A3.1})$$

hence,

$$\frac{\text{Calculated Li Mass}}{0.05 \text{ g}} = \frac{6.941x}{M_r \text{ of } (\text{NH}_4)_{2-x}(\text{Li})_x[\text{Zn}_2(\text{O}_3\text{PCH}_2\text{CH}_2\text{COO})_2] \cdot 5\text{H}_2\text{O}^\dagger}$$

Table A3.1 Flame photometry data of Li⁺-BIRM-1.

	Sample 1	Sample 2	Sample 3
Reading 1	70	71.5	70
Reading 2	70	71	70.5
Reading 3	71	72	70
Average	70.33	71.5	70.17
Concentration	6.96 ppm	7.08 ppm	6.94 ppm
Mass (in 100ml)	0.696 mg	0.708 mg	0.694 mg
<i>x</i>	1.10	1.12	1.09
Exchange rate	55%	56%	55%

[†] Due to not having enough information of the exchanged structure, the amount of contained water was assumed to be the same with BIRM-1, so five contained water per mole were used here for calculation.

3.2 Na⁺-BIRM-1

3.2.1 Na⁺-BIRM-1 Sample Solution Preparation

All the sodium-exchanged products were made by mixing 0.02 g of exchanged sample into 1 L of volumetric flask with the help of 1.5 ml of HNO₃ (1M).

3.2.2 Sodium ion Content Calculation

Sodium ion concentrations of three different exchanged samples can be obtained from the standard curve. Then the exchange rate can be calculated from the equation (Equation A3.2). So for the sodium-exchanged product, the exchange rate is approximately 84% (Table A3.2).

$$\frac{\text{Calculated Na mass}}{\text{Mass of Na}^+\text{-BIRM-1}} = \frac{A_r \text{ of Sodium}}{M_r \text{ of Na}^+\text{-BIRM-1}} \quad (\text{Equation A3.2})$$

hence,

$$\frac{\text{Calculated Na Mass}}{0.05 \text{ g}} = \frac{6.941x}{M_r \text{ of } (\text{NH}_4)_{2-x}(\text{Na})_x [\text{Zn}_2(\text{O}_3\text{PCH}_2\text{CH}_2\text{COO})_2] \cdot 5\text{H}_2\text{O}^\dagger}$$

Table A3.2 Flame photometry data of Na⁺-BIRM-1.

	Sample 1	Sample 2	Sample 3
Reading 1	48	48.5	47
Reading 2	47.5	48	47.5
Reading 3	48	48	47.5
Average	47.83	48.17	47.33
Concentration	1.36 ppm	1.37 ppm	1.345 ppm
Mass (in 1L)	1.36 mg	1.37 mg	1.35 mg
x	1.68	1.69	1.67
Exchange rate	84%	85%	84%

[†] Due to not having enough information of the exchanged structure, the amount of contained water was assumed to be the same with BIRM-1, so five contained water per mole were used here for calculation.

Appendix 4 Crystallographic Data of K⁺-BIRM-1

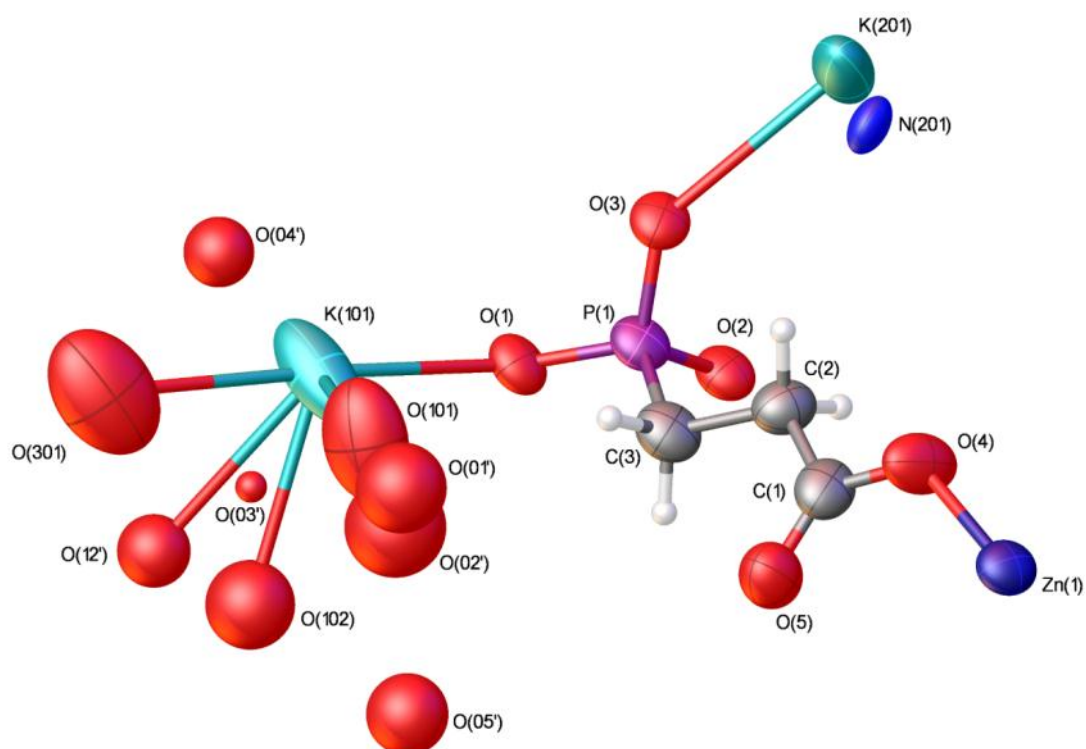


Fig.A4.1 The asymmetric unit of K⁺-BIRM-1 with ellipsoids drawn at the 50 % probability level.

Table A4.1 Crystallographic data for K⁺-BIRM-1.

Empirical formula	(NH ₄) _{0.49} (K) _{1.51} [Zn ₂ (O ₃ PCH ₂ CH ₂ COO) ₂] 5.97H ₂ O
Formula weight	608.25
Temperature	100(2) K
Wavelength	0.71075 Å
Crystal system	Tetragonal
Space group	<i>I</i> 4 ₁ / <i>acd</i>
Unit cell dimensions	<i>a</i> = 22.153(9) Å <i>c</i> = 17.873(1) Å
Volume	8771(7) Å ³
Cell formula units Z	16
Density (calculated)	1.842 mg/m ³
Absorption coefficient	2.689 mm ⁻¹

F(000)	4924
Crystal size	$0.30 \times 0.02 \times 0.02 \text{ mm}^3$
Theta range for data collection	2.93 to 25.03°
Index ranges	$-20 \leq h \leq 24$, $-26 \leq k \leq 9$, $-12 \leq l \leq 21$
Reflections collected	8244
Independent reflections	1946 [R(int) = 0.0410]
Completeness to $\theta = 27.51^\circ$	99.8%
Absorption correction	Semi-empirical from equivalents
Max. and min. transmission	0.9482 and 0.4993
Refinement method	Full-matrix least-squares on F^2
Data / restraints / parameters	1946 / 0 / 162
Goodness of fit on F^2	1.225
Final R indices [I > 2sigma(I)]	R1 = 0.0890, wR2 = 0.1950
R indices (all data)	R1 = 0.1008, wR2 = 0.2019
Largest diff. peak and hole	0.808 and -0.438 e/\AA^3

Table A4.1 Atomic coordinates ($\times 10^4$), occupancies and equivalent isotropic displacement parameters ($\times 10^3$) for K^+ -BIRM-1, U_{eq} is defined as one third of the trace of the orthogonalized U_{ij} tensor.

Atom	Mult.	<i>x</i>	<i>y</i>	<i>z</i>	Occupancy	U_{eq}
C(1)	32	3056(5)	2335(4)	1666(5)	1	55(2)
C(2)	32	3022(4)	3013(4)	1777(5)	1	53(2)
C(3)	32	3491(5)	3281(4)	2294(5)	1	55(2)
O(1)	32	3855(3)	4308(3)	2943(3)	1	50(2)
O(2)	32	2724(3)	4092(3)	2932(3)	1	47(1)
O(3)	32	3245(3)	4385(3)	1749(3)	1	49(2)
O(4)	32	2670(4)	2137(3)	1221(4)	1	72(2)
O(5)	32	3420(3)	2010(3)	2013(4)	1	68(2)
P(1)	32	3324(1)	4061(1)	2499(1)	1	46(1)
Zn(1)	32	2498(1)	1283(1)	1126(1)	1	48(1)
K(101)	32	5080(3)	4264(5)	2750(3)	0.420(9)	121(5)
O(101)	32	5339(12)	3238(19)	1999(19)	0.420(9)	143(13)
O(102)	32	5455(18)	3584(18)	4050(20)	0.28	119(12)
O(12')	32	5840(20)	4050(20)	4080(30)	0.15	80(14)
O(01')	32	5289(13)	2840(14)	1947(16)	0.44(4)	123(13)
O(02')	32	4815(14)	3473(14)	3251(16)	0.43(3)	153(18)
O(03')	32	5595(9)	3739(9)	3083(11)	0.189(16)	15(7)
O(04')	16	5440(20)	5000	2500	0.24(3)	74(18)
O(05')	8	5000	2500	3750	0.20	100(30)

O(301)	32	6397(7)	4172(7)	2598(8)	0.91(3)	175(9)
K(201)	32	2339(4)	4557(4)	657(7)	0.337(11)	113(5)
N(201)	16	2059(7)	4560(7)	1250	0.49	46(5)

Table A4.2 Bond lengths [\AA] for K^+ -BIRM-1.

Bond	Bond Length	Bond	Bond Length
C(1)-O(5)	1.245(11)	O(3)-K(201)	2.825(10)
C(1)-O(4)	1.247(10)	O(4)-Zn(1)	1.938(6)
C(1)-C(2)	1.517(13)	O(4)-K(101) ^[f]	2.830(10)
C(2)-C(3)	1.513(12)	O(4)-K(101) ^[g]	3.075(10)
C(2)-H(2A)	0.99	Zn(1)-O(3) ^[g]	1.931(6)
C(2)-H(2B)	0.99	Zn(1)-O(2) ^[b]	1.940(5)
C(3)-P(1)	1.804(10)	Zn(1)-O(1) ^[f]	1.964(6)
C(3)-H(3A)	0.99	K(101)-O(101)	2.70(3)
C(3)-H(3B)	0.99	K(101)-O(4) ^[a]	2.830(10)
O(1)-P(1)	1.522(6)	K(101)-O(102)	2.89(4)
O(1)-Zn(1) ^[a]	1.964(6)	K(101)-O(301)	2.937(17)
O(1)-K(101)	2.738(9)	K(101)-O(12')	2.96(5)
O(2)-P(1)	1.540(6)	K(101)-O(4) ^[e]	3.075(10)
O(2)-Zn(1) ^[b]	1.940(5)	O(301)-K(201) ^[e]	2.96(2)
O(2)-K(201) ^[c]	2.819(11)	K(201)-O(3) ^[d]	2.824(11)
O(2)-K(201) ^[d]	2.952(10)	K(201)-O(2) ^[h]	2.819(11)
O(3)-P(1)	1.531(6)	K(201)-O(2) ^[d]	2.952(10)
O(3)-Zn(1) ^[e]	1.931(6)	K(201)-O(301) ^[g]	2.96(2)
O(3)-K(201) ^[e]	2.824(11)	K(201)-O(301) ^[f]	2.305(17)
O(301)-K(201) ^[a]	2.305(17)		

Note: Symmetry transformations used to generate equivalent atoms: [a] $y+1/4, x+1/4, z+1/4$; [b] $-x+1/2, -y+1/2, -z+1/2$; [c] $y-1/4, -x+3/4, z+1/4$; [d] $y-1/4, x+1/4, -z+1/4$; [e] $y+1/4, -x+3/4, -z+1/4$; [f] $y-1/4, x-1/4, z-1/4$; [g] $-y+3/4, x-1/4, -z+1/4$; [h] $-y+3/4, x+1/4, z-1/4$.

Table A4.3 Bond angles [$^\circ$] for K^+ -BIRM-1.

Bond Angle	Angle	Bond Angle	Angle
O(5)-C(1)-O(4)	124.0(9)	H(3A)-C(3)-H(3B)	108
O(5)-C(1)-C(2)	122.6(8)	P(1)-O(1)-Zn(1) ^[a]	122.8(3)
O(4)-C(1)-C(2)	113.3(9)	P(1)-O(1)-K(101)	133.5(3)
C(3)-C(2)-C(1)	115.7(8)	Zn(1) ^[a] -O(1)-K(101)	100.8(3)
C(3)-C(2)-H(2A)	108.4	P(1)-O(2)-Zn(1) ^[b]	129.5(3)
C(1)-C(2)-H(2A)	108.4	P(1)-O(2)-K(201) ^[c]	124.2(4)
C(3)-C(2)-H(2B)	108.4	Zn(1) ^[b] -O(2)-K(201) ^[c]	95.9(3)
C(1)-C(2)-H(2B)	108.4	P(1)-O(2)-K(201) ^[d]	97.2(3)
H(2A)-C(2)-H(2B)	107.4	Zn(1) ^[b] -O(2)-K(201) ^[d]	133.3(3)
C(2)-C(3)-P(1)	110.9(7)	K(201) ^[c] -O(2)-K(201) ^[d]	50.2(5)

C(2)-C(3)-H(3A)	109.5	P(1)-O(3)-Zn(1) ^[e]	124.5(3)
P(1)-C(3)-H(3A)	109.5	P(1)-O(3)-K(201) ^[e]	102.7(3)
C(2)-C(3)-H(3B)	109.5	Zn(1) ^[e] -O(3)-K(201) ^[d]	110.1(3)
P(1)-C(3)-H(3B)	109.5	P(1)-O(3)-K(201)	138.4(4)
Zn(1) ^[e] -O(3)-K(201)	95.9(3)	O(101)-K(101)-O(301)	71.6(7)
K(201) ^[d] -O(3)-K(201)	48.0(5)	O(1)-K(101)-O(301)	177.3(5)
C(1)-O(4)-Zn(1)	122.2(7)	O(4) ^[a] -K(101)-O(301)	116.8(4)
C(1)-O(4)-K(101) ^[f]	139.1(7)	O(102)-K(101)-O(301)	75.7(9)
Zn(1)-O(4)-K(101) ^[f]	98.4(3)	O(101)-K(101)-O(12')	98.2(13)
C(1)-O(4)-K(101) ^[g]	98.8(6)	O(1)-K(101)-O(12')	117.9(11)
Zn(1)-O(4)-K(101) ^[g]	108.5(3)	O(4) ^[a] -K(101)-O(12')	79.5(11)
K(101) ^[f] -O(4)-K(101) ^[g]	69.8(4)	O(102)-K(101)-O(12')	26.4(12)
O(1)-P(1)-O(3)	112.0(3)	O(301)-K(101)-O(12')	59.9(11)
O(1)-P(1)-O(2)	112.9(3)	O(101)-K(101)-O(4) ^[e]	89.2(8)
O(3)-P(1)-O(2)	108.8(3)	O(1)-K(101)-O(4) ^[e]	77.1(2)
O(1)-P(1)-C(3)	106.9(4)	O(4) ^[a] -K(101)-O(4) ^[e]	97.2(3)
O(3)-P(1)-C(3)	107.2(4)	O(102)-K(101)-O(4)	172.6(9)
O(2)-P(1)-C(3)	108.8(4)	O(301)-K(101)-O(4) ^[e]	105.4(4)
O(3) ^[g] -Zn(1)-O(4)	119.6(3)	O(4)-K(101)-O(12')	159.7(12)
O(3) ^[g] -Zn(1)-O(2) ^[b]	102.5(2)	K(101)-O(301)-K(201) ^[e]	118.8(6)
O(4)-Zn(1)-O(2) ^[b]	113.0(3)	O(3) ^[d] -K(201)-O(2) ^[h]	79.6(3)
O(3) ^[g] -Zn(1)-O(1) ^[f]	112.7(2)	O(3) ^[d] -K(201)-O(3)	109.7(4)
O(4)-Zn(1)-O(1) ^[f]	97.3(3)	O(2) ^[h] -K(201)-O(3)	64.7(2)
O(2) ^[b] -Zn(1)-O(1) ^[f]	112.1(2)	O(3) ^[d] -K(201)-O(2) ^[d]	51.2(2)
O(101)-K(101)-O(1)	107.6(8)	O(2) ^[h] -K(201)-O(2) ^[d]	96.6(3)
O(101)-K(101)-O(4) ^[a]	167.3(10)	O(3)-K(201)-O(2) ^[d]	157.1(4)
O(1)-K(101)-O(4) ^[a]	63.5(2)	O(3) ^[d] -K(201)-O(301) ^[g]	138.7(5)
O(101)-K(101)-O(102)	84.2(11)	O(3)-K(201)-O(301) ^[g]	73.9(3)
O(1)-K(101)-O(102)	101.7(8)	O(2) ^[d] -K(201)-O(301) ^[g]	111.2(5)
O(4)-K(101)-O(102)	88.7(8)	K(201) ^[a] -O(301)-K(101)	123.0(6)
K(201) ^[a] -O(301)-K(201) ^[e]	53.8(6)	O(301) ^[f] -K(201)-O(2) ^[h]	144.0(7)
O(301) ^[f] -K(201)-O(3) ^[d]	112.8(5)	O(301) ^[f] -K(201)-O(3)	132.1(5)
O(2) ^[h] -K(201)-O(3)	64.7(2)	O(301) ^[f] -K(201)-O(2) ^[d]	70.8(4)
O(301) ^[f] -K(201)-O(301) ^[g]	88.0(7)		

Note: Symmetry transformations used to generate equivalent atoms: [a] y+1/4, x+1/4, z+1/4; [b] -x+1/2, -y+1/2, -z+1/2; [c] y-1/4, -x+3/4, z+1/4; [d] y-1/4, x+1/4, -z+1/4; [e] y+1/4, -x+3/4, -z+1/4; [f] y-1/4, x-1/4, z-1/4; [g] -y+3/4, x-1/4, -z+1/4; [h] -y+3/4, x+1/4, z-1/4.

Table A4.4 Anisotropic displacement parameters ($\text{\AA}^2 \times 10^3$) for K⁺-BIRM-1.

	U ¹¹	U ²²	U ³³	U ²³	U ¹³	U ¹²
C(1)	66(6)	65(6)	33(4)	-5(4)	1(4)	-12(5)
C(2)	70(6)	50(5)	40(5)	0(4)	1(4)	-5(5)
C(3)	66(6)	64(6)	35(4)	-7(4)	-2(4)	5(5)
O(1)	52(4)	65(4)	33(3)	-8(3)	-9(3)	4(3)

O(2)	54(3)	59(4)	29(3)	-2(3)	-2(2)	4(3)
O(3)	59(4)	61(4)	27(3)	-5(3)	1(3)	-4(3)
O(4)	114(6)	49(4)	51(4)	-8(3)	-26(4)	-12(4)
O(5)	72(5)	57(4)	75(5)	-3(4)	-14(4)	-5(3)
P(1)	56(1)	55(1)	26(1)	-6(1)	-3(1)	3(1)
Zn(1)	63(1)	53(1)	29(1)	-5(1)	-6(1)	-3(1)
K(101)	77(5)	233(12)	52(4)	-28(5)	-3(3)	47(6)
O(101)	100(19)	150(30)	180(30)	-70(20)	-8(18)	27(18)
O(301)	190(16)	164(14)	173(15)	-78(11)	-43(11)	52(11)
K(201)	88(8)	75(6)	178(11)	46(7)	-67(7)	-16(5)
N(201)	43(9)	43(9)	53(13)	-3(8)	3(8)	-21(10)

Table A4.5 Hydrogen coordinates ($\times 10^4$) and isotropic displacement parameters ($\text{\AA}^2 \times 10^3$) for K^+ -BIRM-1.

Atom	x	y	z	U_{eq}
H(2A)	3060	3210	1282	64
H(2B)	2617	3113	1976	64
H(3A)	3894	3252	2058	66
H(3B)	3502	3047	2767	66

Table A4.6 Torsion angles [$^\circ$] for K^+ -BIRM-1.

Bond	Angle	Bond	Angle
O(5)-C(1)-C(2)-C(3)	4.5(13)	C(2)-C(3)-P(1)-O(2)	64.3(7)
O(4)-C(1)-C(2)-C(3)	-178.4(8)	C(1)-O(4)-Zn(1)-O(3) ^[g]	-65.0(8)
C(1)-C(2)-C(3)-P(1)	-170.4(6)	K(101) ^[f] -O(4)-Zn(1)-O(3) ^[g]	120.0(3)
O(5)-C(1)-O(4)-Zn(1)	9.9(13)	K(101) ^[g] -O(4)-Zn(1)-O(3) ^[g]	48.7(4)
C(2)-C(1)-O(4)-Zn(1)	-167.1(6)	C(1)-O(4)-Zn(1)-O(2) ^[b]	55.8(8)
O(5)-C(1)-O(4)-K(101) ^[f]	-177.7(7)	K(101) ^[f] -O(4)-Zn(1)-O(2) ^[b]	-119.2(3)
C(2)-C(1)-O(4)-K(101) ^[f]	5.3(14)	K(101) ^[g] -O(4)-Zn(1)-O(2) ^[b]	169.5(3)
O(5)-C(1)-O(4)-K(101) ^[g]	-108.6(9)	C(1)-O(4)-Zn(1)-O(1) ^[f]	173.7(8)
C(2)-C(1)-O(4)-K(101) ^[g]	74.4(8)	K(101) ^[f] -O(4)-Zn(1)-O(1) ^[f]	-1.3(3)
Zn(1) ^[a] -O(1)-P(1)-O(3)	87.5(4)	K(101) ^[g] -O(4)-Zn(1)-O(1) ^[f]	-72.7(4)
K(101)-O(1)-P(1)-O(3)	-69.1(6)	P(1)-O(1)-K(101)-O(101)	-28.7(11)
Zn(1) ^[a] -O(1)-P(1)-O(2)	-35.7(5)	Zn(1) ^[a] -O(1)-K(101)-O(101)	171.2(9)
K(101)-O(1)-P(1)-O(2)	167.7(5)	P(1)-O(1)-K(101)-O(4) ^[a]	161.1(5)
Zn(1) ^[a] -O(1)-P(1)-C(3)	-155.4(4)	Zn(1) ^[a] -O(1)-K(101)-O(4) ^[a]	1.0(3)
K(101)-O(1)-P(1)-C(3)	48.1(6)	P(1)-O(1)-K(101)-O(301)	-103(9)
Zn(1) ^[e] -O(3)-P(1)-O(1)	3.6(5)	Zn(1) ^[a] -O(1)-K(101)-O(301)	97(10)
K(201) ^[d] -O(3)-P(1)-O(1)	-122.1(4)	P(1)-O(1)-K(101)-O(4) ^[e]	56.2(6)

K(201)-O(3)-P(1)-O(1)	-160.9(5)	Zn(1) ^[a] -O(1)-K(101)-O(4) ^[e]	-103.9(3)
Zn(1) ^[e] -O(3)-P(1)-O(2)	129.1(4)	O(101)-K(101)-O(301)-K(201) ^[e]	122.2(11)
K(201) ^[d] -O(3)-P(1)-O(2)	3.4(4)	O(1)-K(101)-O(301)-K(201) ^[e]	-163(9)
K(201)-O(3)-P(1)-O(2)	-35.4(7)	O(4) ^[a] -K(101)-O(301)-K(201) ^[e]	-68.2(6)
Zn(1) ^[e] -O(3)-P(1)-C(3)	-113.3(5)	O(4) ^[e] -K(101)-O(301)-K(201) ^[e]	38.3(6)
K(201) ^[d] -O(3)-P(1)-C(3)	121.0(4)	P(1)-O(3)-K(201)-O(3) ^[d]	106.2(6)
K(201)-O(3)-P(1)-C(3)	82.1(7)	Zn(1) ^[e] -O(3)-K(201)-O(3) ^[d]	-61.0(4)
Zn(1) ^[b] -O(2)-P(1)-O(1)	-60.5(5)	K(201) ^[d] -O(3)-K(201)-O(3) ^[d]	50.8(5)
K(201) ^[c] -O(2)-P(1)-O(1)	75.6(5)	P(1)-O(3)-K(201)-O(2) ^[h]	173.7(5)
K(201) ^[d] -O(2)-P(1)-O(1)	121.7(4)	Zn(1) ^[e] -O(3)-K(201)-O(2) ^[h]	6.5(3)
Zn(1) ^[b] -O(2)-P(1)-O(3)	174.5(4)	K(201) ^[d] -O(3)-K(201)-O(2) ^[h]	118.3(3)
K(201) ^[c] -O(2)-P(1)-O(3)	-49.4(5)	P(1)-O(3)-K(201)-O(2) ^[d]	136.3(11)
K(201) ^[d] -O(2)-P(1)-O(3)	-3.2(4)	Zn(1) ^[e] -O(3)-K(201)-O(2) ^[d]	-30.9(14)
Zn(1) ^[b] -O(2)-P(1)-C(3)	58.0(5)	K(201) ^[d] -O(3)-K(201)-O(2) ^[d]	80.9(14)
K(201) ^[c] -O(2)-P(1)-C(3)	-165.9(5)	P(1)-O(3)-K(201)-O(301) ^[g]	-117.1(6)
K(201) ^[d] -O(2)-P(1)-C(3)	-119.8(4)	Zn(1) ^[e] -O(3)-K(201)-O(301) ^[g]	75.6(4)
C(2)-C(3)-P(1)-O(1)	-173.5(6)	K(201) ^[d] -O(3)-K(201)-O(301) ^[g]	-172.6(4)
C(2)-C(3)-P(1)-O(3)	-53.2(7)	P(1)-O(1)-K(101)-O(102)	-116.3(9)
Zn(1) ^[a] -O(1)-K(101)-O(102)	83.6(8)	P(1)-O(1)-K(101)-O(12')	-138.5(13)
Zn(1) ^[a] -O(1)-K(101)-O(12')	61.4(13)	O(101)-K(101)-O(301)-K(201) ^[a]	-174.3(13)
O(1)-K(101)-O(301)-K(201) ^[a]	-100(10)	O(4) ^[a] -K(101)-O(301)-K(201) ^[a]	-4.7(11)
O(102)-K(101)-O(301)-K(201) ^[a]	-85.8(12)	O(12')-K(101)-O(301)-K(201) ^[a]	-62.8(15)
O(4) ^[e] -K(101)-O(301)-K(201) ^[a]	101.9(8)	O(102)-K(101)-O(301)-K(201) ^[e]	-149.3(9)
O(12')-K(101)-O(301)-K(201) ^[e]	-126.3(14)	P(1)-O(3)-K(201)-O(301) ^[f]	-45.2(12)
Zn(1) ^[e] -O(3)-K(201)-O(301) ^[f]	147.6(9)	K(201) ^[d] -O(3)-K(201)-O(301) ^[f]	-100.6(9)

Note: Symmetry transformations used to generate equivalent atoms: [a] $y+1/4, x+1/4, z+1/4$; [b] $-x+1/2, -y+1/2, -z+1/2$; [c] $y-1/4, -x+3/4, z+1/4$; [d] $y-1/4, x+1/4, -z+1/4$; [e] $y+1/4, -x+3/4, -z+1/4$; [f] $y-1/4, x-1/4, z-1/4$; [g] $-y+3/4, x-1/4, -z+1/4$; [h] $-y+3/4, x+1/4, z-1/4$.

Appendix 5 Crystallographic Data of the Previously Partially Solved Co²⁺-BIRM-1

Table A5.1 Crystal data and structure refinement.

Empirical formula	C ₆ H ₈ O ₁₀ P ₂ Zn ₂
Formula weight	432.74
Temperature	120(2) K
Wavelength	0.71073 Å
Crystal system	Orthorhombic
Space group	<i>Ibca</i>
Unit cell dimensions	$a = 17.9820(6)$ Å $b = 21.9627(1)$ Å $c = 22.2266(1)$ Å
Volume	8878.0(7) Å ³
Z	16
Density (calculated)	1.816 mg/m ³
Absorption coefficient	3.126 mm ⁻¹
F(000)	4816
Crystal size	0.14 × 0.04 × 0.01 mm ³
Theta range for data collection	2.91 to 27.48 °
Index ranges	-23 ≤ h ≤ 22, -27 ≤ k ≤ 28, -28 ≤ l ≤ 28
Reflections collected	28408
Independent reflections	5006 [R(int) = 0.0576]
Completeness to theta = 27.48 °	99.1%
Absorption correction	Semi-empirical from equivalents
Max. and min. transmission	0.9694 and 0.6688
Refinement method	Full-matrix least-squares on F ²
Data / restraints / parameters	5006 / 0 / 181
Goodness of fit on F2	1.066
Final R indices [I>2sigma(I)]	R1 = 0.1000, wR2 = 0.2195
R indices (all data)	R1 = 0.0776, wR2 = 0.2041
Largest diff. peak and hole	0.664 and -0.655 e/Å ³

Table A5.2 Atomic coordinates ($\times 10^4$), occupancies and equivalent isotropic displacement parameters ($\times 10^3$) for the framework of the previously solved Co^{2+} -BIRM-1, U_{eq} is defined as one third of the trace of the orthogonalized U_{ij} tensor.

Atom	Mult.	<i>x</i>	<i>y</i>	<i>z</i>	Occupancy	U_{eq}
C(1)	16	3380(4)	1936(4)	2364(3)	1	45(2)
C(2)	16	3262(4)	1983(4)	3035(3)	1	47(2)
C(3)	16	2746(4)	1510(3)	3307(3)	1	40(2)
C(4)	16	4129(4)	171(3)	4428(4)	1	46(2)
C(5)	16	4261(5)	-516(3)	4468(4)	1	53(2)
C(6)	16	5221(4)	4214(4)	1005(3)	1	43(2)
O(1)	16	4280(3)	1896(2)	755(2)	1	40(1)
O(2)	16	3786(4)	2342(3)	2145(2)	1	65(2)
O(3)	16	3062(4)	1556(3)	2047(2)	1	64(2)
O(4)	16	2043(3)	1159(2)	4302(2)	1	43(2)
O(5)	16	2081(3)	2286(2)	4063(2)	1	43(1)
O(6)	16	3221(3)	1775(2)	4416(2)	1	43(1)
O(7)	16	3698(3)	355(3)	4819(3)	1	61(2)
O(8)	16	4461(4)	492(3)	4061(3)	1	63(2)
O(9)	16	4574(3)	3433(2)	232(2)	1	47(1)
O(10)	16	4537(3)	3203(2)	1359(2)	1	47(1)
P(1)	16	25098(10)	16893(8)	40595(7)	1	36(4)
P(2)	16	49957(11)	34486(8)	8272(8)	1	39(4)
Zn(1)	16	38772(5)	25052(4)	12950(3)	1	40(2)
Zn(2)	16	36203(4)	12222(4)	50074(4)	1	39(2)

Table A5.3 Bond lengths [\AA] for the framework of the previously solved Co^{2+} -BIRM-1.

Bond	Bond Length	Bond	Bond Length
C(1)-O(3)	1.231(10)	O(4)-P(1)	1.534(5)
C(1)-O(2)	1.251(10)	O(4)-Zn(2) ^[b]	1.949(4)
C(1)-C(2)	1.510(10)	O(2)-Zn(1)	1.931(5)
C(2)-C(3)	1.519(10)	O(7)-Zn(2)	1.955(6)
C(2)-H(2A)	0.9900	O(1)-P(2) ^[a]	1.516(5)
C(2)-H(2B)	0.9900	O(1)-Zn(1)	1.937(5)
C(3)-P(1)	1.770(7)	O(9)-P(2)	1.525(6)
C(3)-H(3A)	0.9900	O(9)-Zn(2) ^[e]	1.941(5)
C(3)-H(3B)	0.9900	O(10)-P(2)	1.539(5)
C(4)-O(7)	1.233(9)	O(10)-Zn(1)	1.944(5)
C(4)-O(8)	1.233(10)	P(2)-O(1) ^[a]	1.516(5)
C(4)-C(5)	1.530(11)	Zn(1)-O(5) ^[d]	1.952(5)
C(5)-C(6) ^[c]	1.523(11)	Zn(2)-O(9) ^[e]	1.941(5)
C(5)-H(5A)	0.9900	Zn(2)-O(4) ^[b]	1.949(4)

C(5)-H(5B)	0.9900	O(5)-P(1)	1.521(5)
C(6)-C(5) ^[c]	1.523(11)	O(5)-Zn(1) ^[d]	1.952(5)
C(6)-P(2)	1.773(8)	O(6)-P(1)	1.517(5)
C(6)-H(6A)	0.9900	O(6)-Zn(2)	1.928(5)
C(6)-H(6B)	0.9900		

Note: Symmetry transformations used to generate equivalent atoms: [a] -x, -y+1/2, z; [b] -x+1/2, y, -z; [c] -x+1, y+1/2, -z+1/2; [d] -x+1/2, -y+1/2, -z+1/2; [e] x, -y+1/2, z+1/2.

Table A5.4 Bond angles [°] for the framework of the previously solved Co²⁺-BIRM-1.

Bond Angle	Angle	Bond Angle	Angle
O(3)-C(1)-O(2)	122.1(7)	O(6)-P(1)-O(4)	111.8(3)
O(3)-C(1)-C(2)	123.1(7)	O(5)-P(1)-O(4)	112.1(3)
O(2)-C(1)-C(2)	114.6(7)	O(6)-P(1)-C(3)	108.6(3)
C(1)-C(2)-C(3)	115.6(7)	O(5)-P(1)-C(3)	108.5(3)
C(1)-C(2)-H(2A)	108.4	O(4)-P(1)-C(3)	107.1(3)
C(3)-C(2)-H(2A)	108.4	O(1) ^[a] -P(2)-O(9)	108.9(3)
C(1)-C(2)-H(2B)	108.4	O(1) ^[a] -P(2)-O(10)	111.5(3)
C(3)-C(2)-H(2B)	108.4	O(9)-P(2)-O(10)	113.1(3)
H(2A)-C(2)-H(2B)	107.4	O(1) ^[a] -P(2)-C(6)	107.5(3)
C(2)-C(3)-P(1)	111.7(5)	O(9)-P(2)-C(6)	109.1(3)
C(2)-C(3)-H(3A)	109.3	O(10)-P(2)-C(6)	106.5(3)
P(1)-C(3)-H(3A)	109.3	O(2)-Zn(1)-O(10)	97.3(2)
C(2)-C(3)-H(3B)	109.3	O(2)-Zn(1)-O(1)	120.6(3)
P(1)-C(3)-H(3B)	109.3	O(10)-Zn(1)-O(1)	111.2(2)
H(3A)-C(3)-H(3B)	107.9	O(2)-Zn(1)-O(5) ^[d]	111.5(2)
O(7)-C(4)-O(8)	125.6(7)	O(10)-Zn(1)-O(5) ^[d]	112.6(2)
O(7)-C(4)-C(5)	112.4(7)	O(1)-Zn(1)-O(5) ^[d]	103.8(2)
O(8)-C(4)-C(5)	121.9(7)	O(9) ^[e] -Zn(2)-O(6)	105.0(2)
C(6) ^[c] -C(5)-C(4)	116.0(7)	O(9) ^[e] -Zn(2)-O(7)	111.9(2)
C(6) ^[c] -C(5)-H(5A)	108.3	O(6)-Zn(2)-O(7)	119.6(3)
C(4)-C(5)-H(5A)	108.3	O(9) ^[e] -Zn(2)-O(4) ^[b]	111.5(2)
C(6) ^[c] -C(5)-H(5B)	108.3	O(6)-Zn(2)-O(4) ^[b]	110.7(2)
C(4)-C(5)-H(5B)	108.3	O(7)-Zn(2)-O(4) ^[b]	98.2(2)
H(5A)-C(5)-H(5B)	107.4	P(1)-O(6)-Zn(2)	126.3(3)
C(5) ^[c] -C(6)-P(2)	110.8(5)	P(1)-O(4)-Zn(2) ^[b]	123.9(3)
C(5) ^[c] -C(6)-H(6A)	109.5	C(1)-O(2)-Zn(1)	124.3(6)
P(2)-C(6)-H(6A)	109.5	C(4)-O(7)-Zn(2)	121.1(6)
C(5) ^[c] -C(6)-H(6B)	109.5	P(2) ^[a] -O(1)-Zn(1)	126.9(3)
P(2)-C(6)-H(6B)	109.5	P(2)-O(9)-Zn(2) ^[e]	130.8(3)
H(6A)-C(6)-H(6B)	108.1	P(2)-O(10)-Zn(1)	123.1(3)
P(1)-O(5)-Zn(1) ^[d]	130.4(3)	O(6)-P(1)-O(5)	108.5(3)

Note: Symmetry transformations used to generate equivalent atoms: [a] -x, -y+1/2, z; [b] -x+1/2, y, -z; [c] -x+1, y+1/2, -z+1/2; [d] -x+1/2, -y+1/2, -z+1/2; [e] x, -y+1/2, z+1/2.

Table A5.5 Anisotropic displacement parameters ($\text{\AA}^2 \times 10^3$) for the framework of the previously solved Co^{2+} -BIRM-1.

	U^{11}	U^{22}	U^{33}	U^{23}	U^{13}	U^{12}
C(1)	42(4)	56(5)	39(4)	4(3)	12(3)	4(3)
C(2)	50(4)	57(5)	34(3)	9(3)	0(3)	-11(4)
C(3)	35(3)	42(54)	43(4)	-6(3)	5(3)	-5(3)
C(4)	36(4)	42(4)	60(5)	-16(4)	0(3)	5(3)
C(5)	59(5)	35(4)	66(5)	-10(4)	3(4)	-17(3)
C(6)	38(4)	48(4)	44(4)	-2(3)	3(3)	-15(3)
O(1)	39(2)	43(3)	37(3)	0(2)	-9(2)	4(2)
O(2)	76(4)	85(5)	83(3)	11(3)	16(3)	-28(3)
O(3)	79(4)	75(4)	36(3)	1(3)	8(3)	-10(3)
O(4)	49(3)	37(3)	41(3)	-3(2)	20(2)	-17(2)
O(5)	44(3)	32(2)	57(3)	2(2)	16(2)	-4(2)
O(6)	39(3)	50(3)	39(2)	-2(2)	-1(2)	14(2)
O(7)	65(4)	38(3)	79(4)	10(3)	25(3)	13(3)
O(8)	77(4)	36(3)	76(4)	-4(3)	18(3)	-8(3)
O(9)	38(5)	52(3)	50(3)	-1(3)	10(2)	-10(2)
O(10)	62(3)	43(3)	35(2)	-4(2)	10(2)	-18(2)
P(1)	43(9)	36(9)	31(8)	-26(7)	10.3(7)	-71(7)
P(2)	43(9)	32(8)	41(9)	1(7)	8(8)	8(7)
Zn(1)	50(5)	37(4)	33(4)	1(3)	9(3)	-8(4)
Zn(2)	43(5)	36(4)	38(4)	-4(3)	11(3)	5(3)

Appendix 6 Crystallographic data of Mg²⁺-BIRM-1

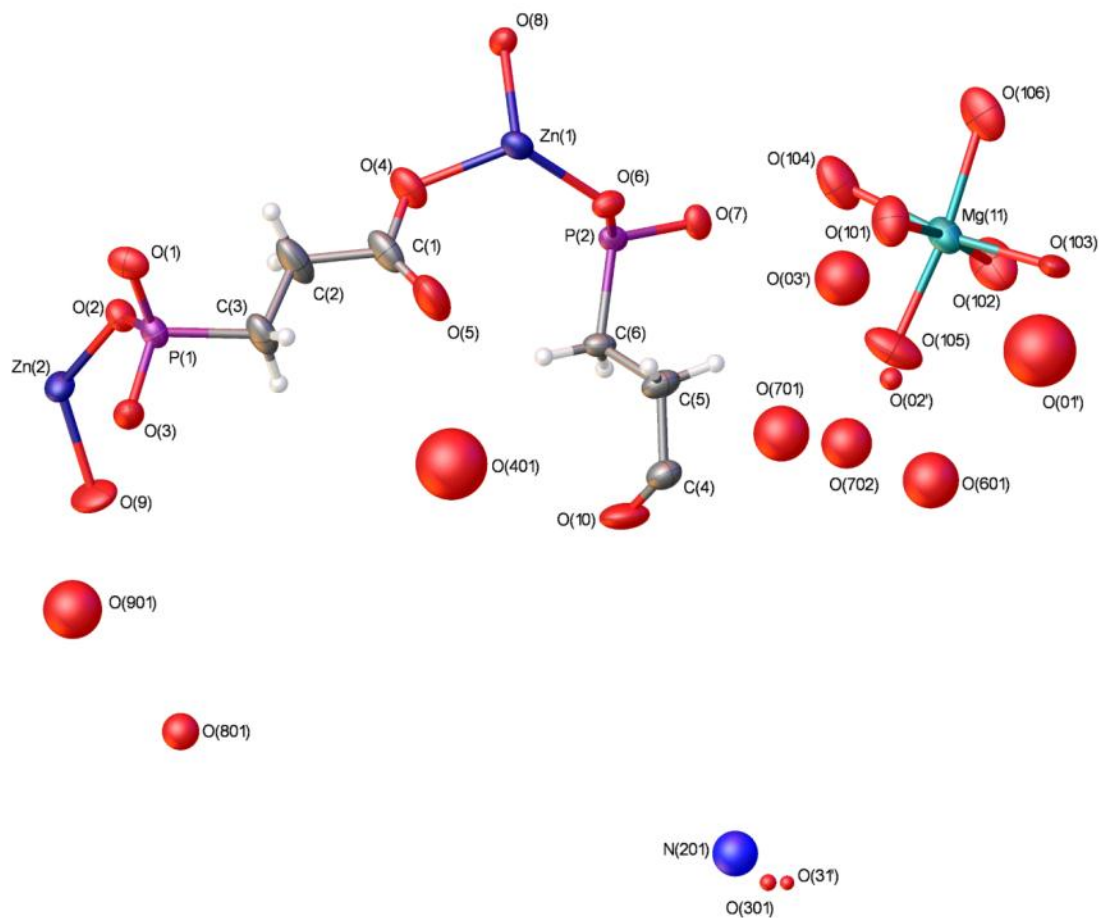


Fig. A6.1 The asymmetric unit of Mg²⁺-BIRM-1 with ellipsoids drawn at the 50 % probability level.

Table A6.1 Crystallographic data for Mg²⁺-BIRM-1.

Empirical formula	(NH ₄)[Mg(H ₂ O) ₆] _{0.5} [Zn ₂ (O ₃ PCH ₂ CH ₂ COO) ₂] 4.40H ₂ O
Formula weight	596.34
Temperature	100(2) K
Wavelength	0.71075 Å
Crystal system	Orthorhombic
Space group	<i>Ibca</i>
Unit cell dimensions	<i>a</i> = 18.1497(9) Å <i>b</i> = 21.5905(1) Å <i>c</i> = 22.4538(2) Å
Volume	8798.8(9) Å ³
Cell formula units <i>Z</i>	16
Density (calculated)	1.801 mg/m ³

Absorption coefficient	2.417 mm ⁻¹
F(000)	4880
Crystal size	0.19 × 0.02 × 0.01 mm ³
Theta range for data collection	3.45 to 27.49 °
Index ranges	-23 ≤ h ≤ 14, -28 ≤ k ≤ 10, -29 ≤ l ≤ 20
Reflections collected	12533
Independent reflections	5019 [R(int) = 0.0522]
Completeness to theta = 27.49 °	99.3%
Absorption correction	Semi-empirical from equivalents
Max. and min. transmission	0.9762 and 0.6566
Refinement method	Full-matrix least-squares on F ²
Data / restraints / parameters	5019 / 21 / 289
Goodness of fit on F2	1.076
Final R indices [I>2sigma(I)]	R1 = 0.0842, wR2 = 0.2064
R indices (all data)	R1 = 0.1228, wR2 = 0.2290
Largest diff. peak and hole	1.237 and -0.637 e/Å ³

Table A6.1 Atomic coordinates (×10⁴), occupancies and equivalent isotropic displacement parameters (×10³) for Mg²⁺-BIRM-1, U_{eq} is defined as one third of the trace of the orthogonalized U_{ij} tensor.

Atom	Mult.	x	y	z	Occupancy	U_{eq}
C(1)	16	853(5)	5205(5)	581(5)	1	42(2)
C(2)	16	720(6)	4515(5)	545(5)	1	53(3)
C(3)	16	168(5)	4252(4)	980(5)	1	41(2)
C(4)	16	1609(5)	6961(4)	2603(4)	1	35(2)
C(5)	16	1752(6)	7024(5)	1950(4)	1	37(2)
C(6)	16	2241(5)	6531(4)	1673(3)	1	27(2)
O(1)	16	-433(3)	3400(3)	243(3)	1	36(1)
O(2)	16	704(3)	3120(3)	788(3)	1	30(1)
O(3)	16	-495(3)	3231(3)	1355(2)	1	34(1)
O(4)	16	1307(3)	5389(3)	197(3)	1	43(2)
O(5)	16	508(5)	5548(4)	917(4)	1	63(2)
O(6)	16	1795(3)	6829(3)	573(2)	1	28(1)
O(7)	16	2932(3)	7331(3)	953(3)	1	28(1)
O(8)	16	2049(3)	6181(3)	-693(2)	1	27(1)
O(9)	16	1203(4)	2629(4)	2175(3)	1	54(2)
O(10)	16	1914(4)	6566(4)	2917(3)	1	56(2)
P(1)	16	-33(1)	3459(1)	834(1)	1	27(1)
P(2)	16	2498(1)	6726(1)	934(1)	1	23(1)

Zn(1)	16	1386(1)	6259(1)	-7(1)	1	27(1)
Zn(2)	16	1116(1)	2509(1)	1319(1)	1	28(1)
O(101)	16	993(8)	9082(7)	844(7)	0.5	55(4)
O(102)	16	3057(8)	9528(8)	1556(8)	0.5	63(4)
O(103)	16	1703(8)	10180(6)	1433(5)	0.5	43(3)
O(104)	16	2435(8)	8525(7)	719(8)	0.5	64(4)
O(105)	16	1754(9)	8847(8)	1901(7)	0.5	67(4)
O(106)	16	2324(7)	9727(7)	329(8)	0.5	61(4)
Mg(11)	16	2016(3)	9338(3)	1147(3)	0.5	36(1)
N(201)	16	943(5)	7150(5)	5380(4)	1	60(2)
O(01')	16	3103(13)	9774(13)	2247(11)	0.6(4)	153(15)
O(02')	16	717(9)	8937(7)	1972(7)	0.29(2)	15(5)
O(03')	16	430(20)	8723(19)	1140(18)	0.27(3)	88(18)
O(301)	8	0	7500	5488(9)	0.65	8(5)
O(31')	16	36(8)	7640(9)	5513(9)	0.35	6(4)
O(401)	16	453(10)	5509(9)	2159(8)	0.85(4)	149(10)
O(601)	16	864(11)	9101(10)	2783(9)	0.54(3)	91(9)
O(701)	16	313(14)	8090(15)	2218(11)	0.42(4)	90(12)
O(702)	16	370(20)	8570(20)	2359(18)	0.24(3)	74(18)
O(801)	16	225(9)	3151(9)	3858(8)	0.37(2)	40(6)
O(901)	8	0	2500	2820(30)	0.29(5)	100(30)

Table A6.2 Bond lengths [\AA] for Mg^{2+} -BIRM-1.

Bond	Bond Length	Bond	Bond Length
C(1)-O(5)	1.228(13)	O(3)-Zn(2) ^[c]	1.955(6)
C(1)-O(4)	1.257(11)	O(4)-Zn(1)	1.940(7)
C(1)-C(2)	1.512(14)	O(6)-P(2)	1.528(6)
C(2)-C(3)	1.508(12)	O(6)-Zn(1)	1.940(6)
C(2)-H(2A)	0.9900	O(7)-P(2)	1.527(6)
C(2)-H(2B)	0.9900	O(7)-Zn(2) ^[d]	1.950(6)
C(3)-P(1)	1.781(9)	O(8)-P(2) ^[e]	1.535(6)
C(3)-H(3A)	0.9900	O(8)-Zn(1)	1.962(5)
C(3)-H(3B)	0.9900	O(9)-C(4) ^[a]	1.257(11)
C(4)-O(10)	1.237(11)	O(9)-Zn(2)	1.946(6)
C(4)-O(9) ^[a]	1.257(11)	P(2)-O(8) ^[e]	1.535(6)
C(4)-C(5)	1.494(12)	Zn(1)-O(1) ^[b]	1.953(6)
C(5)-C(6)	1.520(12)	Zn(2)-O(7) ^[f]	1.950(6)
C(5)-H(5A)	0.9900	Zn(2)-O(3) ^[c]	1.955(6)
C(5)-H(5B)	0.9900	O(101)-Mg(11)	2.054(16)
C(6)-P(2)	1.775(8)	O(102)-Mg(11)	2.140(15)
C(6)-H(6A)	0.9900	O(103)-Mg(11)	2.011(14)
C(6)-H(6B)	0.9900	O(104)-Mg(11)	2.139(18)
O(1)-P(1)	1.519(6)	O(105)-Mg(11)	2.052(16)

O(1)-Zn(1) ^[b]	1.953(6)	O(106)-Mg(11)	2.095(17)
O(2)-P(1)	1.528(6)	O(31')-O(31') ^[g]	0.62(4)
O(2)-Zn(2)	1.929(6)	O(31')-N(201) ^[g]	1.857(17)
O(3)-P(1)	1.522(6)		

Note: Symmetry transformations used to generate equivalent atoms: [a] x+0, -y+1, -z+1/2; [b] -x, -y+1, -z; [c] -x+0, -y+1/2, z+0; [d] -x+1/2, y+1/2, z; [e] -x+1/2, y+0, -z+0; [f] -x+1/2, y-1/2, z; [g] -x+0, -y+3/2, z+0.

Table A6.3 Bond angles [°] for Mg²⁺-BIRM-1.

Bond Angle	Angle	Bond Angle	Angle
O(5)-C(1)-O(4)	124.4(9)	P(1)-C(3)-H(3A)	109.2
O(5)-C(1)-C(2)	123.1(8)	C(2)-C(3)-H(3B)	109.2
O(4)-C(1)-C(2)	112.2(10)	P(1)-C(3)-H(3B)	109.2
C(3)-C(2)-C(1)	116.1(9)	H(3A)-C(3)-H(3B)	107.9
C(3)-C(2)-H(2A)	108.3	O(10)-C(4)-O(9) ^[a]	121.4(8)
C(1)-C(2)-H(2A)	108.3	O(10)-C(4)-C(5)	123.0(8)
C(3)-C(2)-H(2B)	108.3	O(9) ^[a] -C(4)-C(5)	115.3(8)
C(1)-C(2)-H(2B)	108.3	C(4)-C(5)-C(6)	116.0(8)
H(2A)-C(2)-H(2B)	107.4	C(4)-C(5)-H(5A)	108.3
C(2)-C(3)-P(1)	112.1(7)	C(6)-C(5)-H(5A)	108.3
C(2)-C(3)-H(3A)	109.2	C(4)-C(5)-H(5B)	108.3
C(6)-C(5)-H(5B)	108.3	O(6)-Zn(1)-O(4)	118.9(3)
H(5A)-C(5)-H(5B)	107.4	O(6)-Zn(1)-O(1) ^[b]	106.3(3)
C(5)-C(6)-P(2)	111.7(6)	O(4)-Zn(1)-O(1) ^[b]	111.3(3)
C(5)-C(6)-H(6A)	109.3	O(6)-Zn(1)-O(8)	110.3(2)
P(2)-C(6)-H(6A)	109.3	O(4)-Zn(1)-O(8)	98.5(3)
C(5)-C(6)-H(6B)	109.3	O(1) ^[b] -Zn(1)-O(8)	111.3(2)
P(2)-C(6)-H(6B)	109.3	O(2)-Zn(2)-O(9)	123.4(3)
H(6A)-C(6)-H(6B)	107.9	O(2)-Zn(2)-O(7) ^[f]	102.6(2)
P(1)-O(1)-Zn(1) ^[b]	128.9(4)	O(9)-Zn(2)-O(7) ^[f]	111.7(3)
P(1)-O(2)-Zn(2)	128.8(3)	O(2)-Zn(2)-O(3) ^[c]	111.2(2)
P(1)-O(3)-Zn(2) ^[c]	123.3(3)	O(9)-Zn(2)-O(3) ^[c]	96.6(3)
C(1)-O(4)-Zn(1)	121.0(7)	O(7) ^[f] -Zn(2)-O(3) ^[c]	111.6(2)
P(2)-O(6)-Zn(1)	125.7(3)	O(103)-Mg(11)-O(105)	97.9(7)
P(2)-O(7)-Zn(2) ^[d]	129.6(3)	O(103)-Mg(11)-O(101)	95.3(7)
P(2) ^[e] -O(8)-Zn(1)	122.6(3)	O(105)-Mg(11)-O(101)	85.7(7)
C(4) ^[a] -O(9)-Zn(2)	122.4(6)	O(103)-Mg(11)-O(106)	89.6(6)
O(1)-P(1)-O(3)	112.5(3)	O(105)-Mg(11)-O(106)	172.5(8)
O(1)-P(1)-O(2)	108.6(3)	O(101)-Mg(11)-O(106)	93.4(7)
O(3)-P(1)-O(2)	112.3(3)	O(103)-Mg(11)-O(104)	170.2(6)
O(1)-P(1)-C(3)	109.8(4)	O(105)-Mg(11)-O(104)	91.7(7)
O(3)-P(1)-C(3)	106.4(4)	O(101)-Mg(11)-O(104)	87.3(7)
O(2)-P(1)-C(3)	107.1(4)	O(106)-Mg(11)-O(102)	80.9(7)
O(7)-P(2)-O(6)	108.8(3)	O(103)-Mg(11)-O(102)	86.5(7)

O(7)-P(2)-O(8) ^[e]	112.9(3)	O(105)-Mg(11)-O(102)	87.1(7)
O(6)-P(2)-O(8) ^[e]	111.9(3)	O(101)-Mg(11)-O(102)	172.8(7)
O(7)-P(2)-C(6)	108.3(4)	O(106)-Mg(11)-O(102)	93.7(6)
O(6)-P(2)-C(6)	108.1(4)	O(104)-Mg(11)-O(102)	92.1(7)
O(8) ^[e] -P(2)-C(6)	106.7(4)		

Note: Symmetry transformations used to generate equivalent atoms: [a] x+0, -y+1, -z+1/2; [b] -x, -y+1, -z; [c] -x+0, -y+1/2, z+0; [d] -x+1/2, y+1/2, z; [e] -x+1/2, y+0, -z+0; [f] -x+1/2, y-1/2, z; [g] -x+0, -y+3/2, z+0.

Table A6.4 Anisotropic displacement parameters ($\text{\AA}^2 \times 10^3$) for Mg^{2+} -BIRM-1.

	U ¹¹	U ²²	U ³³	U ²³	U ¹³	U ¹²
C(1)	30(5)	36(5)	59(6)	19(5)	0(4)	-11(4)
C(2)	48(6)	34(5)	79(8)	22(5)	24(6)	1(5)
C(3)	36(5)	28(4)	58(6)	10(4)	13(4)	-7(4)
C(4)	41(5)	39(5)	26(4)	-5(4)	4(4)	-1(4)
C(5)	43(5)	45(5)	24(4)	-6(4)	5(4)	5(4)
C(6)	31(4)	32(4)	18(4)	2(3)	4(3)	3(3)
O(1)	23(3)	50(4)	35(3)	8(3)	2(2)	-7(3)
O(2)	32(3)	26(3)	33(3)	5(2)	-1(2)	2(2)
O(3)	43(3)	29(3)	30(3)	-3(2)	11(3)	-5(3)
O(4)	33(3)	37(4)	58(4)	13(3)	10(3)	-8(3)
O(5)	75(6)	38(4)	76(6)	13(4)	25(5)	-10(4)
O(6)	30(3)	31(3)	22(3)	-2(2)	1(2)	6(2)
O(7)	24(3)	21(3)	40(3)	1(2)	6(2)	3(2)
O(8)	30(3)	26(3)	26(3)	-5(2)	8(2)	-7(2)
O(9)	67(5)	72(6)	24(3)	-9(3)	-15(3)	-18(4)
O(10)	74(5)	72(5)	21(3)	3(3)	7(3)	8(4)
P(1)	25(1)	23(1)	33(1)	4(1)	2(1)	-3(1)
P(2)	23(1)	24(1)	22(1)	2(1)	6(1)	2(1)
Zn(1)	23(1)	31(1)	27(1)	5(1)	5(1)	-2(1)
Zn(2)	31(1)	28(1)	25(1)	-2(1)	-8(1)	-1(1)
O(101)	49(8)	44(8)	73(11)	-2(8)	-14(8)	-5(7)
O(102)	44(5)	67(8)	79(8)	16(7)	-26(5)	-9(5)
O(103)	82(10)	28(6)	20(6)	5(5)	13(6)	-6(7)
O(104)	50(7)	46(7)	95(9)	24(7)	4(7)	6(6)
O(105)	54(6)	84(8)	64(7)	41(6)	5(6)	5(6)
O(106)	35(8)	57(10)	90(12)	16(9)	-6(7)	-14(7)
Mg(11)	31(3)	36(3)	40(3)	10(3)	-8(2)	-3(3)

Table A6.5 Hydrogen coordinates ($\times 10^4$) and isotropic displacement parameters ($\text{\AA}^2 \times 10^3$) for Mg^{2+} -BIRM-1.

Atom	x	y	z	U_{eq}
H(2A)	552	4415	137	64
H(2B)	1196	4301	608	64
H(3A)	-293	4498	957	49
H(3B)	365	4294	1390	49
H(5A)	1981	7433	1879	45
H(5B)	1272	7020	1740	45
H(6A)	1975	6130	1670	33
H(6B)	2690	6480	1918	33

Table A6.6 Torsion angles [°] for Mg²⁺-BIRM-1.

Bond	Angle	Bond	Angle
O(5)-C(1)-C(2)-C(3)	-4.0(16)	Zn(2) ^[d] -O(7)-P(2)-C(6)	64.6(5)
O(4)-C(1)-C(2)-C(3)	-178.6(9)	Zn(1)-O(6)-P(2)-O(7)	138.0(4)
C(1)-C(2)-C(3)-P(1)	172.3(8)	Zn(1)-O(6)-P(2)-O(8) ^[e]	12.6(5)
O(10)-C(4)-C(5)-C(6)	6.0(14)	Zn(1)-O(6)-P(2)-C(6)	-104.6(4)
O(9) ^[a] -C(4)-C(5)-C(6)	-180.0(8)	C(5)-C(6)-P(2)-O(7)	61.2(7)
C(4)-C(5)-C(6)-P(2)	-169.9(7)	C(5)-C(6)-P(2)-O(6)	-56.5(7)
O(5)-C(1)-O(4)-Zn(1)	-11.3(14)	C(5)-C(6)-P(2)-O(8) ^[e]	-177.0(6)
C(2)-C(1)-O(4)-Zn(1)	163.2(7)	P(2)-O(6)-Zn(1)-O(4)	46.7(5)
Zn(1) ^[b] -O(1)-P(1)-O(3)	56.2(6)	P(2)-O(6)-Zn(1)-O(1) ^[b]	173.3(4)
Zn(1) ^[b] -O(1)-P(1)-O(2)	-178.8(4)	P(2)-O(6)-Zn(1)-O(8)	-65.9(5)
Zn(1) ^[b] -O(1)-P(1)-C(3)	-62.9(6)	C(1)-O(4)-Zn(1)-O(6)	69.8(8)
Zn(2) ^[c] -O(3)-P(1)-O(1)	40.2(6)	C(1)-O(4)-Zn(1)-O(1) ^[b]	-54.4(8)
Zn(2) ^[c] -O(3)-P(1)-O(2)	-82.7(5)	C(1)-O(4)-Zn(1)-O(8)	-171.3(7)
Zn(2) ^[c] -O(3)-P(1)-C(3)	160.4(5)	P(2) ^[e] -O(8)-Zn(1)-O(6)	-35.5(5)
Zn(2)-O(2)-P(1)-O(1)	-129.4(4)	P(2) ^[e] -O(8)-Zn(1)-O(4)	-160.8(4)
Zn(2)-O(2)-P(1)-O(3)	-4.2(6)	P(2) ^[e] -O(8)-Zn(1)-O(1) ^[b]	82.3(4)
Zn(2)-O(2)-P(1)-C(3)	112.2(5)	P(1)-O(2)-Zn(2)-O(9)	-51.8(6)
C(2)-C(3)-P(1)-O(1)	-66.7(8)	P(1)-O(2)-Zn(2)-O(7) ^[f]	-178.7(4)
C(2)-C(3)-P(1)-O(3)	171.3(7)	P(1)-O(2)-Zn(2)-O(3) ^[c]	61.9(5)
C(2)-C(3)-P(1)-O(2)	51.1(9)	C(4) ^[a] -O(9)-Zn(2)-O(2)	-64.4(9)
Zn(2) ^[d] -O(7)-P(2)-O(6)	-178.1(4)	C(4) ^[a] -O(9)-Zn(2)-O(7) ^[f]	58.5(9)
Zn(2) ^[d] -O(7)-P(2)-O(8) ^[e]	-53.3(5)	C(4) ^[a] -O(9)-Zn(2)-O(3) ^[c]	174.8(8)

Note: Symmetry transformations used to generate equivalent atoms: [a] $x+0, -y+1, -z+1/2$; [b] $-x+0, -y+1, -z$; [c] $-x+0, -y+1/2, z+0$; [d] $-x+1/2, y+1/2, z$; [e] $-x+1/2, y+0, -z+0$; [f] $-x+1/2, y-1/2, z$; [g] $-x+0, -y+3/2, z+0$.

Appendix 7 IR Spectra

7.1 Dehydrated and rehydrated BIRM-1

IR spectra of dehydrated and rehydrated BIRM-1 and ion-exchanged products, Figure A7.1–A7.6

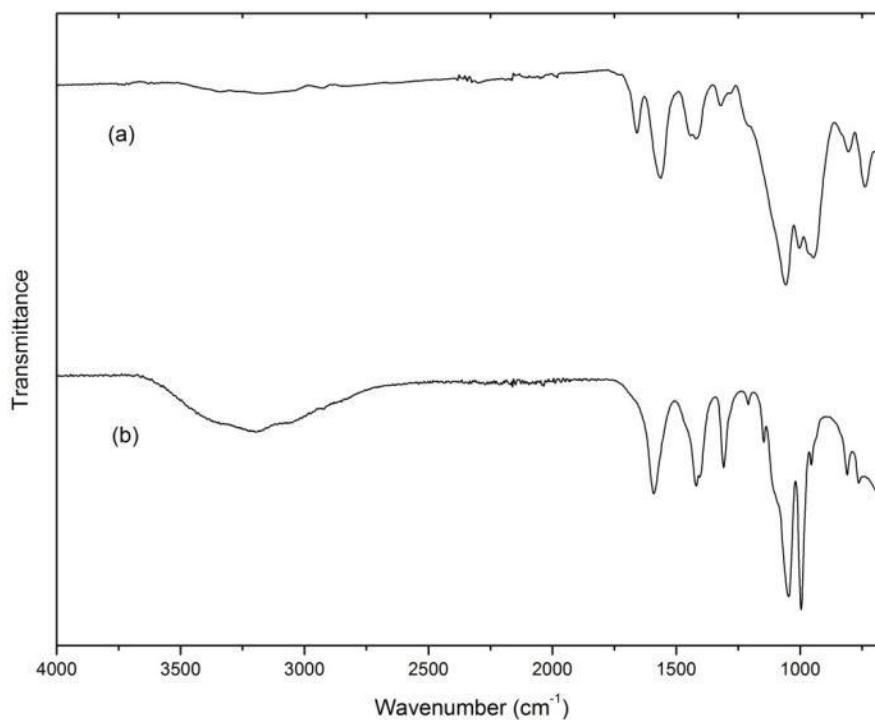


Fig. A7.1 FTIR spectra of (a) dehydrated BIRM-1 and (b) rehydrated BIRM-1.

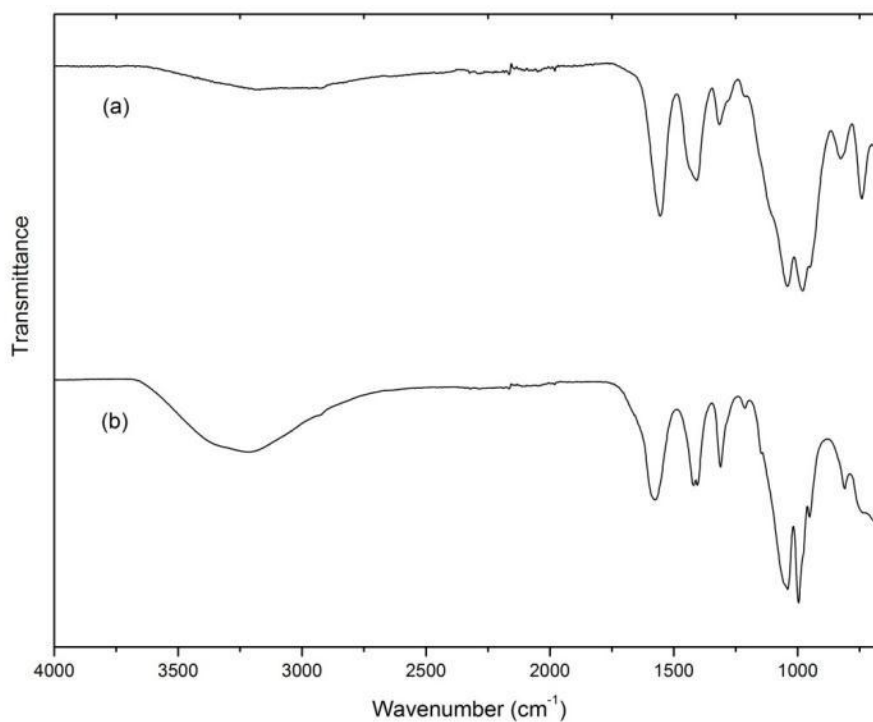


Fig. A7.2 FTIR spectra of (a) dehydrated Mn²⁺-BIRM-1 and (b) rehydrated Mn²⁺-BIRM-1.

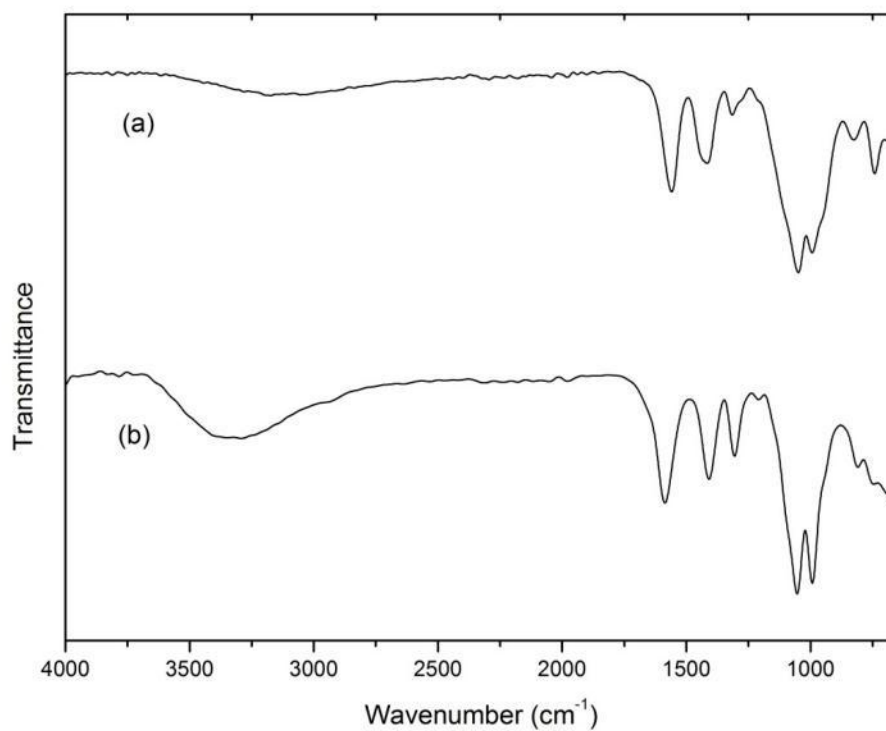


Fig. A7.3 FTIR spectra of (a) dehydrated Mg²⁺-BIRM-1 and (b) rehydrated Mg²⁺-BIRM-1.

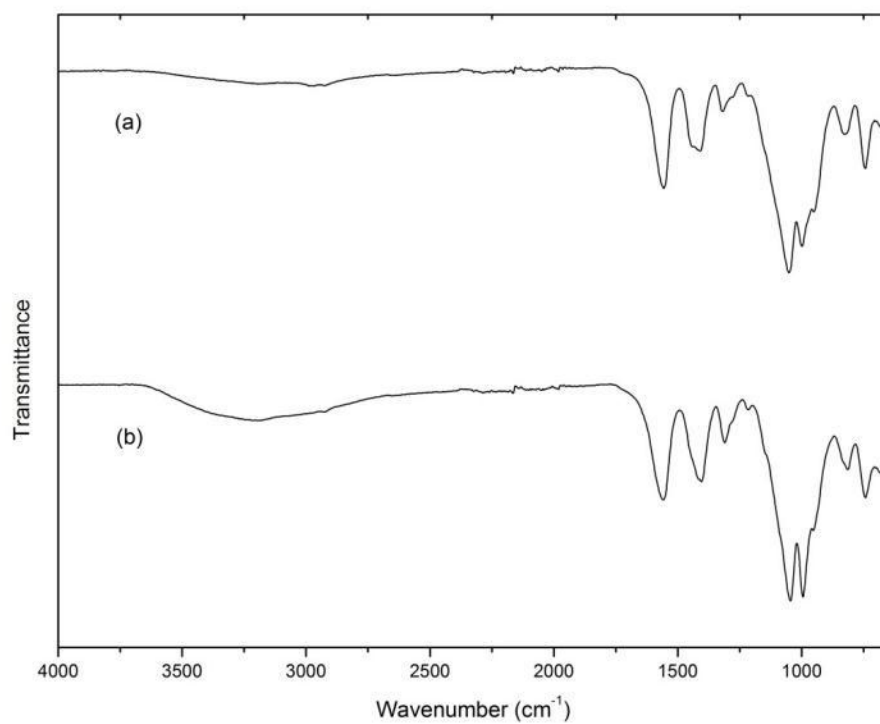


Fig. A7.4 FTIR spectra of (a) dehydrated Na⁺-BIRM-1 and (b) rehydrated Na⁺-BIRM-1.

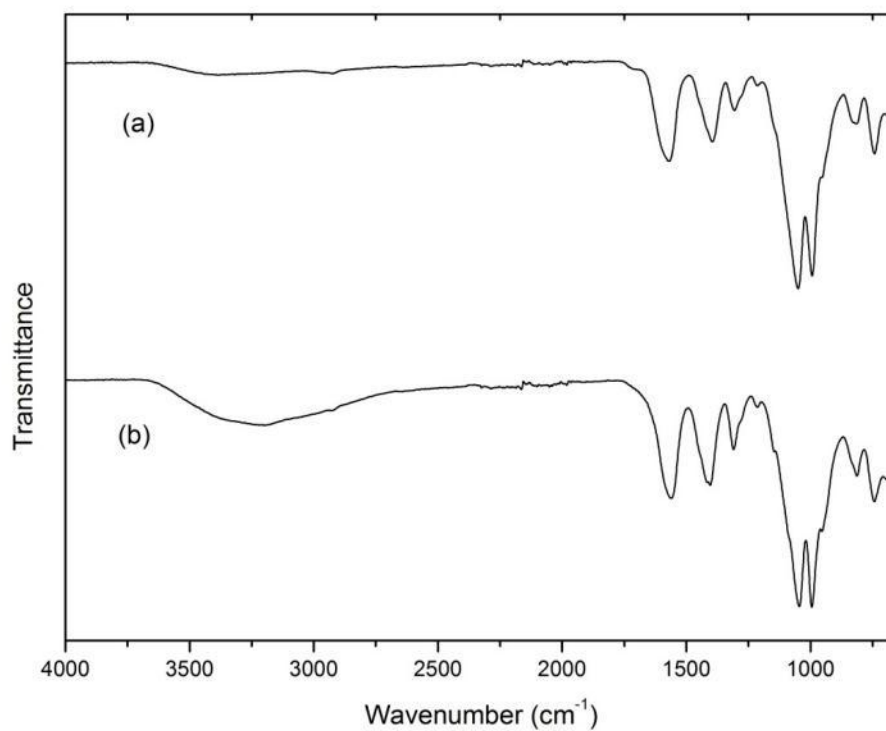


Fig. A7.5 FTIR spectra of (a) dehydrated Li^+ -BIRM-1 and (b) rehydrated Li^+ -BIRM-1.

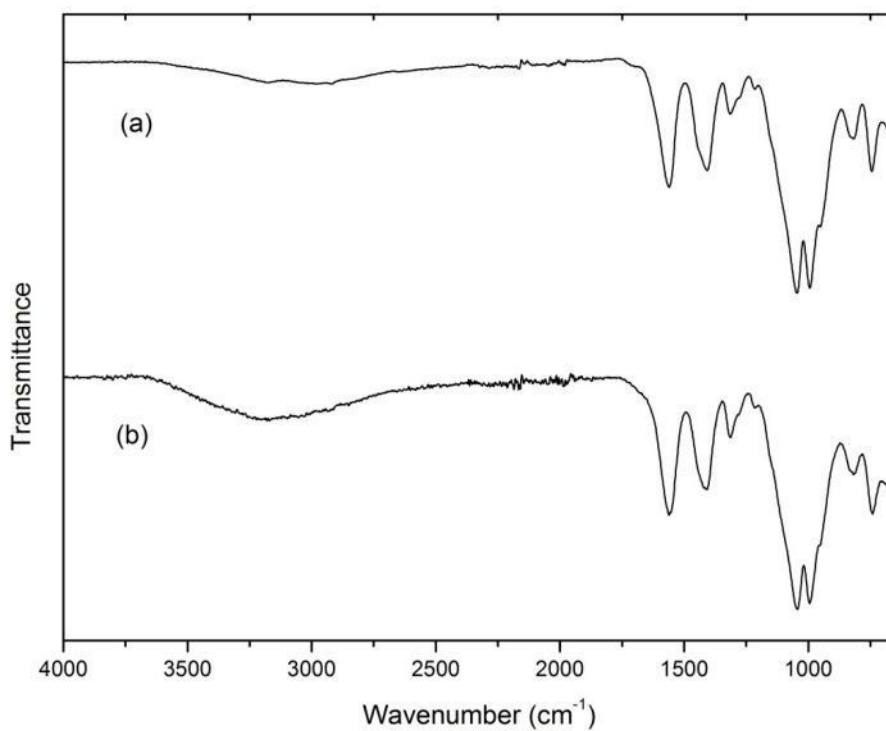


Fig. A7.6 FTIR spectra of (a) dehydrated Co^{2+} -BIRM-1 and (b) rehydrated Co^{2+} -BIRM-1.

7.2 IR spectra for organic treated K⁺-BIRM-1

FTIR spectra for organic treated K⁺-BIRM-1 and its evacuated products, Figure A7.7–A7.11.

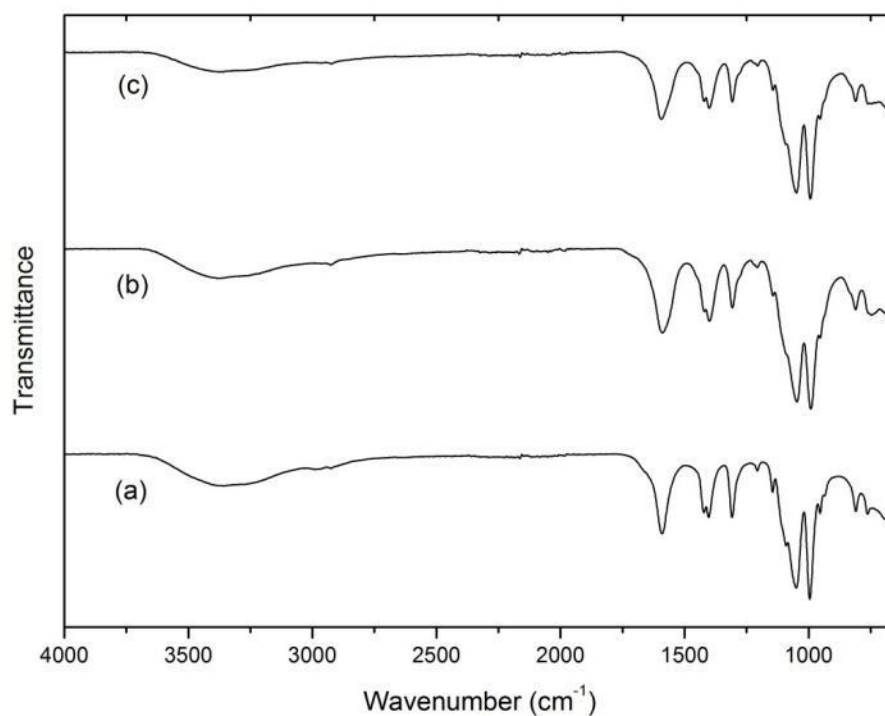


Fig. A7.7 FTIR spectra of (a) dichloromethane treated K⁺-BIRM-1, (b) after 5 hours evacuation and (c) after 15 hours evacuation.

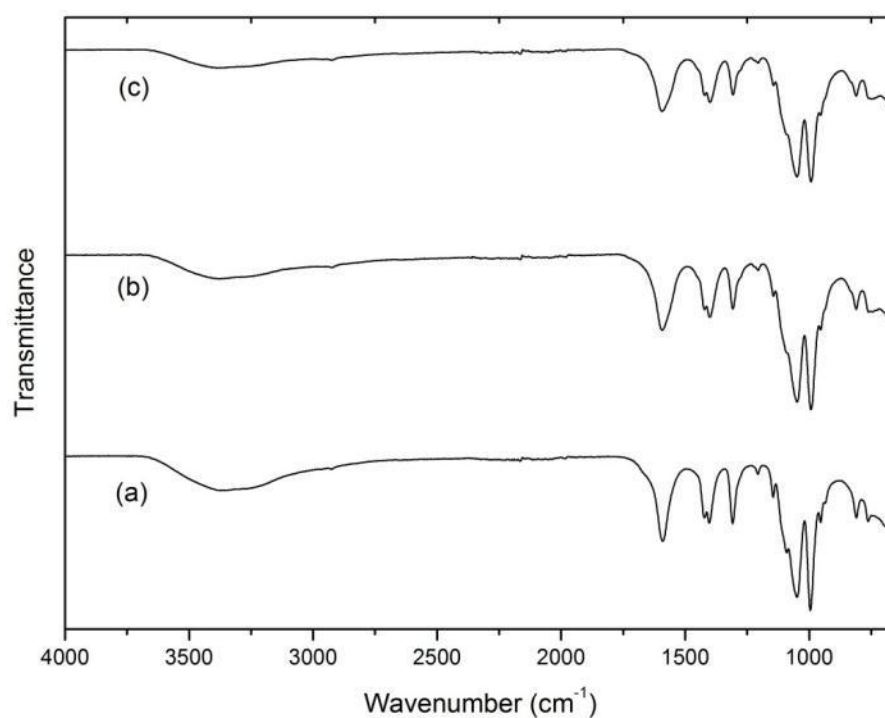


Fig. A7.8 FTIR spectra of (a) chloroform treated K⁺-BIRM-1, (b) after 5 hours evacuation and

(c) after 15 hours evacuation.

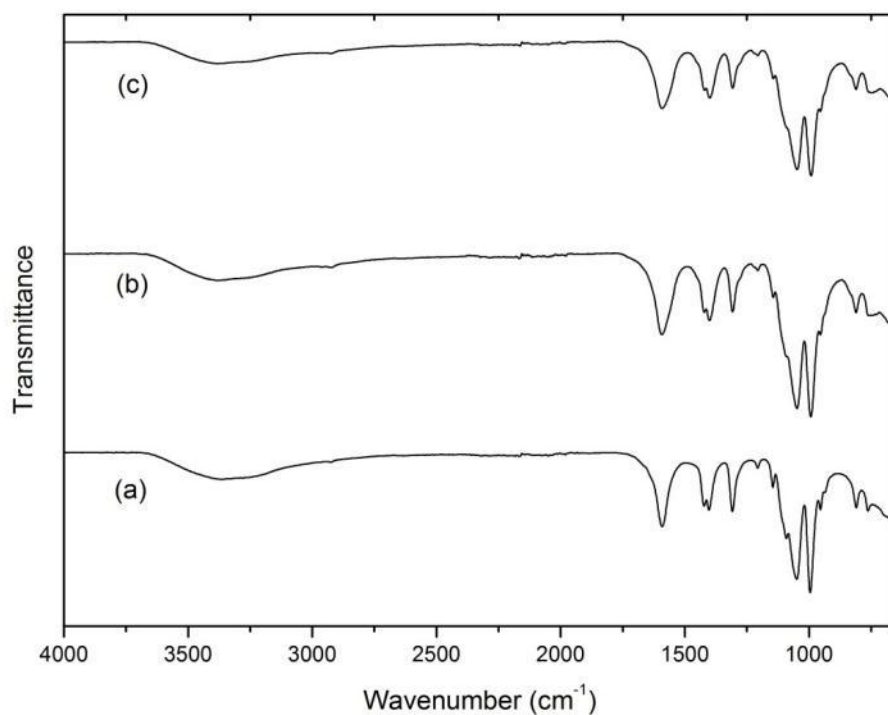


Fig. A7.9 FTIR spectra of (a) methanol treated K⁺-BIRM-1, (b) after 5 hours evacuation and (c) after 15 hours evacuation.

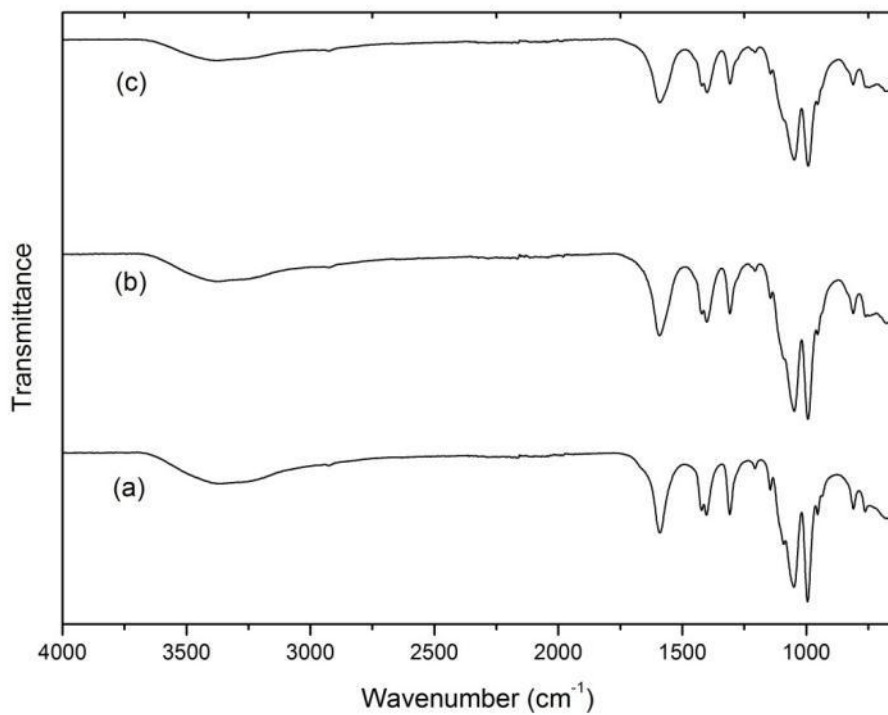


Fig. A7.10 FTIR spectra of (a) ethanol treated K⁺-BIRM-1, (b) after 5 hours evacuation and (c) after 15 hours evacuation.